

Modelling and parametrization of turbulent convective processes over leads in sea ice

Dissertation

zur Erlangung des akademischen Grades
Doktor der Naturwissenschaften
–Dr. rer. nat.–

Vorgelegt von
Janosch Michaelis

am 06. Oktober 2020

im Fachbereich 1 (Physik/Elektrotechnik)
der Universität Bremen

Erster Gutachter: Prof. Dr. Thomas Jung
Zweiter Gutachter: Prof. Dr. Christian Haas

Die Dissertation wurde angefertigt am Alfred-Wegener-Institut Helmholtz-Zentrum für Polar- und Meeresforschung in Betreuung durch Prof. Dr. Thomas Jung als ersten Gutachter sowie durch Dr. Christof Lüpkes und Dr. Jörg Hartmann.

Eingereicht am 06. Oktober 2020
Datum des Kolloquiums: 14. Dezember 2020

Abstract

In the polar ocean regions, the Earth's climate system is characterised by many different interaction processes between atmosphere, ocean, and sea ice. Especially between late autumn and spring, the sea ice cover plays a very important role in this system due to its mainly insulating effect, which minimises the exchange of energy between the ocean and the atmosphere. Nonetheless, also in the cold season with large sea ice cover, a strong turbulent transport of heat and moisture is possible between the relatively warm ocean and the cold atmosphere, for example, through elongated open-water channels in sea ice, which are called leads. The convective atmospheric transport over leads is driven mainly by large spatial temperature differences causing plumes with enhanced turbulent transport, which strongly affect the characteristics of the atmospheric boundary layer (ABL) depending on both lead geometry and meteorological forcing. Understanding and quantifying these rather small-scale physical processes is crucial for improving model results also on larger scales and for obtaining accurate projections of the future climate.

The focus of this thesis lies on a detailed investigation of the atmospheric processes related to the flow over leads, predominantly by means of small-scale numerical modelling. The applied model uses grid sizes so that the convective plume but not the single turbulent eddies are resolved, which requires turbulence parametrization and validation of the corresponding results. The central part of this thesis is the derivation of an improved parametrization to describe the turbulent fluxes over leads of different width. The new parametrization follows a non-local approach and it is derived based on an already existing closure, but, as a new feature, the lead width is included as a parameter.

Small-scale model results obtained with the new parametrization as well as with already existing approaches are evaluated in this thesis for different idealised and observed situations. As a first step, for the idealised cases, the corresponding model results are compared with new time-averaged large eddy simulation results. It is shown that an improved representation of several ABL patterns is obtained when using the new approach for situations of a lead-perpendicular flow in a neutrally stratified ABL below a strong capping inversion.

As a second step, small-scale model results are validated using airborne observations. As compared with the idealised cases, also stable inflow conditions and shallower boundary layers are considered. A basic representation of the observed patterns is obtained by the model also for these situations, but some effects remain underestimated. Therefore, further modifications of the new parametrization are introduced, which cause an improved agreement between model results and observations.

Besides the new parametrization, also model results obtained with a local turbulence closure are evaluated for the idealised and observed cases. Several drawbacks are shown in the corresponding results, especially for the idealised cases, whereas some of the observed ABL characteristics can be basically reproduced also with this closure type. However, the advantage of applying a non-local approach is clearly shown by the physically most reasonable representa-

tion of atmospheric processes, especially in regions of both upward heat transport in neutral or even slightly stable conditions (counter-gradient transport) and vertical entrainment.

Finally, a preliminary study is carried out to point at potential implications of small-scale lead-generated atmospheric effects on larger scales. The small-scale model is applied to simulate the flow over different spatial distributions of sea ice and leads and over a region of continuous fractional sea ice cover representing a few grid cells of a regional climate model with the same sea ice concentration in each cell. It is shown by comparison of domain-averaged profiles that the distribution of leads and their geometry has a profound impact on ABL characteristics also on a larger scale. Moreover, differences are obtained depending on the applied turbulence parametrization. Although at the moment this result cannot be validated by observations, it points clearly to the necessity of an improved treatment of leads in large-scale models.

Zusammenfassung

Im Nord- und Südpolarmeer ist das Klimasystem der Erde durch viele unterschiedliche Wechselwirkungsprozesse zwischen Atmosphäre, Ozean und Meereis geprägt. Die Meereisbedeckung spielt dabei in diesem System durch ihren isolierenden Effekt und dem folglich minimierten Austausch zwischen Ozean und Atmosphäre eine wichtige Rolle, speziell zwischen Spätherbst und Frühling. Nichtsdestotrotz, auch in der kalten Jahreszeit mit großflächiger Meereisbedeckung ist ein starker turbulenter Transport von Wärme und Feuchte zwischen dem relativ warmen Ozean hinein in die kalte Atmosphäre möglich, zum Beispiel durch längliche Öffnungen (Rinnen) im Meereis. Der konvektive atmosphärische Transport über Rinnen wird durch starke Temperaturunterschiede verursacht, was zu konvektiven Plumes mit verstärktem turbulenten Transport führt. Die Plumes haben einen starken Einfluss auf die Charakteristika der atmosphärischen Grenzschicht, welcher wiederum von der Rinnengeometrie und den meteorologischen Bedingungen abhängt. Das Verständnis und die Quantifizierung dieser eher kleinskaligen Prozesse ist entscheidend, um Modellergebnisse zu verbessern, was auch die Ergebnisse großskaliger Modelle sowie genaue Projektionen des zukünftigen Klimas mit einschließt.

In dieser Dissertation wird eine detaillierte Untersuchung von Prozessen durchgeführt, die der atmosphärischen Strömung über Rinnen zuzuordnen sind, vornehmlich mithilfe von kleinskaliger numerischer Modellierung. Durch die im Modell verwendete Gittergröße können konvektive Plumes aufgelöst werden, nicht jedoch einzelne turbulente Wirbel, sodass eine Parametrisierung turbulenter Flüsse sowie eine Validierung der zugehörigen Ergebnisse vonnöten sind. Hauptsächlich geht es in dieser Arbeit um die Herleitung einer verbesserten Parametrisierung der turbulenten Flüsse über Rinnen mit verschiedener Breite. Die neue Parametrisierung folgt einem nicht-lokalen Ansatz und sie basiert auf einer bereits vorhandenen Schließung. Jedoch ist als eine der zentralen Neuerungen die Rinnenbreite als Parameter in dem neuen Ansatz mit berücksichtigt.

Die Ergebnisse, die mit dem kleinskaligen Modell unter Verwendung der neuen sowie bereits existierender Schließungen erzielt wurden, werden in dieser Arbeit für verschiedene idealisierte und beobachtete Situationen evaluiert. Der erste Schritt besteht aus einem Vergleich der zugehörigen Ergebnisse mit neuen, zeitlich gemittelten Ergebnissen eines Grobstrukturmodells (LES Modell, "large eddy simulation model") für die idealisierten Fälle. Für rinnensenkrechte Strömungen in einer neutral geschichteten Grenzschicht, die von einer starken abgehobenen Inversion nach oben begrenzt ist, zeigt sich, dass eine verbesserte Darstellung von verschiedenen Strukturen der Grenzschicht erzielt werden kann, wenn die neue Schließung verwendet wird.

Der zweite Schritt ist dann eine Validierung von weiteren Ergebnissen des kleinskaligen Modells mithilfe von flugzeuggestützten Beobachtungen. Verglichen mit den idealisierten Fällen werden in den beobachteten Fällen auch Effekte durch eine stabile Schichtung im Einströmbereich sowie durch flachere Grenzschichten berücksichtigt. Die beobachteten Muster und Strukturen werden vom Modell grundlegend wiedergegeben, jedoch werden manche beobachteten Effekte unterschätzt. Folglich werden weitere Modifikationen der neuen Parametrisierung vor-

gestellt, mit denen eine verbesserte Übereinstimmung zwischen beobachteten und simulierten Strukturen erzielt wird.

Neben der neuen Parametrisierung werden auch Modellergebnisse evaluiert, die mit einem lokalen Schließungsansatz erzielt wurden. In den zugehörigen Modellergebnissen zeigen sich einige Nachteile, speziell für die idealisierten Fälle, wohingegen manche von den beobachteten Grenzschichtcharakteristika auch mit dieser Schließung vom Modell grundlegend wiedergegeben werden können. Jedoch zeigen sich die Vorteile eines nicht-lokalen Ansatzes deutlich, nämlich durch die physikalisch betrachtet vernünftigste Darstellung atmosphärischer Prozesse, speziell in Regionen mit zwar neutraler oder sogar leicht stabiler Schichtung bei gleichzeitig immer noch aufwärts gerichteten Flüssen (den Gradienten entgegengerichtetem Transport, "counter-gradient transport") und in Regionen mit vertikalem Einmischen wärmerer Luft aus der abgehobenen Inversion in die Grenzschicht ("entrainment").

Schließlich wird noch eine vorläufige Studie durchgeführt, mit der mögliche Auswirkungen von kleinskaligen, rinnengenerierten atmosphärischen Prozessen auf größeren Skalen gezeigt werden sollen. Das kleinskalige Modell wird dabei dafür verwendet, die Strömung über verschiedenen Rinnenkonfigurationen sowie über einer Region mit kontinuierlicher, mosaikartiger Meereisbedeckung zu simulieren, wobei letztere eine kleine Anzahl von Gitterzellen eines regionalen Klimamodells mit derselben Meereiskonzentration in jeder Zelle repräsentiert. Anhand eines Vergleichs von gebietsgemittelten Vertikalprofilen wird gezeigt, dass sowohl die Rinnen selbst als auch ihre Geometrie auch auf der größeren Skala umfassende Auswirkungen auf Grenzschichtcharakteristika haben. Des Weiteren zeigen sich Unterschiede je nach verwendeter Parametrisierung. Auch wenn diese Ergebnisse momentan nicht mit Messungen validiert werden können, wird hierdurch sehr deutlich aufgezeigt, dass großskalige Modelle im Hinblick auf kleinskalige Prozesse über Rinnen verbessert werden müssen.

Table of contents

| | |
|---|-------------|
| Abstract | I |
| Zusammenfassung | III |
| List of figures | VIII |
| List of tables | XII |
| 1 Introduction | 1 |
| 1.1 Lead characteristics and their role for the polar atmosphere | 2 |
| 1.1.1 Convective heat transport and turbulence over leads | 3 |
| 1.1.2 Convective plumes over leads and their overall impact | 4 |
| 1.1.3 Local effects of leads on the near-surface atmosphere | 4 |
| 1.1.4 Local effects of leads on the entire turbulent ABL | 5 |
| 1.1.5 Modelling of the ABL over leads and turbulence parametrizations | 6 |
| 1.1.5.1 Local approach for first-order closures | 7 |
| 1.1.5.2 Non-local approach for first-order closures | 8 |
| 1.1.6 Regional and large-scale relevance of ABL processes over leads | 8 |
| 1.2 Scope and structure of the thesis | 9 |
| 2 Idealised lead scenarios: Modelling and derivation of a new turbulence parametrization | 11 |
| 2.1 Introduction | 12 |
| 2.2 Models | 14 |
| 2.2.1 LES model | 14 |
| 2.2.2 Microscale model | 16 |
| 2.2.2.1 Model description | 16 |
| 2.2.2.2 Local and non-local turbulence parametrizations in METRAS | 16 |
| 2.2.2.2.1 Local mixing-length closure | 17 |
| 2.2.2.2.2 Non-local closure of L08 | 17 |
| 2.2.3 Scenarios and setup of models | 20 |
| 2.3 LES results | 21 |
| 2.4 Microscale model results with different turbulence closures | 24 |
| 2.5 New turbulence parametrization | 27 |
| 2.5.1 Principles and derivation | 27 |
| 2.5.2 Results for wide leads | 30 |
| 2.5.2.1 Cold cases | 30 |
| 2.5.2.2 Warm cases | 31 |
| 2.5.2.3 Variance of vertical velocity | 31 |

| | | |
|----------|--|-----------|
| 2.5.3 | Results for narrow leads | 33 |
| 2.5.3.1 | Lead width: 1 km | 34 |
| 2.5.3.2 | Lead width: 0.5 km | 35 |
| 2.5.4 | Sensitivity studies | 36 |
| 2.5.4.1 | Variation of parameters | 36 |
| 2.5.4.2 | Momentum transport | 38 |
| 2.6 | Discussion | 38 |
| 2.6.1 | Importance of non-local closure and L as parameter | 38 |
| 2.6.2 | Methodological limitations | 42 |
| 2.7 | Conclusions on the derivation of the new non-local approach | 43 |
| 2.8 | Further refinements of the parametrization | 45 |
| 2.8.1 | Entrainment | 45 |
| 2.8.1.1 | Increased upper limit for the upper plume boundary | 46 |
| 2.8.1.2 | Explicit entrainment term | 47 |
| 2.8.2 | Idealised scenarios including humidity | 51 |
| 2.8.3 | Fetch-dependent surface layer parameters and IBL growth | 53 |
| 2.8.4 | Conclusions on further refinements of the parametrization | 57 |
| 3 | Modelling and parametrizing convection over leads compared with airborne measurements | 59 |
| 3.1 | Introduction | 60 |
| 3.2 | The campaign STABLE | 62 |
| 3.2.1 | March 10, 2013 | 63 |
| 3.2.2 | March 25, 2013 | 64 |
| 3.2.3 | March 26, 2013 | 64 |
| 3.3 | Model description | 64 |
| 3.3.1 | Model setup | 65 |
| 3.4 | Simulation results with non-modified parametrizations | 67 |
| 3.4.1 | Model runs 1003-MIX and 1003-NL1 | 68 |
| 3.4.2 | Model runs 2503-MIX and 2503-NL1 | 71 |
| 3.4.3 | Model runs 2603-MIX and 2603-NL1 | 75 |
| 3.5 | Modification of the M20 parametrization | 78 |
| 3.5.1 | Determination of the ABL height z_i | 78 |
| 3.5.2 | Adjustment of parameter a to stably stratified inflow conditions | 80 |
| 3.5.3 | Model runs 1003-NL2 and 1003-NL3 | 81 |
| 3.5.4 | Model runs 2503-NL2 and 2503-NL3 | 83 |
| 3.5.5 | Model run 2603-NL2 | 85 |
| 3.6 | Discussion | 86 |
| 3.7 | Conclusions for the study on the cases from STABLE | 90 |
| 3.8 | Atmospheric flow over a lead in the Weddell Sea (Antarctica) | 91 |
| 3.8.1 | Observations | 92 |
| 3.8.2 | Model setup | 93 |
| 3.8.3 | Results | 94 |

| | | |
|----------|---|------------|
| 3.8.4 | Discussion and conclusions of the UAS-study | 95 |
| 4 | Modelling of the flow over idealised lead ensemble scenarios | 97 |
| 4.1 | Effects on lead-generated convection due to an upwind neighbouring lead . . . | 97 |
| 4.2 | Potential implications of small-scale lead effects in non-convection-resolving models | 101 |
| 4.2.1 | Scenarios and methods | 101 |
| 4.2.2 | Results | 103 |
| 4.2.2.1 | Vertical cross-sections for case ENS-C | 103 |
| 4.2.2.2 | Horizontal developments of different ABL quantities | 104 |
| 4.2.2.3 | Domain-averaged profiles of different ABL quantities | 107 |
| 4.2.3 | Discussion | 111 |
| 5 | Summary and outlook | 113 |
| | Acknowledgements | 118 |
| A | Appendix for chapter 1 | 120 |
| B | Appendix for chapter 2 | 122 |
| B.1 | Determination of the parameters d_w and d_θ | 122 |
| B.2 | Determination of the parameters c and a | 123 |
| B.3 | Sensitivity of microscale model results on the horizontal resolution | 125 |
| B.4 | Supplementary figures | 128 |
| C | Appendix for chapter 4 | 133 |
| | Publications within this thesis | 137 |
| | Acronyms | 139 |
| | List of symbols | 140 |
| | Latin symbols | 140 |
| | Greek symbols | 142 |
| | Mathematical operators | 143 |
| | Bibliography | 144 |

List of figures

| | | |
|------|---|----|
| 1.1 | Photographs of leads in sea ice in the marginal ice zone Northwest of Svalbard. | 3 |
| 1.2 | Sketch of the convective plume developing in the convective ABL over a lead in sea ice. | 5 |
| 1.3 | Spectral energy distribution of turbulence in the ABL and the corresponding ranges typically resolved and parametrized in LES or microscale RANS models. | 7 |
| 2.1 | Sketch of a convective plume developing in an ABL over a polar lead and illustration of the principles of the new non-local parametrization. | 15 |
| 2.2 | Vertical cross-sections of sensible heat flux and vertical potential temperature gradient obtained by LES for four different idealised cases of the flow over wide leads. | 23 |
| 2.3 | Vertical cross-sections of horizontal wind speed and vertical momentum flux obtained by LES for four different idealised cases of the flow over wide leads. | 25 |
| 2.4 | Vertical cross-sections of four different quantities obtained for the idealised case L5c-U5 by METRAS using the local closure or the non-local closure by L08. | 26 |
| 2.5 | Vertical cross-sections of non-local sensible heat flux and vertical velocity variance obtained for the idealised case L5c-U5 by METRAS using the L08 closure. | 27 |
| 2.6 | Horizontal development of the non-local term Γ at different height levels as obtained by METRAS using the new parametrization with two different equations for the idealised case L5c-U5. | 29 |
| 2.7 | Vertical cross-sections of sensible heat flux and vertical potential temperature gradient obtained by METRAS using the new parametrization for four different idealised cases of the flow over wide leads. | 32 |
| 2.8 | Vertical cross-sections of horizontal wind speed and vertical momentum flux obtained by METRAS using the new parametrization for four different idealised cases of the flow over wide leads. | 33 |
| 2.9 | Vertical cross-sections of sensible heat flux and vertical potential temperature gradient obtained by LES and by METRAS using the new parametrization for the idealised case L5w-U5. | 34 |
| 2.10 | Vertical cross-sections of the vertical velocity variance obtained by LES and by METRAS using the new parametrization for four different idealised cases of the flow over wide leads. | 35 |
| 2.11 | Vertical cross-sections of sensible heat flux and potential temperature obtained by METRAS using the new parametrization for four different idealised cases of the flow over narrow leads. | 36 |
| 2.12 | Vertical cross-sections of sensible heat flux and vertical potential temperature gradient obtained by LES and by METRAS using two different parametrizations for the idealised case L0.5c-U5. | 37 |
| 2.13 | Vertical cross-sections of horizontal wind speed and vertical momentum flux for the idealised case L5c-U5 obtained by METRAS using the new parametrization with two alternative calculations for either the eddy diffusivity for momentum or the maximum mixing-length. | 39 |

| | | |
|------|---|----|
| 2.14 | Vertical cross-sections of the non-local sensible heat flux obtained by METRAS using the L08 closure or the new parametrization for four different idealised cases of the flow over leads. | 40 |
| 2.15 | Differences in potential temperature between LES and METRAS using either the new parametrization or the local closure for four idealised cases of the flow over leads. | 41 |
| 2.16 | Differences in potential temperature between LES and METRAS using the local closure with a much lower maximum mixing-length than in other simulations with that closure for two idealised cases of the flow over leads. | 42 |
| 2.17 | Vertical cross-sections of the potential temperature obtained by LES and by METRAS using the new parametrization for four idealised cases of the flow over wide leads. | 46 |
| 2.18 | Vertical cross-sections of sensible heat flux and potential temperature obtained by METRAS using the new parametrization with an increased upper limit for the upper IBL height for the idealised cases L5c-U5 and L10c-U5. | 48 |
| 2.19 | Vertical cross-sections of three different quantities obtained by METRAS using an alternative approach for the kinematic heat flux equation for the cases L5c-U5 and L10c-U5. | 50 |
| 2.20 | Vertical cross-sections of latent heat flux and specific humidity obtained by METRAS using the new parametrization for four different idealised cases of the flow over wide leads. | 53 |
| 2.21 | LES results of different surface layer parameters as a function of non-dimensional distance over the lead for all idealised cases. | 55 |
| 3.1 | Observed surface temperatures for three cases of the flow over leads observed during the campaign STABLE on March 10, 25, and 26, 2013. | 63 |
| 3.2 | Observed profiles of atmospheric temperature and horizontal wind speed, and the corresponding inflow profiles obtained by METRAS for the three observed cases from STABLE. | 66 |
| 3.3 | Vertical cross-sections obtained by the runs 1003-MIX and 1003-NL1 for March 10, 2013. | 69 |
| 3.4 | Vertical profiles obtained by the runs 1003-MIX and 1003-NL1 and the corresponding observations for March 10, 2013. | 70 |
| 3.5 | Vertical cross-sections obtained from the saw-tooth leg on March 25, 2013. | 72 |
| 3.6 | Vertical cross-sections obtained by the runs 2503-MIX and 2503-NL1 for March 25, 2013. | 73 |
| 3.7 | Vertical profiles obtained by the runs 2503-MIX and 2503-NL1 and the corresponding observations for March 25, 2013. | 74 |
| 3.8 | Vertical cross-sections obtained by the runs 2603-MIX and 2603-NL1 for March 26, 2013. | 76 |
| 3.9 | Vertical profiles obtained by the runs 2603-MIX and 2603-NL1 and the corresponding observations for March 26, 2013. | 77 |
| 3.10 | Upper IBL height $\delta(y)$ for March 10, 2013 obtained by METRAS using the M20 parametrization with a varying ABL height $z_i(y)$ obtained with three different methods. | 79 |
| 3.11 | Vertical cross-sections obtained by the runs 1003-NL2 and 1003-NL3 for March 10, 2013. | 81 |
| 3.12 | Vertical profiles obtained by the runs 1003-NL2 and 1003-NL3 and the corresponding observations for March 10, 2013. | 82 |

| | | |
|------|---|-----|
| 3.13 | Vertical cross-sections obtained by the runs 2503-NL2 and 2503-NL3 for March 25, 2013. | 83 |
| 3.14 | Vertical profiles obtained by the runs 2503-NL2 and 2503-NL3 and the corresponding observations for March 25, 2013. | 84 |
| 3.15 | Vertical cross-sections obtained by the run 2603-NL2 for March 26, 2013. | 85 |
| 3.16 | Vertical profiles obtained by the run 2603-NL2 and the corresponding observations for March 26, 2013. | 86 |
| 3.17 | Values of the parameter a of the new parametrization against the observed upwind vertical potential temperature gradient including a hyperbolic fit derived based on these values. | 88 |
| 3.18 | Observed and simulated temperature difference from the corresponding values at the upwind lead edges for the height of the lowest flight legs for all three cases from STABLE considered in chapter 3. | 89 |
| 3.19 | Photographs of the M ² AV and of the ice situation during the observations performed over a lead located in Weddell Sea (Antarctica) on August 2, 2013. | 92 |
| 3.20 | Observations with the M ² AV at different altitudes on August 2, 2013. | 93 |
| 3.21 | Measured and modelled vertical profiles of potential temperature and sensible heat flux for August 2, 2013. | 95 |
| 3.22 | Horizontal development of air temperature and horizontal wind speed obtained by two different model simulations for the case observed on August 2, 2013. | 96 |
| 4.1 | Model domain and modelled domain-averaged vertical profiles of sensible heat flux and potential temperature for a flow over two 1 km-wide leads. | 98 |
| 4.2 | Model domain and modelled domain-averaged vertical profiles of sensible heat flux and potential temperature for a flow over two 5 km-wide leads. | 99 |
| 4.3 | Vertical cross-sections of sensible heat flux and potential temperature obtained by four different simulations of the flow over a 5 km-wide lead downwind of another lead. | 100 |
| 4.4 | Sketch of the five different model domains used for the sensitivity study in section 4.2. | 102 |
| 4.5 | Vertical cross-sections of potential temperature and horizontal wind speed obtained by a large-scale simulation with METRAS for the flow over a region of fractional sea ice concentration (climate model run). | 104 |
| 4.6 | Horizontal development of different quantities at a height of 10 m as a function of distance obtained by microscale model runs using the M20 closure for the four lead cases and by the climate model run. | 105 |
| 4.7 | Horizontal development of different quantities at a height of 290 m as a function of distance obtained by microscale model runs using the M20 closure for the four lead cases and by the climate model run. | 107 |
| 4.8 | Domain-averaged vertical profiles of sensible heat flux and potential temperature obtained by all simulations for the five cases considered for the sensitivity study. | 108 |
| 4.9 | Domain-averaged vertical profiles of horizontal wind speed and vertical momentum flux obtained by all simulations for the five cases considered for the sensitivity study. | 110 |
| B1 | Illustration of the determination of the constant parameters d_w and d_θ in the M20 parametrization. | 123 |
| B2 | Distribution of the parameter $c(y, z)$ as derived from LES and averaged values. | 125 |

| | | |
|----|---|-----|
| B3 | Vertical cross-sections of sensible heat flux and potential temperature for the idealised case L5c-U5 obtained by METRAS with the new parametrization using different horizontal grid sizes. | 126 |
| B4 | Vertical cross-sections of horizontal wind speed and vertical momentum flux for the idealised case L5c-U5 obtained by METRAS with the new parametrization using different horizontal grid sizes. | 127 |
| B5 | Vertical cross-sections of the Richardson number for the idealised case L5c-U5 as obtained by LES and by METRAS using different parametrizations. | 129 |
| B6 | Vertical cross-sections of sensible heat flux and vertical potential temperature gradient obtained by METRAS using the M20 parametrization with alternative values for the parameter b | 129 |
| B7 | Vertical cross-sections of sensible heat flux and potential temperature obtained by LES for four different idealised cases of the flow over narrow leads. | 130 |
| B8 | Vertical cross-sections of sensible heat flux for all idealised cases of wide leads obtained by LES used to determine the linearly approximated upper plume boundaries. | 131 |
| B9 | Vertical cross-sections of sensible heat flux for all idealised cases of narrow leads obtained by LES used to determine the linearly approximated upper plume boundaries. | 132 |
| C1 | Horizontal development of different quantities at a height of 10 m as a function of distance obtained by microscale model runs using the M20 closure with a varying ABL height for the four lead cases and by the climate model run. | 133 |
| C2 | Horizontal development of different quantities at a height of 290 m as a function of distance obtained by microscale model runs using the M20 closure with a varying ABL height for the four lead cases and by the climate model run. | 134 |
| C3 | Horizontal development of different quantities at a height of 10 m as a function of distance obtained by microscale model runs using the local closure for the four lead cases and by the climate model run. | 135 |
| C4 | Horizontal development of different quantities at a height of 290 m as a function of distance obtained by microscale model runs using the local closure for the four lead cases and by the climate model run. | 136 |

List of tables

| | | |
|-----|---|-----|
| 2.1 | Summary of all idealised cases of the flow over leads investigated in chapter 2. | 21 |
| 3.1 | Overview of the settings for the numerical simulations of the observed cases from STABLE. | 66 |
| 3.2 | Initial conditions for the model runs of the discussed case-studies from STABLE. | 67 |
| B1 | Values derived for the parameter a in the M20 parametrization based on LES results. | 124 |

1 Introduction

The Earth's climate system is characterised by many different complex interaction processes and feedback mechanisms among its components. The understanding of at least the most important processes is a key factor to project future stages of the climate system. On the one hand, many interactions are at least conceptually well-understood, for example, the surface albedo feedback (Budyko, 1969; Sellers, 1969). In polar sea ice regions, it is a positive feedback mechanism since an increase in surface temperature leads to enhanced sea ice melt, causing a lowered surface albedo and, in turn, further increasing surface temperatures due to a higher amount of absorbed solar radiation. In present-day coupled Earth system models, which are used for projections of the future state of the climate system assuming different scenarios, this feedback mechanism is approximately included and improved parametrizations of the detailed physics more and more help to improve model results. Hence, for example, according to the latest report of the Intergovernmental Panel of Climate Change (IPCC), an improved representation of the observed September minimum sea ice extent was obtained with the latest generation of such models (Flato et al., 2013). On the other hand, there are plenty of other processes, for which an improved understanding is needed and whose impact on climate-relevant scales is yet to be quantified. Furthermore, starting with the industrial revolution, Earth is facing substantial modifications due to the huge anthropogenic emissions of greenhouse gases (IPCC, 2013). At first glance, this might become visible only in terms of a fundamental change in the atmospheric composition and a corresponding increase of the global mean surface temperature due to the anthropogenically increased greenhouse effect (IPCC, 2013). Currently, the global mean surface temperature has increased by about +1.1 K compared to pre-industrial levels¹, which is a warming rate most probably unprecedented at least in the past 2000 years (e.g., IPCC, 2014; Neukom et al., 2019).

At the second glance, there are also fundamental changes concerning the other climate system components, such as sea level rise, ocean acidification, or rapidly decreasing sea ice concentration (SIC), as also shown, for example, in the latest IPCC report (IPCC, 2013). The polar regions, especially the Arctic, face an amplified warming exceeding the global mean temperature increase by a factor of two to three since the late 20th century, the so-called Arctic Amplification (see, for example, Serreze & Francis, 2006; Serreze et al., 2009; Serreze & Barry, 2011; Wendisch et al., 2017). Thus, there is also growing evidence of a practically ice-free Arctic ocean at the time of the annual minimum sea ice extent by the mid of the 21st century (e.g., SIMIP Community, 2020). However, there are various uncertainties related to such projections since many processes are described only inadequately in climate models (Flato et al., 2013). For example, physical processes over inhomogeneous surfaces, such as surface fluxes from different sea ice patterns, seem to play a crucial role for the polar climate system (see, for example, the review by Vihma et al., 2014). In turn, to correctly consider those fluxes

¹the annual global mean surface temperature of the years 2015-2019 compared to the corresponding mean value of the baseline period 1850-1900, data from GISTEMP Team (2020)

in climate models, it is important to understand the underlying physical background and the mathematical relations of the determining quantities. Moreover, since it already marks quite an expensive task for models to obtain a well-represented picture of all mechanisms in the Earth's climate system (e.g., the seasonal cycle of the sea ice extension, which is now well-represented by the latest model generation, see Flato et al., 2013), it is most likely even more difficult when aiming at projecting implications due to a warming climate, such as the declining sea ice cover.

The important role of sea ice in the climate system is mainly expressed by its strong and also highly variable influence on the energy budget in the polar ocean regions. Especially in winter, sea ice is an important component for the energy exchange between ocean and atmosphere. During that season, the near-surface air temperature over sea ice can reach values below -40°C (e.g., Lindsay & Rothrock, 1994) leading to a strong temperature difference as compared to the warm ocean below with its near-surface temperature close to the freezing point. Following the laws of thermodynamics, this would result in a strong upward heat transport in the order of 10^2 to 10^3 Wm^{-2} and, thus, net heat loss of the ocean. However, the sea ice cover minimises this transport due to its insulating effect and the upward heat transport through sea ice is then limited to molecular diffusion. Nonetheless, even in winter and even in the central polar ocean regions, openings in the sea ice cover are formed, so-called polynyas and leads, which enable a direct transfer of heat, moisture, and momentum between ocean and atmosphere, followed by a strong impact not only on the surface energy budget but also on the energy budget of the polar atmosphere. They represent highly inhomogeneous areas accompanied with processes acting on rather small meteorological scales, but with a high relevance also for the polar climate. This thesis deals with a detailed investigation of the physical atmospheric processes connected with leads in the polar sea ice regions with a focus on modelling and parametrization.

1.1 Lead characteristics and their role for the polar atmosphere

Leads are defined as elongated, predominantly linearly shaped open-water channels in sea ice, which are formed due to divergent sea ice drift as a result of inhomogeneous forcing by ocean currents and wind (Smith et al., 1990). They are either ice-free or covered with thin, new ice (see Figure 1.1). Unlike polynyas, which typically "occur quasi-continuously in the same region", leads do not have fixed locations (Smith et al., 1990). The length of leads ranges from hundreds of meters to hundreds of kilometres and their width from a few meters to a few kilometres, as shown by in situ observations and remote sensing (e.g., Andreas et al., 1979; Lindsay & Rothrock, 1995; Miles & Barry, 1998; Tetzlaff et al., 2015, henceforth abbreviated by T15). As shown by, for example, Lindsay and Rothrock (1995); Marcq and Weiss (2012); Wernecke and Kaleschke (2015) based on different remote sensing data sets, the lead width distribution follows a power law. Such a distribution was also found for the leads observed during the aircraft campaign STABLE in 2013 (SpringTime Atmospheric Boundary Layer Experiment, see T15).

Open-water areas in the polar sea ice regions including leads are important in many aspects. From a biological perspective, leads provide areas with access to oxygen for marine mammals and for polar bears to hunt seals, especially near shorelines (e.g., Massom, 1988; Stirling, 1997). Leads also facilitate navigation for vessels and submarines in pack ice regions (Smith

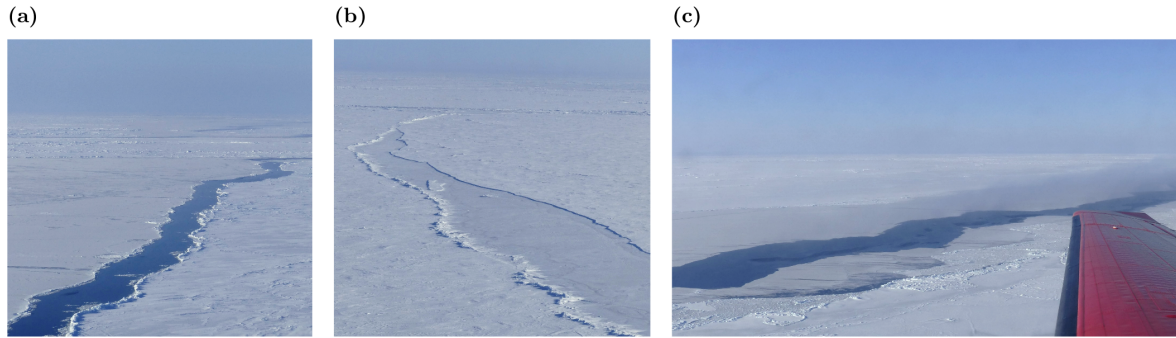


Figure 1.1: Photographs, which were taken from a research aircraft, showing three different leads observed in the marginal sea ice zone Northwest of Svalbard on April 8, 2019. (a) shows an ice-free lead, (b) a lead covered with thin, new ice (nilas), and (c) a lead consisting of both ice-free and nilas-covered regions. In (c), some sea smoke is shown above the ice-free regions.

et al., 1990). Skillingstad and Denbo (2001) showed that plumes of higher-salinity water form beneath leads in sea ice. Results from Kort et al. (2012) indicate a correlation of lead areas and emissions of methane in polar ocean regions. Refreezing leads are also a major driver of the production of new ice in winter (Maykut, 1982). These are only a few examples how leads affect the polar environment, where in this thesis the focus is mainly on their atmospheric impact described in the following in more detail.

1.1.1 Convective heat transport and turbulence over leads

Leads strongly affect the polar atmosphere on various spatial scales, especially in wintertime due to the large temperature contrast between the lead surface and the near-surface atmospheric flow (Smith et al., 1990). Combined with a step change in surface roughness, the abrupt change in surface temperature causes a strong vertical heat transport over leads (e.g., Andreas & Murphy, 1986). This so-called convective heat transport reduces the temperature difference. While its horizontal component is mainly due to advection of air masses with the mean flow, its vertical component is dominated by diffusion due to atmospheric turbulence, which, in turn, represents a chaotic or an irregular fluctuation superimposed on the mean flow (Stull, 1988). Mathematically spoken, for an arbitrary quantity ϕ , this relation is given by $\phi = \bar{\phi} + \phi'$, where $\bar{\phi}$ represents the mean value and ϕ' the turbulent fluctuations of ϕ (e.g., Kraus, 2008).

Turbulent motion is often visualised by eddies of different time and length scales (Stull, 1988). The eddies reach from $\mathcal{O}(10^{-3})$ m with a lifespan of a few second to $\mathcal{O}(10^3)$ m, where these can persist for hours (Stull, 1988). Turbulent transport is predominantly found in the lowest part of the troposphere, the atmospheric boundary layer (ABL), which marks the layer directly affected by the presence of the Earth's surface (Stull, 1988; Garratt, 1994). The lowest 10 % of the ABL mark the surface layer (Stull, 1988). At the top of a surface-heated convective ABL (mixed layer), often a layer of strongly increasing temperature with height is found, the capping inversion, which separates the ABL from the layer above (Stull, 1988). Above the inversion, in the free atmosphere, turbulent transport becomes less important (Stull, 1988). Thus, the vertical extent of the largest turbulent eddies in the ABL is typically in the range of the thickness of the ABL (Stull, 1988).

Turbulence in the ABL is generated mechanically (wind-shear) and thermally (buoyancy)

(e.g., Garratt, 1994). For a flow over a lead with a certain background wind $> 0 \text{ ms}^{-1}$ and in a neutrally stratified ABL, turbulent motion is already present upwind of the lead only due to vertical wind-shear caused by the frictional drag on the flow over sea ice (see, for example, Vihma et al., 2014). Above the lead, rising thermals of warm air (positive buoyancy) enhance turbulent mixing (Figure 1.2). The resulting upward turbulent heat transport is typically $\mathcal{O}(10^2 - 10^3) \text{ Wm}^{-2}$ and it can exceed the molecular heat transport through the surrounding thick sea ice by two orders of magnitude (Badgley, 1966; Maykut, 1978).

1.1.2 Convective plumes over leads and their overall impact

The area dominated by the enhanced turbulence developing over a lead is described as a convective plume (see Figure 1.2). This term is often used in literature to describe both dry and moist lead-generated convection as, for example, by Glendening and Burk (1992); Pinto et al. (1995); Burk et al. (1997); Zulauf and Krueger (2003b), or Lüpkes, Gryanik, et al. (2008, henceforth abbreviated by L08). For leads covered with thin, new ice, those plumes mostly do not become visible since then the latent heat flux becomes very small (see also Lüpkes et al., 2012). Due to the low humidity, almost no condensation occurs. The lead-generated plumes can also be understood as the area of a convective internal boundary layer (IBL) developing over the lead. Especially for lead-perpendicular inflow conditions, the IBL grows with increasing distance over the lead (fetch) and strongly influences ABL characteristics, such as temperature, wind, and flux profiles, depending on the meteorological conditions (e.g., Alam & Curry, 1995; Pinto et al., 1995; Zulauf & Krueger, 2003a, 2003b, L08, T15). The plume may also interact with the capping inversion at the top of the convective ABL (e.g., T15). In the central Arctic Ocean ($> 80^\circ \text{N}$), capping inversions occur at altitudes of a few hundred meters or even below 100 m (Wetzel & Brümmer, 2011). Hence, the convective ABL in the Arctic is often much shallower as a comparable ABL in mid- or low-latitudes. Both the strong depth and the large strength of polar capping inversions often lead to a decoupling between the ABL and the free atmosphere (Esau & Sorokina, 2010). Thus, although very wide leads might cause plumes which rise even up to 4 km height (see Schnell et al., 1989), the strong convection generated over leads predominantly affects the ABL.

1.1.3 Local effects of leads on the near-surface atmosphere

Studies of lead-generated effects on the ABL started in the 1970's. Among others, the "Arctic Ice Joint Dynamics Experiment" (AIDJEX; Paulson & Smith, 1974; Andreas et al., 1979) was an important study addressing the quantification of near-surface processes, namely, surface heat fluxes over natural and artificial leads. Results of this campaign clearly showed an influence of lead-generated heat transport on the near-surface temperature and wind downstream of leads. Other important campaigns were "Arctic Leads Experiment" (LEADEX; Ruffieux et al., 1995; Persson et al., 1997) and "Surface Heat Budget of the Arctic Ocean" (SHEBA; Overland et al., 2000; Persson et al., 2002; Pinto et al., 2003), where the corresponding data served as a basis for quantifying mainly near-surface ABL characteristics over leads. Regarding the derivation of surface heat fluxes, several studies showed the importance of the lead geometry, namely, the lead width (e.g., Alam & Curry, 1997; Andreas & Cash, 1999; Marcq & Weiss, 2012).

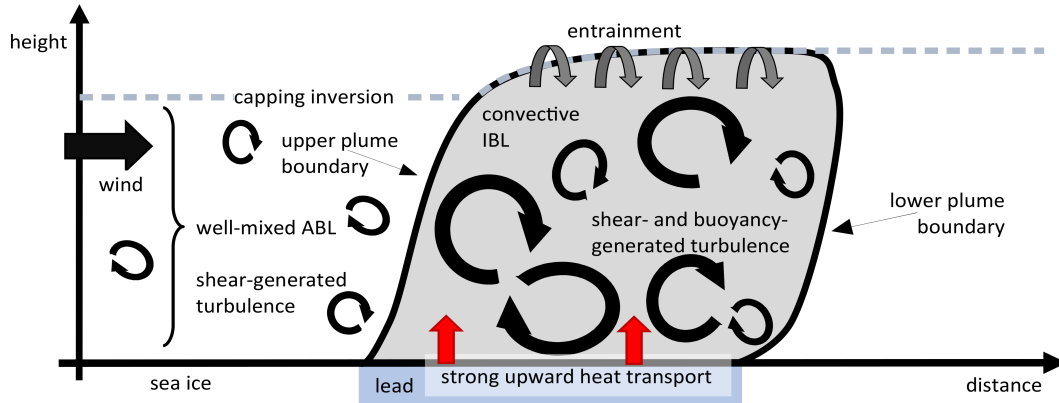


Figure 1.2: Sketch of the turbulent atmospheric boundary layer (ABL) for a lead-perpendicular flow over a lead in sea ice and of the corresponding effects on the ABL by enhanced turbulence due to strong upward convective heat transport over the lead, such as the formation of a convective internal boundary layer (IBL), also referred to as convective plume. The upwind ABL is capped by a strong inversion and penetrating convection may cause downward transport of heat through this layer (vertical entrainment). Modified after L08, Vihma et al. (2014), T15, and Michaelis et al. (2020).

1.1.4 Local effects of leads on the entire turbulent ABL

Besides the cited studies addressing the near-surface effects of leads, several studies were carried out dealing with an investigation of the whole turbulent ABL. These objectives were also the main focus of the campaign STABLE, which was a German campaign coordinated by C. Lüpkes from the Alfred-Wegener-Institute (AWI) in 2013. Airborne observations were performed in the whole turbulent ABL over four different leads providing a data set well-suited for the evaluation of model results (T15). For example, the corresponding observations showed the existence of weak low-level jets (LLJ) upwind of the leads, which had been destroyed due to lead-generated plumes, and also a strong interaction between the plume and the capping inversion was observed causing vertical entrainment (see T15). Apart from those observations, most studies of the ABL flow over leads used numerical models, typically either large eddy simulation (LES, e.g., Glendening & Burk, 1992; Glendening, 1994; Weinbrecht & Raasch, 2001; Esau, 2007; Witha, 2013, and L08), or plume- but non-eddy-resolving small-scale models, mostly Reynolds-Averaged Navier-Stokes (RANS) models for the meteorological micro- or mesoscale (e.g., Alam & Curry, 1995; Pinto et al., 1995; Dare & Atkinson, 1999, 2000; Zulauf & Krueger, 2003a, 2003b; Mauritsen et al., 2005; Wenta & Herman, 2018; Li et al., 2020, and L08).

Typically, with both model types, simulations of idealised or observed situations are investigated to describe the lead-generated effects. To this aim, first an area of interest is selected, which defines the model domain (e.g., Fröhlich, 2006; Pielke Sr., 2013). This area is then discretised on a numerical grid, which is characterised by finite spatial and temporal differences (Pielke Sr., 2013). Both domain and grid size are selected with respect to the modelled phenomena. For the turbulent flow over a polar lead, this concerns the meteorological microscale, which summarises phenomena with a horizontal extension of less than approximately 1 km (e.g., Orlandi, 1975).

In this thesis, simulations of both an LES and a microscale RANS model are analysed. In principle, with both models, the Navier-Stokes equations (see Appendix A) are numerically solved, where the fundamental difference between LES and RANS is the filtering technique;

hence, the way how the turbulent fluctuations ϕ' are treated (Fröhlich, 2006). Unlike LES, a RANS model uses filtered equations obtained by averaging via integration in time and space (Pielke Sr., 2013). Thus, all turbulent deviations from the mean ABL flow, so the entire turbulent scale, is not explicitly resolved (see Figure 1.3). For modelling the convective flow over leads with microscale RANS models, typically, horizontal grid sizes of $\Delta_{x_1} = \Delta_{x_2} = \mathcal{O}(10^2)$ m and vertical grid sizes of $\Delta_{x_3} = \mathcal{O}(10^1)$ m are used (see, for example, Zulauf & Krueger, 2003b; Mauritsen et al., 2005, L08). Hence, also with the RANS model applied in this thesis, the integrated effects of the convective plumes over leads can be resolved, but not the single turbulent eddies.

In LES, the filtering technique is to separate the turbulent scale into a large and a small scale, where the energy-contributing eddies in the production range ("large eddies") are directly resolved (e.g., Stull, 1988; Fröhlich, 2006, and see also Figure 1.3, here). This allows a detailed and instantaneous representation of the turbulent flow. To obtain such a high resolution of the turbulent flow over leads, the corresponding LES models are typically operated using grid sizes of $\mathcal{O}(10^0)$ m or even $\mathcal{O}(10^{-1})$ m in all three directions (see, for example, Glendening & Burk, 1992; Weinbrecht & Raasch, 2001; Esau, 2007; Witha, 2013).

1.1.5 Modelling of the ABL over leads and turbulence parametrizations

In both RANS and LES models, processes that are not resolved (subgrid-scale phenomena) are parametrized (i.e., approximated) to close the system of the governing equations (Pielke Sr., 2013). These processes include turbulence, radiation, or cloud microphysics, depending on the complexity of the model and the phenomena to be modelled, where in this thesis, the focus is on turbulence. Unlike in RANS models, only the dissipation range and parts of the inertial subrange of the turbulent scales are parametrized in LES models (Figure 1.3). Since on this range turbulence can be regarded as isotropic, universal turbulence laws are valid and model results are less sensitive to the applied parametrization (Blackadar, 2012). In RANS models, the entire turbulence spectrum is not explicitly resolved due to the applied filtering technique (Figure 1.3). Furthermore, due to the often anisotropic characteristics of the turbulence in the production range (Stull, 1988; Blackadar, 2012), the model results strongly depend on the applied parametrization. Thus, with LES, many more processes are directly resolved than with RANS, but this also causes much higher computational costs (e.g., Fröhlich, 2006).

For both RANS and LES modelling of the effects of leads on the turbulent ABL, the simulations are typically performed until quasi-stationary conditions are reached (e.g., Glendening & Burk, 1992). The corresponding results obtained with RANS then already allow a derivation of the integrated effects by leads on the ABL, provided the applied parametrization represents a suitable approximation of the subgrid-scale processes, which also depends on the used closure type (see below). Thus, RANS applications are commonly used to investigate relationships among physical quantities and to develop and improve parametrizations, which are then validated either with observations or (quasi-stationary) time-averaged LES results (e.g., Lüpkes & Schlünzen, 1996, L08).

Turbulent fluxes of heat, moisture, and momentum (see appendix A) occur in all spatial directions. Here, the focus lies on their vertical components since they dominate in the con-

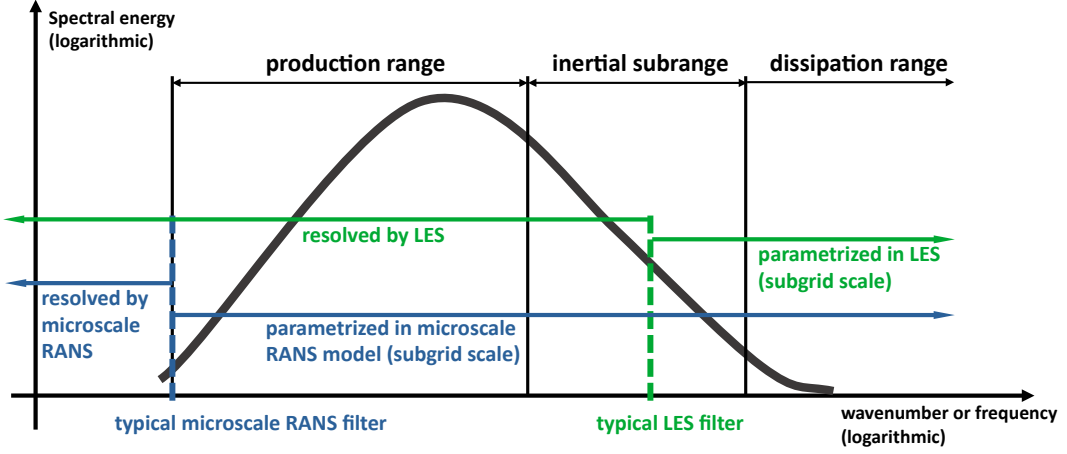


Figure 1.3: Sketch of the spectral energy distribution of turbulence in the atmospheric boundary layer against wavenumber or frequency (logarithmic scales), of the corresponding ranges (production range, inertial subrange, and dissipation range), and of the ranges typically resolved and parametrized with LES and microscale RANS models. Modified based on Stull (1988), Fröhlich (2006), Kraus (2008), and Witha (2013).

vective ABL (Garratt, 1994). The vertical transport terms can be expressed using covariances of the vertical wind component w and the transported quantity, namely, $\overline{w'\theta'}$ for temperature transport, $\overline{w'q'_v}$ for humidity transport, and $\overline{w'u'}$ and $\overline{w'v'}$ for momentum transport. These terms result from filtering the Navier-Stokes equations (e.g., Kraus, 2008). In microscale and mesoscale RANS models, different closure types are applied to parametrize the transport terms, depending on the order of the moment to be approximated. At least, first-order closures are needed, where prognostic equations for the first moments $\overline{\phi}$ are made; hence, the turbulent transport terms (second moments) are diagnostically determined via parametrizations using the resolved model quantities (Stull, 1988). The nature of first-order closures is explained in more detail below. Besides this closure type, for modelling the turbulent flow over leads, also 1.5-order closures (e.g., Dare & Atkinson, 1999, 2000; Wenta & Herman, 2018; Li et al., 2020) or even higher-order closures (e.g., Alam & Curry, 1995; Pinto et al., 1995; Zulauf & Krueger, 2003a, 2003b; Mauritsen et al., 2005) had already been used. The higher the order of the closure, the larger is also the number of unknown quantities in the equation system (see Stull, 1988), which increases the required computer resources.

1.1.5.1 Local approach for first-order closures

The turbulence parametrizations discussed in this thesis follow first-order closures, in which the turbulent fluxes are related to the gradients of mean quantities using K -theory (see Stull, 1988). For example, for $\overline{w'\theta'}$, such a closure is given by

$$\overline{w'\theta'} = -K_h \frac{\partial \overline{\theta}}{\partial x_3}, \quad (1.1)$$

where $\partial \overline{\theta} / \partial x_3$ is the vertical potential temperature gradient and K_h is the eddy diffusivity for heat. Equation 1.1 represents a local approach for $\overline{w'\theta'}$ since the subgrid-scale flux is connected with the local gradient. Following this approach, K_h can be obtained, for example, using a mixing-length approach (e.g., Herbert & Kramm, 1985). A mixing-length closure represent a suitable

approach for parametrizing the eddy diffusivities in a statically neutral environment wherein turbulence is generated mechanically (Stull, 1988). However, this approach is accompanied by some drawbacks if applied to strongly convective regimes of the homogeneously surface-heated boundary layer dominated by thermals and plumes since, mainly in the upper half of the ABL, upward heat fluxes are present in regions with neutral or even slightly positive vertical potential temperature gradient (Deardorff, 1972; Stull, 1988; Holtslag & Moeng, 1991; Lüpkes & Schlünzen, 1996). L08 show that this holds also for the horizontally strongly inhomogeneous convective ABL over leads in a neutral or slightly stable environment.

1.1.5.2 Non-local approach for first-order closures

A method to overcome the drawbacks accompanied with local closures when aiming at parametrizing turbulent fluxes in the convective ABL over leads is to consider a non-local approach, where still K -theory is considered, but with a gradient correction. For $\overline{w'\theta'}$, such an approach is expressed by

$$\overline{w'\theta'} = -K_h \left(\frac{\partial \bar{\theta}}{\partial x_3} - \Gamma \right), \quad (1.2)$$

with the gradient correction term Γ . L08 used Equation 1.2 to formulate a corresponding parametrization for K_h and Γ for the inhomogeneous convection over leads based on the approach by Lüpkes and Schlünzen (1996), which had been derived for the homogeneous convective ABL. However, unlike for horizontally homogeneous conditions, L08 considered the distance to the leads and, thus, proposed a fetch-dependent parametrization. They showed that microscale model results obtained with their approach agree well with comparable time-averaged LES results for a lead of 1 km width, an ABL height of 300 m, and for a certain range of meteorological forcing. Furthermore, they stated that especially the downstream stratification as obtained with a local closure does not agree with their LES results. Moreover, the observations from STABLE, where the turbulent fluxes were calculated with the eddy covariance method using high-frequent atmospheric measurements, showed indications for the existence of these non-gradient or counter-gradient fluxes (T15). Since L08 focused on a single lead width, they stressed that their closure can be regarded as a basis for further refinements, where especially the lead width should be taken into account for a further development.

1.1.6 Regional and large-scale relevance of ABL processes over leads

Besides the above-mentioned local atmospheric impact of leads, also regional and large-scale effects were found in many studies. Averaged over a certain region, the upward heat transport over leads can be balanced by downward heat fluxes over sea ice, where this balance mainly occurs by the effect of leads on atmospheric temperature (see Overland et al., 2000; Lüpkes, Vihma, et al., 2008). As Lüpkes, Vihma, et al. (2008) also show, this temperature effect, which is due to a change in SIC, can amount to 3.5 K for concentrations larger than 95 % in clear-sky conditions during polar night. A large sensitivity of air temperature on the SIC was also found by Valkonen et al. (2008). Moreover, Lüpkes, Vihma, et al. (2008) and also Chechin et al. (2019) show that leads can increase the atmospheric stability over sea ice, mainly at low wind speeds during polar night (see also Grachev et al., 2005). In addition, also the near-surface relative

humidity over sea ice is probably influenced by the presence of leads in the entire Arctic sea ice region (Andreas et al., 2002).

An effect of leads on atmospheric conditions can be found even several hundred kilometres away from the ice edge as shown by Batrak and Müller (2018). Furthermore, they outline that such an effect is in the range of 12 hr weather forecast accuracy (see also Müller et al., 2017). In addition, also Grötzner et al. (1996), Flato and Ramsden (1997), and Wenta and Herman (2018) suppose that the spatial distribution of open-water and sea ice surfaces might have an effect on large-scale model results. All this clearly shows the importance of the rather small-scale physical processes induced by leads on much larger atmospheric scales.

1.2 Scope and structure of the thesis

Compared to the above-mentioned regional and large-scale effects due to multiple leads, the effects caused by single leads on, for example, temperature might be relatively small (Vihma et al., 2014). However, the strong lead-generated convection considerably modifies the structure of the polar ABL, and there is a certain demand on the complexity of turbulence parametrizations to properly simulate the integrated lead-generated effects (e.g., L08). Furthermore, an insufficient representation of the microscale atmospheric effects due to a single lead might cause drawbacks also for large-scale studies of ensembles of leads, for example, when the conditions upstream of an individual lead are affected by upwind neighbouring leads. Since computer resources are continuously increasing, it is to be expected that leads and their atmospheric effects will be resolved explicitly also in operational numerical weather prediction and climate models any time soon. Namely, for the explicit resolution of leads in sea ice models, some attempts already exist (e.g., Wang et al., 2016; Hutter et al., 2018). Considering Arctic Amplification and its related implications, which might also affect the climate of the mid-latitudes (Cohen et al., 2014), certainly there is an increasing demand on quantifying small-scale atmospheric processes in the polar regions, such as those over leads, to improve their representation in large-scale models (Vihma et al., 2014; Vihma, 2014; Wendisch et al., 2017; Taylor et al., 2018). All this clearly calls for a detailed investigation of lead-generated convection and its effects on the polar atmosphere, which is the main goal of this thesis. Both idealised and observed situations of the convective flow over leads will be investigated to quantify their impact on the ABL. A small-scale atmospheric RANS model is applied, for which different turbulence parametrizations are used, and the corresponding model results are validated with high-resolved, time-averaged LES results and airborne observations.

The main goal of the investigation shown in chapter 2 is, as the first step, to arrive at an improved parametrization of turbulent fluxes over leads in sea ice for non-eddy-resolving, microscale models. Derived based on the non-local parametrization by L08, the main improvement of the new non-local approach is that it considers the geometry of the lead, namely, the lead width. Furthermore, new time-averaged LES results are used to validate the results of the RANS model and they also serve as a basis for deriving the adjustable parameters of the new parametrization. The LES results also give detailed information on the general characteristics of the turbulent flow over leads of different width for different meteorological forcing in a neutrally

stratified ABL capped by a strong inversion. The main part of chapter 2 (sections 2.1 to 2.7) was published as Michaelis et al. (2020) in *Journal of Geophysical Research: Atmospheres*. An examination of further processes that would further improve the new parametrization in future will be addressed in the remaining section.

In a second step (chapter 3), a modelling study is carried out to investigate the convection over leads for which aircraft measurements had been obtained. This concerns three observed cases from the aircraft campaign STABLE (see T15) and another case with observations obtained by an unmanned aerial system over an Antarctic lead (see Lampert et al., 2020). First, the analysis in chapter 3 aims at discussing the quality of microscale model results using a local closure or the new non-local parametrization derived in chapter 2 when applied to the observed cases. Second, possible modifications of the non-local parametrization are discussed to better reproduce effects by stable stratification and by the interaction between the convective plume and the capping inversion. The main part of this chapter (sections 3.1 to 3.7) was submitted under the title "Modelling and parametrization of the convective flow over leads in sea ice and comparison with airborne observations" to *Quarterly Journal of the Royal Meteorological Society*. The analysis in the remaining section of chapter 3 is an extended investigation of my contribution as a co-author in Lampert et al. (2020) published in *MDPI: Atmospheres*.

In chapter 4, the microscale model is applied to investigate the atmospheric impact due to a series of leads rather than by a single lead. It is considered as a preliminary study to point at potential effects of lead ensembles, and potential implications for large-scale, non-convection-resolving models are also going to be discussed based on microscale model results. First, in section 4.1, the quality of microscale model results for the flow over two consecutive leads is evaluated using LES. Second, section 4.2 consists of a sensitivity study on convection over different configurations of leads in a large-scale domain, which is in the typical range of a small number of grid cells of a present-day regional climate model. This study will help to quantify potential effects of leads and their geometry on results obtained by large-scale models.

Finally, chapter 5 provides a summary of the main results, conclusions, and an outlook.²

Three key research questions should be addressed in this thesis:

1. What kind of approach is useful to arrive at an improved turbulence parametrization for the inhomogeneous convection over leads dependent on the lead geometry?
2. How well are observed ABL structures over leads represented by microscale model simulations using different turbulence parametrizations and how important is the complexity of the parametrization?
3. What are the mean atmospheric effects of different configurations of lead ensembles and which implications can be derived for large-scale models?

²The chapters 2 and 3 consist of the above-mentioned papers compiled together with my co-authors. The content of those papers is almost unaltered compared with the original content, where more detailed explanations on the chapters' contents including differences to the original publication/submitted version are provided at the beginning of both chapters. The individual contribution of all co-authors for each of the papers embedded in this thesis is shown in the section "Publications within this thesis" starting on page 137. Moreover, some minor changes were made regarding formatting and the spelling in chapter 2 was changed from American to British English.

2 Idealised lead scenarios: Modelling and derivation of a new turbulence parametrization ¹

Abstract: A new turbulence parametrization is developed for a non-eddy-resolving, microscale model to study the effects of leads (elongated open-water channels in sea ice) of different width on the polar atmospheric boundary layer (ABL). Lead-dominated sea ice regions are characterised by large horizontal inhomogeneities of the surface temperature causing strong convection. Therefore, the new parametrization is based on a previous formulation where inhomogeneous conditions of dry convection over leads and non-local effects on heat fluxes had already been taken into account for a fixed lead width. A non-local, lead-width-dependent approach is applied now for both heat fluxes and momentum fluxes in the convective region. Microscale model results obtained with the new, the previous non-local, and a local parametrization are shown, where 10 idealised cases of a lead-perpendicular, near-neutral ABL flow below a strong capping inversion are considered. Furthermore, time-averaged large eddy simulation (LES) results of those cases are considered for analysing the integrated effects of the dry convection on ABL characteristics. Microscale model results obtained with the new non-local parametrization agree well with the LES for variable lead widths and different atmospheric forcing although there is room for further improvement. Furthermore, several features obtained with a local closure clearly disagree with LES. Thus, the microscale study also points to difficulties that might occur in mesoscale studies over regions where leads dominate the flow regime when local closures are applied.

¹The sections 2.1 to 2.7 consist of the publication with the title *Influence of lead width on the turbulent flow over sea ice leads: Modeling and parametrization* as published in *Journal of Geophysical research: Atmospheres* by Michaelis et al. (2020) as an open-access article. Also the content of Appendix B is part of the publication, where the appendices B.1-B.3 correspond with the appendices A-C of the publication, and the content of Appendix B.4 was published as supporting information. A difference to the publication is found here in section 2.6, where Figure 2.14 was added with a short description for reasons of better comprehensibility. Section 2.8 is an additional contribution for this thesis.

2.1 Introduction

Polar sea ice forms an important component of the Earth's climate system. It reduces the release of heat from the relatively warm ocean into the cold atmosphere, especially between late autumn and spring. However, even in the central polar regions there are always openings of different shape in the closed sea ice cover, so-called polynyas and leads, mainly due to divergent sea ice drift (e.g., Smith et al., 1990; Andreas & Cash, 1999, and T15). Leads are open-water channels, which are either ice free or covered by thin, new ice. Their shape is often linear, but they can also be curved. As can be seen from in situ observations and satellite images, both their length and width is extremely variable. The length can range from several hundred meters to several hundred kilometres, and the width varies between several meters and a few kilometres (e.g., Andreas et al., 1979; Miles & Barry, 1998; Lindsay & Rothrock, 1995, and T15). Mainly during winter, when the differences between the near-surface atmospheric flow and the lead surface can amount up to 40 K, the release of heat from leads is around two orders of magnitude larger than the molecular heat transport through the surrounding sea ice (Badgley, 1966; Maykut, 1978). Thus, with a lead coverage of 1 % in a certain region, roughly half of the heat transport from the ocean to the atmosphere must then occur through leads (Thorndike et al., 1975). Furthermore, based on data from the SHEBA campaign (e.g., Overland et al., 2000; Pinto et al., 2003), Overland et al. (2000) found that upward heat fluxes over leads are balanced by downward heat fluxes over sea ice. This was also shown by Lüpkes, Vihma, et al. (2008) and Chechin et al. (2019) using a 1-D coupled air-ice box model and prescribing a surface consisting of 95 % sea ice and 5 % slightly refrozen leads. They found for sea ice concentrations > 95 % that changing the concentration by 1 % causes a mixed layer atmospheric temperature change of up to 3.5 K. Batrak and Müller (2018) show that an explicit consideration of leads in kilometre-scale atmospheric models can even have an impact on atmospheric conditions several hundred kilometres away from the ice edge in the range of 12 hr weather forecast accuracy (see also Müller et al., 2017).

Focusing more on the local effects of leads, the large temperature difference between the near-surface air and the open water causes strong turbulent convection (convective plumes). An IBL develops, which significantly modifies the structure of the polar ABL depending on the meteorological forcing (wind speed and direction, temperature, and stratification) in the lead environment (T15). Furthermore, also the geometry of the leads plays an important role, especially the lead width (L). During the campaign AIDJEX (Paulson & Smith, 1974; Andreas et al., 1979) measurements were conducted upwind and downwind of several Arctic leads of different width, based on which Andreas and Cash (1999) found that the heat transport over small leads ($L < 100$ m) is more efficient than over larger ones.

Based on the AIDJEX data and on data obtained over a polynya in the Canadian Archipelago (see Smith et al., 1983), Alam and Curry (1997) developed a fetch-dependent parametrization of the integral (lead-averaged) sensible heat fluxes from leads and they found those fluxes to be strongly dependent on L . Also Andreas and Cash (1999) found an L -dependence for heat fluxes over small leads, and they proposed a corresponding parametrization of near-surface heat fluxes. Besides the observations used in Alam and Curry (1997), Andreas and Cash (1999) also used data obtained over a refrozen polynya at drifting station North Pole 23 (see Makshtas &

Nikolaev, 1991). Using both parametrizations, for the flux calculation of an observed distribution of leads near 80 °N, 108 °W in 1996, Marcq and Weiss (2012) found up to 55 % larger fluxes than with a parametrization ignoring the L -dependence. The surface flux dependence found in all those studies shows that L is an important parameter for the quantification of lead-generated effects.

Besides the cited observational and modelling studies focusing on surface fluxes over leads, several modelling studies of the whole turbulent ABL over leads have been performed, for example using LES models (e.g., Glendening & Burk, 1992; Glendening, 1994; Weinbrecht & Raasch, 2001; Esau, 2007). With LES, large turbulent eddies can be resolved which gives detailed information on the turbulence structure. Glendening and Burk (1992) simulated the lead-perpendicular ABL flow over a 200 m wide lead with a temperature difference of 27 K between water and sea ice surface. Upstream of the lead they prescribed stable stratification and weak wind ($< 2.5 \text{ ms}^{-1}$). They proposed an L -dependent equation for the plume penetration height z_{hp} with $z_{hp} \propto L^{2/3}$. Zulauf and Krueger (2003b) transferred that equation to other lead widths and they found rather $z_{hp} \propto L^{1/2}$. Overall, results of both studies show the importance of L also for the quantitative analysis of the convective IBL over leads.

Extensions of the study of Glendening and Burk (1992) were performed by Glendening (1994) regarding the inflow direction and by Weinbrecht and Raasch (2001), who found that the model resolution strongly influences the results, especially in high wind regimes. Esau (2007) investigated leads with different widths for zero geostrophic wind.

Besides pure LES applications, several modelling studies on lead effects using microscale and mesoscale atmosphere models have been carried out as, for example, by Alam and Curry (1995); Dare and Atkinson (2000); Mauritsen et al. (2005); L08; Wenta and Herman (2018); Li et al. (2020). Such types of numerical models are used to determine the integral lead effect on the ABL flow, but the structure of single turbulent eddies is not resolved as with LES. Due to grid sizes of usually 10^2 m horizontally and 10^1 m vertically, parametrizations of the turbulent processes are required to close the system of the governing equations. Alam and Curry (1995), Dare and Atkinson (2000), Mauritsen et al. (2005), Wenta and Herman (2018), and Li et al. (2020) use local closures (1.5-, 2-, or 2.5-order turbulent kinetic energy (TKE) schemes, or a first-order Smagorinsky scheme), where the turbulent fluxes are related to the gradients of mean quantities using K -theory (see Stull, 1988). However, especially in the upper half of a homogeneously surface-heated convective ABL, upward heat fluxes are present in regions with neutral or even slightly positive vertical potential temperature gradient (Holtslag & Moeng, 1991). L08 show based on LES results that this holds also for the convective ABL over leads for a near-perpendicular flow in typical springtime conditions. Indications for the existence of these non-gradient or counter-gradient fluxes were also found in the aircraft-based measurement study STABLE over the marginal ice zone (MIZ) North of Svalbard in 2013 by T15. To account for such phenomena, L08 derived a parametrization for the turbulent sensible heat flux, F_h , over leads using K -theory, but with a gradient correction scheme based on the parametrization of Lüpkes and Schlünzen (1996), which was derived for horizontally homogeneous conditions. L08 account for the horizontal inhomogeneities over leads by considering the distance to the lead's upstream edge in their approach and by distinguishing different convective regimes in the plume's core and at its boundaries. They investigated 10 idealised scenarios with $L = 1 \text{ km}$, an ABL

height of 300 m, and different meteorological forcing in a microscale modelling study, where the results obtained with their non-local parametrization agreed well with time-averaged LES results.

L08 concluded that their findings could be the basis for studies investigating the impact of lead ensembles in much larger domains by saving computational time with respect to a comparable study using LES. However, they stress that especially L should be taken into account for further improvements of their parametrization. Moreover, since climate models consider rather a fractional sea ice cover than a clear differentiation between open-water and ice surfaces, a detailed investigation on the effects of lead width on the polar ABL seems necessary. This might also help to develop an improved surface flux parametrization over leads for those models, which seems necessary to improve model results not only for the polar regions but also for mid-latitudes (Vihma et al., 2014).

Therefore, in this chapter, we present a modified version of the parametrization of L08, which includes the lead width as a parameter to be used in small-scale atmosphere models. Results will be compared with new time-averaged LES for 10 different scenarios of a lead-perpendicular flow in the ABL differing by L , wind, and temperature, and we will use those LES results to determine the unknown parameters of the modified closure (henceforth called new closure or new parametrization). Thus, the main goal of our study is to derive, based on LES, an improved parametrization of turbulent fluxes over leads in compact sea ice for non-eddy resolving microscale models. We also aim to investigate drawbacks related to local closures applied on this scale.

The new parametrization is designed for idealised conditions. It represents another step towards turbulence closures designed for small-scale atmospheric models for convective processes in strongly inhomogeneous conditions, after the first step was made by L08. However, further development is necessary in the future, for example, to include moisture transport. We also show that the reproduction of detailed flow structures related to leads requires, independent on the used closure, horizontal grid sizes not larger than $L/5$ to obtain a reasonable agreement with LES.

2.2 Models

As L08, we use two different atmospheric model types, an LES model and a non-eddy-resolving small-scale model. For the non-eddy-resolving model, a parametrization of the subgrid-scale turbulence is required to quantify the integral effects of the turbulent eddies. The LES model allows a much more detailed analysis of the turbulent flow over leads since the individual eddies on all relevant turbulent scales are resolved. With both models, scenarios of a lead-perpendicular flow in the ABL are simulated, where the upstream ABL is capped by a strong inversion of height $z_i = 300$ m. A sketch of such a flow regime over a lead of width L is shown in Figure 2.1.

2.2.1 LES model

For LES, we use the PARallelized Large Eddy Simulation Model PALM (Raasch & Schröter, 2001; Maronga et al., 2015) with revision number 2864 in its dry version. PALM has already

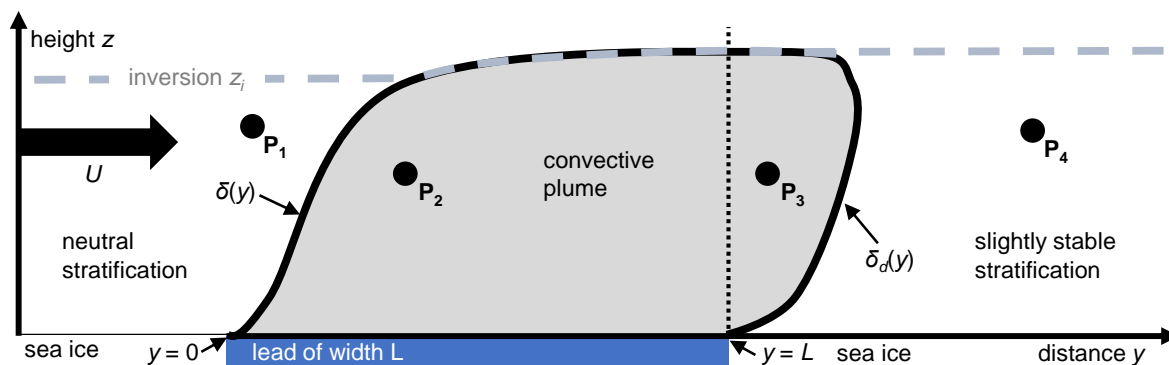


Figure 2.1: Sketch of a convective plume developing in an ABL of height z_i over a polar lead of width L during a lead-perpendicular flow (here: from left to right). Stratification of the incoming flow, where U is the vertically averaged horizontal wind speed, is neutral, and the lead causes stabilisation of the ABL in the downstream region. The convective plume area is defined as the region between the upper and lower boundaries of the internal boundary layer (IBL), $\delta(y)$ and $\delta_d(y)$, where y is the distance to the lead's upstream edge. P_1 to P_4 represent arbitrary points in different regimes of the ABL flow: P_1 is upstream of the convective plume, P_2 and P_3 are inside the plume at $0 \leq y \leq L$ and $y > L$, respectively, and P_4 is downstream of the plume. The dotted vertical black line marks the downstream lead edge. Modified after L08 and T15.

been used to study polar boundary layers over heterogeneous sea ice distributions (Weinbrecht & Raasch, 2001), small-scale processes above leads (L08), and large-scale processes concerning the impact of sea ice heterogeneities on the downstream ABL in cold-air outbreaks (Gryschka et al., 2008, 2014; De Roode et al., 2019). PALM is based on the non-hydrostatic Boussinesq-approximated Reynolds equations with a 1.5-order subgrid-scale closure according to Deardorff and Peterson (1980), in which a prognostic equation of the subgrid-scale TKE is solved. The Poisson equation for pressure is solved with the multi-grid method and for the advection terms the 5th-order Wicker-Skamarock scheme is used. For time integration, the 3rd-order Runge-Kutta scheme is applied.

At the lead-perpendicular lateral boundaries, cyclic boundary conditions are applied. At the lead-parallel inflow boundary, fixed vertical profiles of wind and temperature are prescribed. At the corresponding outflow, a zero gradient is prescribed for temperature, while for the wind components a radiation boundary condition is set. The latter condition assumes that wind components are advected with a transport velocity, which includes wave propagation and advection by the wind itself (see Orlandi, 1976).

To guarantee that resolved turbulent structures reach the upstream edge of the lead, a so-called turbulence recycling method after Lund et al. (1998) and Kataoka and Mizuno (2002) was applied. In a certain distance downstream of the inflow (here: 5 km), deviations of the velocity components from their lateral mean are taken as turbulent signals and superimposed on the inflow profiles at each time step. This method was not applied in L08. For more details on the implementation of the boundary conditions and turbulence recycling method, see Maronga et al. (2015).

Compared to the LES in L08, we chose a smaller grid spacing of 5 m (instead of 10 m) in all directions due to increased computational capacity in the last years. Therefore, in contrast to L08, also the shallow convection in the first half of the leads is resolved. To prove this, we compared vertical cross sections of the resolved and subgrid-scale TKE as well as of the resolved

and subgrid-scale heat flux (not shown). Furthermore, for case L5c-U5 (see Table 2.1 in section 2.2.3), we tested the reliability of the model resolution by performing additional simulations with 10 m and 2.5 m grid spacing, where we found that results do not differ significantly between 5 m and 2.5 m grid spacing (not shown). The vertical grid spacing is equidistant up to $z = 300$ m and smoothly stretched above. The model's top is at $z = 3014$ m. In lead-parallel direction, the model domain of PALM has an extension of 640 m, so more than $2z_j$, to capture also the larger convective structures that contribute to the turbulent fluxes.

Since with the applied spatial resolution the detailed structure of the turbulent eddies is simulated, wind and temperature are strongly variable both spatially and temporally. Therefore, to ensure comparability with the 2-D non-eddy-resolving model results, LES results are averaged in lead-parallel direction and time (see Zhou & Gryschka, 2019, for the data).

2.2.2 Microscale model

2.2.2.1 Model description

We follow the methods of L08 and use the non-hydrostatic atmospheric model METRAS (MEsocale Transport and Stream Model; Schlünzen, Bungert, et al., 2012; Schlünzen, Flagg, et al., 2012) in a dry and 2-D version for microscale simulations of lead scenarios. The Boussinesq-approximated model equations are solved on a staggered ARAKAWA-C grid and for all considered cases with $L \geq 1$ km grid spacing is similar to L08 (200 m horizontally and at least 20 m in vertical direction). For another scenario with $L = 500$ m, the horizontal grid spacing is 100 m. A sensitivity study regarding the horizontal grid spacing shows that the grid size should not be larger than $L/5$ for an appropriate resolution of the lead-generated convection (see Appendix B.3). Moreover, we aim to avoid an overlap of resolved and subgrid-scale transport as far as possible. Thus, we assume that the turbulent transport in METRAS is completely due to subgrid-scale processes in the convective region, which is why we did not consider horizontal grid sizes < 100 m. We also tested model simulations with 10 m vertical grid spacing, but results of those simulations were disturbed by resolved but unrealistic gravity waves (not shown). Unlike L08, we use an equidistant vertical grid spacing for the entire ABL which results in 15 instead of 10 layers below $z = 300$ m. Above $z = 300$ m, the model consists of another 50 layers, and the model's top is at about 9600 m ensuring that gravity waves are damped towards the model's top. Following the strategy of L08, we also do not consider radiation explicitly or condensation processes.

As in the LES model, we prescribe fixed values for temperature at the inflow boundary. For the outflow boundary, we apply a zero gradient condition. For the wind components, boundary conditions are the same at inflow and outflow boundary. Boundary-parallel wind components are calculated from zero gradient boundary condition and boundary-normal wind components are calculated directly as far as possible (see Schlünzen, Flagg, et al., 2012).

2.2.2.2 Local and non-local turbulence parametrizations in METRAS

Since we focus on simulations of a dry atmosphere, we will use the term heat flux for sensible heat fluxes, unless stated otherwise. For the parametrization of both heat and momentum fluxes, local and non-local approaches are considered.

2.2.2.2.1 Local mixing-length closure

The local closure schemes are based on flux-gradient relationships

$$\overline{w'\theta'} = -K_h \frac{\partial \bar{\theta}}{\partial z}, \quad (2.1)$$

for temperature, where $\partial \bar{\theta} / \partial z$ is the vertical potential temperature gradient and K_h is the eddy diffusivity for heat, and

$$\overline{w'u'} = -K_m \frac{\partial \bar{u}}{\partial z}, \quad \overline{w'v'} = -K_m \frac{\partial \bar{v}}{\partial z}, \quad (2.2)$$

for momentum, where $\partial \bar{u} / \partial z$ and $\partial \bar{v} / \partial z$ are the vertical gradients of the x_1 - and x_2 -components of the wind vector and K_m is the eddy diffusivity for momentum. In the surface layer (first grid cell above the surface) both K_m and K_h are calculated according to Monin-Obukhov similarity theory using Businger-Dyer functions (Businger et al., 1971; Dyer, 1974). Above the surface layer, a mixing-length approach by Herbert and Kramm (1985) is applied to calculate K_m and K_h in Equations 2.1 and 2.2:

$$K_m = \begin{cases} l_n^2 \left| \frac{\partial \mathbf{v}_h}{\partial z} \right| (1 - 5Ri)^2 & \text{for } 0 \leq Ri \leq Ri_c \\ l_n^2 \left| \frac{\partial \mathbf{v}_h}{\partial z} \right| (1 - 16Ri)^{1/2} & \text{for } Ri \leq 0 \end{cases}, \quad (2.3)$$

$$K_h = \begin{cases} K_m & \text{for } 0 \leq Ri \leq Ri_c \\ K_m (1 - 16Ri)^{1/4} & \text{for } Ri \leq 0 \end{cases}, \quad (2.4)$$

where Ri is the Richardson number, Ri_c is the critical Richardson number, for which 0.199 is used instead of 0.2 to avoid zero diffusion, $\partial \mathbf{v}_h / \partial z$ is the vertical gradient of the horizontal wind, and $l_n = \kappa z / (1 + \kappa z / l_{max})$ is the mixing length for neutral stratification with Kármán's constant κ . For the determination of l_n , as in L08, we set the maximum mixing length $l_{max} = 0.15z_i$. Originally, this relation was derived by Brown (1996) based on LES. At grid points where $Ri > Ri_c$, both K_m and K_h are calculated with $Ri = Ri_c$. This choice guarantees matching with the surface layer when Businger-Dyer functions are used in case of stable stratification.

Equations 2.3 and 2.4 guarantee continuity of the fluxes at the first grid level. Note that, for example, Grachev et al. (2013) found that a critical Richardson number probably does not exist in nature and an alternative closure is proposed for stable stratification. However, here we do not consider the related implications since in the surface layer the stratification is far from the critical value in all model simulations (not shown).

2.2.2.2.2 Non-local closure of L08

Based on their LES results, L08 found that counter-gradient heat fluxes occur in the convective plume region (Figure 2.1). Those fluxes do not depend on local gradients and have to be parametrized with non-local parameters. Thus, L08 formulated their parametrization based on

$$\overline{w'\theta'} = -K_h \left(\frac{\partial \bar{\theta}}{\partial z} - \Gamma \right), \quad (2.5)$$

with the counter-gradient correction Γ . Equation 2.5 was first proposed by Priestley and Swinbank (1947) and theoretically derived by Deardorff (1972) and Holtslag and Moeng (1991). The

latter formulated Equation 2.5 for horizontally homogeneous conditions, where K_h and Γ are given as functions of z/z_i , with the ABL height z_i , the convective velocity scale w_* (also called Deardorff's convective velocity scale, e.g., Deardorff, 1970), and the convective temperature scale θ_f . The latter two quantities are written as follows:

$$w_* = (B_s z_i)^{1/3}, \quad (2.6)$$

with the surface buoyancy flux B_s , where

$$B_s = \frac{g}{\theta_0} \overline{w'\theta'}|_s = -\frac{g}{\theta_0} u_* \theta_*, \quad (2.7)$$

where g is the gravitational acceleration, θ_0 is the surface layer temperature, u_* is the friction velocity, θ_* is the scaling value for temperature, and $\overline{w'\theta'}|_s$ is the kinematic surface heat flux, and

$$\theta_f = \frac{\overline{w'\theta'}|_s}{w_*}. \quad (2.8)$$

Following Holtslag and Moeng (1991), Lüpkes and Schlünzen (1996) derived K_h and Γ in a way which ensures continuous fluxes at the top of the surface layer. In those equations, w_* acts as scaling velocity, which is defined in Equation 2.6 for convection over a horizontally homogeneous surface and a horizontally homogeneous ABL height z_i . To account for the non-homogeneous flow regime over leads, L08 adjusted the non-local closure of Lüpkes and Schlünzen (1996). We will briefly describe their principles and use Figure 2.1 to illustrate the respective steps.

L08 assume that heat transport inside the convective plume (e.g., at P_2 and P_3) is dominated by non-local effects while outside (e.g., at P_1 and P_4) mixing is local. As switching lines between the two closures they consider the upper and the lower plume boundaries $\delta(y)$ and $\delta_d(y)$ (also called upper and lower IBL height), where y is the distance to the lead's upstream edge. Furthermore, the functional relations of K_h and Γ remain the same as over a homogeneous surface, but z_i is replaced by the fetch-dependent IBL height $\delta(y)$. Moreover, L08 state that the heat flux at any position inside the convective plume is determined by the lead-averaged surface buoyancy flux B_l (same as B_s , but with the index l for the lead's surface). Thus, also at P_3 , which is downstream of the lead but still inside the plume, the characteristics are dominated by the convection generated over the lead. Besides B_l , the dominating parameters inside the plume are the vertically averaged horizontal wind speed in the ABL at the lead's upstream edge (U) and the upstream ABL height z_i . Moreover, z_i is set constant because L08 consider only cases with neutral stratification in a shallow ABL capped by a strong inversion.

To match the non-local and local closures, L08 propose a new formulation of the convective velocity scale (called w_l to avoid confusion). They assume that for the region above the lead ($0 < y < L$, Figure 2.1) w_l can be expressed by $(B_l \delta(y))^{1/3}$, which is similar to Equation 2.6, but with $\delta(y)$ instead of z_i . However, to take into account lateral entrainment and dissipation for $y > L$, which cause decaying convection, an exponential decay of w_l is assumed. Moreover, L08 focused on narrow leads ($L \approx 1$ km) where the horizontal extension of the plume into the lead's downstream region can exceed L by several kilometres ($L \ll D$, where D is a decay length scale specified below). Thus, they neglected L as a governing parameter and applied their decay

function already at $y = 0$:

$$w_l(y) = c (B_l \delta(y))^{1/3} \exp(-y/D), \quad (2.9)$$

with c as an adjustable parameter and with D gained from an equation for $\delta(y)$. The latter is derived by integrating

$$\frac{d\delta}{dy} = \frac{w_e(y)}{U} = \frac{a_e w_{max}(y)}{U} = \frac{a_e a_m w_l(y)}{U}, \quad (2.10)$$

which follows Monin and Yaglom (1971) and Turner (1986), where w_e is the entrainment velocity, w_{max} is the velocity of the strongest eddies, and a_e and a_m are parameters connecting w_e , w_{max} , and w_l . By integrating Equation 2.10, L08 obtained

$$\delta(y) = \delta_{max} (1 - \exp(-y/D))^{3/2} = z_i (1 - \exp(-y/D))^{3/2}, \quad (2.11)$$

where $\delta_{max} = z_i$ is the maximum upper IBL height for a neutral environment, wherein convective turbulence always penetrates up to the inversion. Since

$$\delta_{max} = \left(\frac{2a B_l^{1/3} D}{3 U} \right)^{3/2}, \quad (2.12)$$

with $a = a_e a_m c$, D can be written as

$$D = \frac{3}{2a} \left(\frac{U^3}{B_l} \right)^{1/3} z_i^{2/3}. \quad (2.13)$$

For the determination of $\delta_d(y)$, L08 assume that this switching line is located downstream of the lead where the non-local heat flux is less than $F_{crit} = 2 \text{ Wm}^{-2}$. For the parameters, L08 define the following ranges: $c \approx 1.6 \pm 0.5$, $a_m = 3 \pm 1$, and $a_e = 0.3 \pm 0.1$ so that a is in a range between 0.4 and 3.4. For all their cases, L08 applied $a = 2.3$ and $c = 1.6$. For the convective temperature scale θ_f in the plume, which we call θ_l to avoid confusion with the usual definition, L08 consider Equation 2.8 with $w_l(y)$ instead of w_* . Momentum fluxes are parametrized with the local closure (Equations 2.2 and 2.3).

L08 reformulated the equations of Lüpkes and Schlünzen (1996) for K_h and Γ in a non-dimensional form as a function of the stability parameter

$$S(y) = w_l(y)/u_{*,l}, \quad (2.14)$$

with $u_{*,l}$ as the lead-averaged value for the friction velocity, and of the non-dimensional vertical coordinate

$$Z(y) = z/\delta(y) \quad (2.15)$$

and obtained

$$K_h/K_p = Z \left(1 + \frac{S}{\kappa} Z^{1/3} \right) (1 - Z)^2, \quad Z_p \leq Z \leq 1, \quad (2.16)$$

with the eddy diffusivity at the surface layer's top z_p

$$K_p = \frac{u_{*,l} \kappa z_p}{\Phi_p}, \quad (2.17)$$

where $\Phi_p = (\Phi_h|_{z_p} + \Phi_\Gamma) Z_p (1 + (S/\kappa) Z_p^{1/3}) (1 - Z_p)^2$ with the Monin-Obukhov similarity function for heat Φ_h and with $\Phi_\Gamma = \Gamma|_{z_p} \kappa z_p u_{*,l} / \overline{w'\theta'}|_s$.

For Γ , L08 obtained:

$$\Gamma/\Gamma_0 = 0.63bS \left[(1 - Z)^{3/2} + 0.593S^3 Z (1 - 0.9Z)^{3/2} \right]^{-2/3}, \quad (2.18)$$

with an adjustable parameter b and with $\Gamma_0 = (\overline{w'\theta'}|_s) / (u_{*,l} \delta(y)) = S\theta_l / \delta(y)$. L08 set $b = 0.6$, which is much lower as in previous studies (e.g., Holtslag & Moeng, 1991; Lüpkes & Schlünzen, 1996).

2.2.3 Scenarios and setup of models

We discuss the results of 10 different idealised scenarios (Table 2.1). Nevertheless, our applied model domains are chosen with respect to observations during several campaigns (REFLEX I and II, ARTIST, ARKXIX/1, STABLE; Hartmann et al., 1992; Kottmeier et al., 1994; Hartmann et al., 1999; Lüpkes et al., 2004, T15) and the initialisation data for the simulations are representative for typical springtime conditions in the polar regions.

We distinguish between the convection over wide and over narrow leads. We define wide leads as those where the convection penetrates into the capping inversion already above the leads. Here, this concerns four scenarios with $L = 5$ km and one with $L = 10$ km. For narrow leads, where the convection reaches the inversion further downstream, we consider four scenarios with $L = 1$ km similar to those in L08 and one scenario with $L = 0.5$ km. We focus on results over one lead, but for the cases L1c-U3, L1c-U5, L1c-U7, and L1w-U10 (Table 2.1) as in L08, we consider the results over a lead 10 km downwind of another lead to compare them with the L08 results. This ensures that the effects caused by the first lead, such as slightly increased air temperature and a slightly stable stratification upstream of the second lead, are included.

As L08, we focus on cases with sea ice surface temperatures prescribed to 250 K or 260 K. Surface temperature of the leads is always prescribed to 270 K representing a lead covered by thin, new ice, which is often observed at low air temperatures (Pinto et al., 2003). For both surfaces, temperatures do not change throughout the model integration.

Four different wind regimes are investigated prescribing lead-orthogonal geostrophic wind components u_g upstream of the leads of 3 ms^{-1} , 5 ms^{-1} , 7 ms^{-1} , and 10 ms^{-1} , respectively. The corresponding lead-parallel components, v_g , (see Table 2.1) ensure a lead-perpendicular flow in the ABL. Thus, all simulations can be regarded as quasi-2-D simulations, independent of the lead-parallel component of the coordinate system. That is, we neglect a possible fetch dependence of surface roughness and prescribe the roughness lengths for momentum to $z_0 = 10^{-3}$ m over ice and $z_0 = 10^{-4}$ m over water in both models. For both surfaces, the ratio between the roughness lengths for momentum and heat is assumed as 10. The value of the Coriolis parameter f refers to 79°N .

Table 2.1: Summary of discussed cases^a.

| Wide leads | | | | | |
|-------------------------------------|--------|--------|--------|---------|----------|
| | L5c-U3 | L5c-U5 | L5c-U7 | L10c-U5 | L5w-U5 |
| L (km) | 5 | 5 | 5 | 10 | 5 |
| u_g (ms ⁻¹) | 3.0 | 5.0 | 7.0 | 5.0 | 5.0 |
| v_g (ms ⁻¹) | 0.4 | 1.0 | 2.0 | 1.0 | 1.0 |
| $T_{s,i}$ (K) | 250 | 250 | 250 | 250 | 260 |
| $\bar{F}_{h,s}$ (Wm ⁻²) | 144 | 195 | 245 | 196 | 85 |
| $F_{100,L}$ (Wm ⁻²) | 119 | 163 | 197 | 169 | 75 |
| $F_{100,M}$ (Wm ⁻²) | 127 | 168 | 205 | 169 | 68 |
| $F_{200,L}$ (Wm ⁻²) | 74 | 102 | 113 | 103 | 49 |
| $F_{200,M}$ (Wm ⁻²) | 73 | 95 | 115 | 94 | 39 |
| Narrow leads | | | | | |
| | L1c-U3 | L1c-U5 | L1c-U7 | L1w-U10 | L0.5c-U5 |
| L (km) | 1 | 1 | 1 | 1 | 0.5 |
| u_g (ms ⁻¹) | 3.0 | 5.0 | 7.0 | 10.0 | 5.0 |
| v_g (ms ⁻¹) | 0.4 | 1.0 | 2.0 | 2.5 | 1.0 |
| $T_{s,i}$ (K) | 250 | 250 | 250 | 260 | 250 |
| $\bar{F}_{h,s}$ (Wm ⁻²) | 125 | 163 | 200 | 131 | 166 |
| $F_{100,L}$ (Wm ⁻²) | 83 | 103 | 117 | 21 | 51 |
| $F_{100,M}$ (Wm ⁻²) | 103 | 96 | 91 | 27 | 48 |
| $F_{200,L}$ (Wm ⁻²) | 34 | 41 | 41 | 4 | 15 |
| $F_{200,M}$ (Wm ⁻²) | 60 | 43 | 40 | 11 | 21 |

^a L is the lead width, u_g and v_g are the lead-orthogonal and lead-parallel geostrophic wind components, $T_{s,i}$ is the prescribed sea ice surface temperature, $\bar{F}_{h,s}$ is the lead-averaged surface heat flux, $F_{100,L}$ and $F_{200,L}$ are the maximum heat fluxes at 100 m and 200 m height as simulated with LES, and $F_{100,M}$ and $F_{200,M}$ are the corresponding values as simulated by the microscale model using the new non-local turbulence parametrization (section 2.5.1). For the cases with $L = 1$ km, results correspond to the second lead 10 km downstream of another lead.

As in L08, a neutrally stratified atmosphere with a strong capping inversion at $z_i = 300$ m is prescribed initially in the whole domain of both models and as inflow temperature profile during the whole time integration. The initial and inflow profile of wind in METRAS is determined with the 1-D model version. In PALM, a 3-D LES pre-run with lateral cyclic boundary conditions and smaller model domain than in the main run representative for the situation over ice was performed. Thus, unlike L08, we use a 3-D instead of a 1-D pre-run to initialise the simulations with a turbulent wind field. Hence, at the inflow boundary, the turbulence is produced already at the beginning of each simulation due to the turbulence recycling method causing a faster developing flow.

For both models, we prescribe at least 5 km distance for both in- and outflow boundary to the corresponding lead edges to guarantee that results near the lead are not influenced by the boundaries. In two-lead domains, we prescribe a gap of at least 10 km to the next lead to avoid possible interactions of plumes from different leads.

The model simulations are performed until quasi-stationary conditions are reached with respect to temperature, wind, and flux profiles in the ABL. For METRAS, quasi-stationarity is reached after approximately 2 hrs integration time. With PALM also approximately 2 hrs are required to reach quasi-stationarity, but the total simulation time is longer since the LES results are then averaged over an hour.

2.3 LES results

Time-averaged LES results are presented for the heat flux, vertical potential temperature gradient (Figure 2.2), horizontal wind speed, and momentum flux (Figure 2.3). Both figures show

results of the cases L5c-U3, L5c-U5, L5c-U7, and L10c-U5 (Table 2.1). Thus, in three cases, the same lead width of 5 km and the same inflow temperature but different wind speeds are used. In case L10c-U5 lead width L is doubled. The position of the lead in each plot is between $y = 0$ km and the dashed vertical black line, where y is the distance from the upstream lead edge. The flow is from left to right. For the heat flux, the sum of both resolved and subgrid-scale fluxes is shown in Figure 2.2 (left column). Values of the vertical potential temperature gradient are shown in Figure 2.2 (right column) in K per 100 m.

In three cases, the overall structure of the heat flux patterns seems to be similar (Figures 2.2a, 2.2c, and 2.2e). Above the lead, positive heat fluxes are simulated almost in the entire ABL. At that distance where the convective plume reaches the capping inversion, entrainment is generated with negative fluxes due to turbulence in the inversion layer. The horizontal distribution of heat fluxes is highly inhomogeneous showing a clear maximum over the lead. In the upper third of the mixed layer, the position of this maximum occurs where the plume starts to penetrate into the inversion. Towards the lower part of the mixed layer, the position is shifted slightly downstream. Especially for case L5c-U3, a region of almost horizontally homogeneous heat fluxes is simulated downwind of the maximum, starting at approximately $y = 3$ km (Figure 2.2a). For all three cases, the plume extends also into the downwind region of the lead, followed by a region of negative (downward) fluxes in the entire ABL.

Figures 2.2a, 2.2c, and 2.2e clearly demonstrate the influence of the upstream wind speed on the spatial structure and strength of the lead-generated convection. The higher the wind speed, the higher is the inclination angle of the plume, the stronger is the entrainment, and the stronger is the lead-averaged surface heat flux (see also Table 2.1). Furthermore, with increasing wind speed, the distances of the simulated maximum heat fluxes from the upstream lead edge increase. However, the maximum is more pronounced for weak wind (Figure 2.2a) than for strong wind (Figure 2.2e). The simulated heat flux distribution over the lead with $L = 10$ km (Figure 2.2g) looks similar to the corresponding case with $L = 5$ km (Figure 2.2c) until $y \approx 6$ km. Also in the 10 km-case, a maximum is simulated at $2.5 < y < 3$ km and the entrainment fluxes in the inversion layer reach similar values. Furthermore, the positions of the maximum entrainment fluxes with fetch denote an almost linear growth in ABL thickness for $4 \text{ km} < y < L$. Such an increase is also shown for case L5c-U5, but less strong (Figure 2.2c). Obviously, an increase in lead width leads to a stronger increase in ABL thickness over the lead, which has been studied also for other cases (not shown)

The vertical potential temperature gradient (Figure 2.2, right column) indicates the ABL stratification near the lead. An almost neutrally stratified ABL up to $z \approx 270$ m at the lead's upstream edge is obtained in all cases. This means that the bottom of the inversion is lower at the lead's upstream edge after some simulation time than its initial position at $z = 300$ m at the inflow boundary. This subsidence is probably caused by a thermally-induced convergence directly below the inversion near the lead's upstream edge. Moreover, it is also shown in the corresponding microscale model results (sections 2.4 and 2.5.2). Strong unstable stratification occurs above the lead surface and a stabilisation is seen downwind over sea ice.

Comparing the vertical potential temperature gradient in the convective area with the region of positive heat fluxes (dashed grey lines in Figure 2.2, right column), there is a clear evidence for non-gradient heat fluxes. These fluxes roughly start at that distance where the

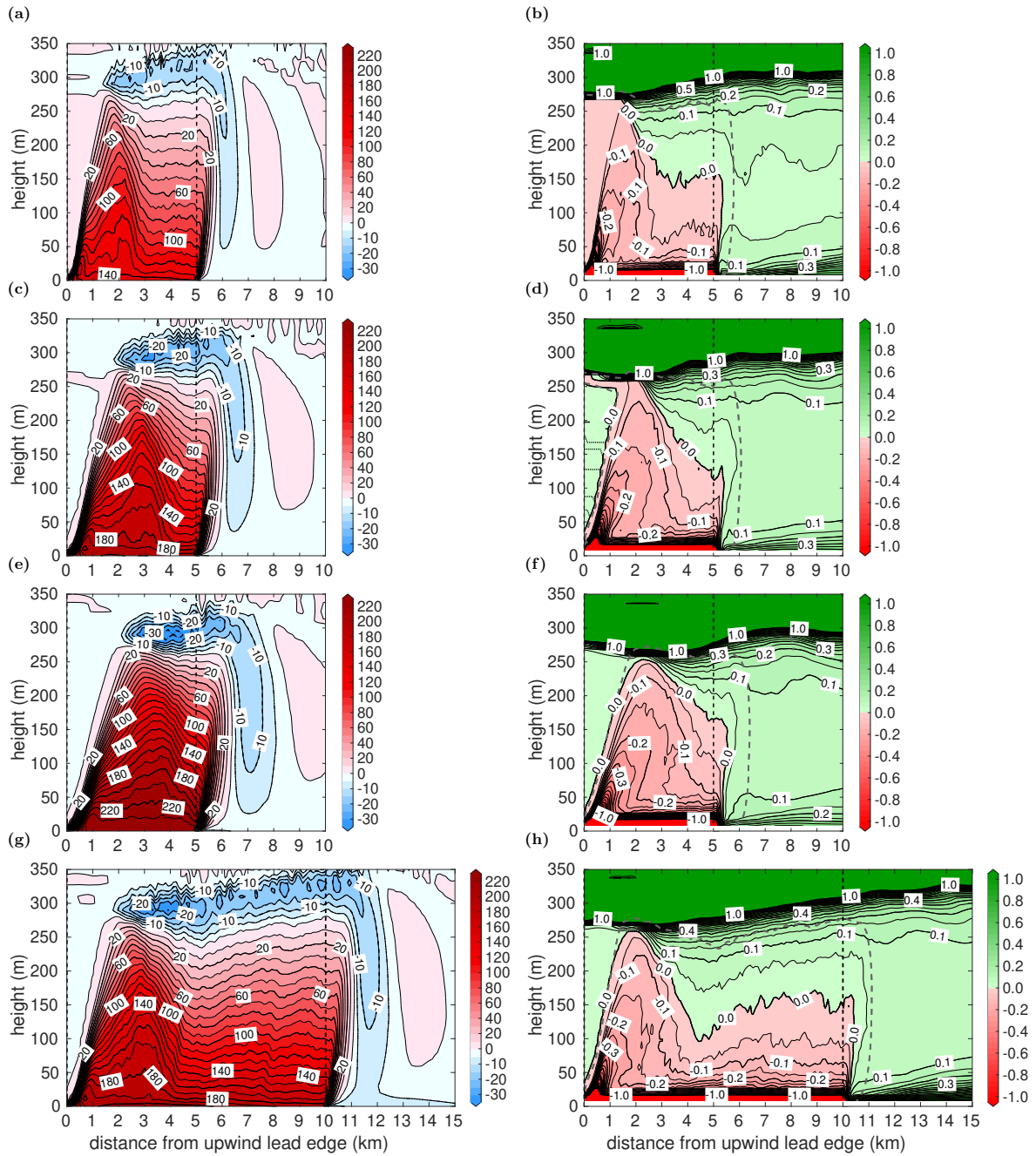


Figure 2.2: LES results of sensible heat flux in Wm^{-2} (left column) and of vertical potential temperature gradient in K per 100 m (right column) for the cases L5c-U3 (a, b), L5c-U5 (c, d), L5c-U7 (e, f), and L10c-U5 (g, h). The position of the lead is between 0 km and the vertical dashed black line. The distance between heat flux contour lines is 5Wm^{-2} for negative fluxes. In the right column, the area inside the dashed grey lines depicts the region of positive fluxes inside the convective plume. For the description of the cases, see Table 2.1.

plume reaches the inversion and they dominate the heat flux pattern especially in the upper part of the ABL near $y = L$ and further downwind. The higher the wind speed, the further those counter-gradient fluxes extend into the downstream region. These results for heat fluxes and stratification agree well with those discussed by L08.

The general structure of the wind field (Figure 2.3, left column) seems to be independent on

the inflow wind speed. For example, in all cases, pronounced wind speed maxima are simulated at the lead's upstream edge with maximum values directly below the inversion. Although these maxima exceed the mean wind speed by only about 10 %, we will call them in the following low-level jet (LLJ). Due to lead-generated convection and, thus, enhanced vertical mixing, the LLJ near the inversion is destroyed and another, slightly less pronounced wind maximum is simulated between approximately $30 < z < 100$ m. The higher the upstream wind speed, the larger are the distances of both maxima from the lead's upstream edge due to increased plume inclination. In the lead's downstream region not directly influenced by the convection, there is some evidence for a recovering LLJ.

Unlike L08, we also analyse vertical momentum fluxes, for which LES results are shown in Figure 2.3 (right column). As for the previously discussed quantities, also the structure of the simulated momentum flux distributions is, basically, similar in all cases, and strong horizontal inhomogeneity is obvious. Moreover, two pronounced maxima are shown. The first maximum is simulated in the unstable region over the lead close to the lead's upstream edge and its magnitude at $0.1z_i$ increases with increasing wind speed. Another, slightly less pronounced maximum is simulated near the lead's downstream edge. This secondary maximum is especially pronounced in the cases L5c-U3 and L10c-U5 (Figures 2.3b and 2.3h), and its centre is near $0.6z_i$. For those two cases, heat fluxes are almost horizontally homogeneous in that part of the ABL (Figures 2.2a and 2.2g). The secondary maximum in the momentum fluxes is not simulated for the case L5c-U7 (Figure 2.3f). In this case, the region of horizontally inhomogeneous heat fluxes extends into the lead's downwind region (Figure 2.2e). In contrast to the first maximum of the momentum flux patterns, the magnitude of the secondary maximum decreases with increasing upstream wind speed.

2.4 Microscale model results with different turbulence closures

In this section, we consider results for case L5c-U5 obtained with METRAS for the same quantities as in section 2.3 using the turbulence closures described in section 2.2.2.2. Results in Figure 2.4 (left column) were obtained with the local closure, those in Figure 2.4 (right column) with the L08 closure. As already stated by L08 and as mentioned in the previous sections, non-gradient heat fluxes occur in the convective environment over leads. Thus, it is not surprising that both heat fluxes and stratification obtained with METRAS using the local closure (Figures 2.4a and 2.4c) disagree with the corresponding LES results (Figures 2.2c and 2.2d). Especially, the stratification downstream of the lead is not represented correctly. No entrainment is simulated, and positive heat fluxes occur over a wide region of several kilometres width downstream of the lead. Also, the positions of maximum heat fluxes disagree with the corresponding LES results.

The lead-generated effects on the wind field (Figure 2.4e) are partly represented with the local closure. The maximum value and the position of the LLJ upstream of the lead agree well with the corresponding LES results (Figure 2.3c) and also a destruction of the LLJ over the lead is simulated. However, this destruction is not as effective as compared to LES.

In the momentum flux distribution obtained with the local closure (Figure 2.4g), the position

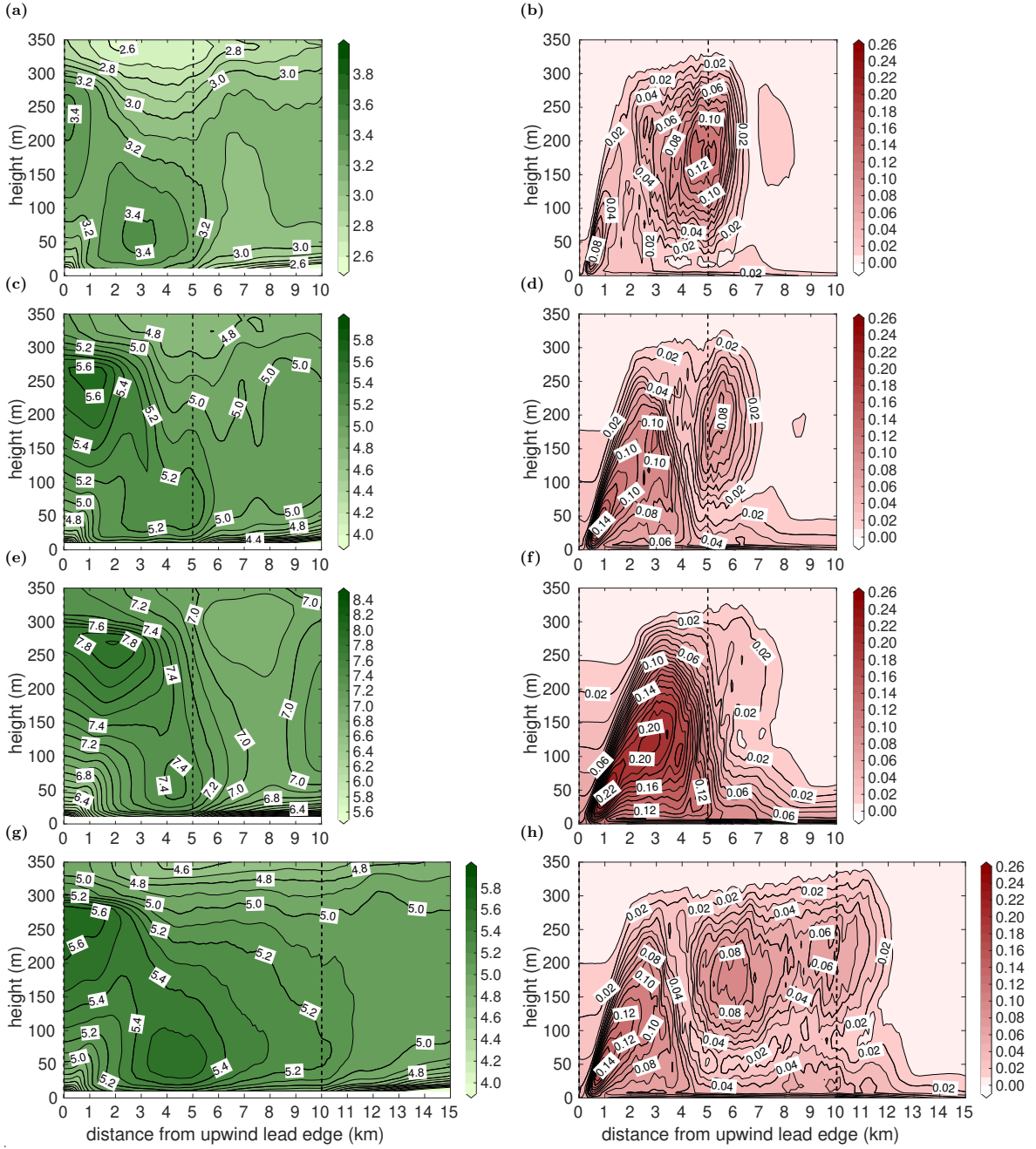


Figure 2.3: LES results as in Figure 2.2, but horizontal wind speed in ms^{-1} (left column) and vertical momentum flux in Nm^{-2} (right column) are shown.

of the main maximum near the upstream edge of the lead agrees with LES (Figure 2.3d), but it is not as pronounced as in the LES. Another maximum is simulated near $y = L$, but it occurs at $z \approx z_i$ rather than at $z \approx 0.6z_i$ as in the LES result. Moreover, this maximum seems to be caused by processes that are not simulated with LES, namely, by an unstable stratification at that location in combination with high vertical wind shear $\partial \mathbf{v}_h / \partial z$ near $z = z_i$ (see also Figure B5 in Appendix B).

Not only an improvement but also a drawback is obvious when the L08 closure is used (Figure 2.4b). A pronounced maximum of heat fluxes is simulated at $y \approx 2 \text{ km}$, but a strong discontinuity occurs at $y \approx 4.5 \text{ km}$ near the downstream lead edge. We found this discontinuity

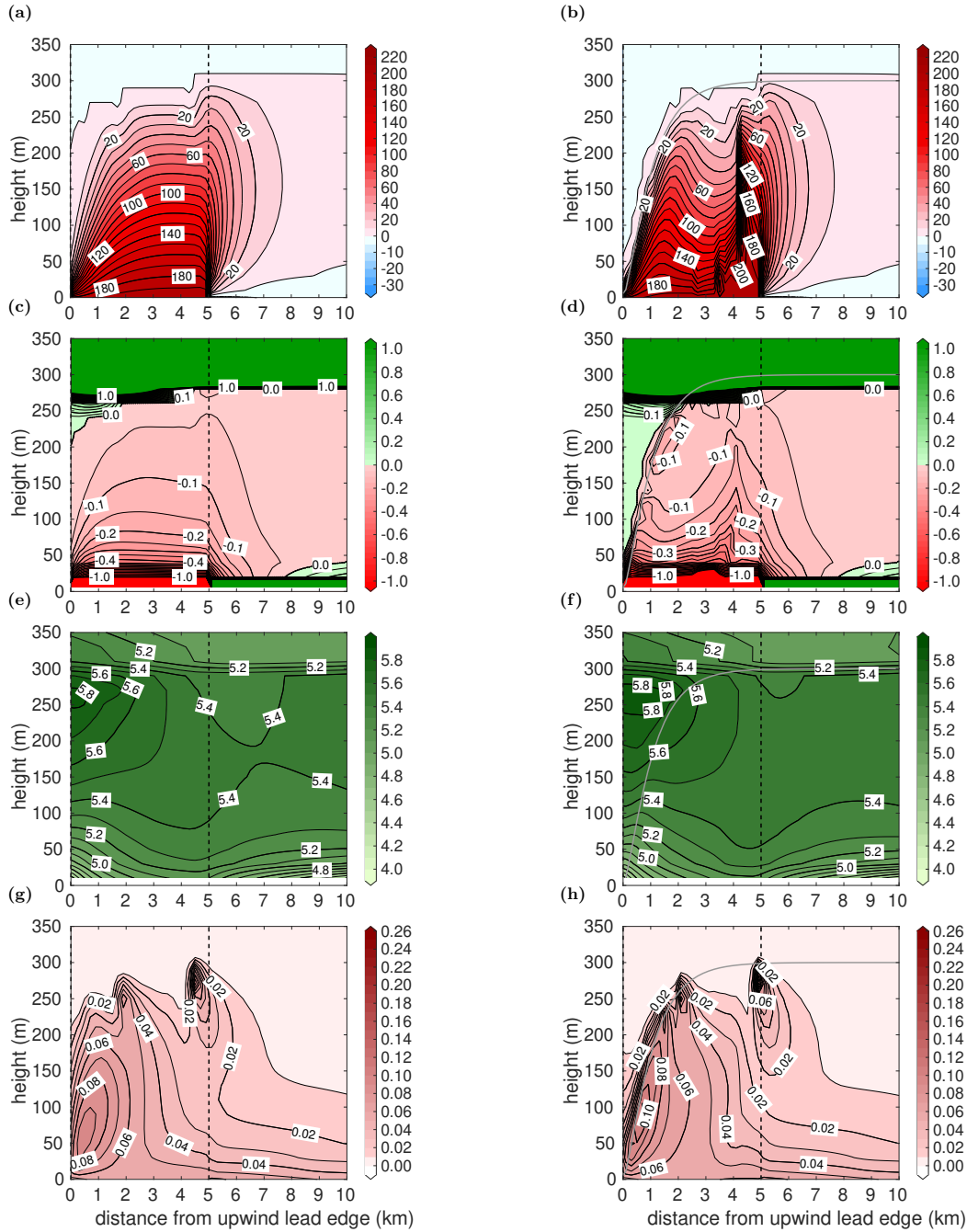


Figure 2.4: Results obtained with METRAS using the local mixing-length closure (left column) and using the L08 parametrization (right column) for case L5c-U5 of heat flux in Wm^{-2} (a, b), vertical potential temperature gradient in K per 100 m (c, d), horizontal wind speed in ms^{-1} (e, f), and vertical momentum flux in Nm^{-2} (g, h). The position of the lead is between 0 km and the vertical dashed black line. The distance between heat flux contour lines is 5Wm^{-2} for negative fluxes. The solid grey lines in the right column show the upper IBL height according to Equation 2.11. Corresponding LES results are shown in Figures 2.2c, 2.2d, 2.3c, and 2.3d.

is sensitive to the applied value for I_{max} and to the matching of the local and non-local closures at the plume's downwind boundary, where the non-local heat flux (see Equation 2.18) is below its assumed critical value F_{crit} . For narrow leads ($L \ll D$), for which the L08 closure is derived, F_{crit} is reached downstream of the lead so that such a discontinuity was not simulated (see L08).

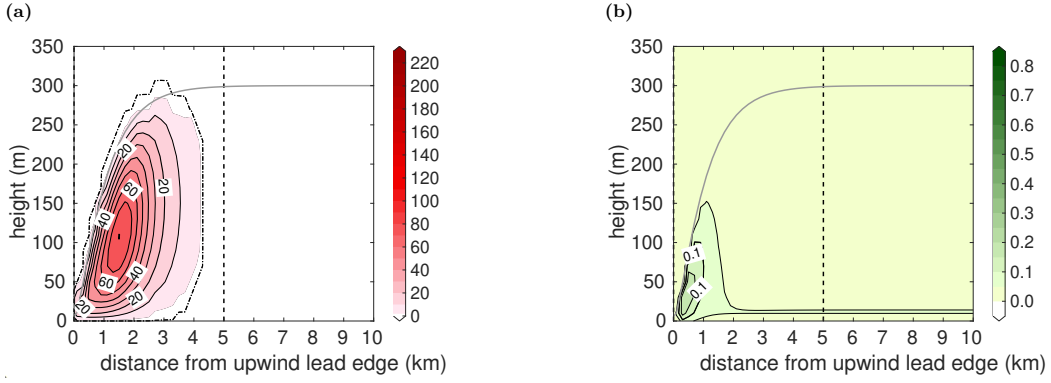


Figure 2.5: Results of the non-local heat flux $F_{h,nl} = \rho_0 c_p K_h \Gamma$ in Wm^{-2} (a) and vertical velocity variance $\overline{w'^2}$ (Equation 2.26) in m^2s^{-2} (b) obtained with METRAS using the L08 closure for case L5c-U5. In (a), the dashed-dotted black contour line denotes where $F_{h,nl} = 0.1 \text{ Wm}^{-2}$ and coloured contour levels start at $F_{h,nl} = 2 \text{ Wm}^{-2}$. In (b), the solid grey line shows the upper IBL height following Equation 2.11.

For wide leads (e.g., $L = 5 \text{ km}$), the non-local scheme is not used any more starting already at $y < L$ so that the results resemble those of the local scheme for the region downstream of the lead. As Figure 2.5a shows, this holds also for a much smaller F_{crit} than the value assumed by L08, for example, $F_{crit} = 0.1 \text{ Wm}^{-2}$. Also the vertical velocity variances $\overline{w'^2}$ (Equation 2.26) approach zero already at $y < L$ (Figure 2.5b). Consequently, the simulated total heat flux above the second half of the lead is mainly due to local effects when the L08 closure is applied to wide leads. Furthermore, the convection does not penetrate into the inversion causing less entrainment than with LES. This prevents the stabilisation of the downstream ABL and stratification remains unstable (Figure 2.4d).

As expected, the patterns of horizontal wind speed and momentum fluxes are similar to the patterns obtained with the local closure (Figures 2.4f and 2.4h) since L08 use a non-local approach for heat but a local closure for momentum (section 2.2.2.2.2). Thus, although small improvements are obvious with the L08 scheme, also these results show discrepancies to the LES when L exceeds the lead width considered by L08 (see also Figure B5 in Appendix B).

2.5 New turbulence parametrization

2.5.1 Principles and derivation

The L08 parametrization was developed for narrow leads ($L \approx 1 \text{ km}$) and, thus, it is not surprising that the application outside of its range of applicability to the much wider lead ($L = 5 \text{ km}$) results in the discussed difficulties. Therefore, in the following, we present a modified version of the L08 parametrization that will avoid the discussed drawbacks. It includes L as a parameter and is as robust against variations of the upstream wind speed U , ABL height z_i , and sea ice – lead surface temperature differences as the original closure. The basic ideas, namely, the separation of the turbulence regimes inside and outside the plume regions and the assumption of decaying turbulence downstream of the lead, remain unchanged. However, in the L08 parametrization, the decay of turbulence starts for simplicity already at the lead's upstream edge, while in our new version, we assume fully developed convection above the lead and apply a decay function only over sea ice. Thus, we will adjust the convective velocity scale $w_l(y)$,

which has consequences also for the internal boundary layer height $\delta(y)$. For reasons that are explained below, we modify also the convective temperature scale θ_l and the parametrization of decaying convection on the lead's downstream side. A similar approach has been proposed by Gollnik (2008), but his determination of the parameters is based on rough estimations compared to the methods described here (see below). Furthermore, based on an LES study of decaying convection (Nieuwstadt & Brost, 1986), we consider two different decay length scales, one for the decay of vertical wind fluctuations, D_w , and one for the decay of temperature fluctuations, D_θ (see Appendix B.1). Unlike L08 and Gollnik (2008), we apply a non-local closure also for the momentum fluxes.

The basic equations of the new parametrization are the same as in L08 (Equations 2.5, 2.16, and 2.18). However, unlike L08, we account for the different behaviour above and downstream of the lead by defining the vertical velocity scale as

$$w_l(y) = \begin{cases} c (\delta(y) B_l)^{1/3}, & 0 \leq y \leq L \\ c (\delta(y) B_l)^{1/3} \exp\left(-\frac{L-y}{D_w}\right), & y > L \end{cases}, \quad (2.19)$$

where D_w is the decay length scale for vertical wind fluctuations (similar to D in L08) and where c is a parameter. By this definition, the decay of w_l starts over the downstream lead edge rather than over the upstream edge as in L08. Moreover, the determination of both D_w and c differs from L08 (see below). Besides these differences, the second line of Equation 2.19 results in the limit $L \rightarrow 0$ in the same equation as in L08.

As L08, we consider Equation 2.10 to determine the upper IBL height $\delta(y)$ assuming $\delta(y) = 0$ at the lead's upstream edge ($y = 0$) as lower boundary condition. To arrive at the final equation for $\delta(y)$, we use Equation 2.10, but limit $\delta(y)$ to z_i . We obtain after integration of Equation 2.10 with Equation 2.19

$$\delta(y) = \begin{cases} \min\left(z_i, \left(\frac{2a}{3} \frac{B_l^{1/3}}{U} y\right)^{3/2}\right), & 0 \leq y \leq L \\ \min\left(z_i, \delta_L \left[1 + \frac{D_w}{L} \left\{1 - \exp\left(-\frac{L-y}{D_w}\right)\right\}\right]^{3/2}\right), & y > L \end{cases}, \quad (2.20)$$

where δ_L is defined as

$$\delta_L = \left(\frac{2a}{3} \frac{B_l^{1/3}}{U} L\right)^{3/2}, \quad (2.21)$$

with the parameter a defined as described below. This formulation guarantees continuity of $\delta(y)$ at $y = L$. Here, the limit $\delta(y) \geq z_i$ is reached for $y < L$ in all cases with $L = 5$ km and $L = 10$ km (wide leads). Equation 2.20 is valid for any possible value of L . For $L \rightarrow 0$, also $\delta(y) \rightarrow 0$. For $L \rightarrow \infty$, two cases have to be regarded. If $\delta_L < z_i$, $\delta(y) \rightarrow \delta_L$. If $\delta_L = z_i$, also $\delta(y) = z_i$.

For parametrizing the decaying convection, unlike L08, we do not assume that $\delta(y)$ approaches z_i for $y \rightarrow \infty$, if the limit $\delta(y) \geq z_i$ is not reached at $y \leq L$. Not only for wide leads, $\delta(y)$ reaches z_i anyway already at $y < L$ but also for narrow leads, the convection reaches z_i in almost all cases between approximately $1 < y < 8$ km (see entrainment fluxes in LES results of L08, their Figures 3 and 8). Thus, we cannot obtain the decay length scale D_w from Equation

2.20 as in L08. Our modified approach for this parameter is explained in Appendix B.1, and we obtain

$$D_w = d_w \cdot U \frac{z_i^{2/3}}{B_l^{1/3}}, \quad (2.22)$$

where d_w is a parameter (see Appendix B.1).

Unlike L08, we apply an exponential decay function also for the convective temperature scale θ_l to account for the decay of temperature fluctuations at $y > L$. We obtain

$$\theta_l(y) = \begin{cases} \frac{\overline{w'\theta'_l}|_s}{\overline{w_l}(y)}, & 0 \leq y \leq L \\ \frac{\overline{w'\theta'_l}|_s}{\overline{w_l}(y)} \exp\left(-\frac{L-y}{D_\theta}\right), & y > L \end{cases}, \quad (2.23)$$

where D_θ is the decay length scale for temperature with

$$D_\theta = d_\theta \cdot U \frac{z_i^{2/3}}{B_l^{1/3}}, \quad (2.24)$$

where d_θ is a parameter (see Appendix B.1). In Figure 2.6, we illustrate the necessity of using Equation 2.23 instead of Equation 2.8 by showing the effect of both equations on the non-local term Γ , exemplarily for case L5c-U5. The dashed lines in Figure 2.6 show that Γ would increase for $y > L$ especially in the upper part of the ABL if we did not consider the second line of Equation 2.23. This would result in unrealistically increasing heat fluxes at $y > L$, which contradicts also LES (Figure 2.2, left column).

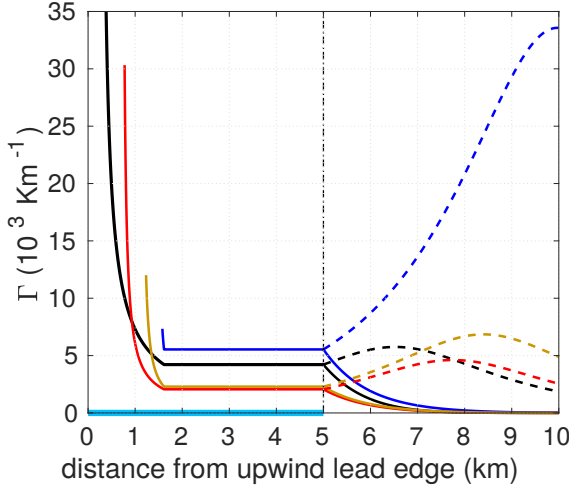


Figure 2.6: METRAS results of the non-local term Γ (in 10^3 Km^{-1}) in the new parametrization (section 2.5.1) at different heights (coloured) obtained with either Equation 2.8 (dashed) or Equation 2.23 (solid) for the convective temperature scale θ_l at $y > L$. Black: $z = 20 \text{ m}$, red: $z = 100 \text{ m}$, brown: $z = 200 \text{ m}$, and blue: $z = 290 \text{ m}$. Case is L5c-U5, and the lead is between 0 and 5 km distance.

Downstream of the lead, we adopt the assumption of L08 that mixing far away from the plume is dominated by local effects. Thus, we also take $\delta_d(y)$ as switching line. Unlike L08, we set $F_{crit} = 0.1 \text{ Wm}^{-2}$ since compared with LES the simulated entrainment was underestimated using the original value (not shown). This new value was found by a systematic variation of F_{crit} in small steps and comparing results for all cases with LES. The modification of the closure has consequences also for the values of the other unknown parameters.

Since the new closure assumes no decay of turbulence over the lead, values obtained for the convective velocity scale w_l with this closure are higher than with the corresponding Equation 2.9 of the L08 closure. A higher value of w_l results in a smaller inclination of the plume. Thus, the parameters c and finally a , which also determine the plume inclination, need to be lowered relative to the values $c = 1.6$ and $a = 2.3$ used by L08, when a similar quality

of agreement shall be reached as for the L08 closure. With our assumption that convection over a lead is similar to convective conditions over homogeneous surfaces, we obtain $w_l = w_*$ if the limit $\delta(y) = z_i$ is reached above the lead (see Equations 2.6 and 2.19); hence, we set $c = 1$. This value was confirmed by determining c with the help of LES results (see Appendix B.2). c might depend on L , but a comparison with LES showed that this dependence can be neglected and, thus, the value $c = 1$ is applicable for the cases considered here.

For a_e and a_m , we apply the same ranges as determined by L08 (section 2.2.2.2). With $c = 1$ and $a = a_e a_m c$, we obtain $a = 1 \pm 0.6$, which is also lower than in L08. Based on the simulated plume inclinations, our results agree best with LES if we set $a = 1.2$ (see also Table B1 and Figures B8 and B9 in Appendix B).

We change also b , which determines the magnitude of Γ (Equation 2.18). By applying smaller values for c and a , results obtained with the value of L08 ($b = 0.6$) disagree with LES (see Figure B6 in Appendix B), namely, due to an underestimated counter-gradient transport. We obtain the best agreement with LES, if we set $b = 2$. This agrees perfectly with the value proposed originally for b used in Γ by Holtslag and Moeng (1991) on the basis of LES for convection over homogeneous surfaces and whose approach forms the basis for our parametrization. For d_w and d_θ , we obtain $d_w \approx 1.7$ and $d_\theta \approx 0.51$ also based on LES (see Appendix B.1).

Regarding the momentum fluxes, we found that results obtained with a non-local instead of a local approach for the eddy diffusivity K_m agree better with LES. We obtain K_m following Lüpkes and Schlünzen (1996), where we apply the corresponding equation only inside the convective plume:

$$K_m = K_h \left(\frac{\Phi_h|_{z_p}}{\Phi_m|_{z_p}} + b \frac{w_l(y) u_{*,l} \kappa z_p}{\Phi_m|_{z_p} \overline{w'^2}|_{z_p} \delta(y)} \right), \quad \delta_d(y) < z \leq \delta(y), \quad (2.25)$$

where Φ_m is the Monin-Obukhov similarity function for momentum and $\overline{w'^2}$ is the vertical velocity variance, which is parametrized as in L08 via

$$\overline{w'^2} = 1.6 u_*^2 \left[(1 - Z)^{3/2} + 0.593 S^3 Z (1 - 0.9Z)^{3/2} \right]^{2/3}. \quad (2.26)$$

with S and Z calculated via Equations 2.14 and 2.15. Originally, Equation 2.26 was derived by Holtslag and Moeng (1991) for horizontally homogeneous convection based on LES and observations.

2.5.2 Results for wide leads

Simulation results of METRAS obtained with the new closure (section 2.5.1) are discussed in the following, mainly for the same cases as in section 2.3.

2.5.2.1 Cold cases

Basically, the simulated patterns of both heat fluxes (Figure 2.7, left column) and ABL stratification (Figure 2.7, right column) agree well with the corresponding LES results (Figure 2.2). Using the new closure, the overall shapes of the convective plumes, the positions of the maximum heat fluxes, and the magnitudes of the simulated entrainment fluxes do not differ considerably from

the LES results. Also the maximum values of heat fluxes at $z = 100$ m and $z = 200$ m agree well with the LES values (Table 2.1). Furthermore, the simulated plume boundaries downstream of the lead are clearly visible, which was not the case in the METRAS results using the local or the non-modified L08 closure (Figures 2.4a and 2.4b). Thus, in contrast to those results, a slightly stable stratification is now simulated downstream of the lead for all cases in good agreement with the LES results. Furthermore, similar effects as simulated with LES are shown for increasing wind speed (Figures 2.7a, 2.7c, and 2.7e) and lead width (Figure 2.7g). Some details are, however, not reproduced with METRAS using the new closure. For instance, an increase in ABL thickness with increasing fetch over the lead is not as pronounced as with LES. Furthermore, fetch-dependent positions of the maximum heat fluxes above the lead are not simulated and entrainment is weaker.

In all four cases, an LLJ is simulated with its core in the upper third of the ABL near the lead's upstream edge (Figure 2.8, left column) and the core region is also inclined towards the surface with increasing fetch. A clear weakening of the LLJ over the lead centre is shown in all cases. Especially for case L5c-U3, a secondary maximum is simulated at $z = 50$ m above the second half of the lead (Figure 2.8a). Downwind of the convective plume, in most cases a regeneration of the LLJ is shown. These simulated wind field structures agree well with the LES results (Figure 2.3, left column). Note that similar effects have been measured by T15, which supports both our LES results and considering non-local effects in the new parametrization also for K_m . Only for case L5c-U7 (Figure 2.8e) the destruction and regeneration of the LLJ obtained with the new parametrization are not as pronounced as with LES.

Unlike L08, we consider also momentum fluxes (Figure 2.8, right column). Their general pattern and the positions of their maxima near the upstream edges are simulated in fair agreement with LES results (Figure 2.3, right column) if the new closure is used. However, the maxima simulated with METRAS are slightly less pronounced than with LES. Furthermore, except for case L5c-U3, the secondary maxima near the lead's downstream edge are not reproduced and the downstream decay seems to be too weak as compared to LES.

2.5.2.2 Warm cases

In Figure 2.9, heat flux and stratification patterns from both models are shown for case L5w-U5. Thus, we consider the effect of strongly increased inflow temperature. The LES results (Figures 2.9a and 2.9b) show that the smaller temperature difference in case L5w-U5 in comparison to L5c-U5 (Figures 2.2c and 2.2d) has several effects on the flow characteristics over the lead: weaker heat fluxes, increased plume inclination, and slightly less pronounced stratification downstream of the lead. Basically, the corresponding METRAS results obtained with the new parametrization (Figures 2.9c and 2.9d) agree well with the LES. This holds for both heat fluxes and ABL stratification. Again, differences concern mainly the positions of the maximum heat fluxes and the magnitude of the entrainment fluxes.

2.5.2.3 Variance of vertical velocity

Basically, also results of the vertical velocity variance $\overline{w'^2}$ (Equation 2.26) obtained with the new closure agree with LES (Figure 2.10). With LES, the highest values are simulated in the

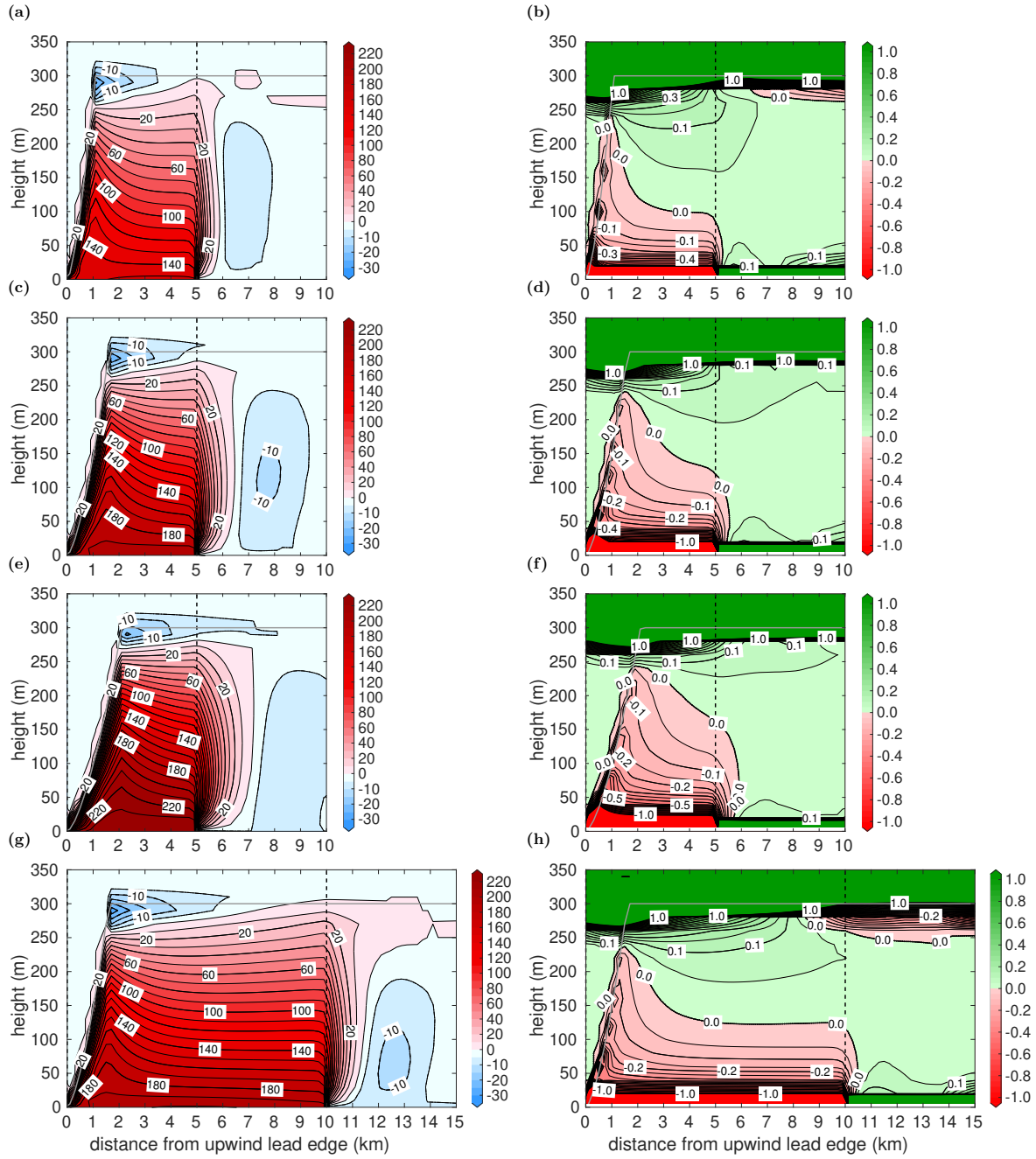


Figure 2.7: Heat flux (Wm^{-2}) and vertical potential temperature gradient (K per 100 m) for the same cases as for the LES results in Figure 2.2, but obtained with METRAS using the new parametrization (section 2.5.1). The solid grey lines show the upper IBL height according to Equation 2.20.

centre of the convective regions for all cases and downstream of the lead $\overline{w'^2}$ decreases (Figure 2.10, left column). This is well reproduced with METRAS using the new closure (Figure 2.10, right column). Differences between the results of both models concern mainly the horizontal inhomogeneity of $\overline{w'^2}$ in the convective core regions, which is especially shown in the LES of the cases L5c-U3 and L10c-U5 (Figures 2.10a and 2.10g), but not reproduced with the new closure (Figure 2.10b and 2.10h). Furthermore, with LES, the maxima of $\overline{w'^2}$ are up to 40% higher. Downstream of the lead, the decrease of $\overline{w'^2}$ starts at $y = L$ near the surface but further downstream towards z_i (Figure 2.10, left column), which is also not reproduced with

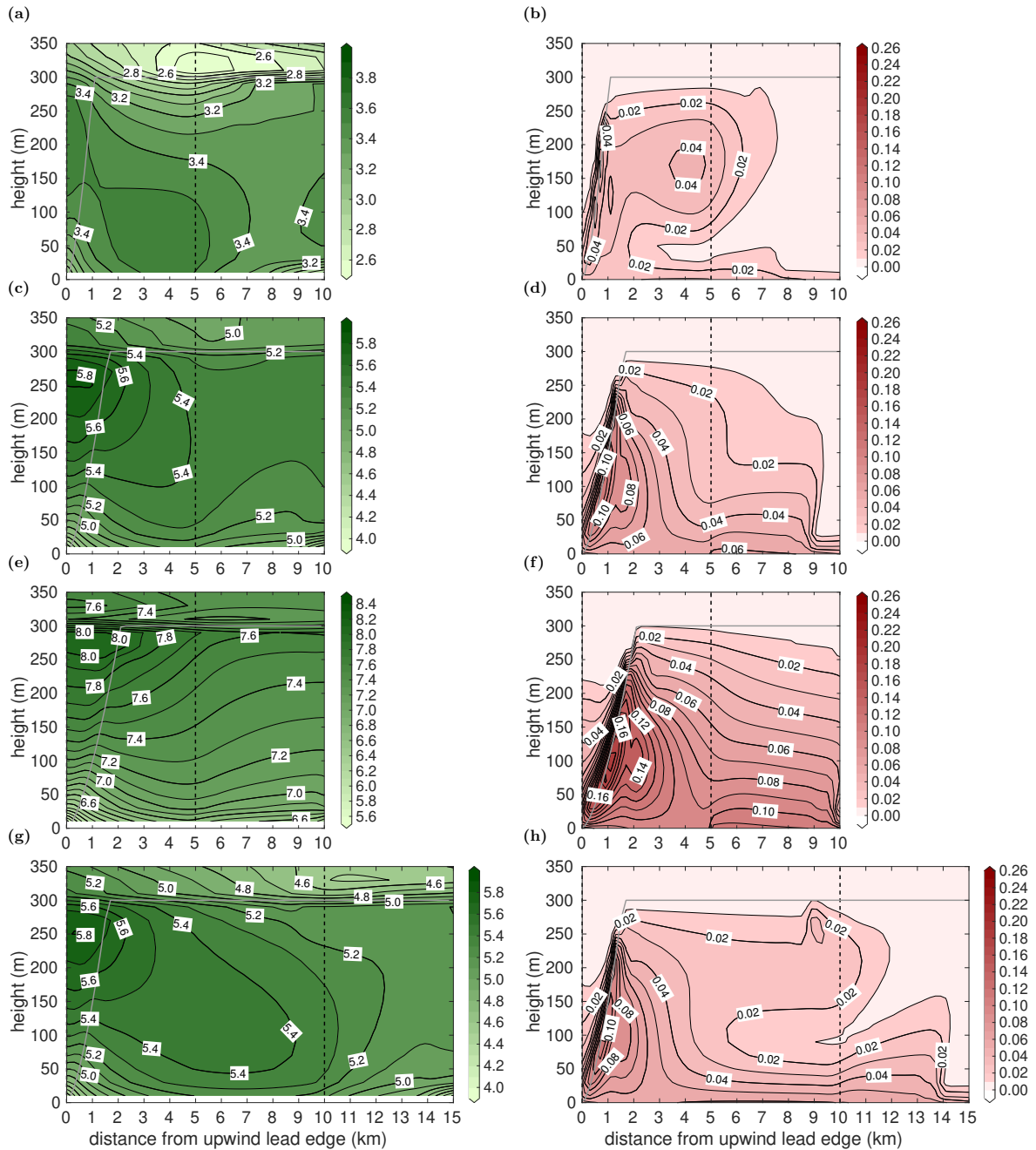


Figure 2.8: Results obtained with METRAS using the new parametrization as in Figure 2.7, but horizontal wind speed in ms^{-1} (left column) and vertical momentum flux in Nm^{-2} (right column) are shown. The corresponding LES results are shown in Figure 2.3.

the new closure (Figure 2.10, right column). This result is related to the same disagreement in the heat and momentum fluxes (Figure 2.7, left column; Figure 2.8, right column).

2.5.3 Results for narrow leads

Within the range of our applied wind regimes and temperature differences (see Table 2.1), the convective plume over narrow leads does not penetrate into the inversion already above the lead. Thus, in contrast to wide leads, for narrow leads the second line of Equation 2.20 is used

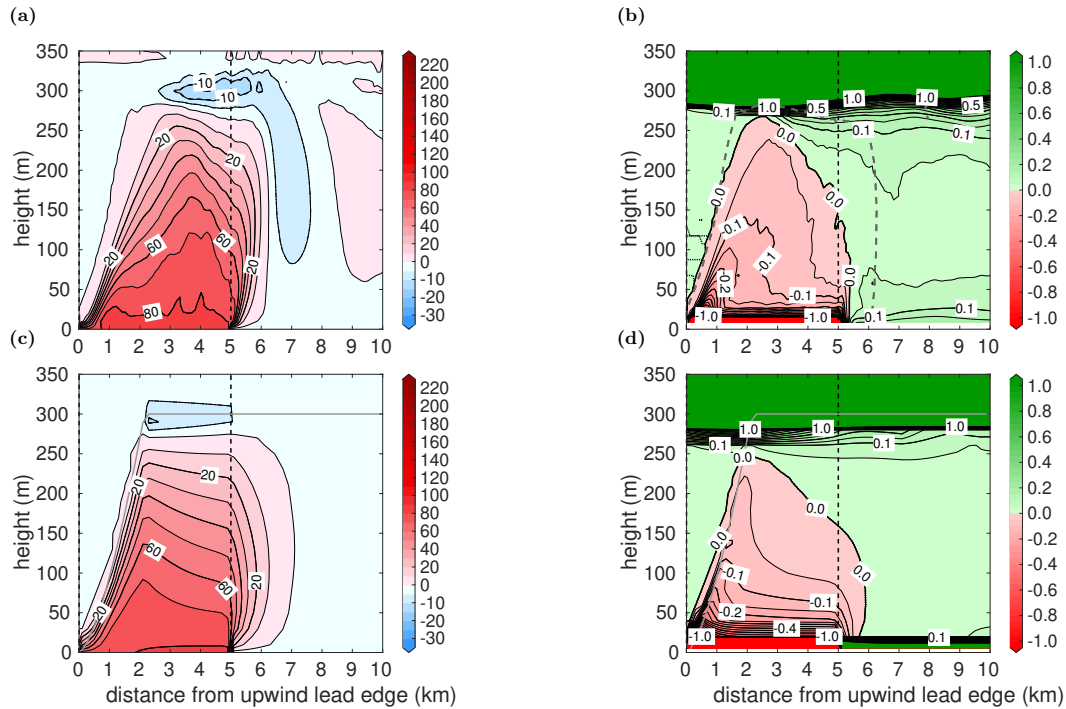


Figure 2.9: (a, b) LES results as shown in Figures 2.2c and 2.2d and (c, d) results obtained with METRAS using new parametrization (section 2.5.1) as shown in Figures 2.7c and 2.7d, but results of heat flux in Wm^{-2} (left column) and vertical potential temperature gradient in K per 100 m (right column) are shown for case L5w-U5 (see Table 2.1).

for $\delta(y)$. We performed L1c-U3, L1c-U5, L1c-U7, and L1w-U10 simulations as in L08 (their Tables 1 and 2). To ensure comparability, we show heat flux patterns and potential temperature distributions for a lead 10 km downstream of another lead (Figure 2.11). New LES results of those scenarios are shown in Figure B7 in Appendix B. Furthermore, LES and METRAS results with both non-local closures are presented for a scenario with $L = 0.5 \text{ km}$ in Figure 2.12 (case L0.5c-U5, Table 2.1).

2.5.3.1 Lead width: 1 km

As Figure 2.11 shows, the simulated patterns of both heat fluxes and potential temperature agree again well with our LES results (Figure B7 in Appendix B). The latter differ only slightly from those shown by L08 (their Figures 3 and 8, lower row), but convection is already fully resolved by the LES close to the upstream lead edge, which results in a more linear increase of the IBL than in the L08 LES result using lower resolution. METRAS results for $L = 1 \text{ km}$ obtained with the new closure agree also well with the results obtained with the original L08 closure (see Figures 6 and 9, lower row of L08), especially plume inclinations and heat flux patterns. Also, the simulated maximum heat fluxes at $z = 100 \text{ m}$ and $z = 200 \text{ m}$ agree well with the corresponding values from LES, except for case L1c-U3 where our results are about 25 Wm^{-2} higher (Table 2.1). A clear improvement is shown in our results concerning the position of the entrainment fluxes as compared to the METRAS results obtained with the L08 closure (see L08, their Figures 6 and 9, left columns).

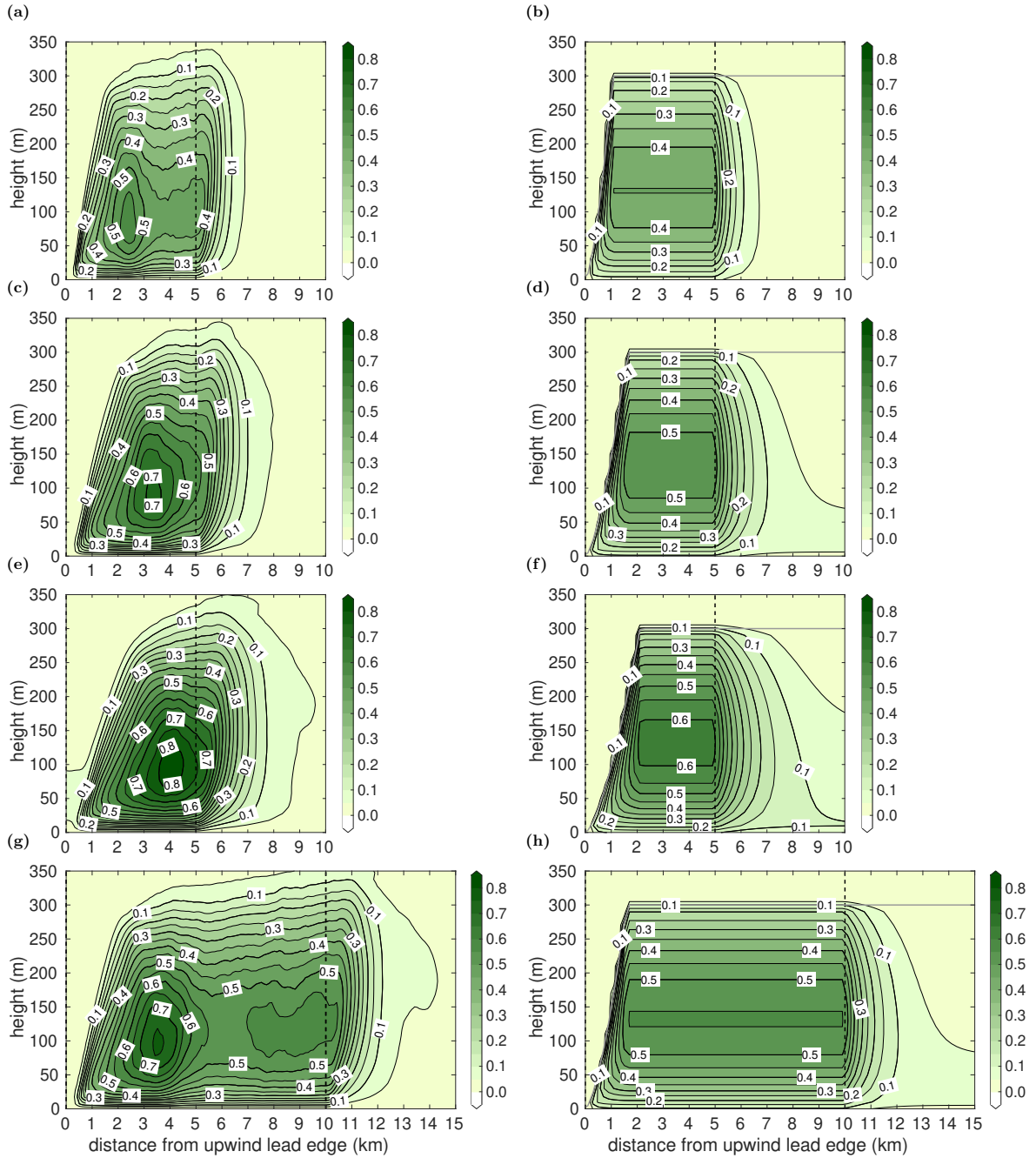


Figure 2.10: Vertical velocity variance $\overline{w'^2}$ (m^2s^{-2}) from LES (left column) and METRAS using the new parametrization from section 2.5.1 (right column) for L5c-U3 (a, b), L5c-U5 (c, d), L5c-U7 (e, f), and L10c-U5 (g, h). In the right column, the solid grey lines show the upper IBL height according to Equation 2.20. For the cases, see Table 2.1.

2.5.3.2 Lead width: 0.5 km

According to Figure 2.12, also for leads of width $L = 0.5$ km results obtained with the new parametrization (Figures 2.12e and 2.12f) agree well with LES (Figures 2.12a and 2.12b), mainly concerning plume inclination and downstream stratification. The plume inclination agrees with LES also if we use the closure of L08 (Figures 2.12c and 2.12d), but the magnitude of heat fluxes downstream of the lead disagrees. This is due to an overestimation of the non-local heat flux with the L08 closure (see Figure 2.14).

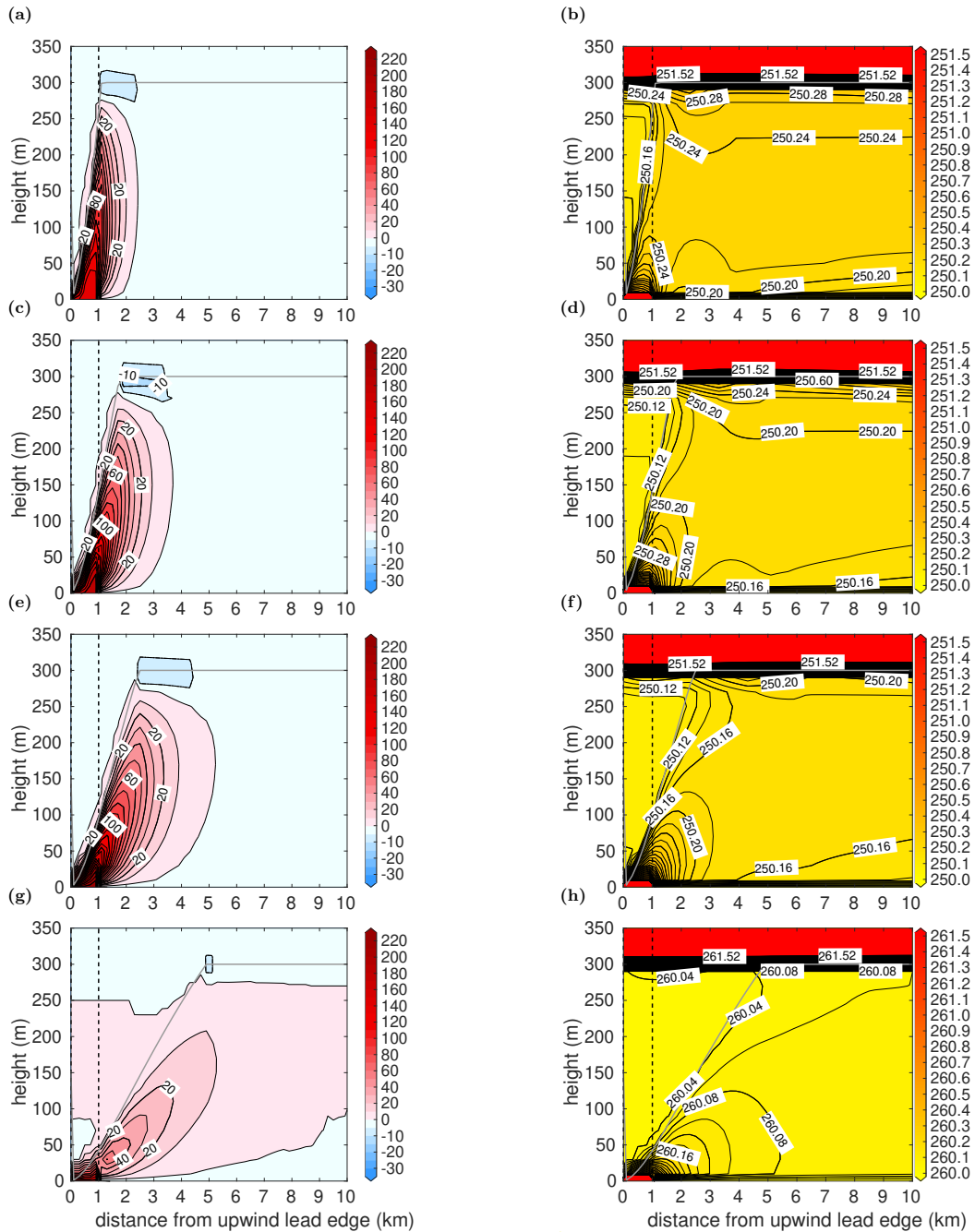


Figure 2.11: METRAS results obtained with the new parametrization (section 2.5.1) of heat flux in Wm^{-2} (left column) and of potential temperature in K (right column) for the cases L1c-U3 (a, b), L1c-U5 (c, d), L1c-U7 (e, f), and L1w-U10 (g, h). The position of the lead is between 0 km distance and the dashed, vertical black line. The spacing between heat flux contour lines is 5Wm^{-2} for negative fluxes. The solid grey lines show the upper IBL height according to Equation 2.20. Note the different temperature scale in (h). Corresponding LES results are shown in Figure B7 in Appendix B and in L08 (their Figures 3 and 8, lower row). See Table 2.1 for a description of the cases.

2.5.4 Sensitivity studies

2.5.4.1 Variation of parameters

The sensitivity of our results was tested with additional simulations using alternative values for the tunable parameters in the new parametrization. For *b* we considered simulations of case

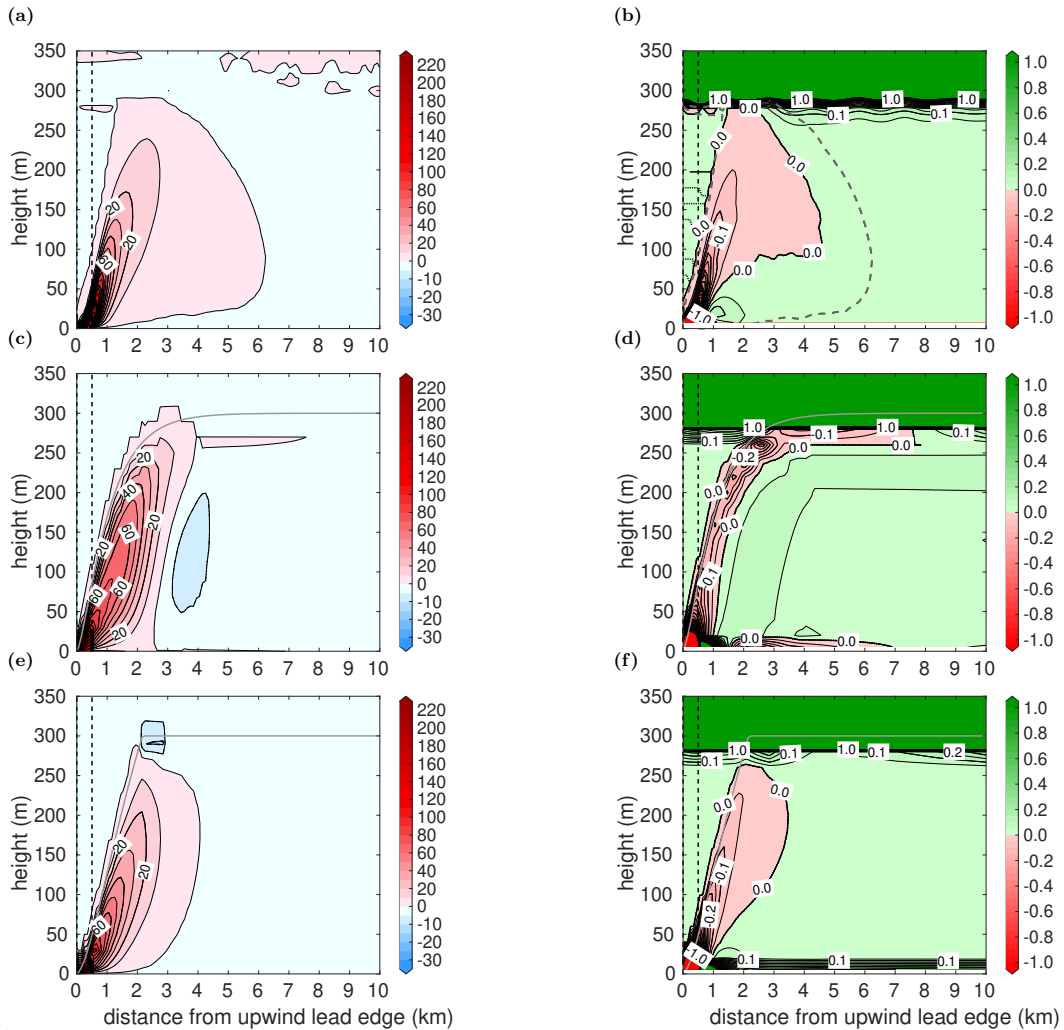


Figure 2.12: Heat flux in Wm^{-2} (left column) and vertical potential temperature gradient in K per 100 m (right column) of case L0.5c-U5 (see Table 2.1) obtained with LES (a, b), METRAS using the L08 parametrization (c, d), and METRAS using the new parametrization from section 2.5.1 (e, f). The position of the lead is between 0 km distance and the dashed, vertical black line. The spacing between heat flux contour lines is 5Wm^{-2} for negative fluxes. In (b), the area inside the dashed grey lines depicts the region of positive fluxes inside the convective plume. In (c) and (b), the solid grey lines show the upper IBL height according to Equation 2.11 and in (e) and (f) according to Equation 2.20.

L5c-U5 with the values applied by Lüpkes and Schlünzen (1996) ($b = 3$) and by L08 ($b = 0.6$), respectively. With $b = 3$, maximum heat fluxes at $z = 100\text{ m}$ and $z = 200\text{ m}$ are overestimated by about 25Wm^{-2} with respect to LES and the stability especially in the upper part of the mixed layer is overestimated, too (Figures B6c and B6d in Appendix B). With $b = 0.6$, the magnitude of non-local heat fluxes especially in the upper part of the mixed layer is underestimated. At, for example, $z = 200\text{ m}$, the maximum heat flux is then more than 40Wm^{-2} lower than with LES and, in contrast to LES, the downstream ABL stratification is slightly unstable (Figures B6a and B6b in Appendix B). Furthermore, with $b = 0.6$, positive fluxes are obtained in the downwind mixed layer in contrast to strong negative fluxes with $b = 3$, which are even stronger than with LES. This is caused by a redistribution of heat in the ABL by adjusting b , where an increase of b causes lower temperatures near the surface and higher temperatures near the ABL

top (see also L08).

Due to our assumption $w_l = w_*$ for convection that reaches z_i already at $y < L$, we set $c = 1$ (Equation 2.19), and we applied this also for narrow leads (section 2.5.1). Thus, $c \neq 1$ would mean that we assumed convection over leads to be stronger or weaker as compared to homogeneous conditions, on average. This would cause a drawback regarding our basic assumption formulated in section 2.5.1. Furthermore, L08 showed that a variation of c by $\pm 25\%$ would have only small effects on the fluxes. For this reason and also because the assumption $c = 1$ is supported by our LES results (Appendix B.2), we did not consider any variations of c .

A variation of a has a strong effect on the plume inclination, whereas the effects on the downstream ABL characteristics are negligible (not shown). Our results show that, especially for weak wind, the plume inclinations are slightly underestimated with $a = 1.2$ for both wide (Figure 2.7a compared to Figure 2.2a) and narrow leads (Figure 2.11a compared to Figure B7a in Appendix B); hence, maximum heat fluxes at a certain height are overestimated (Table 2.1). However, for example, with $a = 1$, plume inclinations for higher wind speeds would then be overestimated (not shown). Therefore, our value for a can be seen as a compromise, where for the majority of our scenarios plume inclinations obtained with the new closure agree with LES (see also Appendix B.2).

2.5.4.2 Momentum transport

Our application of a non-local parametrization for K_m (Equation 2.25) causes an improved agreement with LES as can be seen by comparing the corresponding results in Figure 2.8 (METRAS with the new closure) and Figure 2.3 (LES). Obviously, when the local approach is used for K_m only (Figure 2.13a), the destruction of the LLJ with increasing fetch over the lead is not as effective as compared to the simulation with non-local K_m (Figure 2.8c) and to LES (Figure 2.3c). Furthermore, momentum fluxes in the upper downstream half of the ABL over the lead are smaller than with LES (Figure 2.13b).

Results of a simulation using a non-local approach for both K_h and K_m but with a maximum mixing length l_{max} lowered to 15 m instead of about 45 m resulting from $l_{max} = 0.15z_i$ are shown in Figures 2.13c and 2.13d. With $l_{max} = 15$ m, the LLJ position upstream of the lead is at $z \approx 220$ m (Figure 2.13c), which is about 50 m lower than obtained with $l_{max} = 0.15z_i$ (Figure 2.8c) and with LES (Figure 2.3c). Regarding the maximum momentum transport, the value obtained with $l_{max} = 15$ m agrees better with LES (Figure 2.3d) than the value obtained with $l_{max} = 0.15z_i$ (Figure 2.8d). However, the position of that maximum is rather at $0.4z_i$ than at $0.1z_i$ as in LES, and it is simulated further downstream than with LES.

2.6 Discussion

2.6.1 Importance of non-local closure and L as parameter

First, our results clearly show the importance of using fetch-dependent non-local turbulence closures for non-eddy-resolving atmospheric models to simulate the characteristics of lead-

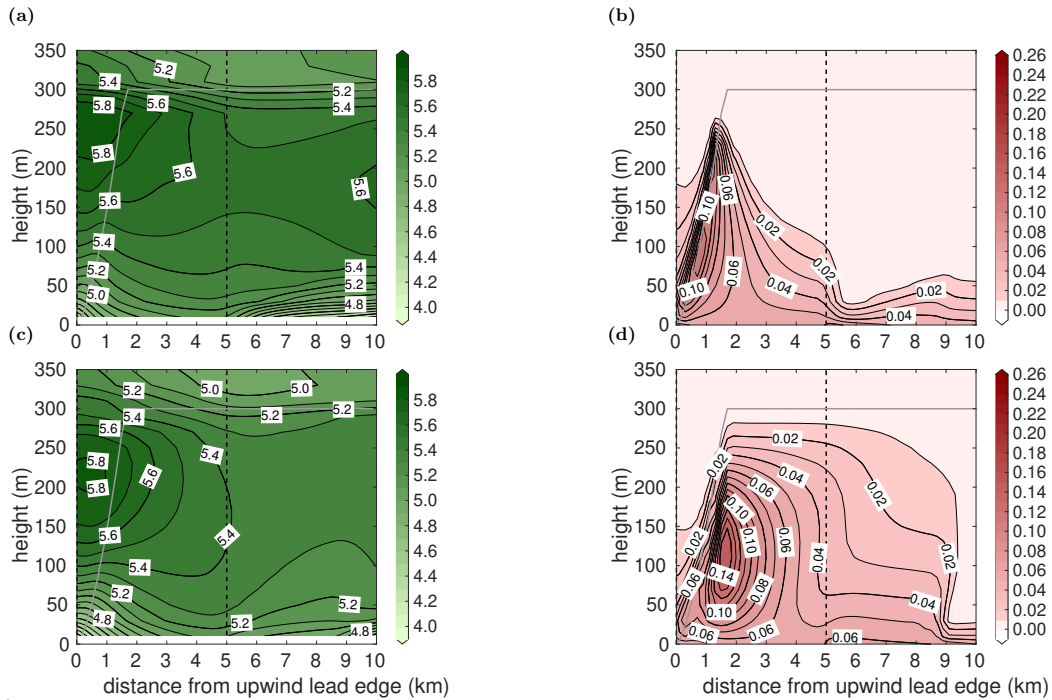


Figure 2.13: Horizontal wind speed (ms^{-1}) and vertical momentum flux (Nm^{-2}) for case L5c-U5 (see Table 2.1) obtained with METRAS using the new parametrization for heat transport as in Figures 2.8c and 2.8d. For panels (a) and (b), a local closure is applied for the eddy diffusivity for momentum (Equation 2.3 instead of the non-local parametrization in Equation 2.25 used for panels (c) and (d)). In (c) and (d), the maximum mixing length l_{max} (see Equation 2.3) is set to 15 m instead of $0.15z_i$. See Figures 2.3c and 2.3d for the corresponding LES results.

generated convection in the ABL, properly. Results and drawbacks obtained with the used local closure can be considered as representative in the sense that also the use of a more sophisticated TKE-closure cannot improve results as long as the non-locality of heat fluxes is not reproduced.

Second, we stress that with our modification of the L08 closure the simulated patterns agree well with LES for different lead widths L . The non-local L08 closure was developed for narrow leads and, indeed, we showed drawbacks, especially for wide leads. The main step for an improvement of the L08 closure was to assume that the decay of turbulence starts at the downstream lead edge and not over the lead as in L08. Compared with LES, this is still a simplification because LES shows that the position of decay is height-dependent. Nevertheless, our approach allowed the introduction of the lead width L as a parameter in our parametrization and, despite the still simplified treatment of decay, results for wide leads improved considerably as compared with LES. Furthermore, we showed that for $L = 0.5$ km results obtained with the new parametrization agree also slightly better with LES than those with the non-modified L08. As illustrated in Figure 2.14, the improvements for both wide leads and $L = 0.5$ km are mainly achieved by an optimised representation of non-local heat transport due to the L -dependence in the new closure.² This shows the importance of L in the parametrization.

Closures describing counter-gradient transport were designed for an improved representation of the temperature field. Thus, we show in Figure 2.15 the improvement achieved with the new

²This sentence and Figure 2.14 are not part of the original publication Michaelis et al. (2020).

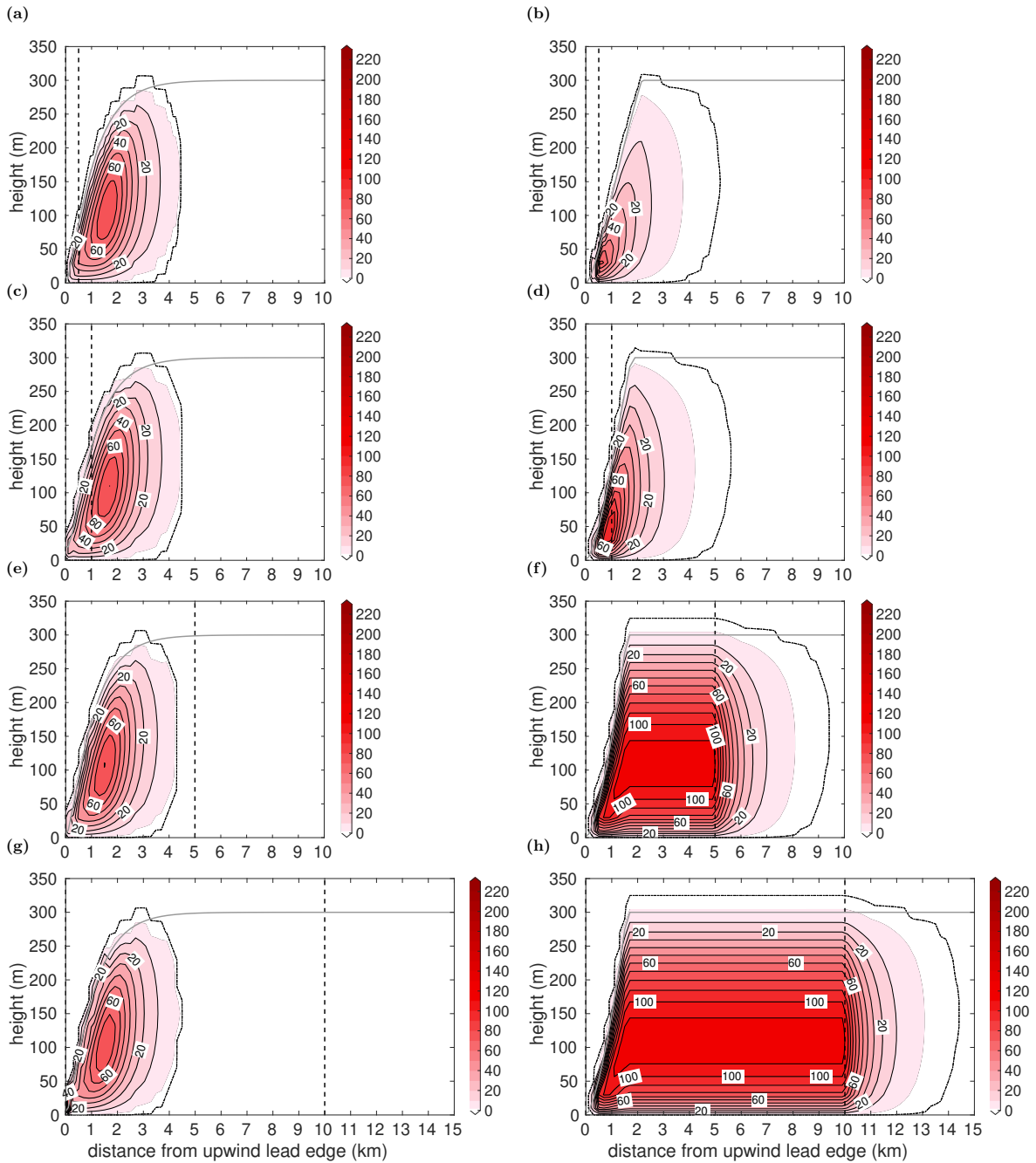


Figure 2.14: Non-local heat flux $F_{h,nl}$ in Wm^{-2} obtained with METRAS using the L08 closure from section 2.2.2.2 (left column) and the new parametrization from section 2.5.1 (right column). Cases are L0.5c-U5 (a, b), L1c-U5 (c, d), L5c-U5 (e, f), and L10c-U5 (g, h). The position of the lead is between 0 km and the vertical, dashed black line. In the left column, the solid grey lines show the upper IBL height according to Equation 2.11 and in the right column according to Equation 2.20. For the description of the cases, see Table 2.1.

non-local closure compared to results obtained with a local closure in terms of temperature deviations from the LES result. Note that we did not use the same contour lines and colour scales in each case since ABL warming and, thus, the absolute temperature differences between LES and METRAS are larger for wide leads than for narrow leads. As Figure 2.15 shows, differences between LES and METRAS are smaller when the new non-local instead of the local

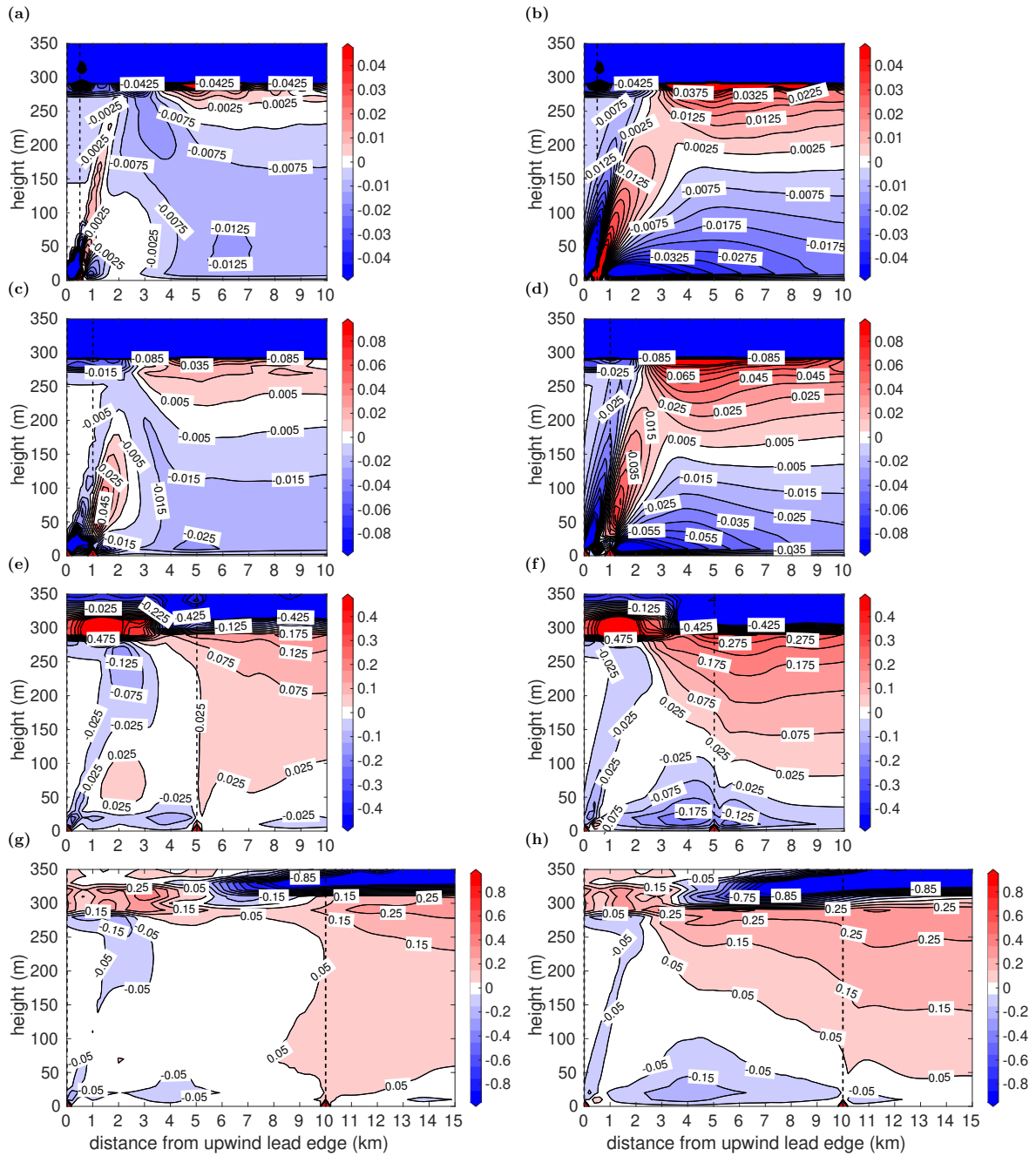


Figure 2.15: Differences in potential temperature (K) between LES and METRAS using the new parametrization from section 2.5.1 (left column) and the local closure from section 2.2.2.2 (right column). Cases are L0.5c-U5 (a, b), L1c-U5 (c, d), L5c-U5 (e, f), and L10c-U5 (g, h). The position of the lead is between 0 km and the vertical dashed black line. Note the different colour scales. For the description of the cases, see Table 2.1.

mixing-length closure is used. This holds independent on the value of L . Another interesting point is that the results on the downstream side of the plume agree perfectly with LES in almost all cases. For case L0.5c-U5 this concerns, for example, the region between $y = L$ and $y = 3L$, which means that our relatively rough approximation of the decay of turbulence is sufficient.

The approach proposed in section 2.2.2.2 for the maximum mixing length in the local closure results in a much larger value compared with the often used value based on Blackadar (1962),

where l_{max} is proportional to the ratio of friction velocity and the Coriolis parameter. Basically, with the smaller value, METRAS results are much worse than those shown in all figures for the local closure. This causes also a larger temperature deviation from LES (Figure 2.16).

2.6.2 Methodological limitations

Our assumption of two decay length scales to describe the decaying convection downstream of the lead is based on Nieuwstadt and Brost (1986), and LES results of, for example, case L5c-U5 support our approach (see Figure B1b in Appendix B.2). Furthermore, Figure 2.10 shows that the decay rates for vertical velocity fluctuations agree well with LES also for the other cases with $L \geq 5$ km. Thus, the value we obtained for d_w by linear regression can be considered as reasonable. Similarly, results of $\overline{\theta'^2}$ for cases other than L5c-U5 might help to evaluate our assumed ratio $d_\theta/d_w = 0.3$. Figure 2.10 (left column) also shows that the decay of vertical velocity fluctuations near the surface starts at $y = L$, but towards z_i , this decay starts further downstream. Moreover, $\overline{w'^2}$ seems to be highly inhomogeneous over the lead in the centre of the ABL. Both features are not captured by the new closure since we had to assume horizontally homogeneous conditions for $\overline{w'^2}$ to avoid a discontinuity in $\overline{w'^2}$ at $y = L$ and, thus, also in the fluxes. This would occur due to the necessary assumption of y -independent u_* for $y > L$ in

Equation 2.19. Thus, any improvement with respect to the y -dependence of $\overline{w'^2}$ does not necessarily improve the other results. Nevertheless, our results for $\overline{w'^2}$ with the new closure represent a clear improvement compared to results obtained with the non-modified L08 closure (see Figure 2.5b for case L5c-U5) and even more with the local closure.

Regarding the derivation of the parameters, especially for a , a_e , and a_m , a more detailed study of the relations between w_e , w_{max} , and w_l for different wind regimes seems necessary. Furthermore, as L08, we also neglected horizontal entrainment u_e since we focus on plumes with small inclination angles where $U \gg u_e$. However, particularly at low wind, u_e becomes more important (Deardorff & Peterson, 1980; Esau, 2007, L08). Thus, considering u_e for deriving $\delta(y)$ could lead to a better representation of the IBL growth over leads at small U .

Our LES results show that the penetrating convection plays a critical role regarding entrainment and ABL thickness. In principle, the fetch-dependent increase in ABL thickness (Figures

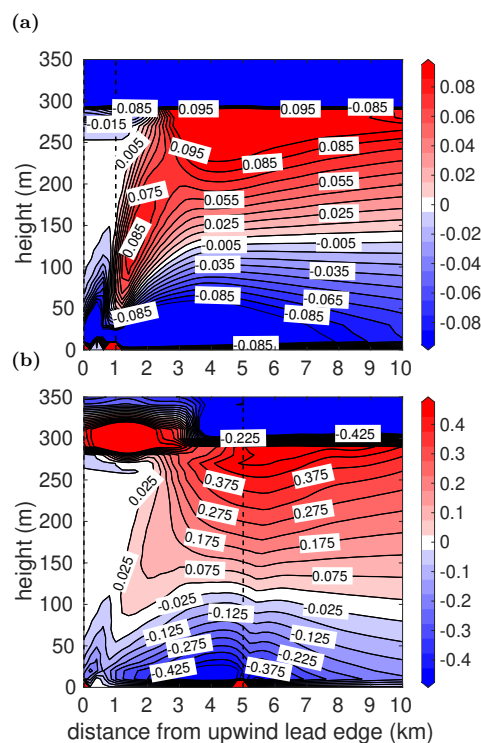


Figure 2.16: Differences in potential temperature (K) between LES and METRAS using the local closure as in Figure 2.15, but for the maximum mixing length $l_{max} = 0.007u_*/f$ is applied based on Blackadar (1962) instead of $l_{max} = 0.15z_i$ as in Figure 2.15. Cases are L1c-U5 (a) and L5c-U5 (b). Note the different colour scales.

2.2c and 2.2g) agrees with results of the modelling studies from Glendening and Burk (1992) and Zulauf and Krueger (2003b), who found L -dependent relations for the plume penetration height. In our microscale model results obtained with the new parametrization, both increase in ABL thickness and entrainment are, however, partly underestimated as compared to LES. Consequently, the downwind warming of the ABL obtained with the new parametrization is less pronounced than with LES, mainly near the inversion and especially for wide leads (Figure 2.15, left column). This drawback is mainly caused by assuming a fixed value for z_i also for $y > 0$, which causes less entrainment and prevents an increase in ABL thickness. Therefore, to better capture the effects of penetrating lead-generated convection, considering a fetch-dependent z_i seems necessary. This is supported by observations from T15, who found different values for up- and downstream ABL thickness in case of penetrating lead-generated convection. Moreover, an explicit consideration of entrainment (e.g., Noh et al., 2003) could be implemented, which is, however, challenging (see also section 2.8.1).

The downstream distribution of the turbulent momentum transport obtained with the new parametrization shows two additional differences as compared to LES. Secondary maxima near the lead's downstream edge were not reproduced, and the downstream decay seems to be underestimated, except for case L5c-U3. The reason could be another non-local component in the momentum transport, which is not yet represented by the new closure.

Improvements might also be achieved with other approaches for the treatment of the convection in the non-eddy-resolving model. As a promising alternative to the application of Equation 2.5, the so-called eddy-diffusivity mass-flux scheme (EDMF, Siebesma et al., 2007) could be applied. Following Equation 2.5, the small-scale fluxes and those generated by larger convective structures depend on each other via K_h in both terms. The EDMF approach has the advantage that these fluxes form separate contributions. Tetzlaff (2016), who compared both approaches in a modelling study of cold-air outbreaks, shows not only some advantages but also disadvantages of the EDMF approach. For example, modifications of the existing EDMF schemes are necessary with respect to the matching of fluxes at the top of the surface layer, especially for shallow boundary layers. Furthermore, we expect that the decay of turbulence downstream of the lead would require modifications of the EDMF closure.

2.7 Conclusions on the derivation of the new non-local approach

Our main goal was to derive an improved parametrization of the turbulence over sea ice leads for a microscale, non-eddy-resolving atmosphere model that accounts for the convection over leads of variable width. As a side effect, the derivation of the parametrization and related sensitivity studies helped to better understand the processes involved in the formation and decay of convective plumes in a neutral or slightly stable environment. As a starting point, a previous parametrization by L08 was used, who considered leads of only one particular width (1 km). However, the new and modified parametrization should be more general by including the lead width L as a parameter.

We considered 10 idealised scenarios of a lead-perpendicular flow in a neutrally stratified ABL capped by a strong inversion, and, as in L08, time-averaged LES results were considered

for the detailed analysis of the overall lead impact on the ABL. Our LES results revealed that the general characteristics of the flow over leads of different width remained similar to those of the 1 km-lead. Namely, a strong plume was developing over the lead and rapidly decaying over the downstream sea ice. This caused an increase of temperature combined with a stabilisation downstream of the lead, but with still upward heat fluxes. Thus, the transport was clearly of non-local nature. Hence, the basic ideas of L08, applying a non-local closure, assuming a separation of turbulence regimes in- and outside the plume region, and assuming decaying turbulence downstream of the lead, remained the same. Thus, also the new parametrization accounts for the inhomogeneous conditions of convection over leads so that both eddy diffusivity for heat and the non-local transport term depend on the distance to the upstream lead edge.

In our parametrization, we assumed fully developed convection above the lead and applied a decay function only over sea ice at the downstream side of a lead. By this assumption, it became possible to consider L as a parameter in the equations. This formulation had a consequence on the parametric equation for the development of the upper IBL height $\delta(y)$, which is equivalent to the top of the convective plume. Two regimes are distinguished in the new formulation, one over the lead and another one downstream of the lead where the decay of turbulence starts. Our assumption is based on the LES results for leads where the convection penetrates into the inversion already above the lead, which we defined as wide leads. Nevertheless, we derived a parametrization where also for narrow leads, where the convection reaches the inversion further downwind, the same set of equations is used. The only difference of our parametrization between wide and narrow leads concerns the development of $\delta(y)$ at $y > L$ since for narrow leads the limit $\delta(y) \geq z_i$ is not reached at $y < L$. In the limiting case of very narrow leads ($L \rightarrow 0$), the new approach coincides with the $\delta(y)$ -formulation of L08.

We showed that results obtained with the new closure agree well with LES, mainly concerning heat flux patterns, plume inclinations, and downstream stratification in the tested range of $z_i = 300$ m, $3 < U < 10$ ms⁻¹, and $85 < \overline{F}_{h,s} < 244$ Wm⁻². Unlike L08, we also applied a non-local closure for the eddy diffusivity for momentum. With this additional modification, also the horizontal wind speed with a diminishing of a weak low-level jet over the lead and momentum flux distributions in the convective region were basically reproduced. Furthermore, we showed that also results obtained with our parametrization of higher order moments, such as the vertical velocity variance, agree well with LES. The new parametrization contains six unknown parameters, which were derived using information from LES. We stress that the same set of values for the parameters was used for all cases considered. Nevertheless, there is room for further improvement of the new approach regarding, for example, the representation of entrainment and the height-dependent start of decaying convection downwind of the lead.

Both our LES and microscale model results also point to difficulties that might occur in mesoscale studies of atmospheric processes over the marginal sea ice zone, where leads strongly affect the flow regime. Mostly, such studies apply local closures, and it is obvious that the results of such modelling would have the same drawbacks as our results obtained with a local closure. The largest drawback is that the stabilising effect of leads on the downstream ABL is completely missing, and the spatial distribution of turbulent fluxes of heat and momentum show large deviations from the detailed LES results. We expect that the deviations might sum up to large errors when lead ensembles are considered since conditions upstream of a lead in

the inner region of such an ensemble might be affected by its upstream neighbouring lead. Furthermore, we showed that a non-local closure was also necessary for momentum fluxes to obtain a reasonable agreement with LES results.

Altogether, our results obtained with the new closure agree well with LES for different L in the wide range of the above-mentioned meteorological forcing. A further development should include explicitly moisture transport as well as variations of the ABL height, wind direction, and upstream stability. Observations of, for example, T15 showed that a stable stratification of the upstream ABL influences the IBL-growth. This might affect the parameter a (Equation 2.20). Nevertheless, the new parametrization represents a clear improvement since now, variable lead widths can be considered for a detailed study of the lead effects on the ABL. We also showed that grid sizes of the microscale model should not exceed $L/5$ to obtain a reasonable agreement of detailed flow structures as with LES. This shows that also for narrow leads in the range of 500 m or 1 km width, horizontal grid sizes of 100 to 200 m are sufficient to reproduce those structures. Thus, compared to LES, numerical costs are much lower for potential sensitivity studies on the lead impact defining also the range of the parameters. Selected studies might then need additional LES for validation. Thus, our findings could help to derive finally an improved surface flux parametrization over the marginal sea ice zone to be used in climate and weather prediction models. Furthermore, the new non-local approach might also help to improve parametrizations of a convective IBL developing over inhomogeneous surfaces, in general.

2.8 Further refinements of the parametrization

The analysis presented so far in this chapter showed that with the new non-local turbulence parametrization (see section 2.5.1, henceforth abbreviated by M20 parametrization) a clear improvement is achieved regarding the representation of convective plumes over leads of different width in a microscale, non-eddy-resolving model. Nevertheless, a few slight discrepancies to LES were outlined, which gives room to further improve the closure. Moreover, some effects are not yet included in the parametrization, like moisture transport. The analysis presented in the following in this section shall provide a first overview how such effects might be considered in future in the M20 parametrization, which might further improve the microscale model results.

2.8.1 Entrainment

One of the above-mentioned limitations of the M20 parametrization is the detailed representation of vertical entrainment. Especially for wide leads, the results obtained by METRAS revealed underestimated entrainment fluxes as compared with LES. The corresponding deviation from the LES result increases with increasing distance so that both ABL warming and downwind stabilisation are underestimated, which is also obvious in terms of the potential temperature distribution downwind of the lead shown in Figure 2.17.

In the centre of the downwind ABL, potential temperatures simulated with METRAS are underestimated by approximately 0.05 K for the cases with $L = 5$ km, or by approximately 0.1 K for the case L10c-U5 (Figure 2.17). Close to the top of the downwind ABL, the deviation from the LES results is even more pronounced. In the case L10c-U5, even a slightly unstable layer

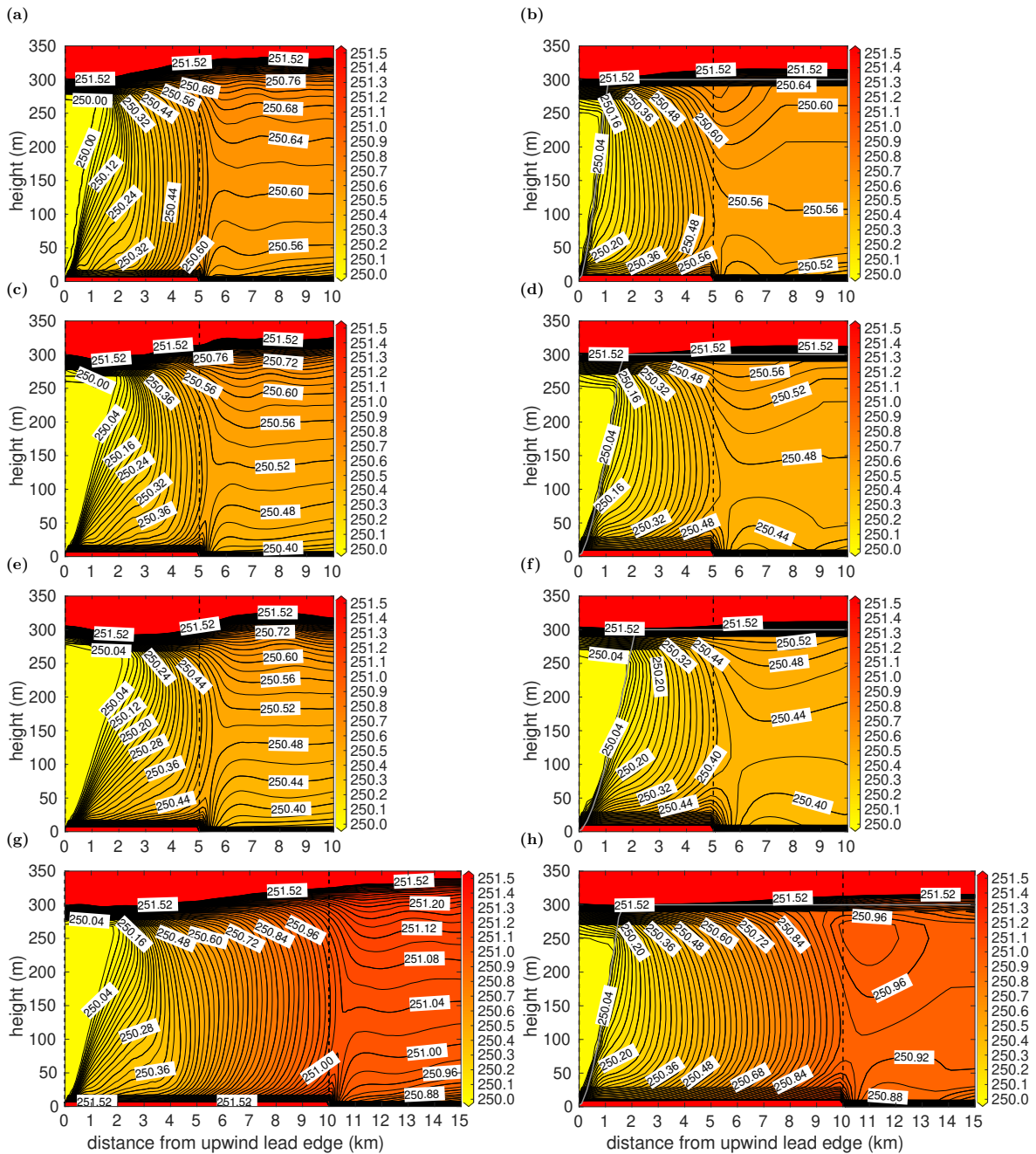


Figure 2.17: Potential temperature (K) obtained by LES (left column) and by METRAS using the new parametrization from section 2.5.1 (right column) for the cases L5c-U3 (a, b), L5c-U5 (c, d), L5c-U7 (e, f), and L10c-U5 (g, h). In the right column, the solid grey lines show the upper IBL height according to Equation 2.20. For the description of the cases, see Table 2.1.

is simulated with METRAS, which contradicts the LES result (see also Figure 2.7h compared with Figure 2.2h). The following analysis shows potential solutions, how these drawbacks might be overcome with further refinements of the M20 parametrization.

2.8.1.1 Increased upper limit for the upper plume boundary

As discussed in section 2.6.2, the reason for the above-mentioned drawbacks is most likely due to the assumption of a fixed value for z_i , which prevents a growth of the plume into the inversion

layer so that the associated effects obtained with the LES (entrainment also in the downwind lead region, fetch-dependent increase of the ABL thickness) are underestimated or not well represented. Thus, one approach to obtain an improved representation of vertical entrainment and its effects might be achieved by increasing the upper limit z_i for the upper plume boundary $\delta(y)$ (see Equation 2.20). Hence, METRAS simulations using the M20 parametrization were repeated with $z_i = 310$ m, where results for the cases L5c-U5 and L10c-U5 are shown in Figure 2.18 (model runs henceforth abbreviated by L5c-U5- z_i310 and L10c-U5- z_i310).

Due to the increased upper limit for $\delta(y)$ in the simulations with $z_i = 310$ m, for both cases, heat flux patterns (Figures 2.18a and 2.18b) and downwind temperature distributions (Figures 2.18c and 2.18d) agree better with the LES results (Figures 2.2c, 2.2g, 2.17c, and 2.17g) than in the simulations with $z_i = 300$ m (Figures 2.7c, 2.7g, 2.17d, and 2.17h). In the run L5c-U5- z_i310 , this improvement is clearly visible since the entrainment extends into the lead's downwind region (Figure 2.18a), resulting in an improved representation of the downwind stratification and the ABL warming effect (Figure 2.18c). For example, at $z \approx 175$ m, the downwind potential temperature is 0.08 K higher as compared to the result obtained in the simulation with $z_i = 300$ m so that it agrees almost perfectly with the value obtained by LES (see Figure 2.17c). However, near the capping inversion, both warming effect and ABL stratification are still slightly underestimated as compared with LES. In the run L10c-U5- z_i310 , only a small improvement is obtained (Figure 2.18, right column). The downwind temperature is slightly higher than in the simulation with $z_i = 300$ m, but still a shallow unstable layer is simulated in the upper ABL downwind of the lead.

The main disadvantage of simply prescribing a larger value for z_i for all $y > 0$ is obvious when regarding the entrainment above the lead near y_{z_i} (the distance y , where the plume reaches the inversion), which is overestimated in the simulation L10c-U5- z_i310 (Figure 2.18b) as compared with LES (Figure 2.2g). This holds also for the simulation L5c-U5- z_i310 .

2.8.1.2 Explicit entrainment term

Another approach to improve the representation of vertical entrainment in the model is to include an explicit term for the entrainment heat flux in the basic kinematic heat transport equation. Here, the approach of Noh et al. (2003) should be used, which is an extension of Equation 2.5:

$$\overline{w'\theta'} = -K_h \left(\frac{\partial \bar{\theta}}{\partial z} - \Gamma \right) + \overline{(w'\theta')}|_{z_i} \left(\frac{z}{z_i} \right)^n, \quad (2.27)$$

where n is an empirical constant with $n = 3$, and where $\overline{(w'\theta')}|_{z_i}$ is the entrainment heat flux with $\overline{(w'\theta')}|_{z_i} = -\beta \overline{(w'\theta')}|_s = \beta u_{*,l} \theta_{*,l}$, where $\beta = 0.2$ is a constant entrainment coefficient, and where $\theta_{*,l}$ is the lead-averaged value of the scaling value for temperature θ_* . Due to the fraction $(z/z_i)^n$, the entrainment heat flux is highest near z_i . Noh et al. (2003) also introduce new formulations for K_h and Γ in their scheme as an improved version of the non-local parametrization by Troen and Mahrt (1986). Here, this is neglected so that for K_h and Γ in the plume region still the Equations 2.16 and 2.18 based on Lüpkes and Schlünzen (1996) are used. Note that, for example, Chechin and Lüpkes (2017) also applied Equation 2.27 in a similar way for their simulations of cold-air outbreaks in horizontally homogeneous conditions.

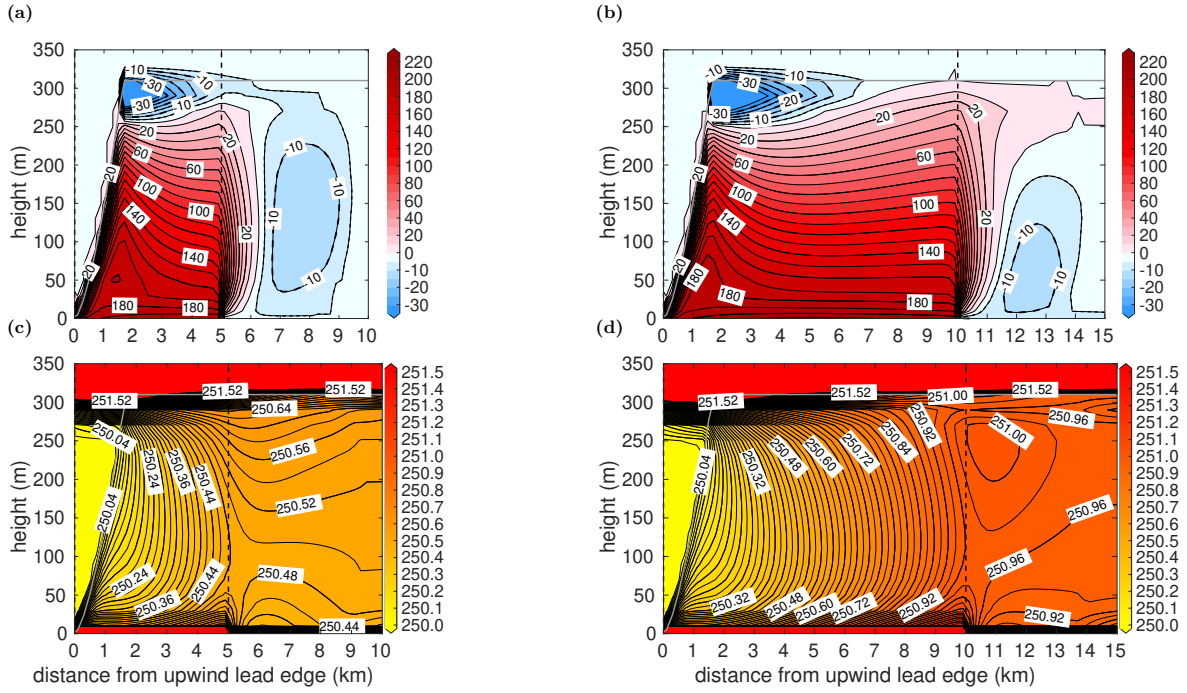


Figure 2.18: Heat flux in Wm^{-2} (upper row) and potential temperature in K (lower row) obtained by the simulations L5c-U5- z_i 310 for case L5c-U5 (a, c) and L10c-U5- z_i 310 for case L10c-U5- z_i 310 (b, d) using the new parametrization with $z_i = 310$ m as upper limit for the upper IBL height instead of $z_i = 300$ m as originally used in the new parametrization from section 2.5.1. The corresponding METRAS results obtained with $z_i = 300$ m are shown in Figures 2.7c and 2.7g for the heat flux and in Figures 2.17d and 2.17h for the potential temperature. The corresponding LES results are shown in Figures 2.3c and 2.3g for the heat flux and in Figures 2.17c and 2.17g for the potential temperature. For the cases, see Table 2.1.

In the following, the implementation of the second term on the right hand side of Equation 2.27, henceforth called entrainment term, is explained. In the simulations for wide leads using Equation 2.27 for the parametrization of $\overline{w'\theta'}$, the entrainment term is treated differently for three different regions. First, upwind of the convective plume (see P_1 in Figure 2.1), the local closure is used. Second, inside the plume, the entrainment term is used starting at $y \geq y_{z_i}$. Thus, the entrainment term is considered only in the region where the plume reaches the inversion layer. Third, for $y > L$, an exponential decay function is considered for the entrainment term to account for the decaying effect of the plume on the capping inversion downwind of the lead over sea ice, similar to the parametrizations of K_h and Γ in that region (see section 2.5.1). Furthermore, a similar decay for the entrainment heat flux as for the decay of the convective velocity (see Equation 2.19) is assumed. For wide leads (see section 2.2.3), this leads to

$$\overline{(w'\theta')}|_{z_i}(y) = \begin{cases} 0, & 0 \leq y < y_{z_i} \\ 0.2u_{*,l} \cdot \theta_{*,l}, & y_{z_i} \leq y \leq L \\ 0.2u_{*,l} \cdot \theta_{*,l} \exp\left(\frac{L-y}{D_w}\right), & y_{z_i} > L \end{cases} \quad (2.28)$$

For narrow leads (see section 2.2.3), the intersection between δ and z_i is assumed to take place downwind of the lead, which means $y_{z_i} > L$. Thus, the calculation of the entrainment term is

separated into two regions:

$$\overline{(w'\theta')}|_{z_i}(y) = \begin{cases} 0, & 0 \leq y < y_{z_i} \\ 0.2u_{*,i} \cdot \theta_{*,i} \exp\left(\frac{L-y}{D_w}\right), & y \geq y_{z_i} \end{cases}. \quad (2.29)$$

In the following, the focus is on results for the wide lead cases since in the narrow lead cases (see section 2.5.3), the downwind lead effects are well captured by the version of the M20 parametrization proposed in section 2.5.1. In Figures 2.19a and 2.19b, the entrainment term resulting from Equation 2.28 is shown for the cases L5c-U5 and L10c-U5, where henceforth the corresponding simulations are abbreviated by L5c-U5-ENT and L10c-U5-ENT, respectively. Both panels show the vertical entrainment fluxes in Wm^{-2} as negative values to indicate downward transport. The magnitude of the entrainment flux amounts to -24Wm^{-2} obtained above the lead close to z_i (Figures 2.19a and 2.19b). Downwind of the lead, the entrainment decays with increasing distance y , as expected. Note that the entrainment term is applied also in the region downwind of the convective plume, where $F_{h,nl} < F_{crit} \hat{=} \delta_d$. As expected from Equation 2.27, the magnitude of the vertical entrainment fluxes decreases continuously towards the lead surface above and downwind of the lead.

Figures 2.19c and 2.19d show the effects on heat flux patterns by considering the explicit entrainment term, as obtained by the run L5c-U5-ENT for case L5c-U5 and by the run L10c-U5-ENT for case L10c-U5. As expected, for both cases, the additional entrainment term leads to stronger vertical entrainment fluxes in total as compared to the results obtained without explicit entrainment term (see Figures 2.19c and 2.19d compared with Figures 2.7c and 2.7g). The magnitude of the entrainment is even slightly larger than with LES in both cases, at least at y_{z_i} , where the plume reaches the capping inversion (see Figures 2.2c and 2.2g for the LES results of the cases L5c-U5 and L10c-U5, respectively). For case L5c-U5, a slight improvement is obtained by the simulation L5c-U5-ENT regarding the downwind extension of negative heat fluxes near z_i , which agrees better with the LES results than in the simulation neglecting the explicit entrainment term. However, the improvement is less pronounced than obtained with the simulation L5c-U5- z_i 310 (see Figure 2.18a).

Effects on the potential temperature distribution obtained by considering the explicit entrainment term in the new parametrization are shown in Figures 2.19e and 2.19f. For case L5c-U5, an improvement is obtained by run L5c-U5-ENT regarding the temperature level of the lower half of the ABL downwind of the lead as compared to the METRAS results obtained without the explicit entrainment term (see Figure 2.19e compared with Figure 2.17d). Obviously, due to the entrainment term, temperature levels obtained in that ABL region agree now almost perfectly with the LES results (see Figure 2.19e compared with 2.17c). However, in the upper half of the downwind ABL and near z_i , a drawback arises in the simulation L5c-U5-ENT, namely, a shallow unstable layer, which contradicts the LES result. This is also shown for the simulation L10c-U5-ENT (Figure 2.19f). Moreover, the improvement obtained for case L5c-U5 by the simulation L5c-U5-ENT is about the same as with the simulation L5c-U5- z_i 310 (see Figure 2.18c), where in the latter simulation the discussed drawback does not occur.

To summarise, the study on entrainment presented here showed quite useful modifications to obtain improved heat flux and ABL temperature patterns. Both modifications, either an

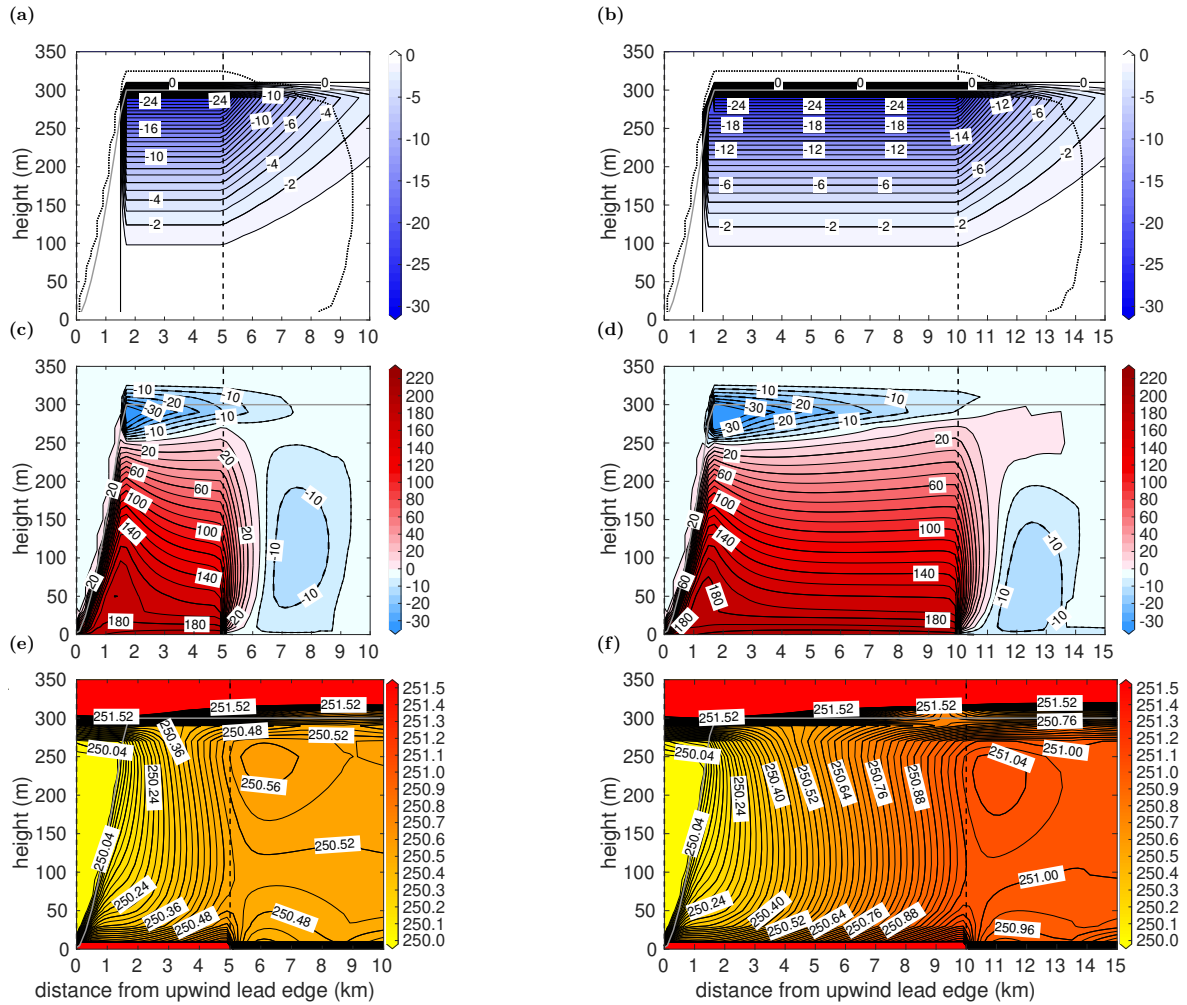


Figure 2.19: Entrainment heat flux $\rho_0 c_p \overline{(w'\theta')}|_{z_i} (z/z_i)^n$ (first row) and total heat flux (second row) in Wm^{-2} , as well as potential temperature in K (third row) obtained by the runs L5c-U5-ENT for case L5c-U5 (a, c, and e) and L10c-U5-ENT for case L10c-U5 (b, d, and f) using the new parametrization proposed for K_h and Γ in section 2.5.1, but with the heat transport equation in the version of Equation 2.27 instead of Equation 2.5. The corresponding METRAS results obtained with Equation 2.5 are shown in Figures 2.7c and 2.7g for the heat flux and in Figures 2.17d and 2.17h for the potential temperature. The corresponding LES results are shown in Figures 2.3c and 2.3g for the heat flux and in Figures 2.17c and 2.17g for the potential temperature. In (a) and (b), the dashed black line indicates where the non-local heat flux exceeds F_{crit} (see section 2.5.1) denoting the extension of the convective plume region. For the cases, see Table 2.1.

increase of the upper limit for the upper IBL height (i.e. a higher value for the ABL height z_i) or considering an explicit term for entrainment following Noh et al. (2003), lead to improved results, where the quality of improvement is almost the same. However, the application of the approach by Noh et al. (2003) is accompanied by additional drawbacks so that further refinements seem necessary, perhaps including modified parametrizations for K_h and Γ . Thus, further potential refinements of that approach will not be pursued any longer in this thesis. Using the new parametrization with a higher value for z_i seems to be the more promising option to improve the representation of entrainment and its effects. Moreover, such an approach could be simply further refined, for example, by prescribing different values for z_i dependent on the distance y to obtain not a generally but rather a locally increased ABL height as compared to

its upstream value. A derivation of such a spatially varying ABL height to be considered in the M20 parametrization is proposed in chapter 3.

2.8.2 Idealised scenarios including humidity

In the following, a first step is shown how humidity might be included in the applied non-eddy-resolving model for modelling the turbulent ABL over leads. As for the previously discussed idealised cases in this chapter, the assumption of refrozen leads without sea smoke, fog, or cloud formation is made also for the corresponding simulations presented in this subsection. In such situations, which are often observed in polar sea ice regions at low air temperatures (e.g., Pinto et al., 2003, T15), humidity acts almost as a passive tracer with only very little impact on other variables so that the heat transport is similar to the transport of potential temperature. This allows a straight forward extension of the new parametrization to include humidity assuming that phase transitions can be neglected. This applies also for the local mixing-length closure. Here, simulation results of the idealised cases L5c-U3, L5c-U5, L5c-U7, and L10c-U5 (see Table 2.1) are discussed and the suffix "-hum" is used to denote model runs using the M20 parametrization including humidity implemented as described in the following (for example: L5c-U5-hum is the simulation of case L5c-U5 including humidity).

For the parametrization of the turbulent humidity flux $\overline{w'q'_v}$, where q_v is the specific humidity, the same formulation as for the temperature flux $\overline{w'\theta'}$ (see Equation 2.5) is used,

$$\overline{w'q'_v} = -K_{q_v} \left(\frac{\partial \bar{q}_v}{\partial z} - \Gamma_{q_v} \right), \quad (2.30)$$

where K_{q_v} is the eddy diffusivity for humidity and Γ_{q_v} the counter-gradient correction term for the humidity flux. As Lüpkes and Schlünzen (1996), also here $K_{q_v} = K_h$ is assumed so that inside of the plume, K_{q_v} is obtained with Equation 2.16 (non-local approach for $\overline{w'q'_v}$) and outside with Equation 2.4 following a local approach analogously to Equation 2.1 for the temperature flux. Γ_{q_v} is defined as

$$\Gamma_{q_v} = \Gamma \frac{q_{v,*}}{\theta_*}, \quad (2.31)$$

where $q_{v,*}$ is the scaling value for humidity. Equation 2.31 also goes back to the parametrization of Lüpkes and Schlünzen (1996), which was developed for horizontally homogeneous conditions. The implementation of humidity in METRAS as described here has only marginal effects on, for example, wind and temperature patterns, mainly due to the presence of $q_{v,*}$ in the equations of surface layer parameters such as the surface buoyancy flux B_l or the Monin-Obukhov length (not shown).

For all METRAS runs with enabled humidity, inflow profiles and surface values of the specific humidity are added compared with the runs using the dry model version. A value of $q_v = 0.38 \text{ g(kg)}^{-1}$ is assumed in the ABL below z_i . Above z_i , a strong increase of q_v is considered. Both features corresponds to conditions often observed in springtime polar boundary layers. Regarding the surface humidity of sea ice, saturation over ice is assumed, which is also a typical phenomenon over polar sea ice (Andreas et al., 2002). By considering leads covered with nilas, this assumption is valid also for the lead surfaces in the corresponding model runs.

The surface humidity for both surfaces, $q_{v,0}$, is then obtained via

$$q_{v,0} = q_{v,sat} = \frac{0.622e_{sat,i}}{p_0}, \quad (2.32)$$

where p_0 is the surface air pressure, with $p_0 = 1000$ hPa for all idealised cases in this thesis, and $q_{v,sat}$ and $e_{sat,i}$ are the saturation specific humidity and the saturation water vapour pressure over an ice surface, respectively, where $e_{sat,i}$ is calculated with an empirical formulation depending on the surface temperature following Pruppacher and Klett (2010). The roughness length for humidity, z_{qv} , is set equal to the roughness length for heat z_t .

In Figure 2.20, vertical-cross sections obtained by the runs L5c-U3-hum, L5c-U5-hum, L5c-U7-hum, and L10c-U5-hum are shown, namely, the latent heat flux F_e (left column, definition see Equation A.7 in Appendix A) and the specific humidity (right column). As expected, the patterns of the latent heat flux are similar to those of the sensible heat flux (see Figure 2.7, left column) due to the assumption $K_{qv} = K_h$ and due to the linkage between Γ_{qv} and Γ (Equation 2.31). Thus, also in the patterns of F_e , a clear maximum is shown over the lead and a clear downwind plume boundary is obvious for this quantity, especially in the result of the runs L5c-U3-hum and L10c-U5-hum. Furthermore, similar effects as simulated for the sensible heat flux with LES and METRAS in the dry model versions (see Figures 2.2 and 2.7) are shown for F_e for increasing wind speed (Figures 2.20a, 2.20c, and 2.20e) and lead width (Figure 2.20g).

Figure 2.20 also shows that the simulated increase in specific humidity over a lead of 5 km width is strongest for weak wind (Figure 2.20b) and smallest for strong wind (Figure 2.20f). For doubled lead width, also the increase in q_v is approximately doubled (compare Figure 2.20h for case L10c-U5 with Figure 2.20d for case L5c-U5). Thus, the connection between humidity increase and upstream wind speed or lead width resembles the METRAS results for the temperature (see Figure 2.17 for the potential temperature).

The microscale model results for both quantities shown in Figure 2.20 still require validation by LES. Nevertheless, a rough comparison should be made here using findings from previous studies. Regarding latent heat flux levels compared with sensible heat flux levels over leads, Andreas et al. (1979) state that the latter exceeds the former by two to four times over leads in wintertime conditions. Based on the data used in Andreas and Cash (1999), for a temperature difference of approximately 23.2 K between sea ice and lead surfaces, this ratio can be specified at approximately 34.5% (see Andreas & Cash, 1999, their Table 2). The values proposed by Marcq and Weiss (2012), who also investigated cases with the same temperature difference between the surfaces of sea ice and lead surfaces as in the idealised cases considered here, indicate that surface latent heat fluxes amount to approximately 36 to 37% of the surface sensible heat fluxes for their considered satellite-observed lead distribution. The ratios F_e/F_h obtained here for the surface fluxes for the wide lead cases with $T_{s,i} = 250$ K are between 35.8% and 36.1%. Thus, they agree almost perfectly with the ratios found by Marcq and Weiss (2012). This also shows that the downwind ABL characteristics might be influenced also by the heat released in case of phase transitions of atmospheric water vapour, but most probably to a lesser extent than by the sensible heat transport over leads. However, this would require a more thorough analysis with further extensions of the M20 parametrization regarding evaporation and condensation, which is beyond the scope of this thesis.

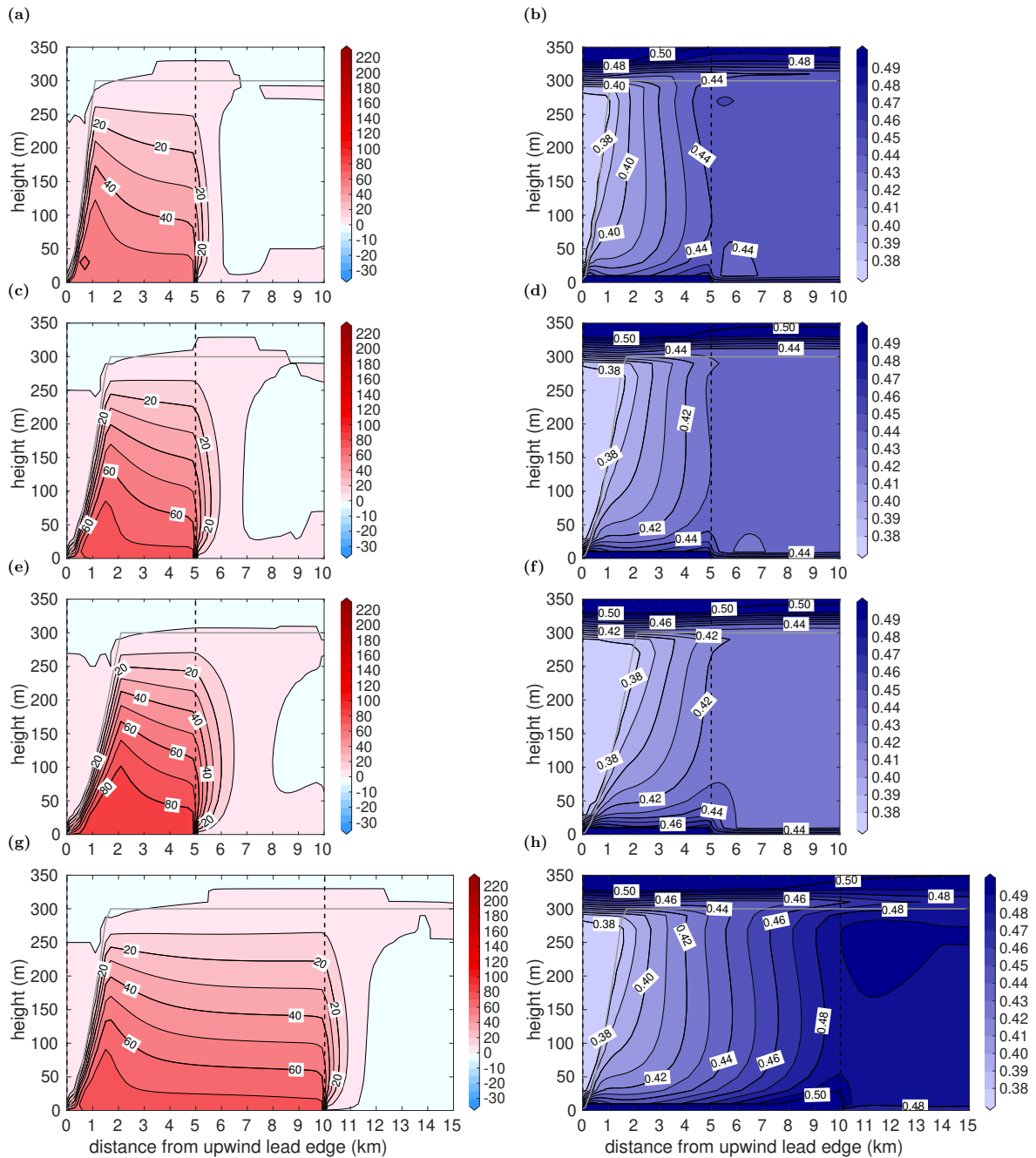


Figure 2.20: Results obtained with METRAS using the new parametrization as in Figure 2.7, but latent heat flux in Wm^{-2} (left column) and specific humidity in g(kg)^{-1} (right column) are shown.

2.8.3 Fetch-dependent surface layer parameters and IBL growth

In the M20 parametrization, there is also room for further improvement regarding a more detailed representation of the heat and momentum flux patterns obtained by LES and concerning the growth and decay of the plume above and downwind of the lead. Thus, although the basic features of the LES results had been well reproduced by METRAS using the new parametrization, some approaches should be discussed in the following in this subsection to obtain an improved agreement with LES also when going into more detail. This should be done here briefly and only qualitatively and also in the context of other studies where parametrizations of the convective

IBL had been proposed.

The first part of this analysis is motivated by horizontal inhomogeneities in the patterns of sensible heat fluxes and the vertical velocity variance $\overline{w'^2}$, which are clearly visible in the LES results but not well captured by the M20 parametrization. As can be noticed from the sensible heat flux patterns obtained by LES for wide leads (Figures 2.2, left column and 2.9a), fetch-dependent maxima are simulated in all cases. Regarding $\overline{w'^2}$, with LES, the maximum values are up to 40 % higher than with METRAS in some cases (see Figure 2.10). One might suppose that these drawbacks arise due to the assumptions of applying lead-averaged values for the surface layer quantities u_* , θ_* , and B_l in the M20 parametrization. Especially for obtaining $\delta(y)$ via integration with Equation 2.10, these assumptions are necessary. However, in the parametrization of $\overline{w'^2}$ (Equation 2.26), u_* occurs also independent on $\delta(y)$. Thus, a brief analysis is provided in the following on the theoretical influence of a fetch-dependent u_* , so $u_*(y)$, on $\overline{w'^2}$ in the M20 parametrization with the help of LES results.

Figure 2.21 shows the deviations of u_* , θ_* , and B_l from their respective lead-averaged values (in %) along non-dimensional fetch y/L for all wide and narrow lead cases considered (see Table 2.1) as obtained by LES. Focusing on the cases with $L \geq 5$ km, deviations of more than 10 % from the mean values are shown for all quantities, mainly at $y/L < 0.1$ and especially for u_* . At the leads' upstream edges ($y/L = 0$), the deviations amount up to almost 25 %. At $0.2 < y/L < 1$, the deviations in u_* are mostly between ± 5 % for those cases. Thus, based on Figure 2.21, the largest improvements in the M20 parametrization can be expected for the region $0 < y/L < 0.2$ for leads with $L \geq 5$ km, which approximately corresponds to the regions where the plumes did not reach the capping inversion (see also Table B1 in Appendix B.2). Furthermore, a change in u_* by ± 10 % has only marginal impact on the values for $\overline{w'^2}$ (less than 1 %, not shown). In conclusion, considering fetch-dependent instead of lead-averaged values of, for example, u_* in the parametrization of $\overline{w'^2}$ alone cannot explain the horizontal inhomogeneities obtained in the corresponding LES results. Perhaps, considering a fetch-dependent B_l in the equation for the convective velocity scale (Equation 2.19) is needed to obtain such an improvement. However, this would complicate the integration of $\delta(y)$ by Equation 2.10 remarkably, and a more detailed analysis on such a derivation is beyond the scope of this thesis.

The second part of this subsection focuses on the function proposed in section 2.5.1 for the upper plume boundary $\delta(y)$. In the corresponding parametrization, $\delta(y)$ represents a fetch-dependent quantity. Basically, the microscale model results obtained with Equation 2.20 for $\delta(y)$ show that upper IBL developments obtained by LES are well reproduced for almost all investigated idealised cases. In addition, as already stated in section 2.7, a further development of the used $\delta(y)$ -parametrization should account for non-neutral stability, especially for stable upwind conditions, which often seem to occur in the polar ocean regions upwind of leads in springtime conditions (e.g., T15). Moreover, an improved development of $\delta(y)$ in the inversion layer and the associated effects resulting from the interaction of the convective plume are yet to be included in the parametrization. In the following, a brief discussion is made on other parametrizations that had already been proposed for the upper IBL height in strongly inhomogeneous conditions, such as over leads and polynyas, which might serve as a basis for combining Equation 2.20 of the M20 parametrization with their formulations for further improvements. For

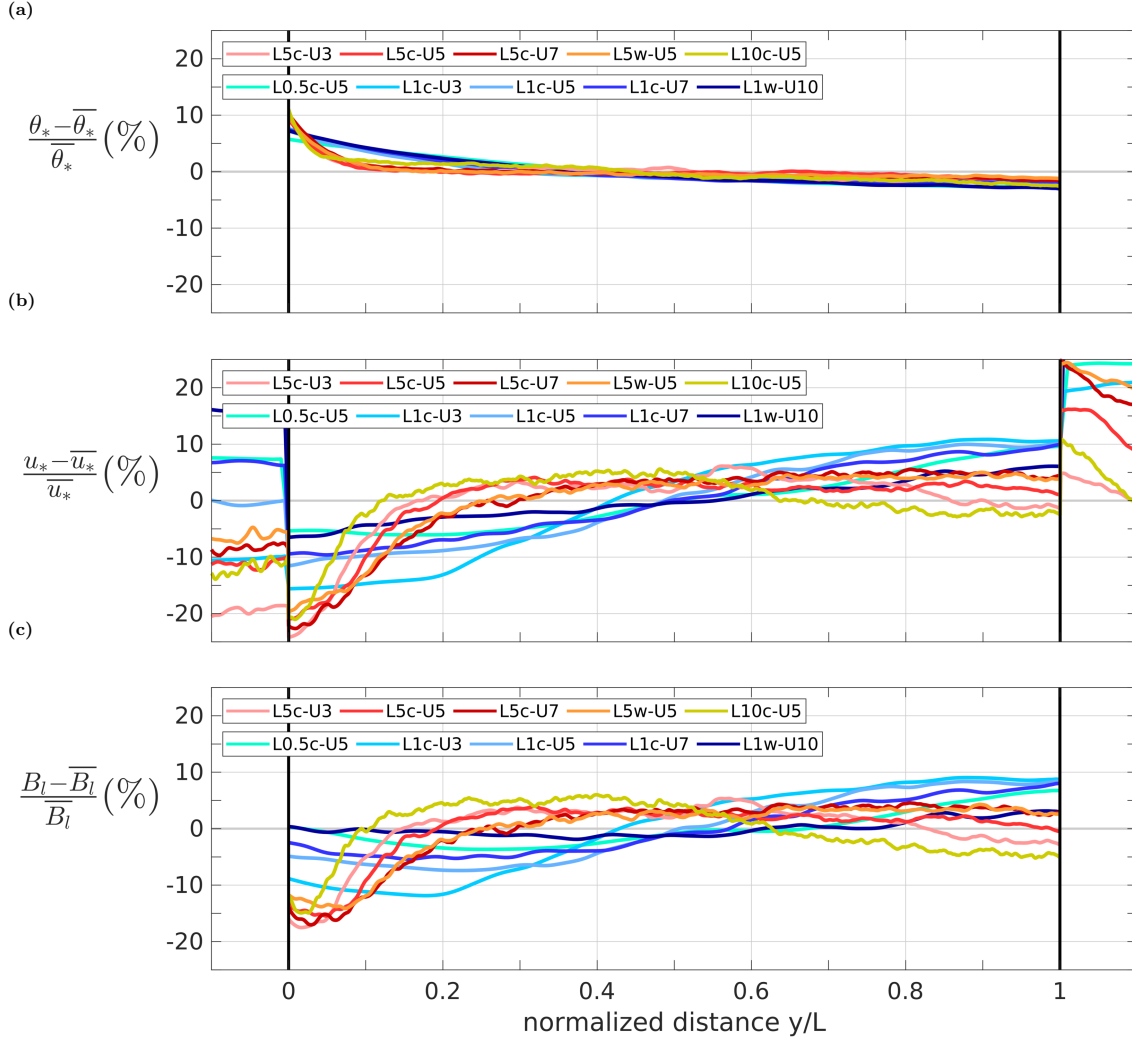


Figure 2.21: Deviations of three surface layer parameters (in %) along non-dimensional fetch (y/L), where y is the distance from the upwind lead edge and L is the lead width, obtained by LES for all idealised cases (see Table 2.1). Panel (a) shows the scaling value for temperature θ_* , (b) the friction velocity u_* , and (c) the surface buoyancy flux B_l .

a more general overview on the convective IBL over inhomogeneous surfaces, see, for example, Garratt (1990) and Savelyev and Taylor (2005).

First, the focus is on formulations for the plume penetration height z_{hp} proposed by other authors, which marks the theoretical height up to that a convective plume can penetrate into a certain layer. An equation for z_{hp} for plumes over leads was first proposed by Glendening and Burk (1992) based on their time-averaged LES results for the flow over a lead of width $L = 200$ m with

$$z_{hp} = \left(\frac{\overline{w'\theta'}|_s L^2}{U_\perp \frac{\partial \theta}{\partial z}} \right)^{1/3}, \quad (2.33)$$

where U_\perp is the lead-perpendicular component of the horizontal wind vector. This equation shows that the plume penetrates the deeper into a layer the wider the lead is, namely, with an $L^{2/3}$ -dependence. z_{hp} increases with increasing lead-averaged surface heat flux and decreases with increasing lead-perpendicular wind component or increasing stability of the upwind layer.

The formulation by Glendening and Burk (1992) was modified by Zulauf and Krueger (2003b) based on their modelling results, and they obtained

$$z_{hp} = C_2 \left(\frac{g\bar{F}_{h,s}}{\theta_0 \rho_0 c_p} \right)^{1/3} \cdot N^{-1} \left(\frac{N}{U_{\perp}} \right)^{1/3} L^{1/2}, \quad (2.34)$$

where $C_2 \approx 1$ is a constant, θ_0 and ρ_0 are a reference potential temperature and a reference air density, and N is the Brunt-Väisälä-frequency. Thus, Zulauf and Krueger (2003b) proposed an $L^{1/2}$ -dependence for z_{hp} based on their results for leads with $L > 200$ m. Note that both Equations 2.33 and 2.34 show singularities for neutral inflow conditions.

In principle, the LES results shown in this chapter also show different maximum penetration heights of the convective plumes depending on the parameters of both above-mentioned equations. For example, for different U_{\perp} and L , this is obvious from Figure 2.17 (left column) following the vertical positions of the potential temperature contour lines near z_i . This indicates an interaction between the plume and the capping inversion, which also causes an increasing ABL thickness with fetch (see section 2.3). This increase is most pronounced in the LES of the cases L5c-U3 and L10c-U5 and least for case L5c-U7, which qualitatively agrees with both formulations for z_{hp} shown here. It is also obvious that the increase in ABL thickness and, thus, z_{hp} is underestimated by METRAS using the M20 parametrization (see Figure 2.17, right column). Unfortunately, a quantitative analysis of results from both models with the theoretical values that would be obtained via Equations 2.33 and 2.34 is challenging since for all the idealised cases considered in this chapter, $\partial\theta/\partial z = 0$ below z_i . Alternatively, the theoretical penetration height of the plume only for its development in the inversion layer could be calculated, but then it would be still challenging to make proper estimates for the parameters θ_0 or $\overline{w'\theta'}$, and for the height level to start from.

Second, an alternative formulation for the upper IBL height $\delta(y)$ as proposed by Renfrew and King (2000) for a cold-air flow over a warm polynya should be analysed here. They obtained

$$\delta^2(y) = \delta_0^2 + \frac{2(1+2\beta)}{U \frac{\partial\theta}{\partial z} c_p} \int \frac{F_{h,s}(y)}{\rho_s(y)} dy, \quad (2.35)$$

where δ_0 is a starting height level, β is an entrainment factor (with $\beta = 0.2$), and $F_{h,s}$ and ρ_s are the fetch-dependent surface sensible heat flux and surface air density, respectively. Assuming constant values for the latter two variables, Equation 2.35 results in the formulation proposed by Weisman (1976), extended by the entrainment factor $\sqrt{2(1+2\beta)}$. Note, T15 found this extension of the approach by Weisman (1976) to be useful since by neglecting the entrainment factor, the plume growth over the lead is underestimated compared with the IBL height derived from the measurements used by T15. Similar to the formulations for z_{hp} , also the formulation by Renfrew and King (2000) for $\delta(y)$ is, inter alia, inversely proportional to $\partial\theta/\partial z$, including the above-mentioned singularity at $\partial\theta/\partial z = 0$. This would result in the same drawback as discussed for the formulations for z_{hp} when applied to the idealised cases considered in this thesis. Furthermore, the approach proposed in Equation 2.35 is not applicable for the plume development downwind of the lead since the downwind decay of the convection is not considered. Nevertheless, it might serve as a useful basis for a potential extension of the new parametrization

derived in section 2.5.1 towards non-neutral inflow conditions.

2.8.4 Conclusions on further refinements of the parametrization

The analysis of this section shows three major findings. First, the small limitations of the new parametrization regarding a detailed representation of entrainment and downwind ABL warming might be overcome with only little adjustments in the treatment of the ABL height z_i . Slightly improved results were obtained by prescribing a higher value for z_i as proposed originally (310 m instead of 300 m), which allowed a stronger interaction of the convective plume with the inversion layer and which improved the representation of the associated effects as compared with LES. Not only a similar level of improvement but also further drawbacks arise when the parametrization is formulated based on Equation 2.27, which is similar to Equation 2.5 but extended by an explicit term for vertical entrainment following Noh et al. (2003). Hence, especially the consideration of spatial variations in z_i might represent a promising way to further improve the new parametrization and the corresponding non-eddy-resolving, microscale model results with only little effort.

Second, the first steps were shown here towards an explicit consideration of atmospheric humidity in future in the microscale simulations using the new parametrization. In the corresponding approach, humidity was considered neglecting phase transitions and the resulting patterns shown for the latent heat flux and specific humidity still require validation by LES. Nevertheless, a rough comparison of the obtained ratio between surface fluxes of sensible and latent heat showed a good agreement with ratios derived in other studies.

Third, a qualitative discussion was made regarding fetch-dependent surface layer parameters, and concerning the growth of the upper plume boundary or upper IBL height as proposed in section 2.5.1 as related to other formulations already existing in literature. It was shown that a consideration of fetch-dependent surface layer parameters in the new parametrization alone could not explain the discrepancies to LES regarding the detailed inhomogeneities in the turbulent flux patterns. In addition, regarding the comparison of different approaches for the plume growth over leads, only a qualitative evaluation of the other already existing formulations was possible since those had been derived for non-neutral upwind stratification. Positively spoken, especially the approach by Renfrew and King (2000) might represent a promising starting point to propose an extended version of the $\delta(y)$ -formulation of the M20 parametrization in future, in which it would be accounted also for non-neutral inflow conditions.

3 Modelling and parametrizing convection over leads compared with airborne measurements¹

Abstract: A non-eddy-resolving, microscale model is applied to simulate convection over three different leads (elongated channels in sea ice), which have been observed by aircraft over the Arctic Marginal Ice Zone in 2013. The study aims to evaluate the quality of a local and a non-local turbulence parametrization. The latter represents a lead-width-dependent approach for the turbulent fluxes designed for idealised conditions of a lead-perpendicular inflow in a near-neutral ABL capped by a strong inversion at around 250 m to 350 m height. The observed cases considered here are also characterised by an almost lead-perpendicular flow, but in comparison to the idealised conditions, our analysis covers effects due to stable inflow conditions and a much shallower ABL. The model simulations are initialised with observed surface parameters and upwind profiles, and the results are compared with measurements obtained above and downwind of the leads. The basic observed features related to the lead-generated convection can be reproduced with both closures, but the observed plume inclination and vertical entrainment near the inversion layer due to the penetrating plume are underestimated. The advantage of the non-local closure becomes clearly obvious by the more realistic representation of regions with observed counter-gradient transport. It is shown by comparison with the observations that results obtained with the non-local closure can be further improved by including the determination of a fetch-dependent inversion height and by specifying a parameter determining the plume inclination as a function of the upwind ABL stratification. Both effects improve the representation of fluxes, boundary layer warming, and vertical entrainment. The model is also able to reproduce the observed vanishing of a weak low-level jet over the lead, but its downwind regeneration and related momentum transport are not always well captured, independent on the used closure.

¹The sections 3.1 to 3.7 consist of the manuscript with the title *Modelling and parametrization of the convective flow over leads in sea ice and comparison with airborne observations* as submitted to *Quarterly Journal of the Royal Meteorological Society* on September 9, 2020, which has been peer-reviewed, revised, and finally accepted for publication on December 1, 2020 (see Michaelis et al. (accept.) for the accepted/published version). A difference to the manuscript in its originally submitted form is made in this thesis in section 3.3 (corresponds with section 3 in Michaelis et al. (accept.)), where here the content was shortened due to an overlap with contents from the sections 2.2.2 and 2.5.1 in this thesis. Section 3.8 is an additional contribution for this thesis based on my contribution as a co-author in the publication Lampert et al. (2020) published in *Atmosphere* as an open-access article.

3.1 Introduction

Elongated open-water channels in sea ice, so-called leads, may play a key role for surface-atmosphere interactions in the polar regions (e.g., Ebert & Curry, 1993; Vihma et al., 2014; Lüpkes, Vihma, et al., 2008; Chechin et al., 2019). Over these areas, the atmosphere is in direct contact with the ocean, which leads to an enhanced heat transport especially during wintertime when temperature differences between atmosphere and open water are large. This, in turn, generates several effects on characteristics of the polar atmosphere on different (spatial) scales.

As described, for example, in the above-mentioned studies and most recently by Michaelis et al. (2020) (henceforth abbreviated by M20, see chapter 2 in this thesis), leads are formed mainly due to divergent sea ice drift driven by ocean currents and wind (see also Smith et al., 1990). Their length ranges between hundreds of meters and hundreds of kilometres and their width between a few meters to a few kilometres (e.g., Andreas et al., 1979; Smith et al., 1990; Lindsay & Rothrock, 1995; Marcq & Weiss, 2012, T15). Leads occur predominantly in the MIZ, but they are also found in the central polar ocean regions (Smith et al., 1990). Due to the above-mentioned large temperature difference in wintertime, the heat transport through leads exceeds the molecular heat transport through the surrounding thick ice by two orders of magnitude (Badgley, 1966; Maykut, 1978) so that leads can dominate the heat budgets even if the lead coverage is only a few percent (Maykut, 1978; Smith et al., 1990). Thus, strong turbulent convection (convective plumes) and an IBL are generated, which strongly affect the structure of the polar ABL. The intensity of those effects depends on the lead geometry and the meteorological forcing (temperature, wind speed and direction, and stratification). Furthermore, effects generated over multiple leads or polynyas can have an impact also on the near-surface energy balance and on atmospheric processes at spatial scales in the order of 10^3 km (e.g., Overland et al., 2000; Lüpkes, Vihma, et al., 2008; Ebner et al., 2011; Batrak & Müller, 2018; Chechin et al., 2019), which shows the relevance of leads for climate and numerical weather prediction, especially in high latitudes.

Investigating the effects of leads on the polar ABL has been subject of many studies using observations, numerical models, or both. During the campaigns AIDJEX (Paulson & Smith, 1974; Andreas et al., 1979), LEADDEX (Ruffieux et al., 1995; Persson et al., 1997), and SHEBA (Overland et al., 2000; Pinto et al., 2003), detailed analyses of the near-surface atmospheric processes near leads were conducted using mainly in situ measurements. Based on those measurements, turbulent surface fluxes of heat, moisture, and momentum had been derived and parametrizations for the corresponding transfer coefficients were proposed (e.g., Andreas & Murphy, 1986; Alam & Curry, 1997; Andreas & Cash, 1999). All those investigations revealed a strong influence of lead-generated convection on the near-surface ABL characteristics.

During the Winter Arctic Polynya Study (WARPS, Lüpkes et al., 2004, 2012) additional in situ measurements were performed also above leads, supplemented by helicopter-borne turbulence measurements with the HELIPOD system (Bange et al., 2002). Thus, one of the main shortcomings during previous campaigns with measurements only over sea ice had been overcome. In contrast to the LEADDEX and SHEBA campaigns, the focus was mainly on leads of width $L = \mathcal{O}(10^3)$ m rather than $L = \mathcal{O}(10^1 - 10^2)$ m. In March 2013, detailed observations of the whole turbulent ABL over leads of similar width as during WARPS were performed during

the aircraft-based study STABLE (see T15). Measurements from STABLE revealed that in case of convection penetrating the capping inversion not only the surface heat fluxes but also fluxes entrained through the inversion significantly contribute to the warming of the ABL (T15).

Lead-generated convection was also subject of several modelling studies using either LES (e.g., Glendening & Burk, 1992; Glendening, 1994; Weinbrecht & Raasch, 2001; Esau, 2007), high-resolved non-hydrostatic models (e.g., Alam & Curry, 1995; Dare & Atkinson, 2000; Zulauf & Krueger, 2003a, 2003b; Mauritsen et al., 2005; Wenta & Herman, 2018; Li et al., 2020) or both (e.g., L08 and M20). Most of these studies focused on idealised case-studies to analyse the impact of lead geometry and meteorological forcing on the convective ABL. LES models provide detailed information on the turbulence structure since the energy-contributing turbulent scales are directly resolved. Typically, grid sizes in the order of a few meters or less are used in all directions, where the resolution increased consecutively in the past years due to increased computer capacity. The computational costs of a non-eddy-resolving model amount to only 0.1-1 % of an LES model due to the much coarser resolution ($\mathcal{O}(10^2 - 10^3)$ m horizontally and $\mathcal{O}(10^1)$ m vertically), but if the latter is appropriate, the main characteristics of the developing plume can still be provided. However, parametrizations of the dominating subgrid-scale processes are required so that the simulation results strongly depend on the applied closure.

Among others, the above-mentioned modelling studies all showed the formation of convective plumes over single leads or polynyas with distinct upper and lower boundaries and a significant influence on temperature and wind patterns of the ABL. Regarding the parametrizations applied in the non-LES applications, predominantly local turbulence closure following 1.5-, 2-, or 2.5-order TKE schemes were applied. However, for example, Deardorff (1972); Holtslag and Moeng (1991) found fluxes directed against the prevailing temperature gradient, especially in the upper half of a homogeneously surface-heated ABL. As stressed by L08 and M20 based on their LES results, such non-local fluxes dominate the heat flux pattern also in case of horizontally inhomogeneous convection over leads. Furthermore, the measurements from STABLE indicated that those fluxes exist. To account for non-local fluxes, L08 proposed a corresponding parametrization based on LES using K -theory with a counter-gradient correction for leads of 1 km width. They showed that for such cases non-eddy-resolving model results obtained with their non-local parametrization agree well with their LES results. The basic idea of L08 was also used by M20, who modified and extended the non-local parametrization but accounted additionally for variable lead width. As compared with the local and the previous non-local closure, a considerably improved agreement with LES was obtained especially concerning heat flux patterns and downstream stratification for wide leads with $L \geq 5$ km.

M20 considered idealised cases with neutral stratification and only with a fixed ABL height at $z_i = 300$ m. Neither non-neutral upstream stratification, nor other values for z_i , nor observed leads were investigated. Furthermore, as T15 showed, values for z_i upstream and downstream of the lead might differ due to interactions caused by penetrating convection. This phenomenon was also not captured by the M20 parametrization since z_i was kept constant.

Our goal is, first of all, to discuss the quality of microscale model results using different turbulence closures with a focus on the M20 parametrization (see section 2.5.1 here) when applied to the cases observed during STABLE. The first leading questions is if the non-local closure has advantages as compared to a simpler local closure. We investigate three out of

the four observed cases, all of them with a shallower ABL and two of them with a more stable upwind stratification than the idealised cases considered by M20. The fourth case from STABLE is not modelled due to a rather complex distribution of sea ice cover and surface temperatures.

Another goal is to investigate the need for possible modifications of the M20 parametrization based on the comparison with the measurements. This includes the consideration of ABL warming caused by convection penetrating the capping inversion and of the impact of non-neutral stratification on the plume inclination. A consideration of the latter effect is, furthermore, motivated by analytical models proposed for the IBL developing over heated surfaces, where a functional relation to the upwind temperature gradient was proposed (e.g., Weisman, 1976; Renfrew & King, 2000). All this can be regarded as another step towards a turbulence parametrization for convective processes in strongly inhomogeneous conditions used in non-eddy-resolving but small-scale atmospheric models.

In section 3.2, we describe the STABLE campaign followed by the description and setup of the applied microscale model in section 3.3. Model results obtained with different turbulence closures are shown and compared with the observations in section 3.4. Based on those model results, we introduce two further modifications for the non-local parametrization in section 3.5, where also the corresponding results are shown. A discussion is given section 3.6, and a conclusion is drawn in section 3.7.

3.2 The campaign STABLE

In the following, we briefly summarise the campaign STABLE with focus on the three lead cases considered here and on information relevant for our simulations. For more details on the observations, including flight patterns and measurement techniques, and a detailed discussion on observed ABL effects by the leads, see T15.

STABLE was an aircraft campaign with focus on measurements over leads conducted in the MIZ North of Svalbard in March 2013. Measurements were conducted over four leads (on March 10, 11, 25, and 26) using the Polar 5 research aircraft from the Alfred-Wegener-Institute (AWI) in Germany. Temperature, wind components, and pressure were measured with a frequency of 100 Hz, which is equivalent to measurements every 0.4 m to 0.75 m during horizontal flight legs considering the aircraft's ground speed between 40 ms^{-1} and 75 ms^{-1} . Humidity was measured with a frequency of 1 Hz only so that turbulent fluctuations were not resolved. Upwind and downwind of the lead, ascending and descending profiles were performed, for example, to determine stratification and ABL height. Horizontal, lead-perpendicular flight legs were conducted predominantly at around 40 m height along the main wind direction, mainly to determine humidity, wind, and both surface and air temperature. On March 11 and 25, flight sections following a vertical saw-tooth pattern in lead-perpendicular direction were additionally performed to derive the vertical structure of the ABL. In lead-parallel direction, several horizontal stacks were flown above and downwind of the leads. Turbulent fluxes of sensible heat and momentum were then calculated mainly from those flight legs using the eddy covariance method.

In all cases, the near-surface wind was directed approximately lead-perpendicularly with upstream ABL-averaged speed U of 5.5 ms^{-1} to 10.5 ms^{-1} (see T15, their Table 1) leading

to inclined plumes over the leads, which extended into the downstream region over closed sea ice, and which also penetrated into the capping inversions above the shallow boundary layers with $90 \text{ m} \leq z_i \leq 190 \text{ m}$. The surface temperature of thick sea ice around the leads was near -25°C and lead-averaged surface temperatures, $T_{s,l}$, ranged from -17°C to -5°C , partially with large spatial variations due to different surface cover (Figure 3.1). The widths of the leads, L , ranged from 1.6 km to 8.3 km. Only flight sections over leads with nearly linear edges were taken into account and those ranged from 5.0 km to 20.5 km length. However, the fetch lengths (the distance between the upwind lead edge and a single lead-parallel flight leg) varied also along those sections due to the remaining curvature, which affected the derived turbulent fluxes. Hence, T15 applied a high-pass filter with cut-off frequency at 0.1 Hz for all their flux calculations to account for these effects.

The upwind ABLs were characterised by near-neutral or stable stratification below the strong capping inversions. For all cases considered, the measurements of T15 revealed several effects of the plumes on the ABL structure and on vertical flux profiles above and downwind of the leads.

Note, all leads were covered with nilas except of some small patches of open water. This had two consequences. First, the average lead surface temperatures were far below the temperature of open water (see Figure 3.1); hence, sensible heat fluxes were smaller than over an ice-free lead. Second, since the nilas cover strongly reduces evaporation as compared with open water (see Li et al., 2020), cloud formation over the leads was prevented.

3.2.1 March 10, 2013

The lead observed on March 10 was 2.3 km wide with a neutrally stratified ABL up to $z_i = 95 \text{ m}$ observed upwind of the lead (at $y = -7 \text{ km}$, where we use y in the following to denote the distance to the respective upwind lead edge, at $y = 0 \text{ km}$, for all cases). Note that T15 found the observations derived from this flight leg to be not completely representative for the conditions close to the upwind lead edge due to another narrow lead further upwind. Hence, for example, air temperatures above the lead were lower than at $y = -7 \text{ km}$ over thick sea ice (see T15, their Figure 5a).

The lead was mostly covered by thin ice (grey nilas), whose average surface temperature amounted to $\bar{T}_{s,l} = -10.7^\circ\text{C}$, but some patches of just refreezing open water with $T_{s,l} \approx -3^\circ\text{C}$ occurred, too. This caused a large standard deviation of $\sigma_{T_{s,l}} = 3.9^\circ\text{C}$ in $T_{s,l}$ (Figure 3.1a). Above the open-water areas, some sea smoke was present. The average temperature difference between the surfaces of thick sea ice and the lead amounted to approximately 14.8 K. An average

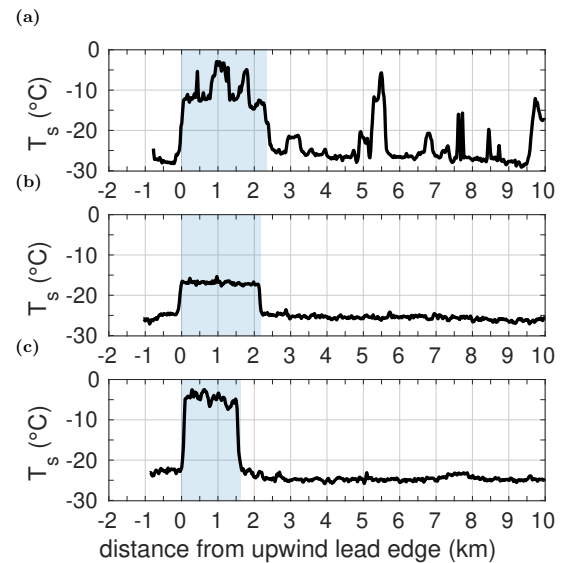


Figure 3.1: Observed surface temperature T_s along distance from the upwind lead edge for three cases from STABLE, where the blue-shaded rectangles denote the position of the leads. Panel (a) refers to the lead of 2.3 km width observed on March 10, 2013, (b) to the lead of 2.1 km width observed on March 25, 2013, and (c) to the lead of 1.6 km width observed on March 26, 2013.

wind speed of $U = 5.5 \text{ ms}^{-1}$ was derived based on the profile at $y = -7 \text{ km}$. T15 found that the plume had penetrated also the capping inversion so that the ABL thickness had slightly increased from 95 m at $y = 0 \text{ km}$ to 101 m near $y = L$, where small entrainment fluxes had been observed. Due to lead-generated convection, mixed layer air temperatures increased by approximately 0.8 K, where the maximum temperature increase was reached near $y = L$.

3.2.2 March 25, 2013

On March 25, the temperature difference between the surfaces of sea ice in the environment of the lead and of nilas in the lead ($L = 2.1 \text{ km}$) was smallest among all cases with only 8 K, where $\bar{T}_{s,l} = -17.0^\circ\text{C}$ and $\sigma_{T_{s,l}} = 0.4^\circ\text{C}$ (Figure 3.1b). The lead was almost completely covered by white nilas with only small areas of grey nilas, which explains the low values of both $\bar{T}_{s,l}$ and $\sigma_{T_{s,l}}$. The upwind ABL with $U = 8.0 \text{ ms}^{-1}$ was stably stratified with a vertical potential temperature gradient $\partial\bar{\theta}/\partial z = 0.014 \text{ Km}^{-1}$ below the inversion at $z_i = 90 \text{ m}$. Especially for this case, T15 found large vertical entrainment fluxes due to the inversion-penetrating plume. Thus, the stable stratification had weakened above and downwind of the lead. Furthermore, z_i increased to approximately $z_i = 115 \text{ m}$ downwind of the lead. The mixed layer temperature increased by approximately 0.6 K until $y = L$ and up to 1.2 K further downwind at $y = 8 \text{ km}$. This indicates the large contribution due to the entrainment (T15). Furthermore, based on the saw-tooth pattern, T15 found a low-level jet (LLJ) upwind of the lead with its maximum near z_i exceeding U by approximately 2 ms^{-1} , which had then been destroyed due to the plume, and which had regenerated near $y = 15 \text{ km}$ downwind of the lead.

3.2.3 March 26, 2013

The lead observed on March 26 was the narrowest one ($L = 1.6 \text{ km}$) and it had the highest surface temperature ($\bar{T}_{s,l} = -5.8^\circ\text{C}$, see Figure 3.1c). The surface was mainly covered by nilas, but locally it also consisted of open-water areas and frazil ice. $\sigma_{T_{s,l}} = 3.8^\circ\text{C}$ was almost as large as on March 10 and also on that day weak sea smoke was present above the open-water areas. However, there were no such clear peaks in $T_{s,l}$ as on March 10. The upwind ABL stratification was $\partial\bar{\theta}/\partial z = 0.003 \text{ Km}^{-1}$ below $z_i = 190 \text{ m}$. The highest altitude for the lead-parallel horizontal flight legs was at 140 m so that no measurements were obtained near z_i , which did not allow us to identify an effect of a growing ABL height downwind of the lead. However, the potential impact of convection on the capping inversion was observed indirectly by measured intermittency of the turbulence in the inversion over the plume region, which had been present also in the other cases.

3.3 Model description²

For our simulations, we use the atmospheric model METRAS (Schlünzen, Bungert, et al., 2012; Schlünzen, Flagg, et al., 2012) in the same microscale, 2-D version as described in chapter 2.

²In this section, the original content of Michaelis et al. (accept.) is shortened to avoid an overlap with the sections 2.2.2.2 and 2.5.1 in chapter 2 of this thesis. In Michaelis et al. (accept.), a more detailed explanation is given on the applied model and the used turbulence parametrizations, but, basically, the same model version and parametrizations are applied as shown in chapter 2. Remaining differences are addressed here in the text.

Humidity is considered but without phase transitions, which is justified due to the absence of clouds in the cases considered (T15).

METRAS is applied with two different turbulence closures in the same version as introduced in chapter 2. Namely, the local mixing-length closure following Herbert and Kramm (1985) (see section 2.2.2.2.1) and the M20 parametrization (see sections 2.5.1 and 2.2.2.2.2) are used including all assumptions and values set for the unknown parameters mentioned in chapter 2. For the local closure, this means that we also use $l_{max} = 0.15z_i$, where z_i is the height of the capping inversion observed upwind of the leads. For the M20 closure, unless stated otherwise, the values proposed in section 2.5.1 ($c = 1$, $a_m a_e = 1 \pm 0.6$, $a = 1.2$, $b = 2$, $d_w = 1.7$, and $d_\theta = 0.51$) are also used in the simulations shown in this chapter. Nevertheless, one of our goals is also to validate these values with the observations from STABLE. For reasons described later, for two cases, we considered in addition results for different values of a (see section 3.5).

3.3.1 Model setup

An overview of all model runs is shown in Table 3.1, where we use abbreviations to denote the case and the applied parametrization (e.g., "1003-MIX" denotes the model run for March 10, where the local closure is used, and "2503-NL1" denotes one of the model run for March 25, where the non-local closure is used). We basically distinguish the surfaces of thick sea ice and leads only by differences in the surface roughness lengths z_0 and surface temperatures ($T_{s,i}$ for sea ice and $T_{s,l}$ for the leads). As in L08 and M20, $z_0 = 10^{-3}$ m is prescribed for thick sea ice and $z_0 = 10^{-4}$ m for lead surfaces. The ratio between the surface roughness lengths for momentum and temperature (z_0/z_t) is assumed as 10. For reasons described later, we performed one model run with $z_{0,l}/z_{t,l} = 100$ (see Table 3.1), where the index l refers to the lead surface. Regarding the surface humidity of both sea ice and leads with nilas, we assume saturation over ice. The temperatures of both surfaces (values see Table 3.2) derived from the observations (see Figure 3.1), are kept constant in time during the whole model integration. For March 25 and 26, $T_{s,l}$ is set constant all over the lead since the observed variability was small (see section 3.2). However, for March 10, we consider the observed fetch-dependence of $T_{s,l}$. Nevertheless, also for model runs of that case obtained with the non-local closure, we apply lead-averaged values for the parameters $\theta_{*,l}$ and B_l so that the integration of Equation 2.10 (see chapter 2) is not violated by the fetch-dependence of $T_{s,l}$.

Inflow profiles are generated with the 1-D model version of METRAS based on measurements at the upwind side of the leads. The inflow profiles of both wind speed and direction are obtained with height-independent values of the observed geostrophic wind components u_g and v_g . Both observed and modelled inflow profiles are shown in Figure 3.2.

As mentioned in section 3.2.1, on March 10, higher temperatures were measured during the profile observed at a distance of about $y = -7$ km to the upwind lead edge than above the lead (see also Figure 3.2a). It seems that also the upwind ABL-averaged wind speed is slightly overestimated when compared to the measurements above the lead (Figure 3.2d). Hence, to ensure comparability, for model runs of this case we assume that the air temperature matches the sea ice surface temperature in the lowest levels. This explains the deviation between the observed and modelled temperature profiles, which is larger than in the other two cases. Moreover, we

Table 3.1: Overview of the settings for the numerical simulations^a.

| Model run | Closure scheme | Method to calculate $z_i(y)$ | Value for a | Further specifications |
|-----------|----------------|---|---------------|-------------------------|
| 1003-MIX | local | fixed value, $z_i(y) = 95$ m | - | - |
| 1003-NL1 | non-local | fixed value, $z_i(y) = 95$ m | 1.2 | - |
| 1003-NL2 | non-local | contour; threshold: $\theta _c = 246.8$ K | 1.2 | - |
| 1003-NL3 | non-local | contour; threshold: $\theta _c = 246.8$ K | 1.2 | $z_{t,l} = 0.01z_{0,l}$ |
| 2503-MIX | local | fixed, $z_i(y) = 90$ m | - | - |
| 2503-NL1 | non-local | fixed, $z_i(y) = 90$ m | 1.2 | - |
| 2503-NL2 | non-local | fixed, $z_i(y) = 90$ m | 0.75 | - |
| 2503-NL3 | non-local | contour; threshold: $\theta _c = 247.4$ K | 0.75 | - |
| 2603-MIX | local | fixed, $z_i(y) = 190$ m | - | - |
| 2603-NL1 | non-local | fixed, $z_i(y) = 190$ m | 1.2 | - |
| 2603-NL2 | non-local | contour; threshold: $\theta _c = 247.2$ K | 0.9 | - |

^a The closure schemes refer to the local mixing-length closure ("MIX", see section 2.2.2.2.1 in chapter 2) and the non-local closure ("NL") of M20 (see section 2.5.1 in chapter 2). $z_i(y)$ is the ABL height in the model, for which the upwind observed value is prescribed in some runs, while in some other runs a y -dependent ABL height is used, with y as the distance from the lead edge (method explained in section 3.5.1). Values shown in the fourth column refer to the parameter a in the non-local closure of M20 (see section 2.5.1 in chapter 2 and section 3.5.2 for further details). $z_{t,l}$ and $z_{0,l}$ are heat and momentum roughness lengths for lead surfaces.

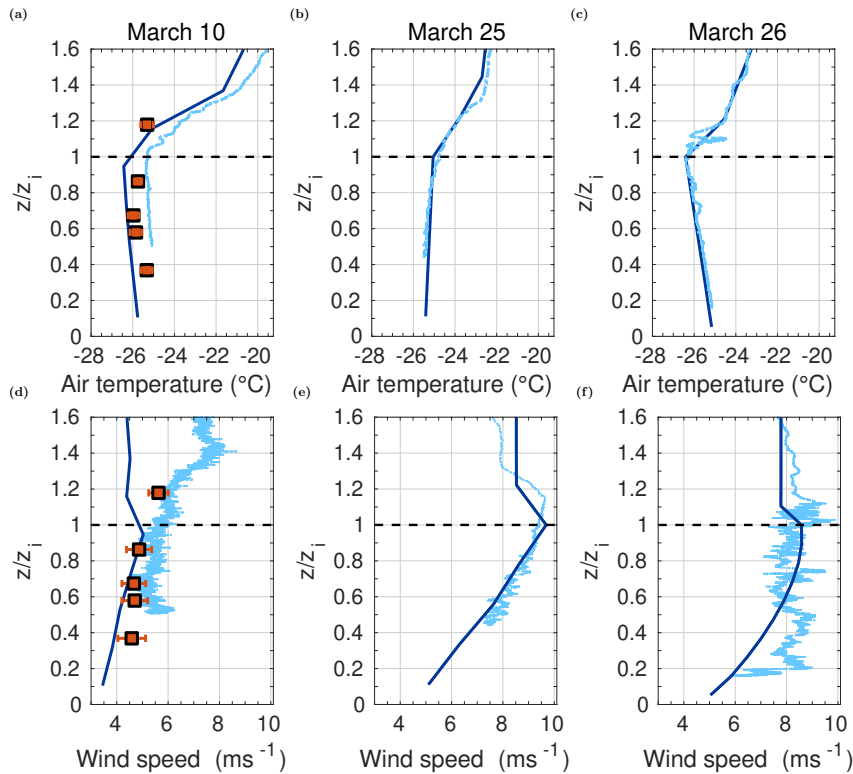


Figure 3.2: Profiles observed near the upstream edges of the three leads (light blue lines) and the corresponding simulated inflow profiles (dark blue lines) of atmospheric temperature and wind speed plotted as functions of the non-dimensional height z/z_i , where z_i is the upwind observed ABL height. Panels (a, d) refer to March 10, 2013, where $z_i = 95$ m and the upwind measured profiles were obtained at $y = -7$ km distance. Profiles measured above the lead at $y = 1.3$ km are also shown (red points). (b, e) refer to March 25, 2013 with $z_i = 90$ m. Measured profiles were obtained at $y = -2$ km. (c, f) refer to March 26, 2013 with $z_i = 190$ m. Measured profiles were obtained at $y = -1.5$ km.

could not obtain the observed increase of wind speed above z_i and prescribed the geostrophic wind to a smaller value to ensure matching with the ABL wind above the lead (red points in Figure 3.2d).

For the other two cases, observed and modelled inflow profiles differ only marginally (Figures

3.2b, 3.2c, 3.2e, and 3.2f). For March 25, only the observed and modelled vertical locations of the wind speed maximum differ slightly (Figure 3.2e). For March 26, the observed inflow wind speed is underestimated between $0.2z_i$ and $0.5z_i$ (Figure 3.2f), but agrees well with the observation outside of this range.

Further initial values for the model runs are shown in Table 3.2. After the initialisation, the model equations are integrated until quasi-stationary conditions are reached (approximately after 2 hrs integration time). Simulation results are then compared to the ABL observations obtained by aircraft above and downstream of the respective leads.

Table 3.2: Initial conditions for the model runs of the discussed case-studies from STABLE^a.

| Parameters | Case where model runs belong to | | |
|---|--|-----------------------------|----------------------------|
| | March 10, 2013 | March 25, 2013 | March 26, 2013 |
| L (km) | 2.3 | 2.1 | 1.6 |
| $T_{s,i}$ (°C) | -25.6 | -25.5 | -25.1 |
| $T_{s,i}(y)$ (°C) | -12.0 for $0.0 \leq y \leq 0.8$ km -3.0 for $0.8 < y \leq 1.2$ km -12.0 for $1.2 < y \leq 1.5$ km -4.0 for $1.5 < y \leq 1.8$ km -13.0 for $1.8 < y \leq 2.3$ km | -17.0 for $0 \leq y \leq L$ | -5.8 for $0 \leq y \leq L$ |
| $\partial\bar{\theta}/\partial z$ (K m^{-1}) | 0.0 | 0.014 | 0.003 |
| z_i (m) | 95 | 90 | 190 |
| u_g (ms $^{-1}$) | -4.0 | -8.4 | -6.9 |
| v_g (ms $^{-1}$) | 0.9 | 0.6 | 3.6 |
| p_0 (hPa) | 1028 | 1034 | 1029 |

^a L is the lead width, $T_{s,i}$ and $T_{s,i}(y)$ are the prescribed surface temperatures of sea ice and lead surfaces, respectively, where y is the distance to the upwind lead edge. $\partial\bar{\theta}/\partial z$ is the average upwind vertical potential temperature gradient below the bottom of the capping inversion at height z_i as observed upwind of the lead. u_g and v_g are the lead-orthogonal and lead-parallel height-independent geostrophic wind components, and p_0 is the observed surface air pressure.

3.4 Simulation results with non-modified parametrizations

We analyse three basic features. First, turbulent fluxes and ABL structures of temperature and wind are examined based on vertical cross-sections in lead-perpendicular direction. Second, vertical structures at individual positions obtained from profiles of both mean quantities and turbulent fluxes are analysed. Third, we discuss the development of variables at a constant height level as a function of distance.

For each case described in the following subsections, all cross-sections are shown using the non-dimensional height z/z_i , where z_i is the upwind observed ABL height (see section 3.2 for the respective values). For figures showing vertical profiles, the potential temperature data including their error bars are based on T15 (their Figures 5a, 14a, and 17a). The turbulent fluxes were recalculated for this work. As T15, we also applied a band-pass filter on measurements of both wind components and potential temperature with cut-off frequencies of 0.1 Hz and 50 Hz, but unlike T15, we slightly modified some legs to reduce inhomogeneity and use the filter function of the latest MatLab version 2020a reducing some artificial noise at the beginning of the legs. Thus, some of our flux values slightly differ from those in T15. Moreover, for March 10 we consider the absolute values of the total vertical momentum flux, F_τ , instead of only its

x_1 -component as in T15. As a new feature, we considered also vertical profiles of the horizontal wind speed.

All simulated vertical profiles are shown as solid, coloured lines with a shaded region around. The lines refer to results at a certain distance from the upwind lead edge, which agrees with the position of the corresponding measurements averaged over the respective lead-parallel flight leg. The shaded region is added to include simulation results of ± 300 m upwind and downwind of the respective position to account for remaining uncertainty of the fetch lengths (although corrected by filtering). Additional uncertainty of the fetch is given due to deviation of modelled and observed local wind direction. This method also allows us to examine, if at least the modelled and observed patterns agree except for a potential horizontal shift of the structures.

3.4.1 Model runs 1003-MIX and 1003-NL1

Simulated vertical cross-sections of the model runs 1003-MIX and 1003-NL1 are shown in Figure 3.3. Some general features can be clearly identified, which are also shown for the other two cases discussed below. First, an inclined plume developing over the lead is obvious from the heat flux patterns of both runs (Figures 3.3a and 3.3b), where the simulated plume shapes differ depending on the applied parametrization. While in run 1003-MIX positive heat fluxes extend far into the lead's downwind region, a clear downwind plume boundary is simulated by the run 1003-NL1 with negative fluxes further downstream starting at $y \approx 3$ km. In run 1003-NL1, entrainment fluxes are simulated near z_i above the lead at $y \approx 0.8$ km, which indicates that the plume reaches the inversion layer at that distance. Second, the developing plume leads to an ABL warming and also affects ABL stratification as shown in the patterns of the potential temperature (Figures 3.3c and 3.3d). While the application of the local closure causes a slightly unstable stratification in almost the whole downwind mixed layer (denoted in Figure 3.3c), a slightly stable stratification is obtained with the non-local closure (denoted in Figure 3.3d). This causes a fundamental difference in the heat fluxes, which are directed upward/downward in this region when the local/non-local closure is applied. Note that a stabilisation of the downwind ABL was also obtained by M20 in their LES of idealised cases at near-neutral upwind stratification.

Modelled horizontal wind speed patterns differ only very slightly from each other (Figures 3.3e and 3.3f). In both simulations, a pronounced wind speed maximum near z_i is indicated, where it is more or less destroyed further downwind due to enhanced vertical mixing caused by the lead-generated convection.

In the pattern of the vertical momentum flux, a clear maximum is obtained with both closure schemes above the lead (Figures 3.3g and 3.3h). In run 1003-MIX, the maximum is slightly more pronounced and it occurs a few hundred meters further downwind than in run 1003-NL1.

Simulated and observed profiles are shown in Figure 3.4 for heat fluxes, potential temperature, and momentum fluxes. The simulation results for $y = -6.45$ km solely show that the applied closure schemes do not affect the upwind results so that inflow conditions were the same for both model runs.

The general observed structure of the heat fluxes is basically represented by both model

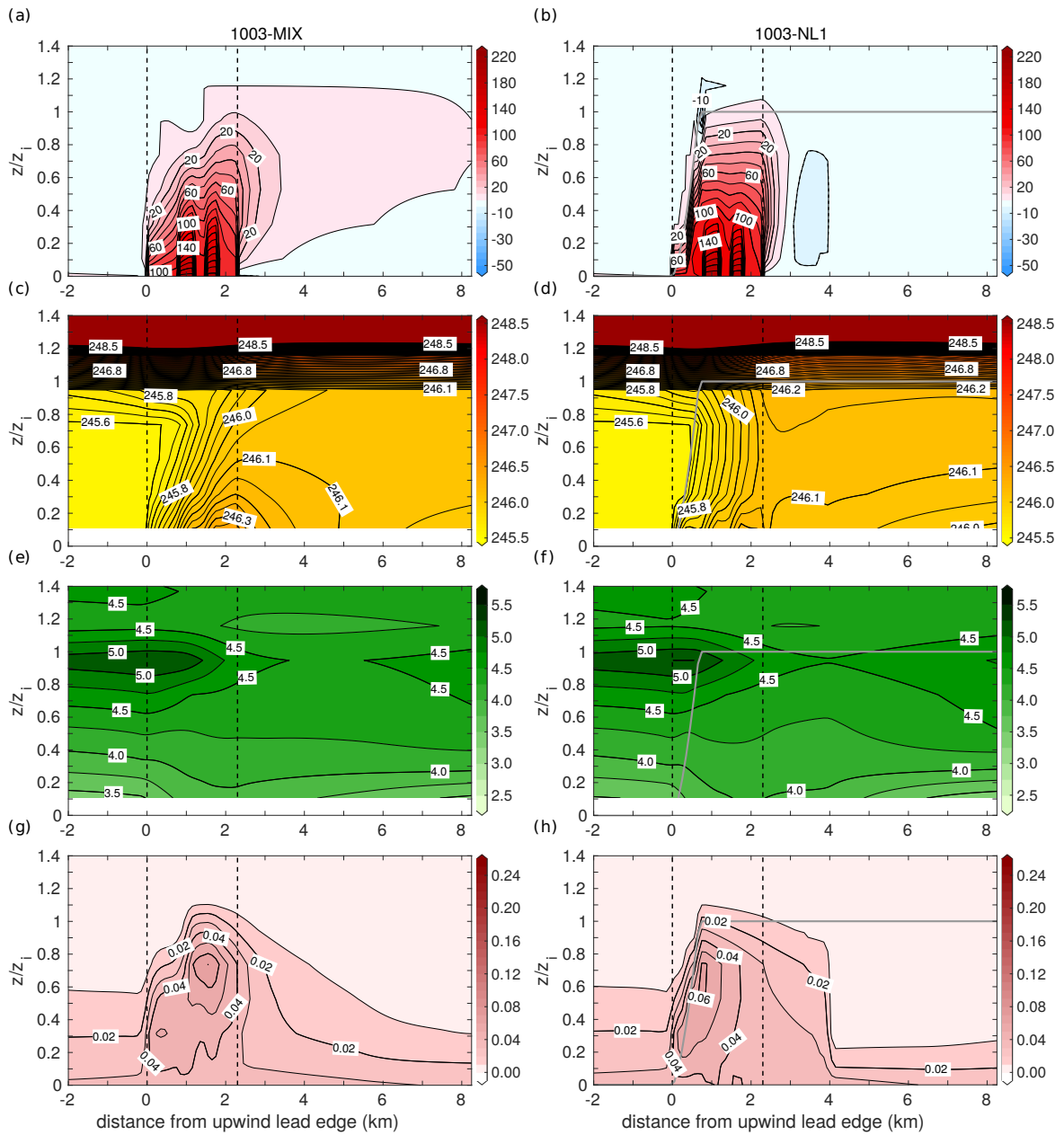


Figure 3.3: Vertical cross-sections obtained with METRAS for March 10, 2013 (runs 1003-MIX and 1003-NL1, see Table 3.1) plotted against the non-dimensional height z/z_i , where $z_i = 95$ m is the upwind observed ABL height. Panels (a, b) show the sensible heat flux in Wm^{-2} , (c, d) the potential temperature in K, (e, f) the horizontal wind speed in ms^{-1} , and (g, h) the vertical momentum flux in Nm^{-2} . The position of the lead is between the vertical dashed black lines. The spacing between heat flux contour lines is 5Wm^{-2} for negative fluxes (dashed contour lines in (a, b)). The solid grey lines show the upper IBL height according to Equation 2.20 from chapter 2 (right column).

runs (Figures 3.4a and 3.4b). Near $y = 1.3$ km, surface heat fluxes of 110Wm^{-2} to 195Wm^{-2} are simulated, where the large range of model results reflects the uncertainty as described above (see sections 3.2, 3.3.1, and 3.4). Above the surface layer, the observed pattern of almost linearly decreasing heat fluxes is well represented with both model runs. Near the downwind lead edge at $y = 2.3$ km, the observed structure of an elevated heat flux maximum in the ABL centre is also reproduced. However, comparing observations and simulation results directly at

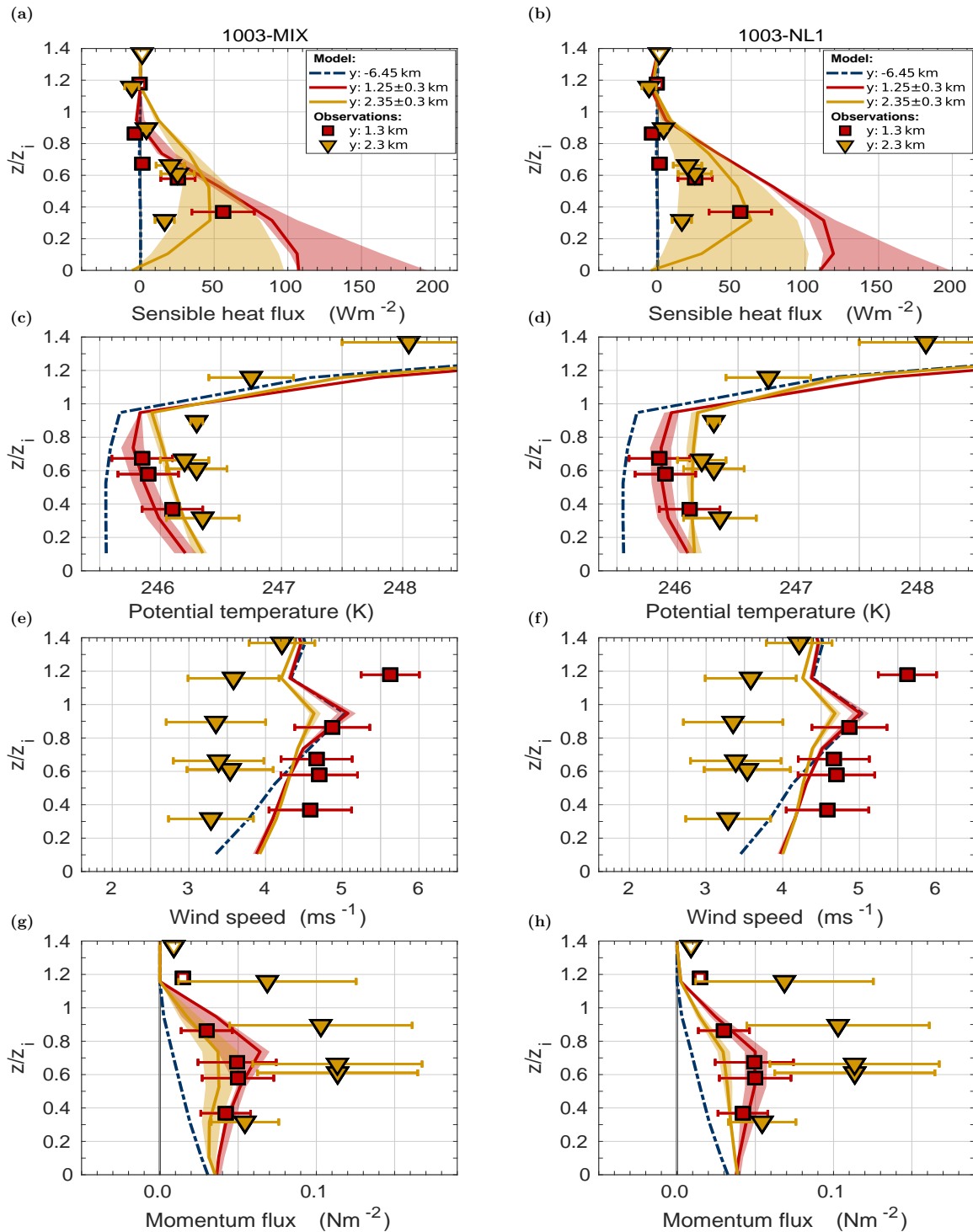


Figure 3.4: Vertical profiles from simulation results obtained with METRAS (coloured lines and shaded regions, runs 1003-MIX and 1003-NL1, see Table 3.1) and the corresponding observations with measurement uncertainties (points with error bars, partly from T15) for March 10, 2013 at different locations y , where y is the distance from the upstream lead edge, plotted against the non-dimensional height z/z_i , where $z_i = 95$ m is the upwind observed ABL height. Panels (a, b) show the sensible heat flux in Wm^{-2} , (c, d) the potential temperature in K, (e, f) the horizontal wind speed in ms^{-1} , and (g, h) the vertical momentum flux in Nm^{-2} . The lead is located between $y = 0$ km and $y = 2.3$ km. Open symbols mark values obtained from legs with observed intermittent turbulence (see T15).

the same location y , the simulated heat fluxes exceed the observed values. This overestimation

concerns especially the position over the lead centre, while at the downwind lead edge the measurements are at least in the scatter of the modelled values (yellow-shaded region) obtained with the non-local closure (Figure 3.4b). Thus, one possible explanation of the overestimation is the uncertainty in the fetch and in the exact position of the aircraft relative to the curved lead edge.

Although the simulated heat fluxes exceed the observed values above the lead, the simulated temperature profiles agree well with the observations at $y = 1.3$ km (Figures 3.4c and 3.4d). Near $y = 2.3$ km, the simulated values are slightly below the mean observed temperatures, especially for the observed value near $0.9z_i$. This is especially obvious for the run 1003-MIX, where an unstable stratification is obtained. Following the run 1003-NL1, rather a neutral or slightly stable stratification is shown, which better resembles the observations. The slight underestimation of observed temperatures might be explained by an underrepresented effect due to vertical entrainment of heat through the capping inversion.

The observed wind profiles are only partially well represented by the model runs (Figures 3.4e and 3.4f). Above the lead at $y = 1.3$ km, measured and simulated profiles agree well below z_i , but the observed increase in wind speed above z_i does not match with the modelled one, which is due to the mismatch in the inflow profile (see Figure 3.2d). Near the lead's downwind edge at $y = 2.3$ km, the simulated values exceed the observations by approximately 1 ms^{-1} in the entire ABL.

Regarding the observed momentum fluxes at the downwind lead edge ($y = 2.3$ km), a strong underestimation is obtained by both model runs (Figures 3.4g and 3.4h). Over the lead's centre ($y = 1.3$ km), results of both runs agree better with the observations, where the observed values are almost perfectly hit by the simulations results of run 1003-NL1.

3.4.2 Model runs 2503-MIX and 2503-NL1

For March 25, vertical cross-sections of potential temperature and wind speed based on the data obtained during a vertical saw-tooth pattern are shown in Figure 3.5. The interpolation method to generate the cross-sections is similar to the method used by T15 (see their Figures 13a and 13c), but the visualisation is adapted to our applied colour scales and ranges. Due to the shallow boundary layer, the lowest height reached by the aircraft was at $0.4z_i$. Thus, only a small part of the ABL structure is visible in the measurements. Nevertheless, three features can be clearly identified. First, compared to March 10, the ABL was more stably stratified in the upwind region, where ABL stratification had slightly weakened in the downwind region (Figure 3.5a). Second, the convection clearly penetrated into the capping inversion downwind of the lead, which strongly lifted the inversion base with increasing distance. Third, two pronounced wind speed maxima occurred near z_i , one upwind of the convective region and another one downwind of the lead near $y = 15$ km (Figure 3.5b). Between approximately $y = 2.5$ km and $y = 11$ km, the wind speed maximum was obviously destroyed due to the convection (see also T15). All three effects can be related to the convective IBL developing over the lead, where the observed position of its upper boundary is also shown in Figure 3.5 (see T15 for more details on their determination of this quantity).

Model results for this case using the local closure (2503-MIX) and the non-local one (2503-

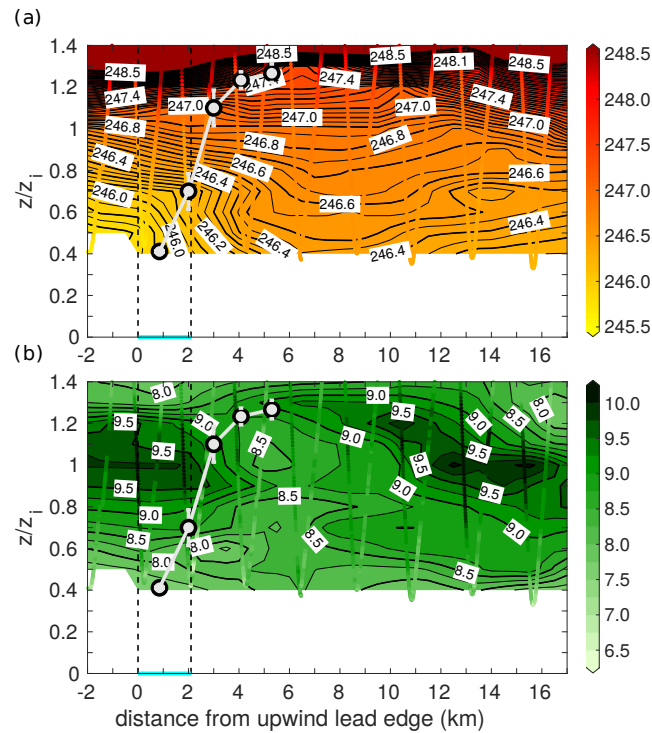


Figure 3.5: Observed potential temperature in K (a) and horizontal wind speed in ms^{-1} (b) in lead-perpendicular direction derived from the saw-tooth leg on March 25, 2013. Smoothed measurements are shown as dots and linear interpolation was applied for the filled contours using a similar method as in T15. In white colour, the observed upper IBL height is shown based on T15, their Figure 22b. The lead edges are denoted by the dashed black lines. The upwind observed ABL height is $z_i = 90 \text{ m}$.

NL1) are shown in Figure 3.6. The differences between both runs are not as pronounced as for March 10. The most important differences concern both structure and vertical extent of the plumes, which is most obvious in the heat fluxes (Figures 3.6a and 3.6b). In the non-local run, an abrupt increase of the upper plume boundary is obtained over the second half of the lead, unlike in run 2503-MIX.

Regarding the ABL temperature, patterns of both model runs obtained for March 25 differ strongly from those for March 10, indicating stable stratification on the upwind and downwind side of the lead (Figures 3.6c and 3.6d). Such a stable stratification for the run with the local closure is a new feature and clearly related to the stable stratification already upwind of the lead, while for 2503-NL1 also the counter-gradient flux contributes to stabilisation. Thus, negative heat fluxes are simulated already below z_i upwind of the lead and above the plume in both runs, 2503-MIX and 2503-NL1. The simulated stability downwind of the lead is slightly stronger with 2503-NL1. In the region between $y = 2 \text{ km}$ and $y = 4 \text{ km}$, this causes also stronger downward heat transport than in 2503-MIX. The observed influence of the plume on the temperature structure in the capping inversion is not represented, neither by 2503-MIX nor by 2503-NL1.

Regarding the wind speed patterns, the model is able to reproduce the wind speed maximum at the upstream side and its destruction by the plume over the lead (Figures 3.6e and 3.6f). However, the observed recovering wind speed maximum further downwind is not captured, independent on the used closure. The modelled maximum on the upstream side is also slightly underestimated, but the onset of decreasing wind speed over the lead in horizontal direction is almost at the same location as in the observations. The modelled minimum is, however, less

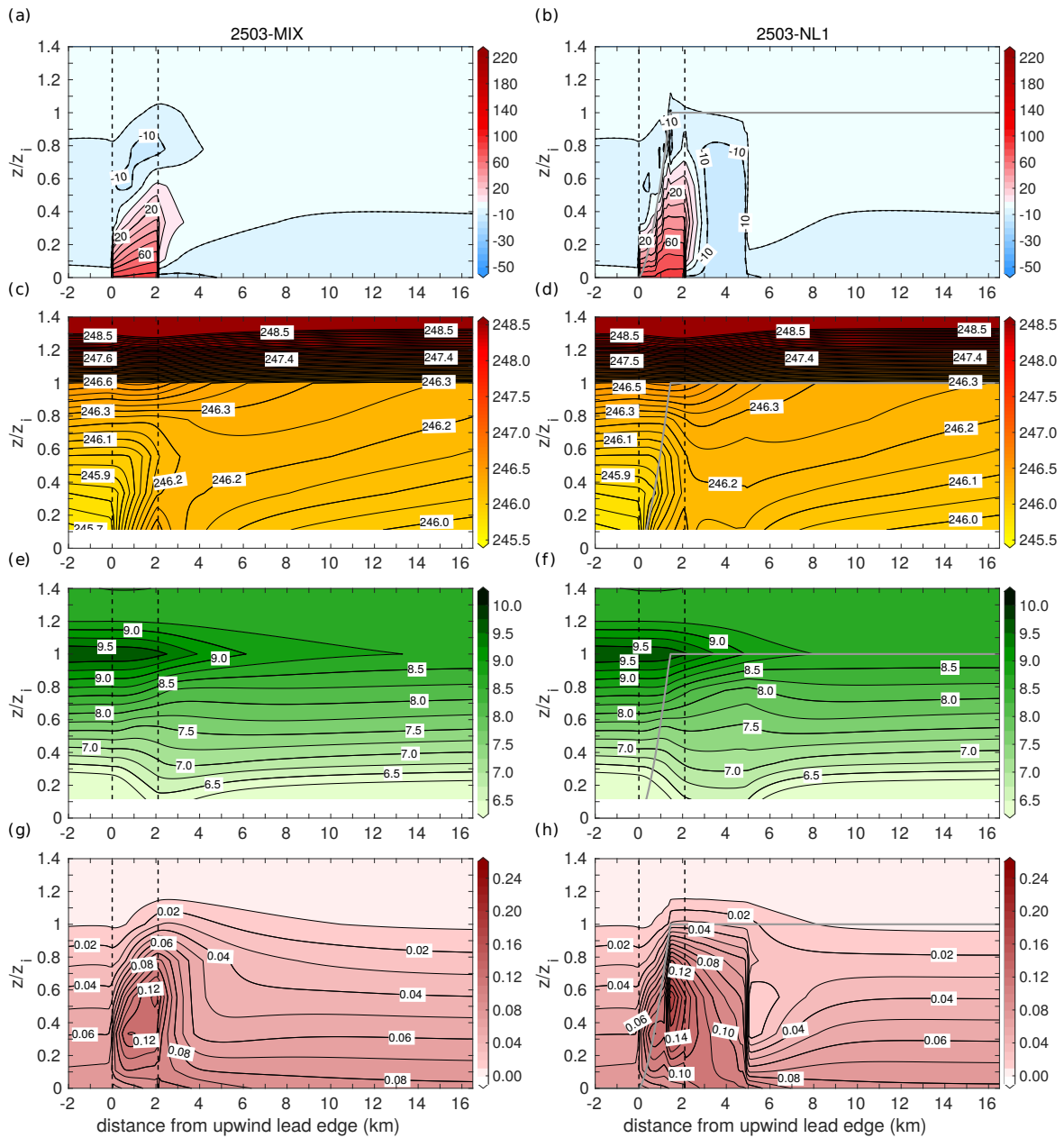


Figure 3.6: Same as Figure 3.3, but for the model runs 2503-MIX and 2503-NL1 (Table 3.1) for March 25, 2013. The upwind observed ABL height is $z_i = 90$ m.

pronounced than in the observations, where the destruction is slightly stronger by 2503-NL1 than by 2503-MIX.

Regarding the momentum fluxes, slightly higher values are obtained with 2503-NL1 than with 2503-MIX (Figures 3.6g and 3.6h). Moreover, the region with increased momentum fluxes depicting the convective plume extends further downwind and reaches higher altitudes in run 2503-NL1. Hence, the whole region with an impact of momentum fluxes is about 20 % larger than in run 2503-MIX.

A comparison between the simulated heat flux profiles of both model runs and the observations on March 25 (Figures 3.7a and 3.7b) points, in general, to a better representation of the observed heat fluxes below z_i than on March 10. Moreover, heat fluxes obtained with the

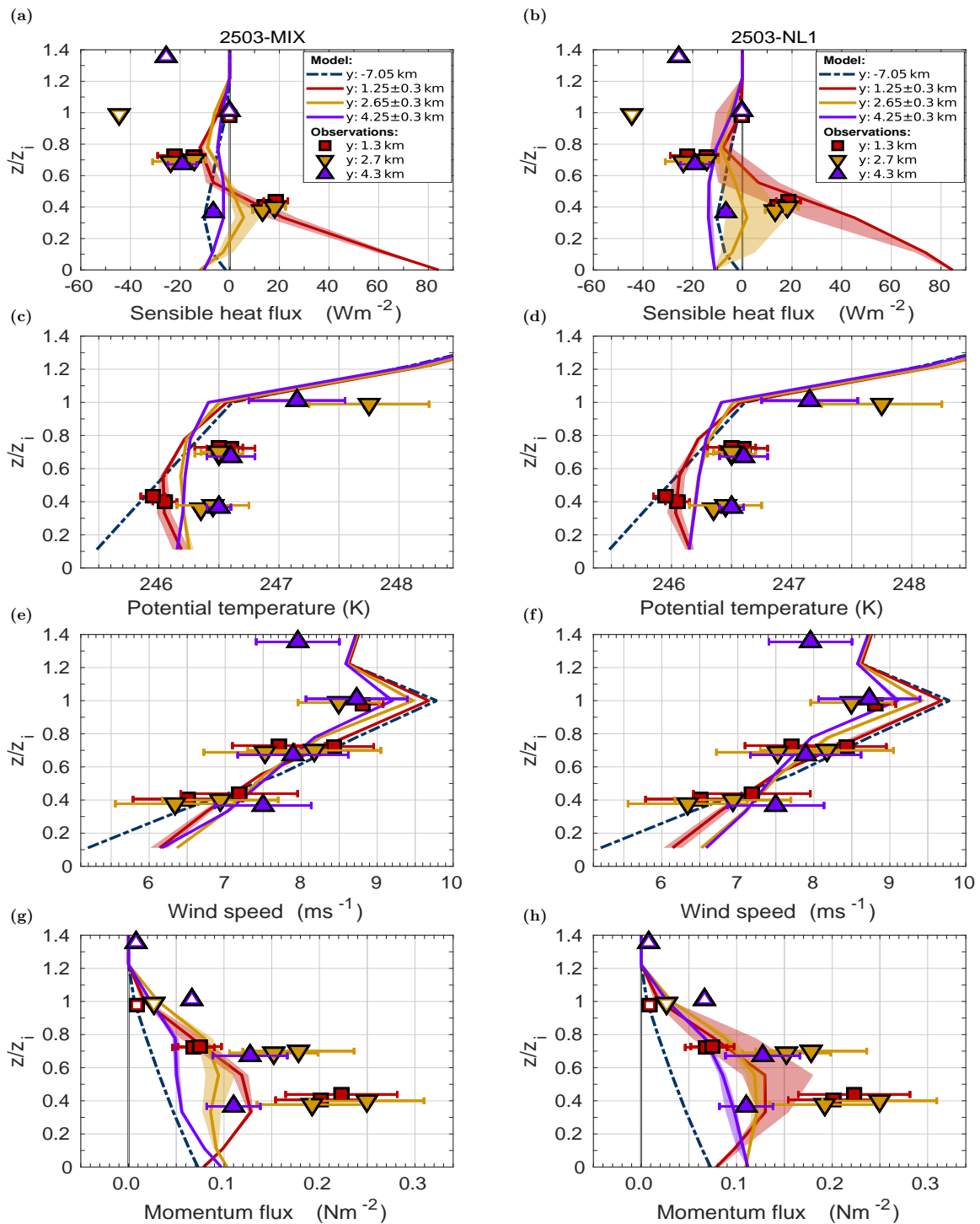


Figure 3.7: Same as Figure 3.4, but model results of the runs 2503-MIX and 2503-NL1 (Table 3.1) and observations for March 25, 2013 are shown. The upwind observed ABL height is $z_i = 90$ m. The lead is located between $y = 0$ km and $y = 2.1$ km.

non-local closure (2503-NL1) vary stronger with distance than those obtained with the local closure (2503-MIX) indicated by the wider shaded areas around the profiles at single locations. This implies a seemingly larger impact of the fetch when the non-local closure is used.

Two major differences between simulated and observed heat fluxes are obvious. First, near $0.7z_i$, the minima with negative heat fluxes are less pronounced in both simulations than in

the observations. Second, the minimum near z_i observed downwind of the lead at $y = 2.7$ km is almost absent in the simulations. In addition, at $y = 2.7$ km, the modelled heat fluxes near $0.4z_i$ are directed downward as in the observations, but their absolute values are slightly underestimated by both 2503-MIX and 2503-NL1.

For the temperature above the lead's centre ($y = 1.3$ km), almost the same profiles are obtained by both runs in good agreement with the corresponding measurements at the lowermost flight level at $0.4z_i$, but between $0.4z_i$ and $0.8z_i$, the observed stability is underestimated by both model runs (Figures 3.7c and 3.7d). The downwind observed ABL warming effect is also underestimated by both runs, where the temperature profile at $y = 2.7$ km simulated by 2503-NL1 agrees slightly better with the observations than by 2503-MIX. There is also an important difference between the results obtained with both closures that concerns the direction of fluxes. Near the lead's downwind edge ($y = 2.7$ km), the observed ABL temperature increases with height between $0.4z_i$ and $0.7z_i$ implying counter-gradient turbulent heat fluxes. This temperature increase is reproduced in the result with the non-local closure, but it cannot be captured by the local closure, where temperature slightly decreases with height at the same location.

The observed wind profiles at all three locations are well reproduced by the model runs, except for the measurements near z_i and further above, where the measured wind speeds are basically lower than the simulation results (Figures 3.7e and 3.7f). The simulated momentum flux profiles show that the observed values are mostly underestimated (Figures 3.7g and 3.7h), especially by run 2503-MIX. In run 2503-NL1, there is a slightly better representation of the observed values, especially in the lead's downwind region near $y = 4.3$ km.

3.4.3 Model runs 2603-MIX and 2603-NL1

For March 26, vertical cross-sections of the model runs 2603-MIX and 2603-NL1 are shown in Figure 3.8, and the profiles in comparison to the observations in Figure 3.9. As for the previously discussed cases, the simulated plumes have different structures. Differences concern the plume's vertical extent and its inclination. A less inclined plume is obtained by run 2603-MIX due to a stronger plume growth above the first half of the lead than by run 2603-NL1. Thus, in run 2603-MIX, the upper plume boundary at $y = L$ is at $0.7z_i$ (Figure 3.8a) and reaches the inversion layer far downwind of the lead at 6 km distance, while in run 2603-NL1 z_i is reached already at $y = L$ (Figure 3.8b).

The temperature distribution downwind of the lead shows an almost neutral layer with 2603-MIX (Figure 3.8c) and a slightly stable layer with 2603-NL1 (Figure 3.8d). In the simulated wind speed patterns (Figures 3.8e and 3.8f), only marginal differences are shown, where the general structure is similar to the previously discussed cases.

The momentum flux patterns show large differences between the local and non-local closures. A sharp decrease of fluxes occurs downwind of the lead above $0.2z_i$ in the run 2603-NL1, while with 2603-MIX only weakly decaying fluxes are modelled.

Compared to the measurements, run 2603-MIX strongly overestimates the heat fluxes above the lead's centre ($y = 0.7$ km), whereas at the lead's downwind edge, the observed flux profile is well represented (Figure 3.9a), but with an underestimation of the flux at the lowermost

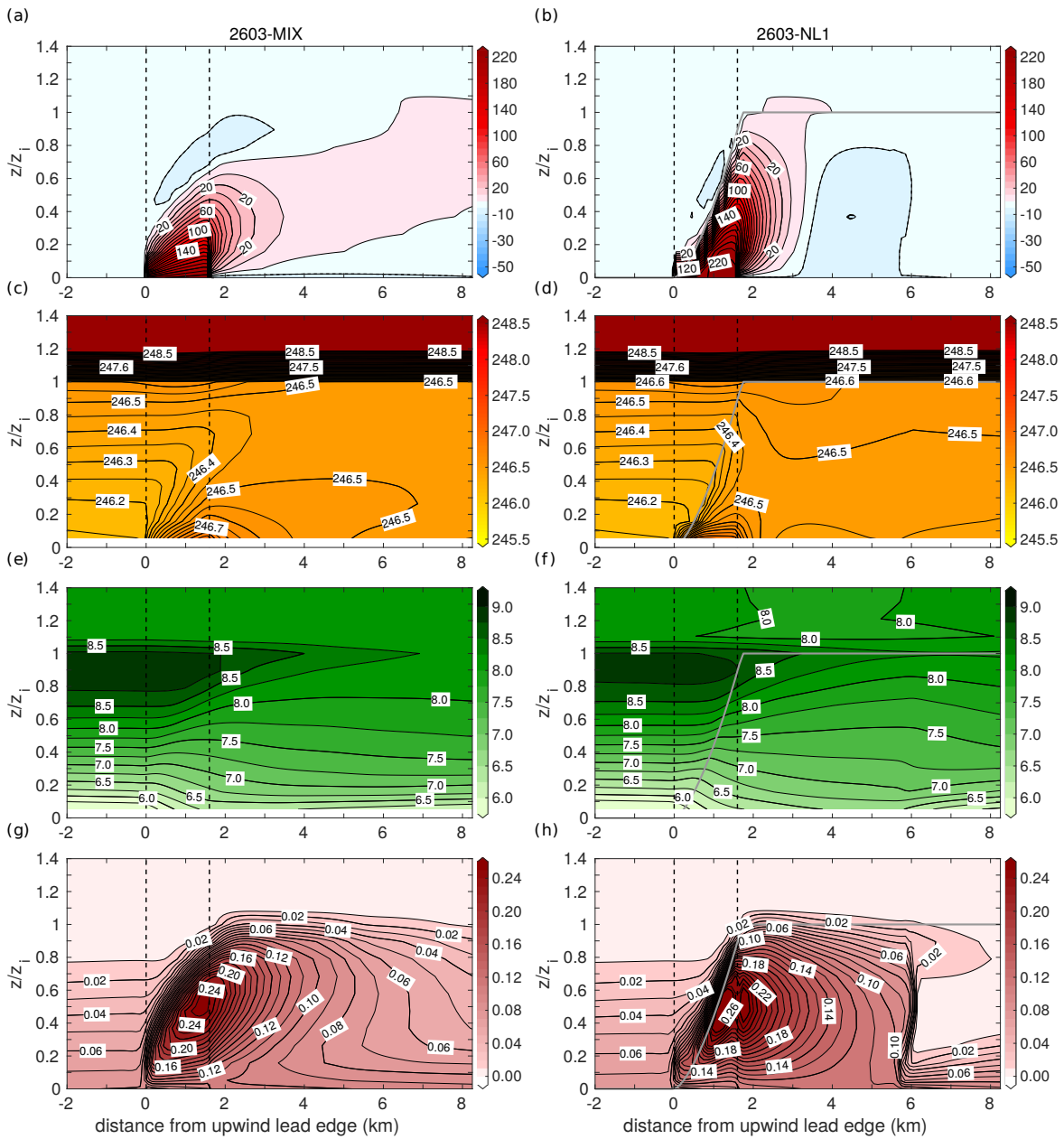


Figure 3.8: Same as Figure 3.3, but for the model runs 2603-MIX and 2603-NL1 (Table 3.1) for March 26, 2013. The upwind observed ABL height is $z_i = 190$ m.

level. Further downwind, observed heat fluxes are extremely underestimated, but at least the structure of an elevated flux maximum is, basically, represented. The corresponding results obtained by run 2603-NL1 show the opposite (Figure 3.9b) with very well reproduced fluxes over the lead centre, but overestimated fluxes in the upper half of the ABL downwind of the lead. As in 2603-MIX, large deviations from the observations are also obvious near $y = 3.0$ km and $y = 4.3$ km. Thus, the plume’s horizontal extent is underestimated by both runs.

The observed temperature profiles are slightly better represented by the simulation using the non-local closure than with the local closure, especially concerning the slightly stable stratification at 4.3 km distance (Figures 3.9c and 3.9d), which is reproduced only by run 2603-NL1.

As for March 25, also for March 26 the observed wind profiles are well reproduced by both

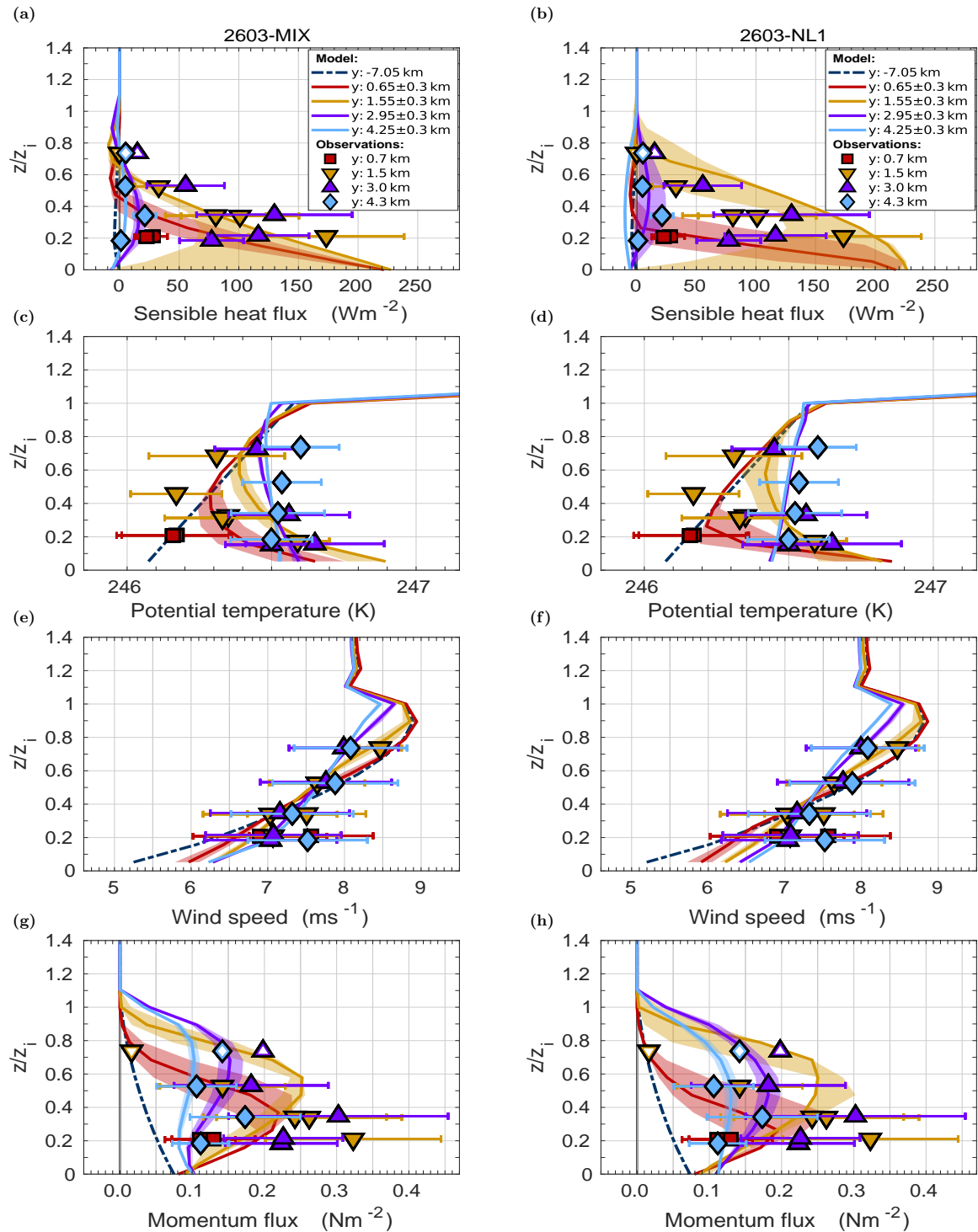


Figure 3.9: Same as Figure 3.4, but model results of the runs 2603-MIX and 2603-NL1 (Table 3.1) and observations for March 26, 2013 are shown. The upwind observed ABL height is $z_i = 190$ m. The lead is located between $y = 0$ km and $y = 1.6$ km.

model runs (Figures 3.9e and 3.9f). This holds also for the observed decrease in wind speed with increasing distance near $0.7z_i$. A slight underestimation is obtained by both model runs at the lowest flight leg downwind of the lead at $y = 4.3$ km.

Elevated momentum flux maxima are simulated in both runs, where their vertical location increases with increasing y (Figures 3.9g and 3.9h). At $y = 0.7$ km, the observed momentum

flux at $0.2z_i$ is slightly overestimated with both runs. Downwind of the lead, the quality of agreement between simulation results and observations is slightly better with run 2603-NL1 than with 2603-MIX, but the observed momentum fluxes are mostly underestimated. As already noted for the other two cases, the simulated vertical positions of the momentum flux maxima are, basically, higher than the corresponding observations. This is especially shown in the downwind profiles at $y = 3.0$ km and $y = 4.3$ km simulated by run 2603-MIX.

3.5 Modification of the M20 parametrization

The simulation results in section 3.4 showed that the general structure of the ABL is fairly represented by model simulations using the local or the non-local closure. Furthermore, there is no such clear difference in the results obtained with the two closure types as in the idealised cases discussed in M20 with neutral stratification upwind of the lead (see, for example, section 2.6 in this thesis). The non-local closure shows slight advantages in some aspects. For example, the downwind temperature profiles and momentum fluxes on March 25 obtained with the M20 parametrization agree slightly better with the observations than those obtained with the local closure. However, in some other aspects the local closure shows advantages. Hence, also the results obtained with the M20 closure revealed two main drawbacks compared to the measurements. The first concerns the underestimation of the observed ABL warming effect downwind of the leads shown for all three cases. We speculate that this is most probably due to underestimated vertical entrainment. Second, for March 25 and 26, the plumes simulated by the runs 2503-NL1 and 2603-NL1 grew too fast compared to the observations. Most probably, this is due to the stable stratification upwind of the leads that might cause the lead-generated plume to grow more slowly than for neutral stratification (T15). This behaviour could not be captured by the closure developed so far for neutral inflow. Therefore, in the following, we present two further modifications of the M20 parametrization to overcome these drawbacks.

3.5.1 Determination of the ABL height z_i

The observations by T15 revealed that the convection over leads can be strong enough to penetrate into the capping inversion, which leads to vertical entrainment fluxes so that z_i increases with distance. Such effects were clearly observed during STABLE, where the measured z_i upwind of the lead differed clearly from the value downwind of the lead (see section 3.2 and Figure 3.5). To include the penetration effect, we consider modifications for the parameter z_i in the M20 parametrization.

We introduce a diagnostic determination of a y -dependent inversion height, $z_i(y)$, following the methods proposed by Sullivan et al. (1998). They investigated the temporal evolution of a surface-heated, initially neutrally stratified convective boundary layer, with a finite potential temperature jump across the inversion followed by a uniform lapse rate above, which includes the evolution of the ABL height z_i . They used a 3-D LES model with nested grid in the inversion layer and analysed three different methods, called "flux method", "contour method" and "gradient method" (Sullivan et al., 1998). These methods are used to determine z_i at every horizontal grid point position (here: at each y). Following the flux method, z_i is defined

as the vertical location of the minimum heat flux. Following the contour method, z_i is defined as the vertical location of a specific contour line of the potential temperature, for which a specific value θ_c has to be prescribed. The selected potential temperature contour is then tracked along distance y and its respective vertical position is set equal to z_i . Following the gradient method, z_i is defined as the vertical location of the maximum vertical potential temperature gradient. Sullivan et al. (1998) also showed that z_i obtained via the flux method is, in general, lower than with the other methods, which corresponds with results of laboratory investigations by Deardorff et al. (1980). Furthermore, Sullivan et al. (1998) found that the flux method underestimated both z_i and turbulence in the inversion.

We performed simulations applying all three methods for the $z_i(y)$ determination. The implementation of the y -dependent z_i in the model was done as follows. First, at each numerical time step, values of the variables needed to determine $z_i(y)$ are vertically linearly interpolated from the numerical grid with 20 m vertical spacing to a 5 m spacing. This concerns the potential temperature for all three methods as well as K_h and Γ for the flux method. Second, based on those interpolated fields, $z_i(y)$ is calculated at each grid point in lead-perpendicular direction using the respective method. Third, the final values for $z_i(y)$ are obtained after applying a running mean over five points in lead-perpendicular direction to smooth spatial oscillations of $z_i(y)$. The values finally obtained for $z_i(y)$ as a function of distance then mark the (fetch-dependent) upper limit for the upper IBL height $\delta(y)$ from the M20 parametrization (see Equation 2.20 in chapter 2). Moreover, we assume that variations in $z_i(y)$ for $y > y_{z_i}$, where y_{z_i} marks the distance where the upper plume boundary intersects with the upwind value of z_i , are only due to the influence of the plume in the inversion layer. For the flux method, we calculate $z_i(y)$ based on the heat flux profile at time step $t - 1$ because z_i itself is needed to calculate the heat flux, and we set the observed upstream ABL height as a minimum value for $z_i(y)$. This is because downwind of the lead the location of the minimum vertical heat flux is likely to be near the surface in the devolving near-surface stable IBL over sea ice (not shown). For θ_c used in the contour method, we prescribe the temperature values 10 m above $z_i(y)$ at the inflow boundary.

For March 10, the results for $\delta(y)$ with the fetch-dependent upper limit $z_i(y)$ are shown

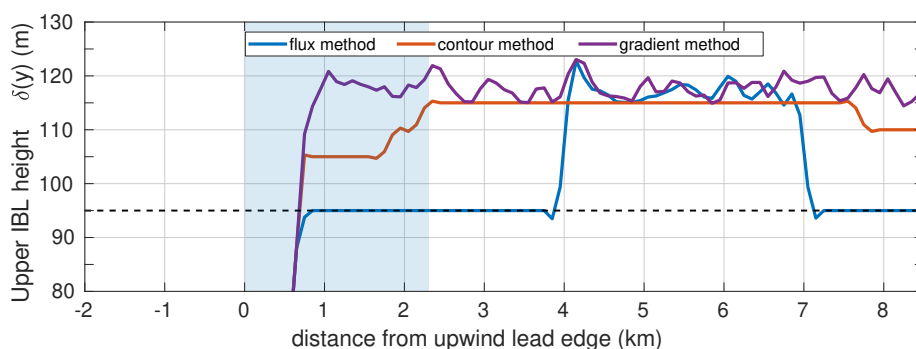


Figure 3.10: Upper IBL height $\delta(y)$ for March 10, 2013 obtained with the M20 parametrization following Equation 2.20 (see chapter 2), but a y -dependent ABL height $z_i(y)$ determined based on three different methods (coloured lines) following Sullivan et al. (1998) (see text) is used as upper limit for $\delta(y)$, where y is the distance from the upwind lead edge at $y = 0$ km. For the contour method, $\theta_c = 246.8$ K. The position of the lead is denoted by the blue-shaded rectangle. The upwind observed ABL height is $z_i = 95$ m (dashed black line).

in Figure 3.10 dependent on the method used for determining $z_i(y)$. Note that the small-scale variation in $z_i(y)$, especially for the gradient method, is caused by the linear interpolation, so by numerical rather than by physical reasons. Following the flux method, $z_i(y)$ remains constant at its upwind level of 95 m until $y = 4$ km and then it strongly increases to about 120 m until $y = 7.5$ km. Thus, the increase in $z_i(y)$ occurs much farther downwind than in the observations (see section 3.2.1). Moreover, $z_i(y)$ increases downwind of the convective plume region for the first time, so downwind of $\delta_d(y)$. Thus, no improvements can be expected by this method for the non-local closure.

Following the gradient method, $\delta(y)$ strongly increases to about 120 m already above the lead's centre and it remains almost constant with increasing y (Figure 3.10). Thus, much higher values than the observed value are obtained for $z_i(y)$ already above the lead causing overestimated entrainment (not shown).

Following the contour method (here with $\theta_c = 246.8$ K), a monotonic increase of $\delta(y)$ is obtained above the lead starting at $y \approx 0.8$ km. Further downwind, $z_i(y)$ remains constant at 115 m, which is higher than the observed value of 101 m (see section 3.2.1). Nevertheless, $z_i(y)$ as obtained with this method seems to be the best representation of a continuously rising ABL height with distance y . Hence, we consider additional simulations only with this method for all cases (see below).

3.5.2 Adjustment of parameter a to stably stratified inflow conditions

For the parameter a , which denotes the simulated plume inclination, M20 obtained the value 1.2 based on their LES results of idealised cases with upwind neutral stratification (see section 2.5.1 and Appendix B.2 in this thesis). However, in a stable environment, it can be expected that a lead-generated plume penetrates into the ABL more slowly than in neutral conditions (T15). This is supported by the findings of T15, who compared the observed IBL height on March 25 with the corresponding parametrization by L08, which forms the basis for the M20 approach and which is also designed for near-neutral conditions. T15 found that the observed IBL height is overestimated when the original value 2.3 of L08 is used for their parameter a (see section 2.2.2.2 in this thesis), but an improved agreement was obtained with $a = 1.9$. Hence, to include the effect of the positive upwind potential temperature gradient on the growth of the plume over the lead for March 25 and 26, we consider further simulations for the two stable cases with alternative values for a . We apply the same equation and methods proposed by M20 to determine a (see Appendix B.2 in this thesis), but use the measurements from STABLE instead of LES results.

M20 obtained a by rearranging Equation 2.20 (see section 2.5.1 and Appendix B.2 here) and calculating open quantities (B_l , D_w , $\delta(y)$ and U) from LES. To determine $\delta(y)$, they applied a linear approximation of LES results in the region $\delta(y) < z_i$. An equivalent procedure is applied here, so that we solve the first line of Equation 2.20 for a assuming $\delta(y) < z_i$ and obtain

$$a = \frac{\delta_{obs}^{2/3}(y)}{\left(\frac{2}{3} \frac{B_l^{1/3}}{U} y\right)}, \quad 0 \leq y \leq L, \quad (3.1)$$

In this equation, δ_{obs} and U can be taken directly from the observations and B_I is determined with measured near-surface temperatures and wind speeds using a bulk formula (e.g., Andreas & Murphy, 1986). Due to our linear approximation of δ_{obs} , a follows from any arbitrary pair of δ_{obs} and y . We found that the variability of a with respect to different positions y was indeed small, and the constant values $a \approx 0.75$ and $a \approx 0.9$ for March 25 and 26 represent a reasonable approximation. Both values are still inside the range defined for a in the M20 parametrization ($a = 1 \pm 0.6$, see section 2.5.1 in chapter 2), but obviously lower than $a = 1.2$ as proposed by M20 for their neutral cases.

3.5.3 Model

runs 1003-NL2 and 1003-NL3

Additional simulation results using the M20 parametrization including a y -dependent z_i (run 1003-NL2) are shown for the case on March 10 as vertical cross-sections (Figure 3.11) and as vertical profiles at single locations together with the corresponding observations (Figure 3.12, left column). In Figure 3.12, right column, results of the run 1003-NL3 are shown together with the observations, where the ratio for $z_{0,I}/z_{t,I}$ was assumed as 100 for reasons explained below.

As Figure 3.11 shows, the application of a varying z_i (run 1003-NL2) causes much more entrainment, a stronger warming effect, more stable stratification at $y = 2.3$ km, a stronger destruction of the upwind wind speed maximum, and slightly higher momentum fluxes near the downwind lead edge ($y = 2.3$ km) than with the runs 1003-MIX and 1003-NL1. This also causes, to some extent, an improved agreement with the observations (Figure 3.12, left column). The main improvement concerns the potential temperature profile at the downwind lead edge ($y = 2.3$ km). Comparing this profile with the one at $y = 1.3$ km shows that the stronger vertical entrainment reproduces the observed weakening of the inversion strength over the lead much better than with runs 1003-MIX and 1003-NL1 (Figure 3.12c compared to Figures 3.4c and 3.4d). A marginal improvement is also obtained

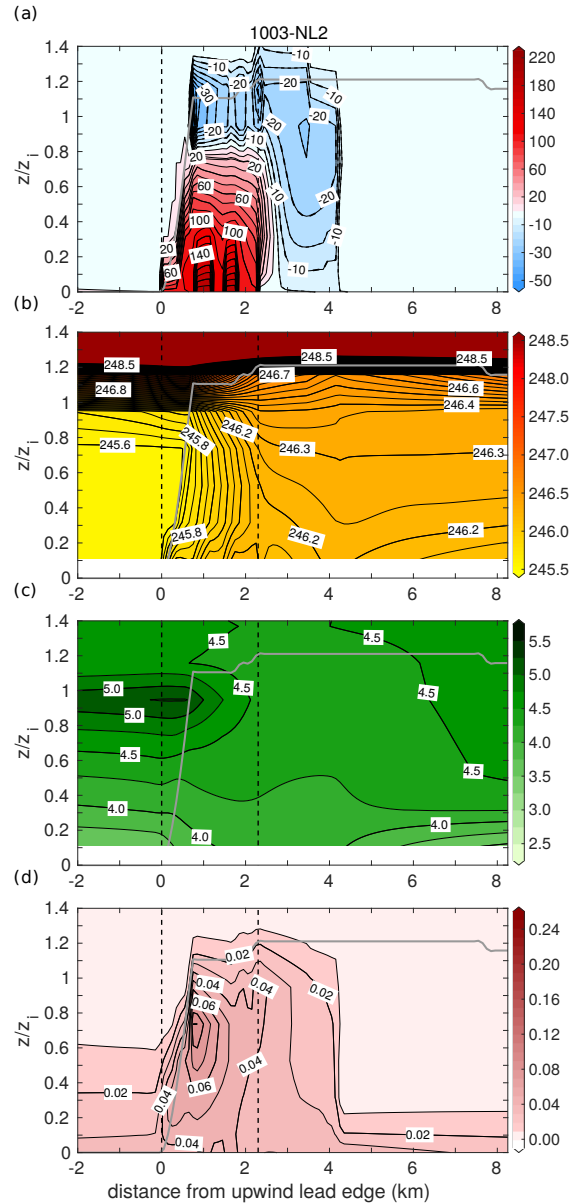


Figure 3.11: Same as Figure 3.3, but for the model run 1003-NL2 (Table 3.1) for March 10, 2013. The upwind observed ABL height is $z_i = 95$ m and for $y > 0$ km with y as distance from the upwind lead edge, a varying upper limit for the upper IBL height (solid grey lines, see Equation 2.20 in section 2.5.1) is used (see section 3.5.1).

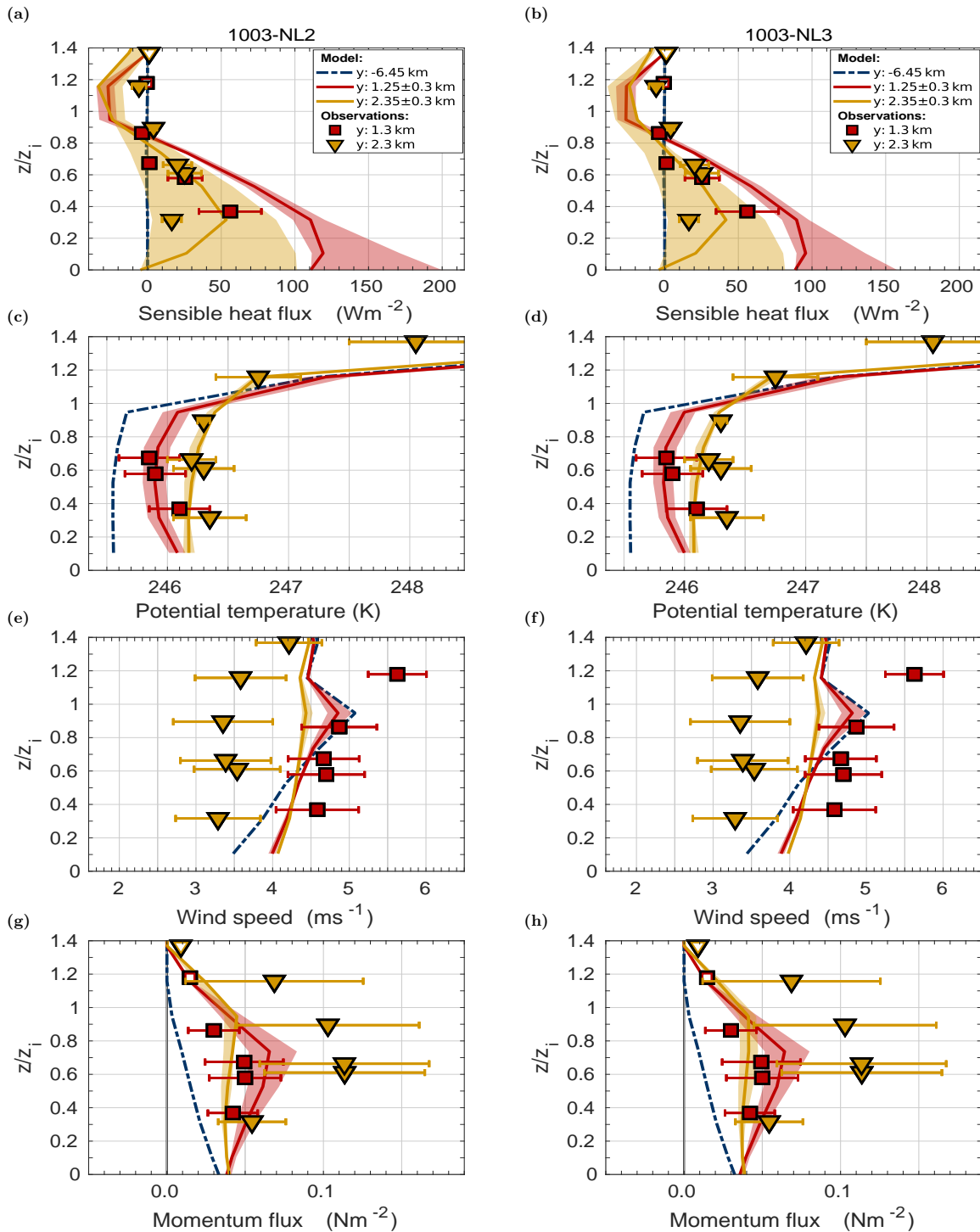


Figure 3.12: Same as Figure 3.4, but runs 1003-NL2 and 1003-NL3 (Table 3.1) for March 10, 2013 are shown. The upwind observed ABL height is $z_i = 95$ m. The lead is located between $y = 0$ km and $y = 2.3$ km.

for the downwind profiles of both wind speed and momentum fluxes, but the observed values remain basically strongly overestimated (wind) or underestimated (momentum fluxes).

At the lead's centre ($y = 1.3$ km), the observed heat fluxes remain overestimated with run 1003-NL2 (Figure 3.12a) but, as indicated in Figure 3.12b, this drawback might be overcome when a lower value of $z_{t,i}$ is applied so that the ratio $z_{0,i}/z_{t,i}$ is strongly increased from 10 to 100

(model run 1003-NL3). Such a large value is still well within the large scatter of observations from other campaigns (e.g., Andreas et al., 2010; Fiedler et al., 2010; Weiss et al., 2011). We consider this as the most realistic explanation for the originally overestimated heat fluxes, but additional factors might play a role, too.

3.5.4 Model runs 2503-NL2 and 2503-NL3

Figures 3.13 and 3.14 show simulated cross-sections and vertical profiles obtained with the runs 2503-NL2 and 2503-NL3 for March 25, which use the M20 parametrization, but with the modifications presented in sections 3.5.1 and 3.5.2. In both runs, the parameter a is lowered to

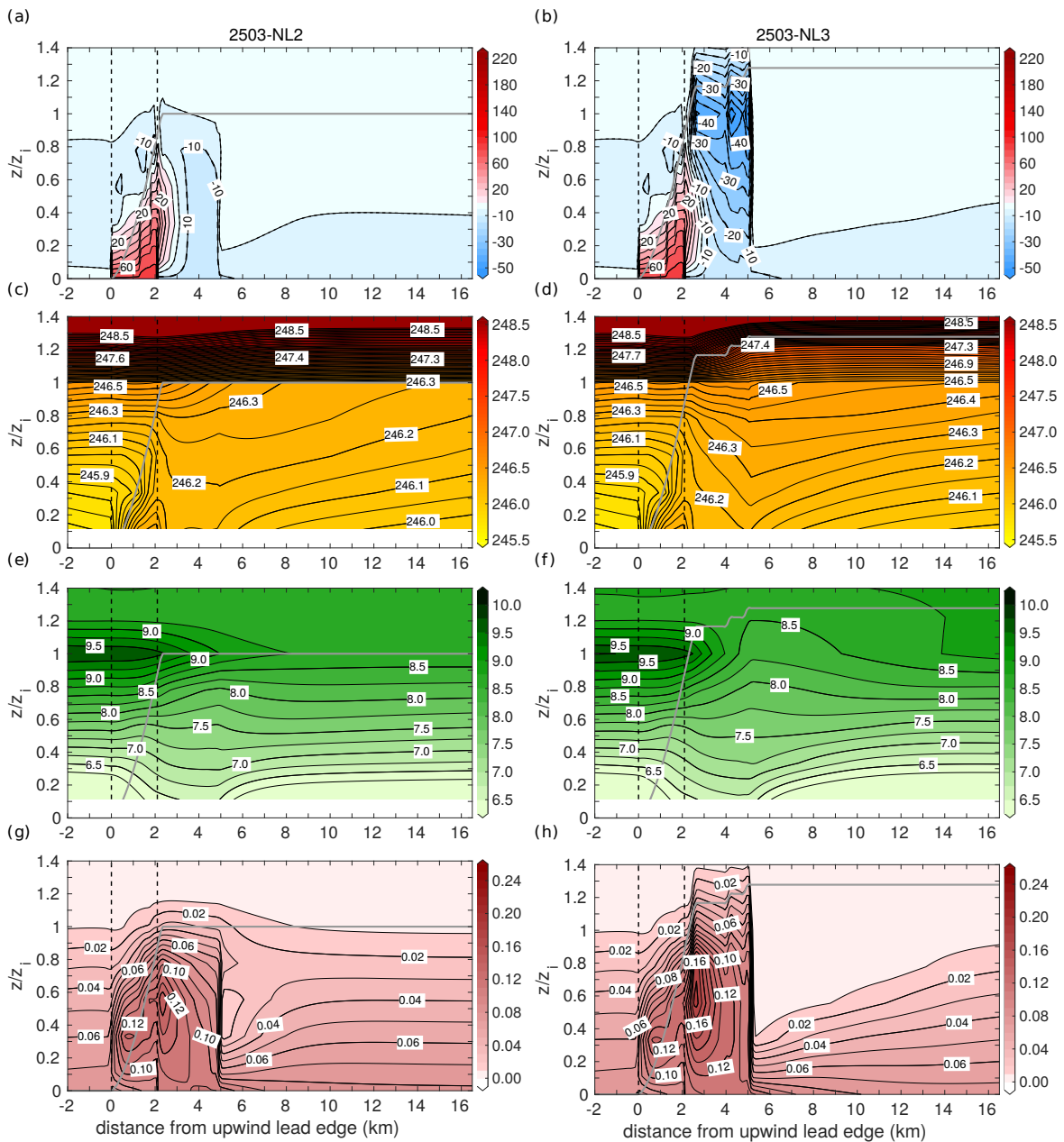


Figure 3.13: Same as Figure 3.6, but for the model runs 2503-NL2 and 2503-NL3 (Table 3.1) for March 25, 2013. The upwind observed ABL height is $z_i = 90$ m. Setup of the plots as described in Figures 3.3 and 3.11.

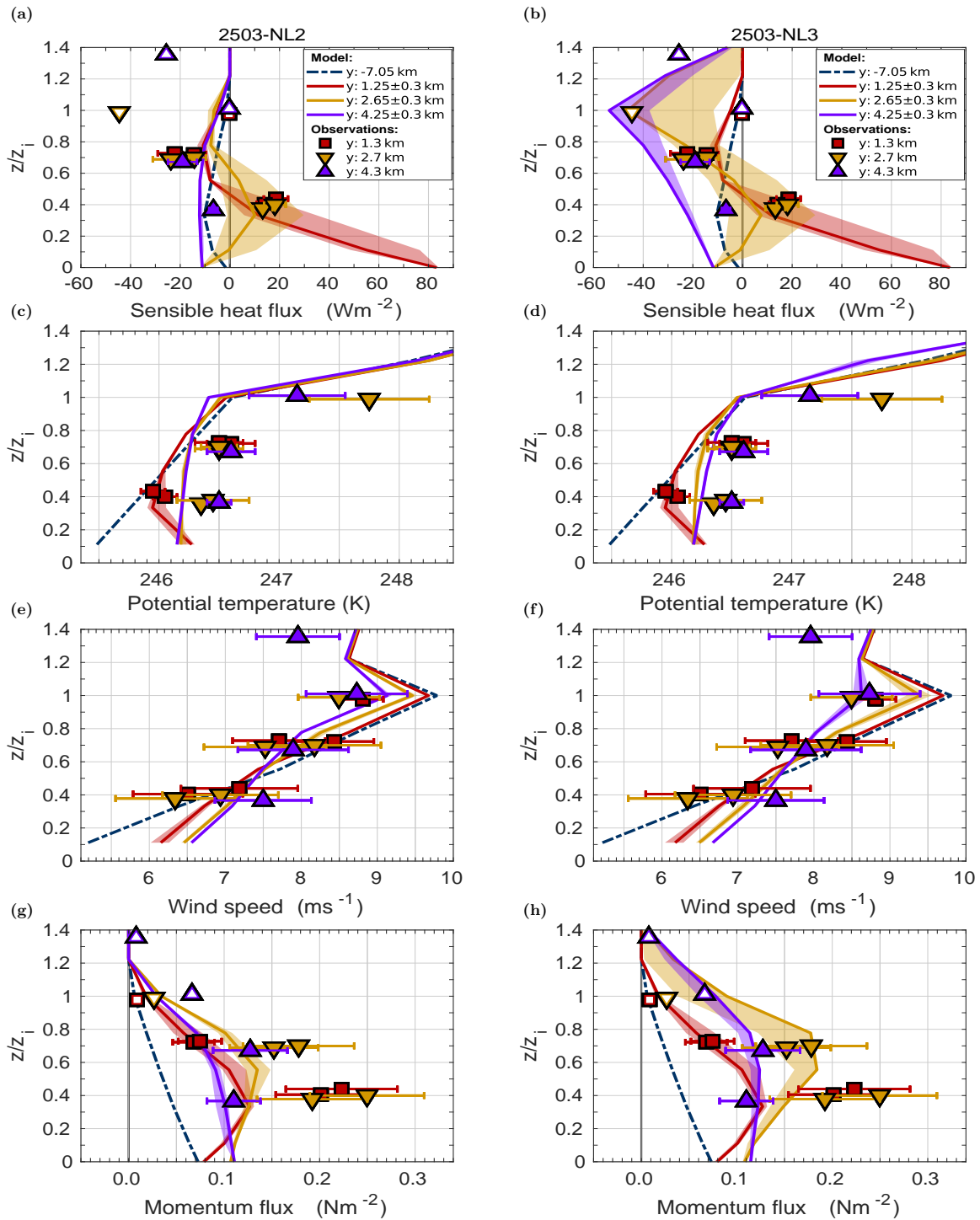


Figure 3.14: Same as Figure 3.7, but runs 2503-NL2 and 2503-NL3 (Table 3.1) for March 25, 2013 are shown. The upwind observed ABL height is $z_i = 90$ m. The lead is located between $y = 0$ km and $y = 2.1$ km. Lines and symbols as explained in Figure 3.4.

$a = 0.75$ and in 2503-NL3 also a y -dependent z_i following the contour method is considered, where $\theta_c = 247.4$ K is set for the potential temperature contour line (see also Table 3.1).

The parameter $a = 0.75$ in the runs 2503-NL2 and 2503-NL3 causes a more inclined plume (Figures 3.13a and 3.13b), which leads to a horizontal shift of the patterns of temperature, wind, and fluxes (Figure 3.13, left column) as compared with run 2503-NL1 where $a = 1.2$.

Using the y -dependent z_i in model run 2503-NL3, basically, causes the same effects as noticed for run 1003-NL2 for March 10 (see section 3.5.3). Due to the much stronger entrainment compared with 2503-MIX, 2503-NL1, and 2503-NL2, observed temperature and wind patterns (see Figure 3.5) are both better represented, except that the observed regeneration of the wind near $y = 15$ km remains underestimated.

For 2503-NL3, there is, obviously, a remarkable improvement for the heat flux in the inversion in the downstream region at $y = 2.7$ km so that entrainment is well captured (Figure 3.14b). The observed upper plume boundary (see Figure 3.5) is also almost exactly reproduced by this simulation due to the monotonic increase of z_i with increasing distance (e.g., Figure 3.13d).

Despite the strong effect on the entrainment fluxes, the temperature profile simulated by 2503-NL3 shows only slight differences compared to the run 2503-NL1, but at least, a slightly improved representation of the observed warming effect is achieved, especially at $y = 4.3$ km (Figure 3.14d). However, the simulated downward flux at that location is much stronger than observed throughout the ABL (Figure 3.14b).

Finally, we obtained another improvement by run 2503-NL3. In the lead's downwind region, the observed decrease of the wind maximum and the observed momentum fluxes are better reproduced than by all other runs for this case (Figures 3.14f and 3.14h).

3.5.5 Model run 2603-NL2

Unlike for March 25, the effects of a lower value for a and a varying z_i are summarised in only one simulation (model run 2603-NL2, Figures 3.15 and 3.16). As expected, the lower value for a causes a stronger inclined plume than in run 2603-NL1 so that it reaches the inversion further downwind at approximately $y = 2.5$ km.

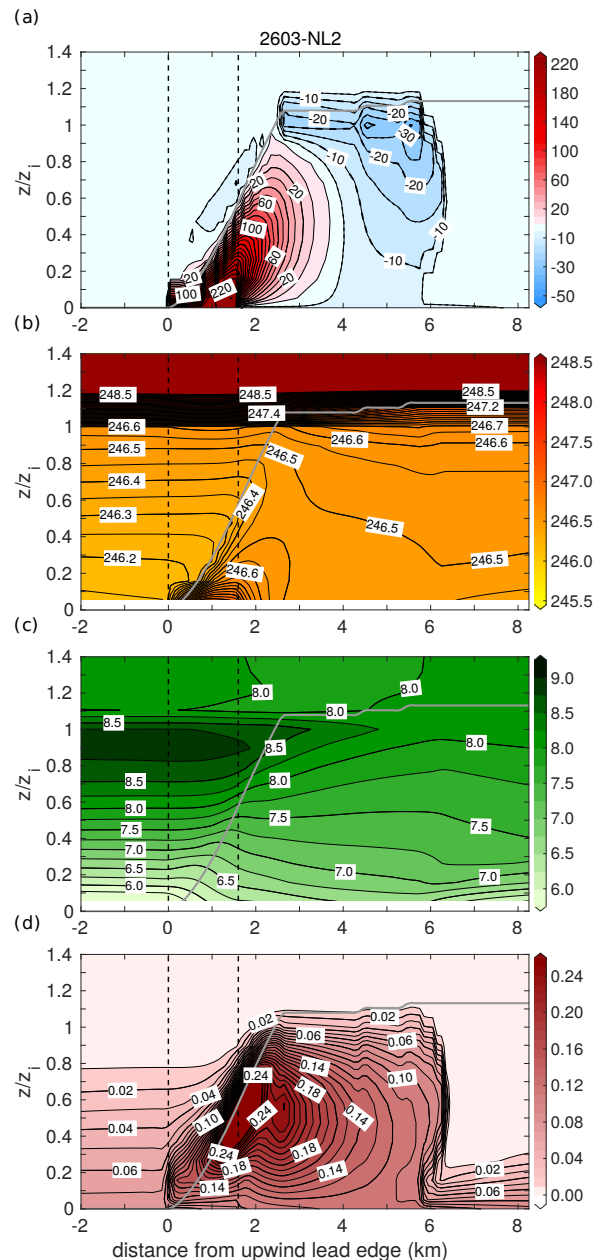


Figure 3.15: Same as Figure 3.8, but for the model run 2603-NL2 (Table 3.1) for March 26, 2013. The upwind observed ABL height is $z_i = 190$ m. Setup of the plots as described in Figures 3.3 and 3.11.

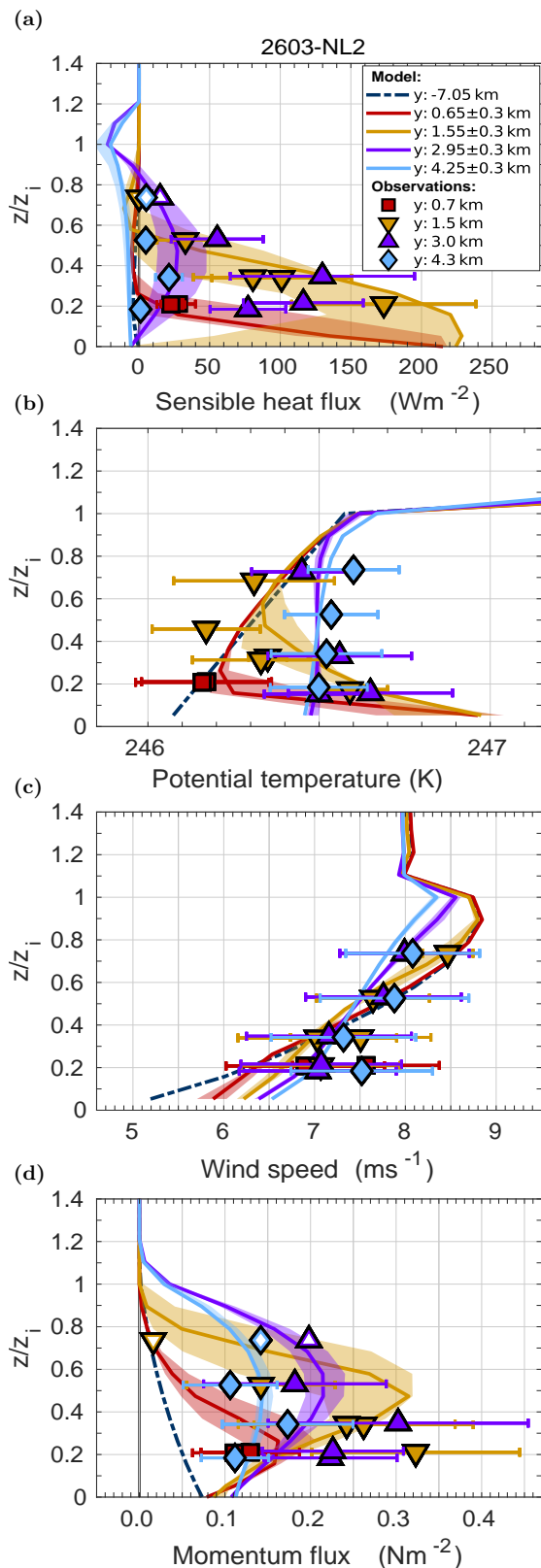


Figure 3.16: Same as Figure 3.9, but run 2603-NL2 (Table 3.1) for March 26, 2013 is shown. The upwind observed ABL height is $z_i = 190$ m. The lead is located between $y = 0$ km and $y = 1.6$ km. Lines and symbols as explained in Figure 3.4.

Due to the varying z_i , entrainment fluxes with a magnitude of about -30 Wm^{-2} are simulated (Figure 3.15a), which cause a stronger ABL warming effect than with run 2603-NL1 (Figure 3.15b). The effects on wind speed and momentum flux distribution due to the increase in ABL thickness (Figures 3.15c and 3.15d) are principally the same as shown for the previous cases.

Compared to the observations, an improvement is obtained by run 2603-NL2 relative to the runs 2603-NL1 and 2603-MIX, especially for the temperature profile above the lead ($y = 0.7$ km) and for profiles of both heat fluxes and temperature near the lead's downwind edge at $y = 1.5$ km (Figures 3.16a and 3.16b). There is also a slight improvement of both the temperature profile at $y = 4.3$ km and the representation of the observed downwind momentum flux profiles (Figure 3.16d). The observed heat fluxes at $y = 3.0$ km and $y = 4.3$ km remain underestimated although a slight improvement is obvious. Regarding the profiles of wind speed, marginal improvements are achieved by run 2603-NL2 (Figure 3.16c).

3.6 Discussion

The airborne observations from STABLE form a valuable data set, which allowed us to compare results of a microscale, non-eddy-resolving model using different turbulence closures with observations over leads in sea ice. Previously, such analyses mainly focused on comparisons with high-resolved LES data for idealised cases (e.g., L08, M20). Thus, for the first time, it was possible to compare modelled and observed convective patterns and ABL structures, and to investigate to which extent observations can be reproduced by microscale modelling.

Our analysis reveals that the basic observed features of the lead-generated convection and its effects on the ABL can be reproduced with both applied closures. The main feature was the

formation of an inclined plume with strongly enhanced fluxes of heat and momentum within the plume. This caused a height dependence of fluxes considerably different to near-linear profiles during convection over homogeneous terrain. However, several results presented point also to some discrepancies between the model results and the observations especially when the observed patterns are most probably strongly influenced by vertical entrainment or by the upwind stratification.

Regarding the advantages of the applied non-local closure as compared to the applied local closure, two consequences can be formulated based on our results. First, the quality of agreement between results obtained with the two different closures is more similar than shown by M20 for their idealised cases (see chapter 2 in this thesis). In principle, this shows that also the results obtained with the applied simple mixing-length closure cannot be completely discarded and that such modelling could be used as a proper rough approximation of (observed) ABL structures over leads.

Second, however, when having a closer look on the detailed patterns, we could show that the local closure has some clear limitations, especially in regions with observed counter-gradient transport or vertical entrainment from the layer above z_i . At least, counter-gradient transport cannot be accounted for in local closures (e.g., L08 and M20), and the parametrization of entrainment would need an additional development for the local closure. The more realistic reproduction of the physical processes over leads related to transport requires a non-local scheme. Moreover, we show that the applied non-local closure can be modified with only little effort regarding entrainment and plume inclination. Thus, especially by including these two effects, we obtained an improved representation of the observed patterns as compared to the non-modified M20 closure and the local closure.

The key parameter for a more realistic inclusion of stable inflow conditions turned out to be the parameter a , which is related to the inclination of the convective plume. The values of a used in section 3.5 point at a dependence of this parameter on the upwind vertical potential temperature gradient $\partial\bar{\theta}/\partial z$. Obviously, a decreases with increasing $\partial\bar{\theta}/\partial z$. The best fit between these two quantities is obtained by

$$a = b_1 + \frac{1}{b_2 \left\{ 1 + \left(\frac{\partial\bar{\theta}}{\partial z} / \left| \left(\frac{\partial\bar{\theta}}{\partial z} \right)_p \right| \right)^{1/3} \right\}}, \quad (3.2)$$

where b_1 , b_2 , and $(\partial\bar{\theta}/\partial z)_p$ are constants. Inserting this formulation into Equation 2.20 (see section 2.5.1), this would result into a $(\partial\bar{\theta}/\partial z)^{-1/2}$ -dependence of the upper IBL height $\delta(y)$. Such a dependence coincides with the formulations of $\delta(y)$ by, for example, Weisman (1976) and Renfrew and King (2000) (see also section 2.8.3 in this thesis). The physical meaning of $(\partial\bar{\theta}/\partial z)_p$ becomes clear from the consideration of the denominator in Equation 3.2. The lower limit for $\partial\bar{\theta}/\partial z$ to obtain a growing plume ($a > 0$) is exactly $(\partial\bar{\theta}/\partial z)_p$. Considering the values derived for a and $\partial\bar{\theta}/\partial z$ in section 3.5.2 and the value $a = 1.2$ for neutral stratification (see section 2.5.1), we obtain $(\partial\bar{\theta}/\partial z)_p \approx -0.63$ and $b_2 \approx 0.55$ (see Figure 3.17). For these values of the constants, the value of $(\partial\bar{\theta}/\partial z)_p$ is approximately -0.41 Km^{-1} . Thus, the parametrization (3.2) does not have any singularity for neutral and stable inflows ($(\partial\bar{\theta}/\partial z) \geq 0$).

Note that the previous formulations of $\delta(y)$ by Weisman (1976) and Renfrew and King (2000) show singularities for neutral conditions (see section 2.8.3). However, we want to stress that the functional relation (3.2) is based only on three values for $\partial\bar{\theta}/\partial z$. Thus, more cases, either observations or LES runs, are needed in the future for a validation. Furthermore, the question arises if an alternative version of the parametrization (3.2) could be derived, for example, based on a dependence of a on the ABL-averaged bulk Richardson number in the inflow region. Further investigation is needed, but our approach can be regarded as a first step, being valid for neutral and stable inflow conditions with a capping inversion.

Simulation results obtained with the non-modified version of the applied non-local closure showed some discrepancies compared with the observations (see section 3.4). We have shown that they can be partly overcome by applying two modifications introduced in sections 3.5.1 and 3.5.2. Despite an improvement in several aspects, some of the observed features still cannot be reproduced. These discrepancies become more obvious by considering another measure to analyse the overall quality of the applied parametrizations. Namely, we compare both simulated and observed warming of the downwind ABL, based on results in Figure 3.18 obtained from low-level horizontal flight sections orthogonal to the leads. Air temperature deviations ΔT from the air temperature at the upwind lead edges ($y = 0$ km) are plotted. Figure 3.18b shows that for March 25, the observed downwind warming effect of approximately 1.2 K is underestimated by approximately 0.8 K in all model runs for that case. This holds also for run 2503-NL3, where we obtained an improved representation of the observed vertical entrainment (see Figure 3.14b), but which seems to improve the modelled downwind ABL temperatures only in the upper ABL close to z_i as compared to the other runs. Thus, perhaps, the observed warming is caused by effects not yet included in the parametrization. Further investigation is needed to show whether this is a unique phenomenon only for this particular case, or if this points at a potential impact of leads in strongly stable environments, in general.

For March 10 and 26, the observed warming effect at the downwind lead edges is well represented by the model simulations, especially by the simulations using the M20 parametrization including the modifications introduced in section 3.5 (run 1003-NL2 for March 10 and run 2603-NL2 for March 26, Figures 3.18a and 3.18c). A discrepancy is shown for the region further downwind, where observed temperatures decreased, while simulated temperatures almost remain constant with increasing distance. This is most probably due to the observed warming of the downwind sea ice surface by the warmer air, which is neglected in our simulations.

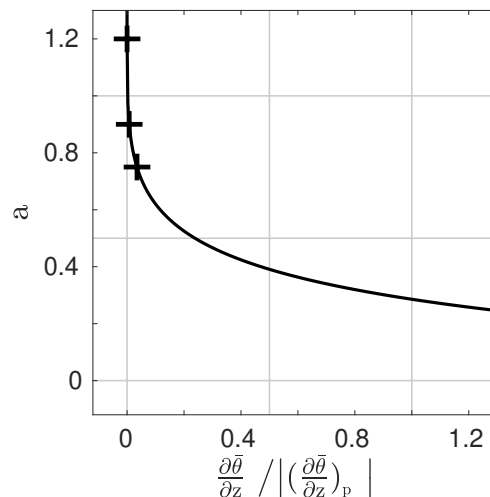


Figure 3.17: Symbols: Parameter a from the M20 parametrization obtained via Equation 3.1 (based on observed values for all open quantities) plotted against $(\partial\bar{\theta}/\partial z) / |(\partial\bar{\theta}/\partial z)_p|$, where $\partial\bar{\theta}/\partial z$ is the upwind observed ABL-averaged vertical potential temperature gradient (see sections 3.2 and 3.5.2 and Table 3.2). Solid curve: Hyperbolic fit with Equation 3.2. The constant $(\partial\bar{\theta}/\partial z)_p \approx -0.41 \text{ Km}^{-1}$ (see text).

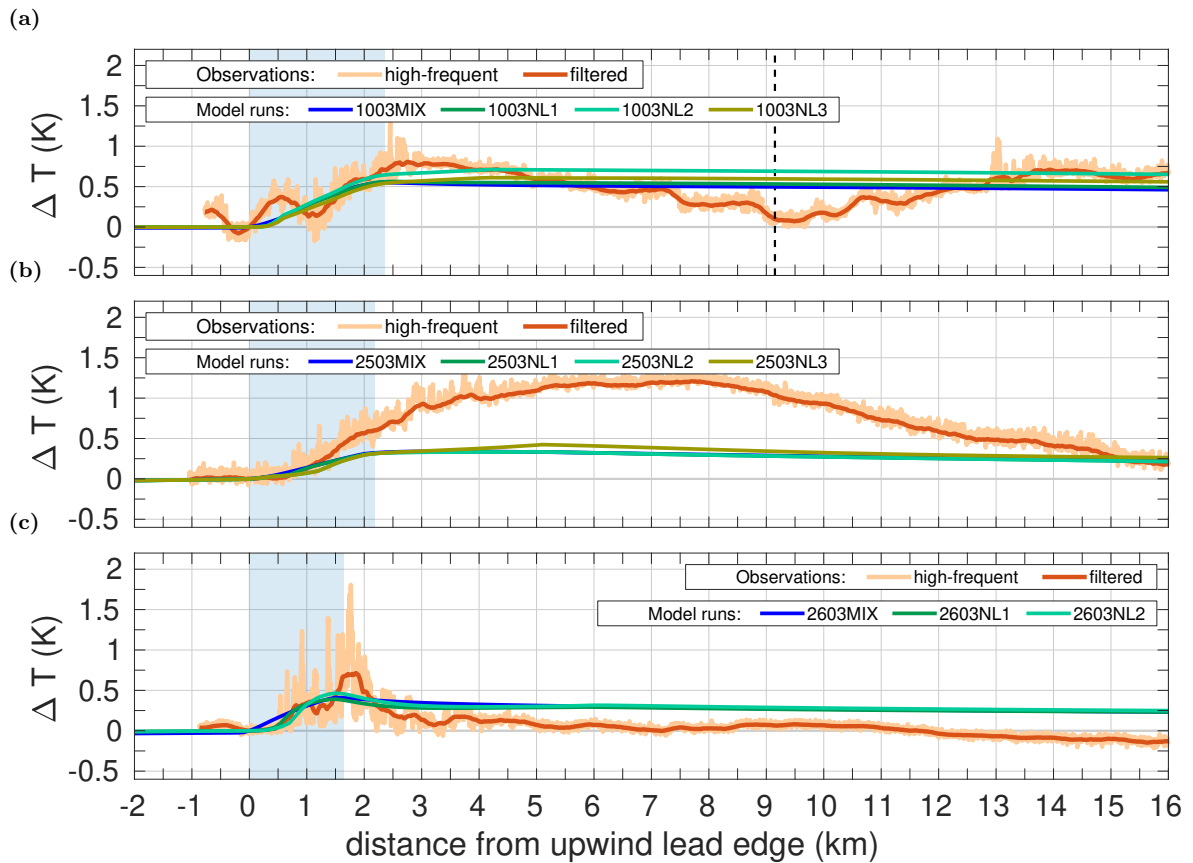


Figure 3.18: Observed and simulated deviation from the upwind lead edge atmospheric temperature, ΔT (K), along distance from the upwind lead edge for March 10, 2013 (a), March 25, 2013 (b) and March 26, 2013 (c). Values are shown for the altitude of the low-level cross-lead flight legs performed on the respective days at 45 m on March 10 and at 35 m on March 25 and 26 (see T15). The observed ΔT is shown in high frequency (light red lines) and as a running mean of approximately 350 m (dark red lines) as also applied by T15 (see their Figure 4c). The other lines refer to the model results of the respective runs (see Table 3.1). The positions of the leads are denoted by the blue-shaded rectangles. In (a), the vertical dashed black line denotes the position of another crack observed on March 10, which is not considered in the corresponding model runs.

There is another drawback raising questions, which could not be solved so far. Namely, the observed regeneration of the LLJ downstream of the leads could not be modelled independent on the used closure. This might be related to the difficulties simulating the observed momentum fluxes, which are partly strongly underestimated by the model. For March 10, this concerns especially the region at the downwind lead edge in the upper half of the ABL and near the inversion layer. Note that for this case the observed wind speed maximum upwind of the lead was located much higher than in the model results, which at least contributed to the deviation in the momentum flux patterns further downwind for that case. For March 25 and 26, the largest deviations between simulated and observed momentum fluxes are found rather in the lower half of the ABL. Regarding the model results obtained with the M20 parametrization, further non-local effects in the momentum transport that are currently not included in the closure might contribute to the deviations. These refer to the inability to simulate maxima in the momentum fluxes on the downstream side of a lead, obtained by LES (see M20 or section 2.6 in this thesis).

We expect that the described drawbacks are of general nature and that they cannot be

overcome by other existing closures such as TKE-based closures. They point to a more fundamental process not included so far. Thus, more measurements are necessary to confirm the existence of this difficulty.

3.7 Conclusions for the study on the cases from STABLE

The main goal of our study was to discuss the quality of microscale, non-eddy-resolving model results obtained with a local and a non-local turbulence parametrization when compared to airborne observations of the convective flow over leads in sea ice. We focused on results obtained with the non-local closure by M20 (see section 2.5.1). It represents a lead-width-dependent approach derived based on LES and designed for idealised conditions of a lead-perpendicular inflow in a near-neutrally stratified ABL capped by a strong inversion. The applied local closure follows a mixing-length approach (see section 2.2.2.2.1).

First, we aimed at identifying advantages of the non-local closure as compared to the simpler local closure. To that aim, we considered three cases from the aircraft measurement campaign STABLE, where convection over leads had been observed over the Arctic MIZ in March 2013. Hence, unlike in previous studies where such analyses were mainly based on comparisons with high-resolved LES data for idealised cases, a comparison of microscale model results with observed convective ABL patterns was possible. The large observational data set includes high-frequent measurements of temperature and wind components, based on which also turbulent fluxes of heat and momentum had been calculated. All cases are characterised by a nearly lead-perpendicular flow in a shallow neutral or stable upwind ABL with a capping inversion at 90 m to 190 m over leads of 1.6 km to 2.3 km width. The surface temperature of the leads, which were mostly completely covered by nilas, ranged from -17.0°C to -5.8°C on average, in one case with large spatial variations. These observations in connection with upwind measured profiles of wind and temperature were used to initialise the model runs. Then, the model results were compared with measurements from above and downwind of the leads.

With both closures, the basic observed patterns caused by the lead-generated convection were reproduced. This includes the formation of inclined plumes with height-dependent fluxes different to typical flux profiles for convection over homogeneous surfaces. Unlike for the idealised cases by M20, here, the overall quality of agreement between the results obtained with the two different closures was more similar. Thus, at first glance, there seems to be no such clear advantage of a non-local closure adapted for the inhomogeneous conditions over leads as compared to a simpler local closure. However, a more realistic reproduction of the transport mechanisms over leads clearly requires a non-local scheme since we showed some substantial limitations of the local closure in regions with observed counter-gradient transport or vertical entrainment.

Second, we investigated the need for further modifications of the M20 parametrization. This was motivated by the underestimation of two observed features, namely, entrainment due to convection penetrating the capping inversion, and a stronger plume inclination as compared to neutral stratification due to more stable inflow conditions. Regarding the first feature, we obtained an improved agreement with the observations by accounting for a varying ABL height as

upper limit for the upper plume boundary $\delta(y)$. An improvement regarding plume inclination was obtained with alternative values for one of the tunable parameters (a) in the M20 parametrization calculated based on the measurements. Furthermore, we postulated a parametrization for the constant a , determining the plume inclination, dependent on the vertical temperature gradient. Its inclusion in the formulation for the upper plume boundary resulted in a similar formulation for $\delta(y)$ as previous parametrizations by other authors. Unlike these previous formulations, the new one is valid for both neutral and stable inflow conditions although further research is necessary including more measurements in future for a validation. Besides that, some of the observed features, especially related to momentum transport, were still not yet reproduced also by model runs using the modified M20 parametrization.

Altogether, after the first two steps were made by L08 and M20, our study provided another step in the development of atmospheric turbulence parametrizations for non-eddy-resolving, small-scale models in a strongly inhomogeneous convective and dry boundary layer. Regarding the used non-local closure, we showed that variations in the ABL height and in upwind stability can be considered. A further development should explicitly include moisture transport and the interaction of a warming downwind ABL with the sea ice surface. A basic agreement with observed ABL patterns was also obtained not only by simulations using the non-local closure but also with a local closure, at least to some extent. Such model applications as used here might be suitable for future sensitivity studies of the large-scale impact of leads at low numerical costs. This might help improving surface flux parametrizations over the MIZ in weather prediction and climate models. All this would certainly help to give a more detailed picture on the quality of different closure schemes applied in non-eddy-resolving model simulations of a strongly inhomogeneous convective environment.

3.8 Atmospheric flow over a lead in the Weddell Sea (Antarctica)

In this section, simulations of another observed case of the flow over a lead shall be examined, where the corresponding measurements had been conducted with an Unmanned Aerial System (UAS) in the ABL over Weddell Sea sea ice in early August 2013. The observations were part of an expedition with the research vessel (RV) *Polarstern*. The observations and some of the model results presented in this section were published under the title "Unmanned Aerial Systems for Investigating the Polar Atmospheric Boundary Layer—Technical Challenges and Examples of Applications" (see Lampert et al., 2020) as an open-access article. The publication is mainly about the presentation of different UAS including discussions of the measurement results obtained with them. For August 2, 2013, the observations were compared with METRAS results obtained with the local mixing-length closure that is presented in section 2.2.2.2.1 in this thesis.³

In this section of the thesis, the content of the corresponding part from Lampert et al. (2020, their section 4.1) is presented with additional information from other parts of the pub-

³I co-authored this paper by performing the corresponding simulations and by comparing modelled and observed ABL characteristics (see also page 137).

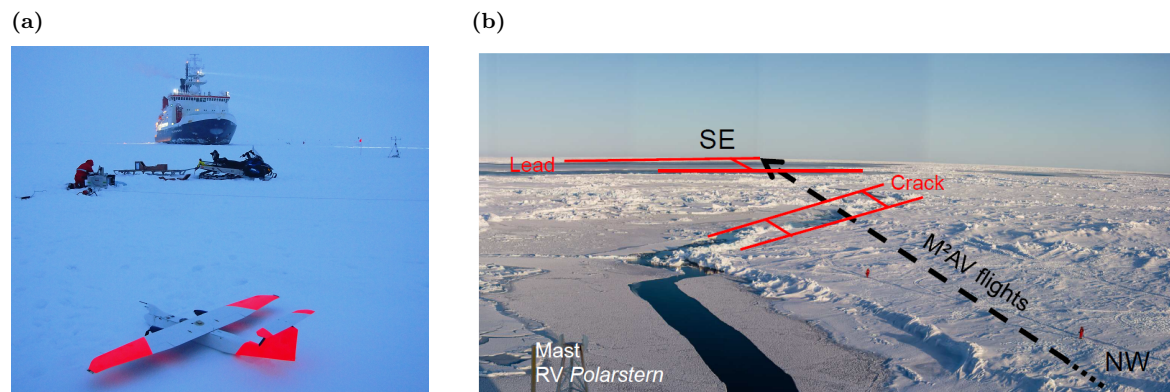


Figure 3.19: (a) The M²AV in front of the RV *Polarstern* in the Weddell Sea on July 11, 2013. Photo: Andreas Scholtz, Technical University Braunschweig. (b) Ice conditions during the ice station of *Polarstern* on August 2, 2013. The flight path of the M²AV is indicated as black dashed line. The locations of open water that were investigated during perpendicular flights are shown in red. Photo: Stefan Hendricks, Alfred-Wegener-Institute. Both (a) and (b) are reprinted from Lampert et al. (2020), their Figures 1 and 13.

lication and supplemented by additional model results using the non-local closure (see section 2.5.1 here). The same goal is pursued as for the analysis shown so far in chapter 3, namely, the validation of microscale model simulation results using airborne observations and the evaluation of turbulence parametrizations.

3.8.1 Observations

The UAS, a fixed-wing aircraft (Meteorological Mini Aerial Vehicle (M²AV)), was applied for measurements during the winter expedition PS81 ANT-XXIX/6 of the RV *Polarstern*, which lasted from June 8 to August 12, 2013. A summary of the whole expedition is given in Lemke (2014). During an ice station of RV *Polarstern* between July 29 and August 2, 2013 in Weddell Sea, the M²AV (shown in Figure 3.19a) was applied for measurements over a lead of width $L \approx 2.1$ km located in a distance of about 4 km to RV *Polarstern*. Note that both position and width of the lead are only based on personal observations since neither a camera system nor a surface temperature sensor were installed on board the M²AV (Lampert et al., 2020). The M²AV was developed at the Institute of Aerospace Engineering of the Technical University Braunschweig in Germany (see, for example, Spiess et al., 2007, for technical details).

On August 2, 2013, lead-perpendicular horizontal flight legs of 2 km to 4.5 km length had been performed with the M²AV at low altitudes (15, 25, 50, 75, and 150 m above sea level, where only observations at 25, 50, and 75 m height are shown in Lampert et al., 2020) with the aim to quantify the effect of the lead-generated convection on the ABL (Lampert et al., 2020). Along the horizontal flight tracks between the upwind lead edge and the ship, another opening in the sea ice cover of approximately 600 m width was present on that day. An overview of the locations of the ship, the crack, and the lead is shown in Figure 3.19b, including the flight direction of the M²AV. Figure 3.19b also shows that no clouds had been observed near the lead at the time of the observations, similar to the cases from STABLE (see section 3.2).

The measurements with the M²AV revealed enhanced turbulent fluctuations of atmospheric temperature and the three wind components with a shifted onset of those fluctuations with

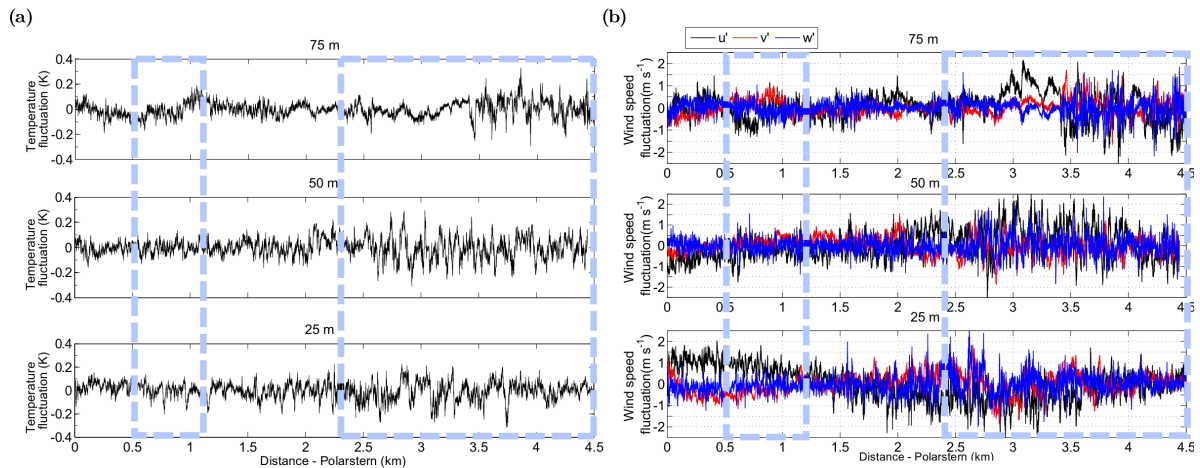


Figure 3.20: Time series of fluctuations during the M²AV flights at 75, 50 and 25 m altitude (from top to bottom). Panel (a) shows temperature and (b) wind speed fluctuations, where the three components of the wind speed vector are defined positive as eastwards (black), northwards (red) and upwards pointing (blue). The parts of the flight track above open water are indicated by light blue boxes, where the position of the lead is between 2.4 km and 4.5 km distance to RV *Polarstern*. Both (a) and (b) are reprinted from Lampert et al. (2020), their Figures 14 and 15.

increasing altitude (Figure 3.20). For the air column above and downwind of the smaller crack closer to the ship, no increase in the temperature fluctuations was observed, at least at the altitudes shown in Figure 3.20. Based on measured vertical wind and temperature, fluxes of heat and momentum were calculated using the eddy covariance method (Lampert et al., 2020).

Approximately two hours before the M²AV measurements, a radiosonde was launched from *Polarstern* at 11:03 UTC to derive the atmospheric conditions in the vicinity of the lead (for the data, see König-Langlo, 2013b). The radiosonde measurements indicated a nearly neutrally stratified ABL below a capping inversion layer between approximately 80 m and 130 m height (see grey circles in Figure 3.21a). The prevailing wind direction was South with an average ABL wind speed of approximately 5.7 ms^{-1} measured at *Polarstern* (see König-Langlo, 2013a) during the M²AV flights. Since the horizontal flight legs were performed from Southeast to Northwest and vice versa, the angle between the wind vector and the lead was approximately 45° .

3.8.2 Model setup

The atmospheric model METRAS is used for simulations of the above-mentioned case observed on August 2, 2013 in the same microscale, 2-D version as described in section 3.3 and in chapter 2 here, including grid spacing, boundary conditions, and assumptions regarding condensation and radiation. Simulations were performed with the local mixing-length closure (see section 2.2.2.2.1) and the M20 parametrization (see section 2.5.1).

Three model runs are investigated in the following, one using the local closure (henceforth run 0208-MIX) and two using the M20 parametrization (runs 0208-NL1 and 0208-NL2), each of them initialised with the same inflow profiles and the same surface values. The inflow temperature profile over ice is derived from the radiosonde data, based on which $T_{s,i} = -23.2^\circ\text{C}$ is prescribed as the sea ice surface temperature upwind and downwind of the lead (see Figure 3.21a). Since the lead surface temperature, $T_{s,l}$, was not measured during the M²AV flights,

only a rough estimate is made for $T_{s,l}$ based on the bulk formula for the surface sensible heat flux $F_{h,s}$ in a neutrally stratified ABL,

$$F_{h,s} = c_p \rho_0 C_{HN,r} U_r (\theta_r - \theta_{s,l}), \quad (3.3)$$

where U_r is the wind speed, θ_r is the potential air temperature, $C_{HN,r}$ is the bulk transfer coefficient for heat at neutral conditions (all of them at a reference height r), and $\theta_{s,l}$ is the potential temperature at the lead surface. An estimate for $C_{HN,r}$ is made with the value applied by Andreas and Murphy (1986) for the transfer coefficient $C_{HN,10}$ and with measured values at 10 m for the reference height r so that we obtain $T_{s,l} \approx -17^\circ\text{C}$, which implies that most probably the lead was covered with nilas. Due to a temperature difference of approximately 6 K between the lead surface and the near-surface air and due to the shallow boundary layer of height $z_i = 80$ m, the conditions on August 2, 2013 were very similar to those observed on March 25, 2013 during STABLE (see section 3.2.2).

The height-independent components of the geostrophic wind in lead-orthogonal and lead-parallel direction are prescribed as 7.9 ms^{-1} and 1.5 ms^{-1} , respectively, to match with the observed ABL wind. For the model runs 0208-NL1 and 0208-NL2, different values are further prescribed for the upstream ABL-averaged wind speed U (used in the M20 parametrization in Equations 2.20, 2.21, 2.22, and 2.24, see section 2.5.1). For the run 0208-NL1, U is set as 6.2 ms^{-1} , which represents the total magnitude of the observed ABL-averaged wind speed. For the run 0208-NL2, U is set as 4.4 ms^{-1} , which represents only the magnitude of the lead-perpendicular wind component. For the surface roughness lengths of sea ice and lead surfaces, the same assumptions are made as explained in section 3.3.1, and the model equations are integrated until quasi-stationarity is reached (after approximately 2 hrs).

3.8.3 Results

The observed lead-averaged sensible heat fluxes show an almost linear flux profile in the mixed layer with almost 30 Wm^{-2} at an altitude of 25 m and with negative fluxes of approximately -8 Wm^{-2} near z_i , which denotes vertical entrainment (Figure 3.21b). Basically, these observations are well represented by all three model runs. The results obtained by the run 0208-MIX agree perfectly with the measurements at 25 m and 50 m, but slightly underestimate the observed negative heat flux at 75 m just below the capping inversion. The results obtained by the runs 0208-NL1 and 0208-NL2 slightly exceed the observed values at 25 m and 50 m, but agree almost perfectly with the observed value at 75 m. Again, this shows that the application of the non-local closure leads to a better representation of observed fluxes and observed vertical entrainment near the inversion than the local one. The marginal differences between the results obtained by the runs 0208-NL1 and 0208-NL2 show that the value of U has only marginal influence on the simulated lead-averaged heat fluxes when the same inflow profiles for the wind components are used. Note that the flights with the M²AV were directed perpendicular and not parallel to the lead, where the latter seems necessary to accurately determine turbulent fluxes over leads (T15).

The observed influence of the lead on ABL temperature and wind is expressed by enhanced turbulent fluctuations (see Figure 3.20). In the microscale model, these fluctuations cannot

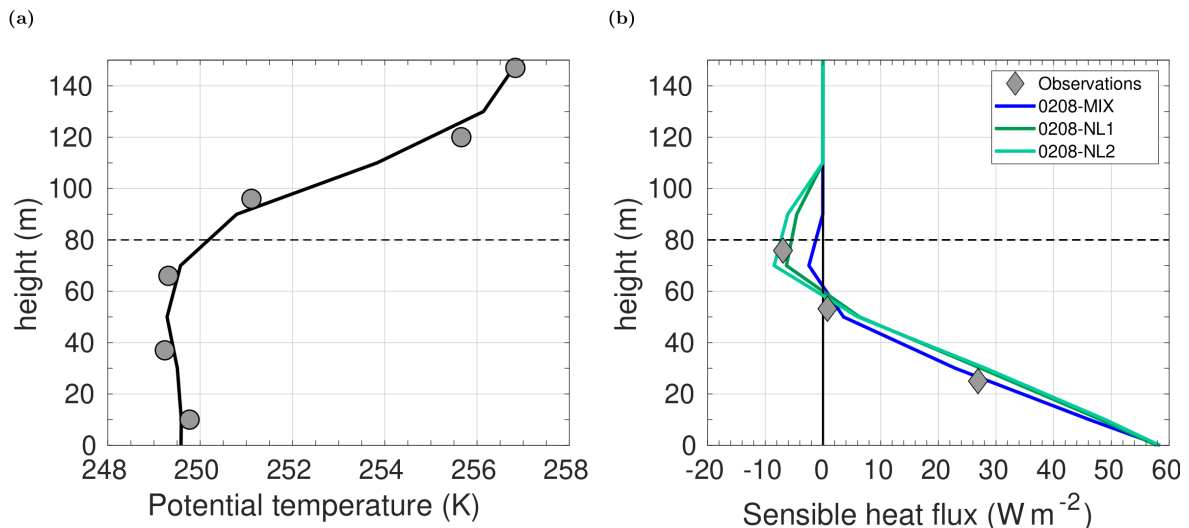


Figure 3.21: Observed and modelled vertical profiles for the area around the lead observed in Weddell Sea on August 2, 2013. (a) Potential temperature (K) measured with the radiosonde near RV *Polarstern* at 11:03 UTC (grey circles, data from König-Langlo, 2013b) and the corresponding inflow profile for the idealised simulations with the non-eddy resolving model METRAS (black line). (b) Lead-averaged sensible heat flux (Wm^{-2}) as measured with the M²AV (grey diamonds) and as simulated by the model runs 0208-MIX, 0208-NL1, and 0208-NL2 (coloured lines). The dashed black line shows the bottom of the capping inversion at $z_i \approx 80$ m. Both (a) and (b) are modified based on Lampert et al. (2020), their Figures 16a and 16c.

be modelled, but an influence due to the lead is obvious as shown in the simulated horizontal development of mean quantities (see Figure 3.22 for air temperature and wind speed obtained by the runs 0208-MIX and 0208-NL2). As Figures 3.22a and 3.22b show, with run 0208-NL2, the lead's effect on temperature, especially at 75 m, is slightly more pronounced than by run 0208-MIX. This is in good agreement with the observed onset of enhanced temperature fluctuations (see Figure 3.20a). The model results obtained at 25 m and 50 m show a modelled ABL warming effect of approximately 0.4 K with slightly higher values obtained by 0208-NL2 than by 0208-MIX. Note, this is similar to the modelled ABL warming as obtained by the model runs for March 25, 2013 from STABLE (see section 3.6). Almost equal simulation results are obtained by both runs regarding the horizontal development of the horizontal wind speed (Figures 3.22c and 3.22d).

3.8.4 Discussion and conclusions of the UAS-study

The implications of the results presented in this section can be summarised in two different aspects. First, also this UAS-study shows the importance of airborne observations in the entire ABL since they represent a valuable data set for comparisons with model results. Moreover, measurements obtained with UAS such as presented here seem to be especially valuable regarding their flight altitude. With these devices, measurements close to the surface can be conducted, which seems necessary for accurately deriving surface fluxes over leads in shallow boundary layers (Lampert et al., 2020). In future, measurements along lead-parallel sections would be very helpful to get a detailed picture of the spatial patterns of the turbulent fluxes over leads and of the lead-generated effects on the downwind ABL.

Second, the overall effects due to the lead on the ABL as well as the observed lead-averaged

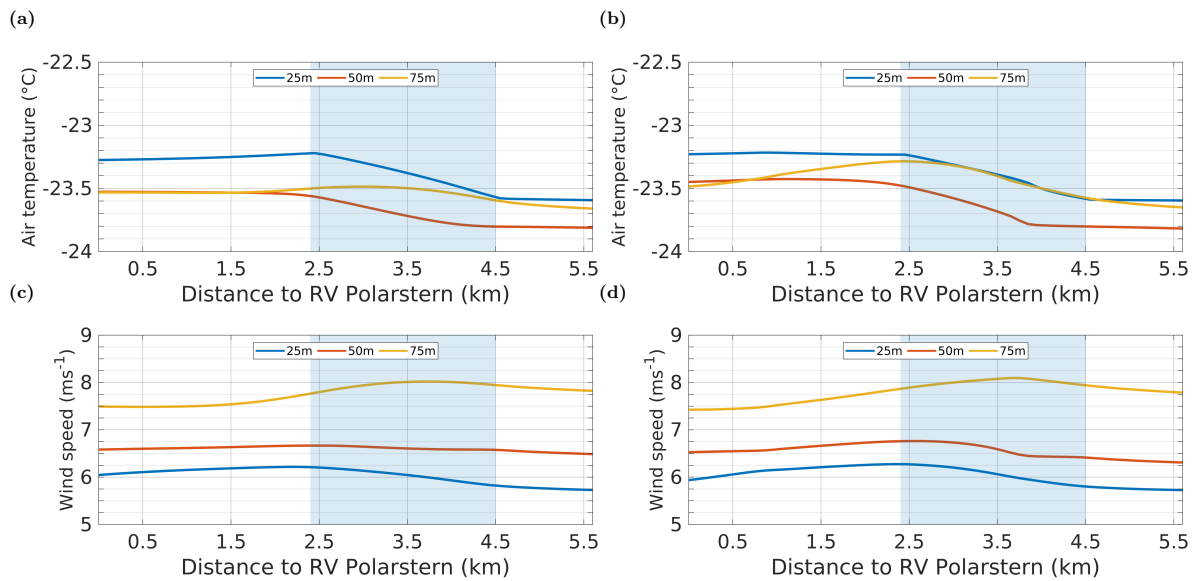


Figure 3.22: Air temperature in °C and horizontal wind speed in ms⁻¹ at different height levels (25 m, 50 m, and 75 m) obtained by the model runs 0208-MIX (left column) and 0208-NL2 (right column) for the ABL flow over the lead observed by the M²AV in Weddell Sea sea ice on August 2, 2013. As in Figure 3.20, the results are shown with respect to the distance to RV *Polarstern* in km (see Figure 3.19b). The flow is from right to left and the position of the lead is denoted by the blue rectangle between 2.4 km and 4.5 km distance. The observed small crack between 0.5 km and 1.1 km distance (see Figure 3.19b) is not considered in the model runs. Panels (a) and (c) are modified based on Lampert et al. (2020), their Figure 17.

heat fluxes were well-represented by the simulations considered here despite the uncertainties in the initial conditions. This holds for both closure schemes used in the small-scale model. Moreover, similar conclusions can be made regarding the quality of the different schemes as noted for the comparison of the cases from STABLE (see section 3.7), where once again the advantage of the non-local closure is shown by the more accurate representation of vertical entrainment; hence, a more realistic representation of the underlying physical processes connected with the lead-generated convection. A more detailed evaluation including observations from downwind of the lead would have helped to better evaluate the quality of the two closure schemes, but here, it was not possible due to the limited number of measured quantities and due to only lead-perpendicular flight legs.

All in all, this UAS-study represents another example of how an observed situation serves as a very useful basis for evaluating model results and how the quality of different parametrizations for microscale atmospheric processes can be performed on a low-cost basis regarding computational time.

4 Modelling of the flow over idealised lead ensemble scenarios

So far, the focus of the thesis was on modelling and parametrizing the atmospheric effects due to a single lead in sea ice. The new turbulence parametrization derived for microscale, non-eddy-resolving models was validated with either LES (chapter 2) or observations (chapter 3). Both LES and the airborne measurements also helped to get a detailed picture of the ABL characteristics over leads. It was clearly shown that atmospheric effects over leads depend not only on the meteorological forcing but also on the lead geometry.

In large-scale models, the microscale effects over leads currently cannot be resolved due to horizontal grid sizes of $\mathcal{O}(10^1 - 10^2)$ km. Moreover, in the polar ocean regions, several leads might occur in an area as large as only a single grid cell of such a model. Therefore, the goal for this chapter is to analyse the atmospheric effects of several leads and of idealised lead ensembles with different lead geometry, and to point at potential implications for large-scale, non-convection-resolving climate models.

4.1 Effects on lead-generated convection due to an upwind neighbouring lead

First, the focus is on the atmospheric effects over two consecutive leads obtained by the microscale, non-eddy-resolving model METRAS compared with corresponding LES results. In chapter 2, the considered model domains consisted of only one lead, except for the cases with leads of width $L = 1$ km. For those cases, a two-leads-domain was considered, mainly to ensure a comparison between the results shown in this thesis with those of L08 (see section 2.2.3). A very good agreement between METRAS and LES results was shown regarding heat flux patterns and temperature distributions (see section 2.5.3) when the new non-local parametrization derived in section 2.5.1 was used.

For the flow over both leads, the agreement among the results of the two models can also be visualised using domain-averaged vertical profiles, where the model results are averaged over a region of the same length in flow direction and of the same mean SIC. In Figure 4.1, such profiles of heat flux and potential temperature are shown for case L1c-U5 (see Table 2.1 in chapter 2) as obtained with LES and with METRAS using the M20 parametrization in the version shown in section 2.5.1 (model run M20), supplemented by METRAS results obtained with the mixing-length closure as explained in section 2.2.2.2.1 (model run MIX). As illustrated in Figure 4.1a, for the considered North-South directed flow, the profiles are averaged along the distance y between the upwind lead edge of the northern lead at $y = 0$ km and $y = 18$ km, which is 6 km downwind of the southern lead and marks the position of the outflow boundary of the LES model (see Figure B7 in Appendix B). The corresponding mean SIC for this area is approximately 89%.

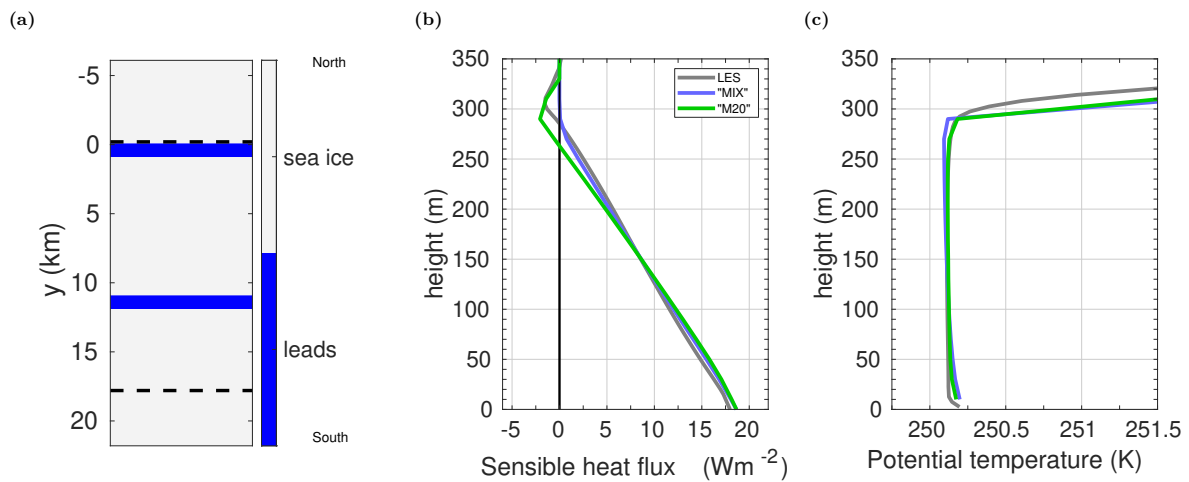


Figure 4.1: (a) Model domain of the idealised case L1c-U5 (see Table 2.1 in chapter 2) with two leads of 1 km width and 10 km distance to each other. The flow is from North to South (y : distance to the upwind lead edge of the northern lead) and model results of the area inside the dashed black lines were used to obtain the domain-averaged vertical profiles shown in (b) for the sensible heat flux and in (c) for the potential temperature with the LES model ("LES") as well as with METRAS using the local closure from section 2.2.2.2.1 ("MIX") or the new non-local closure from section 2.5.1 ("M20"). Domain-averaged profiles are obtained for a region of approximately 89% SIC on average.

The resulting area-averaged heat flux profile obtained by run M20 agrees well with the LES profile below $z \approx 200$ m (Figure 4.1b). A slight discrepancy is shown for the region between $z \approx 200$ m and $z \approx 330$ m, where slightly higher mean fluxes are obtained with LES. Nevertheless, the rate of vertical entrainment (i.e., of negative heat fluxes close to the inversion) as simulated with the LES is well hit by the run M20, where the minimum in the flux profile occurs slightly below the corresponding position in the LES result. A good agreement with LES is also obtained by run MIX, but vertical entrainment is completely missing. This also contributes to a slight decrease of the potential temperature with height. Thus, unstable stratification in the entire ABL is obtained on average with the local closure (see Figure 4.1c). This result differs from the corresponding LES result, which shows a neutrally stratified ABL on average. The LES result is almost perfectly reproduced by run M20 and the remaining differences mainly concern the bottom and the top of the ABL. These domain-averaged profiles underline the good agreement between the results of METRAS using the M20 parametrization and LES results also for the flow over two consecutive leads of 1 km width.

Next, a similar situation is investigated for a domain consisting of wider leads, namely, for a domain with two leads of width $L = 5$ km (Figure 4.2a) for the idealised case L5c-U5 (see Table 2.1 in chapter 2). As for the domain with two 1 km-wide leads, also for this domain, the two leads are located in a distance of 10 km to each other, which ensures that the convective plume emanating from the first lead does not reach the lead further downwind. The corresponding domain-averaged profiles are obtained for the area between the upwind edge of the northern lead at $y = 0$ km and 10 km downwind of the southern lead. The corresponding mean SIC for this area is approximately 67%, which is why the domain-averaged heat fluxes are, basically, larger than for the 1 km-case (compare Figure 4.2b and Figure 4.1b).

For the two-leads-domain of case L5c-U5, METRAS results obtained with the local closure (model run MIX) and with the M20 parametrization (model run M20) tend to overestimate the

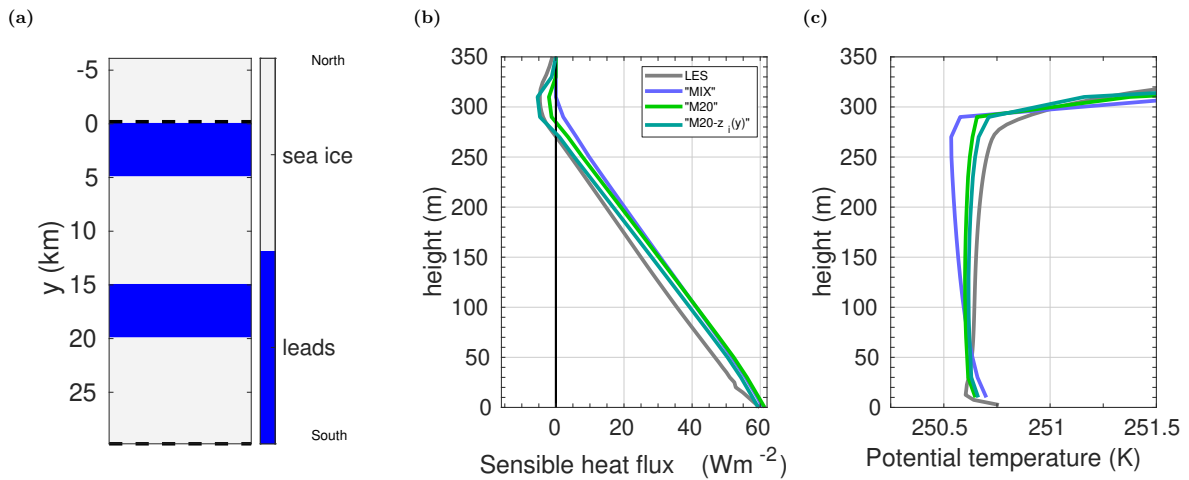


Figure 4.2: Same as Figure 4.1, but for a two-leads-domain of the idealised case L5c-U5 (see Table 2.1 in chapter 2). In (b, c), additional profiles are shown for a simulation obtained with METRAS using the M20 parametrization (see section 2.5.1), but with a varying ABL height as derived in section 3.5.1 ("M20- $z_i(y)$ "). The domain-averaged profiles are obtained for a region of approximately 67 % mean SIC.

fluxes obtained by LES, where the deviation is largest for the run MIX (Figures 4.2b and 4.2c). With the M20 parametrization, an improved representation of the LES profile is obtained, mainly in the upper half of the ABL and near $z = 300$ m due to small vertical entrainment. However, this is also less pronounced than with LES. Hence, unlike for case L1c-U5, for the case L5c-U5, an additional simulation is considered here using the M20 parametrization with the modification of a y -dependent ABL height z_i as derived in section 3.5.1 (model run M20- $z_i(y)$). With this modification, the resulting domain-averaged heat flux profile agrees almost perfectly with the LES result between approximately 230 m and 330 m height (Figure 4.2b). For the heat fluxes in the lower half of the ABL, only a slight improvement is obtained as compared to the results of the runs MIX and M20.

For the domain-averaged potential temperature profiles (Figure 4.2c), a slightly worse representation of the LES profiles is obtained by the METRAS results than for the 1 km-case. Nevertheless, also for the 5 km-case, the advantage of the non-local parametrization as compared to the local closure is obvious. With LES, a slightly stable ABL is obtained on average above the surface layer, which is slightly underestimated but, basically, represented by the model runs M20 and M20- $z_i(y)$. As for the heat flux profiles, also regarding the temperature profiles, the best agreement with the LES result is obtained by run M20- $z_i(y)$. With run MIX, rather an unstable ABL is obtained on average, which clearly contradicts the LES result.

As shown in Figure 4.3, the improvement obtained with the model run M20- $z_i(y)$ for the 5 km-case is obvious also in terms of vertical cross-sections of heat flux and potential temperature over the southern 5 km-wide lead. Compared to the LES result (Figures 4.3a and 4.3b), entrainment and downwind stability are underestimated by the METRAS runs MIX (Figures 4.3c and 4.3d) and M20 (Figures 4.3e and 4.3f), but much better captured by the run M20- $z_i(y)$ (Figures 4.3g and 4.3h).

To summarise, with the help of LES, it was possible to validate microscale model results also for the flow over two consecutive leads. The corresponding analysis shows that the LES results are well represented by the microscale model also for such cases when the new non-local closure

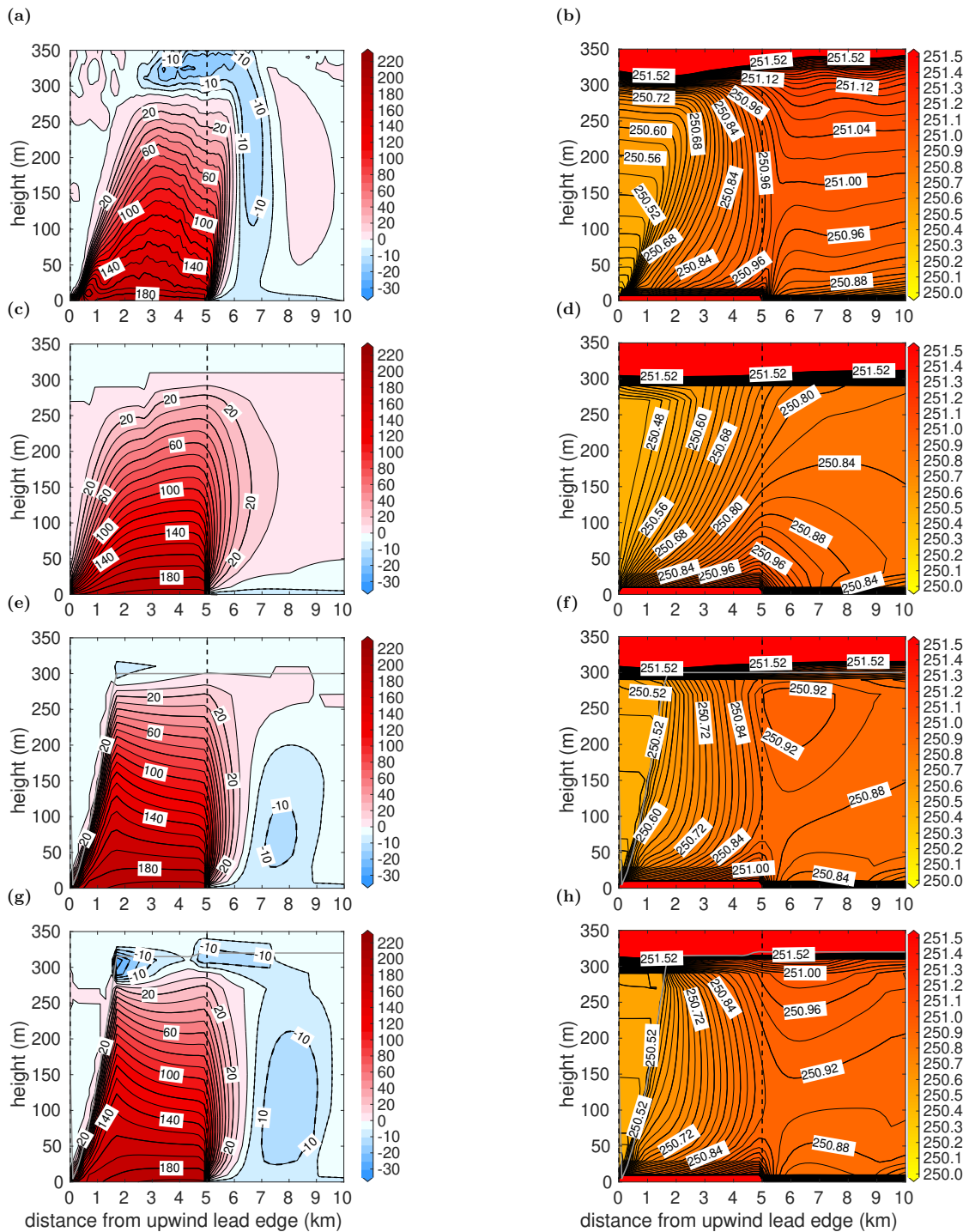


Figure 4.3: Vertical cross-sections in lead-perpendicular direction of sensible heat flux in Wm^{-2} (left column) and potential temperature in K (right column) for the flow over the southern lead (here: from left to right) of the domain shown in Figure 4.2a as obtained by LES (a, b), as well as by METRAS with the simulations MIX (c, d), M20 (e, f), and M20- $z_i(y)$ (g, h) (see text). The spacing between heat flux contour lines is 5Wm^{-2} for negative fluxes (dashed contour lines in panels a, c, e, and g). The solid grey lines show the upper IBL height according to Equation 2.20 in chapter 2 (see panels e, f, g, and h).

is used. Based on the domain-averaged profiles shown in this section, quantitatively, differences in the microscale results obtained with the different closure schemes are rather small. However, qualitatively, the results obtained with a local closure are partly fundamentally different to the

LES result, especially regarding the average ABL stratification. The analysis in the following section will point at a potential relevance of this outcome for larger ensembles of leads.

4.2 Potential implications of small-scale lead effects in non-convection-resolving models

Motivated by the good agreement between domain-averaged profiles obtained with METRAS and LES, in the following, METRAS is applied to investigate the integral effects of leads and lead ensembles. To this aim, five different cases are considered, where each of the corresponding domains is of the same length in the lead-perpendicular flow direction (105 km) and consists of the same average SIC (approximately 91 %). However, the distribution of sea ice and open water differs from case to case. Hence, potential differences in the domain-averaged vertical ABL profiles between the cases could then be linked to an influence of the leads and their width. This would imply a certain relevance of subgrid-scale sea ice characteristics including the corresponding open-water distribution in typical large-scale, non-convection-resolving models. Note, this has already been supposed by other authors based on their results, for example, by Grötzner et al. (1996); Flato and Ramsden (1997); Marcq and Weiss (2012); Batrak and Müller (2018); Wenta and Herman (2018). Moreover, an influence of the lead width on domain-averaged vertical profiles can be expected based on lead-width-dependent surface heat fluxes as found by, for example, Alam and Curry (1997) and Andreas and Cash (1999) based on a large number of in situ observations. The regional contribution of leads to microscale ABL patterns, such as a shallow stable IBL over sea ice as a consequence of the heat input by leads, has also already been emphasised (e.g., Pinto et al., 2003; Lüpkes, Vihma, et al., 2008; Chechin et al., 2019). The model runs considered in this section partly follow Lüpkes (2010), who considered similar simulations but with preliminary versions of the parametrizations. Similar to that study, the domain sizes used here are equal to a few grid cells of a large-scale climate model.

Three goals are pursued in this section. First, the effects related to the above-mentioned different distributions of open water and sea ice should be quantified using microscale model results. The second goal is to investigate potential differences among the microscale model results related to the applied turbulence parametrization. Moreover, as shown in the previous two chapters of this thesis, it is important to evaluate those results always in the context of comparable LES results or observations. The third goal is to discuss potential implications for large-scale, non-convection-resolving models.

4.2.1 Scenarios and methods

Five different cases of the flow over lead ensembles are considered (see Figure 4.4). Four of the model domains contain leads surrounded by 100 % sea ice cover. These cases differ by the width of the leads and their distance to each other (cases ENS-1km, ENS-2km, ENS-5km, and ENS-10km, see Figure 4.4). As in the previous sections, the horizontal grid spacing of METRAS is 200 m in lead-perpendicular direction for those cases. The fifth model domain is considered as representative for a few grid cells of a climate model (case ENS-C, see Figure 4.4), where the horizontal grid spacing is 35 km (in the range of today's typical regional climate models,

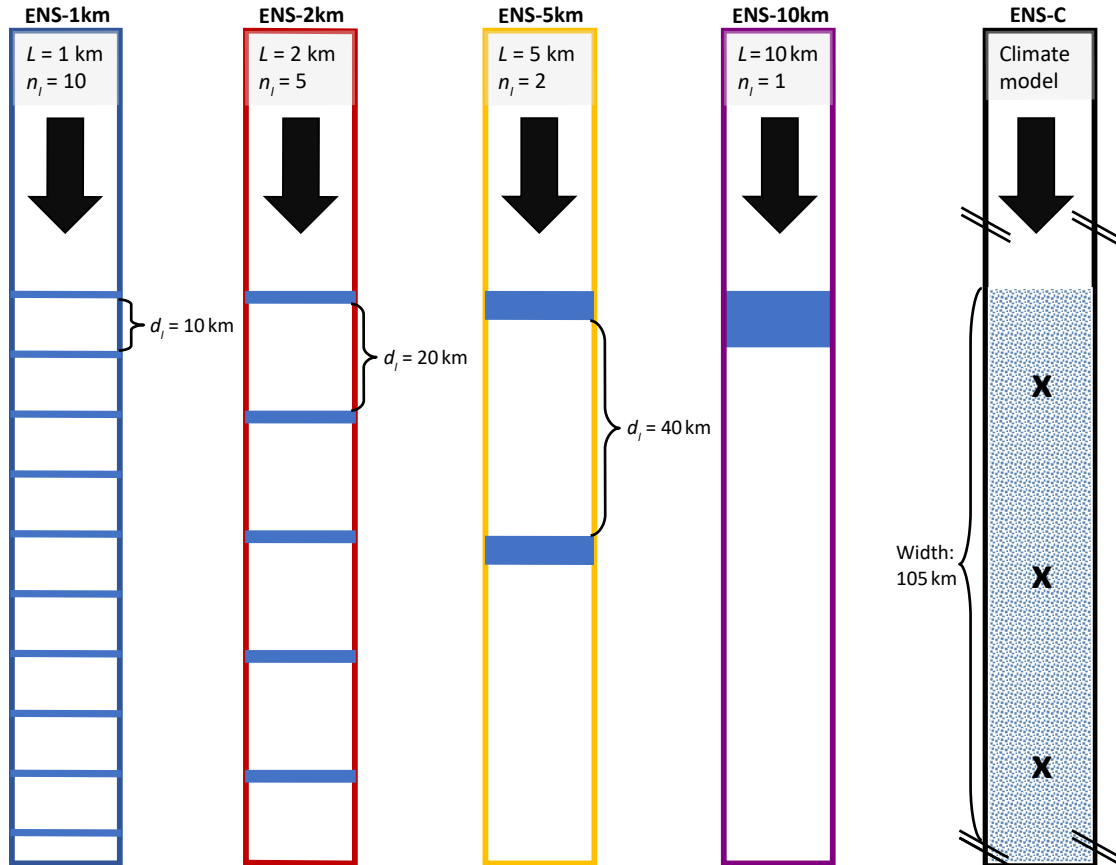


Figure 4.4: Sketch of different model domains representing the five different cases ENS-1km, ENS-2km, ENS-5km, ENS-10km, and ENS-C used for the sensitivity study in section 4.2. The domains consist of 100 % sea ice (white areas), open water (blue rectangles), or a fractional sea ice concentration of 91 % (mosaic area, only in case ENS-C). In the first four cases, L represents the lead width, n_l the number of leads, and d_l the distance between two consecutive leads, and the length of the inflow region over closed sea ice is 50 km. For simulations of these four cases, a horizontal grid spacing of 200m in lead-perpendicular direction is used. Case ENS-C represents a few grid cells of a regional climate model, where the crosses denote the grid point positions in a distance of 35 km to each other in flow direction. The length of the inflow region over closed sea ice is 385 km (see text). Averaged over a region of 105 km width starting from the downwind edges of the inflow regions, all five domains consist of 91 % sea ice concentration. The different cases are distinguished by colour, which is also used to distinguish the corresponding simulation results in the subsequent figures in this section and in Appendix C. A lead-perpendicular flow in the ABL from North to South is considered (black arrows).

see, for example, Flato et al., 2013). For case ENS-C, also an inflow region over 100 % sea ice cover is considered. However, unlike the other four cases, further downwind, the model domain consists of grid cells each of them with a continuous fractional SIC of 91 % on average instead of grid cells consisting of 100 % water or sea ice. The corresponding SIC averaged over an area as wide as the three grid cells of the large-scale model (105 km) is the same in the four lead cases, which ensures comparability of the domain-averaged profiles.

All model simulations for the cases ENS-1km, ENS-2km, ENS-5km, and ENS-10km are performed with the same version of METRAS as used for the idealised lead scenarios in this thesis (see section 2.2.2.1). Basically, this applies also for the case ENS-C. However, the calculation of the subgrid-scale turbulent surface fluxes, more precisely, of the scaling parameters u_* and θ_* ,

differs compared to the cases with explicitly prescribed leads. For simulations of case ENS-C, a flux-averaging method using the concept of the blending height is applied (see, for example, von Salzen et al., 1996). For a more detailed explanation of its implementation in METRAS, see Schlünzen, Flagg, et al. (2012).

Different turbulence parametrizations are applied for the four different cases with explicitly prescribed leads, the local closure as described in section 2.2.2.2.1 and the M20 parametrization in the version described in section 2.5.1. Additional simulations were performed with the M20 parametrization including the varying ABL height as derived in section 3.5.1. As in section 4.1, the corresponding simulations are henceforth abbreviated by "MIX", "M20", and "M20- $z_i(y)$ ". For case ENS-C, only one simulation was performed using the local closure, which is considered as representative for a traditional closure used in large-scale, non-convection-resolving models (henceforth abbreviated by "C(MIX)" and also referred to as climate run). In all simulations, the maximum mixing-length l_{max} is assumed to be equal to 15 % of the ABL height $z_i = 300$ m (see Equations 2.3 and 2.4 in chapter 2).

All model runs analysed in this section are initialised with the same inflow profiles of wind and temperature equivalent to those used for the idealised simulations of the cases with $u_g = 5 \text{ ms}^{-1}$ (see Table 2.1 in chapter 2). It is ensured that the domain-averaged profiles are not influenced by the inflow profiles (not shown). Surface temperatures and surface roughness lengths for sea ice and open water are the same as used in, for example, case L5c-U5 (see section 2.2.3). The same values are also prescribed for case ENS-C. A model integration time of 10 hrs is used for simulations of the four lead cases, which corresponds to the time where quasi-stationarity is reached. For the simulation of case ENS-C, a model integration time of 2 days is required to reach quasi-stationarity due to the extended inflow region over closed sea ice as compared to the lead cases. This extension is required to ensure a sufficiently turbulent inflow upwind of the region with fractional sea ice cover.

4.2.2 Results

First, vertical cross-sections of potential temperature and horizontal wind speed are shown for the simulation C(MIX) of the case ENS-C. Second, the horizontal evolution of four different ABL quantities is shown for two height levels. Third, domain-averaged profiles are shown similar as in section 4.1.

4.2.2.1 Vertical cross-sections for case ENS-C

Vertical cross-sections of the model run C(MIX) are shown in Figures 4.5a and 4.5b for the potential temperature and the horizontal wind speed, respectively. As expected, with increasing distance over the fractionally ice-covered region, the potential temperature continuously increases (Figure 4.5a). Compared to the ABL temperature of 250 K in the inflow region, the potential temperature increases by approximately 0.65 K over a distance of 105 km. Over the whole region of fractional sea ice cover, a neutral or slightly unstable ABL is obtained. Especially in the lower third of the ABL, the stratification becomes more and more unstable with increasing distance.

The horizontal wind speed pattern of case ENS-C shows a pronounced wind speed maxi-

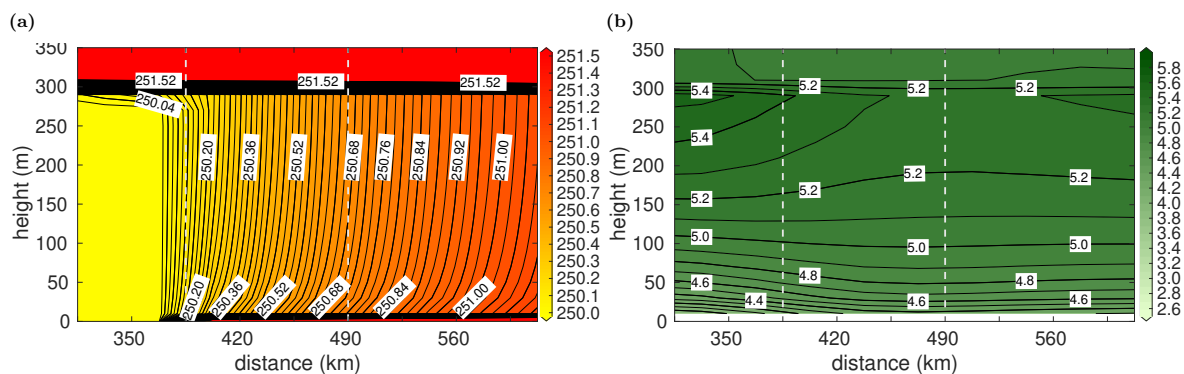


Figure 4.5: Vertical cross-sections of potential temperature in K (a) and horizontal wind speed in ms^{-1} (b) for the ABL flow (from left to right) simulated by the model run C(MIX) for the case ENS-C (see Figure 4.4). The area between the vertical dashed white lines denotes the region for which domain-averaged profiles are calculated (see Figures 4.8 and 4.9). The region with a fractional sea ice concentration of 91 % in each grid cell starts at a distance of 385 km. Further upwind, each grid cell consists of 100 % sea ice cover.

imum just below z_i close to 350 km distance, which exceeds the ABL-averaged wind speed by approximately 10 % (Figure 4.5b). Hence, a wind speed maximum is obtained near the downwind edge of the closed sea ice cover just at the transition to the region of fractional sea ice cover. Further downwind, the wind maximum in the upper ABL weakens over a distance of almost 200 km, which is most probably due to enhanced vertical mixing over the region of fractional sea ice (Figure 4.5b). Starting at a distance of approximately 560 km, a regeneration of the maximum is denoted. It is remarkable that the wind speed pattern obtained with the large-scale simulation for case ENS-C has a similar structure as the small-scale patterns obtained for the flow over single leads (see chapters 2 and 3). This points to some kind of self-similarity and could be further investigated in a future study.

4.2.2.2 Horizontal developments of different ABL quantities

Figure 4.6 shows the horizontal development of four different quantities for the top of the surface layer at $z = 10$ m. The simulations M20 are used for the four lead cases and the simulation C(MIX) for case ENS-C. In the development of all quantities at that height level, the effects of the different lead patterns are obvious. Sensible heat fluxes of up to 190 Wm^{-2} are obtained over the lead surfaces, slightly negative fluxes further downwind near the downwind lead edges, followed by fluxes close to zero (Figure 4.6a). In the cases ENS-1km, ENS-2km, and ENS-5km, the maximum sensible heat fluxes over the lead surfaces decrease with increasing lead number due to the decreasing temperature difference between the lead surfaces and the near-surface airflow with increasing distance. For the case ENS-C, the average heat flux in each of the three grid cells shown is between 10 Wm^{-2} and 20 Wm^{-2} , where also in this case, the fluxes slightly decrease with increasing distance.

The potential temperature at $z = 10$ m increases with increasing distance in all cases (Figure 4.6b), and also here, the influence of the leads is clearly visible. Furthermore, different temperature patterns are obvious for wide and narrow leads. Especially in the cases ENS-10km and ENS-5km (which correspond to wide lead cases, see Table 2.1 in chapter 2), a strong

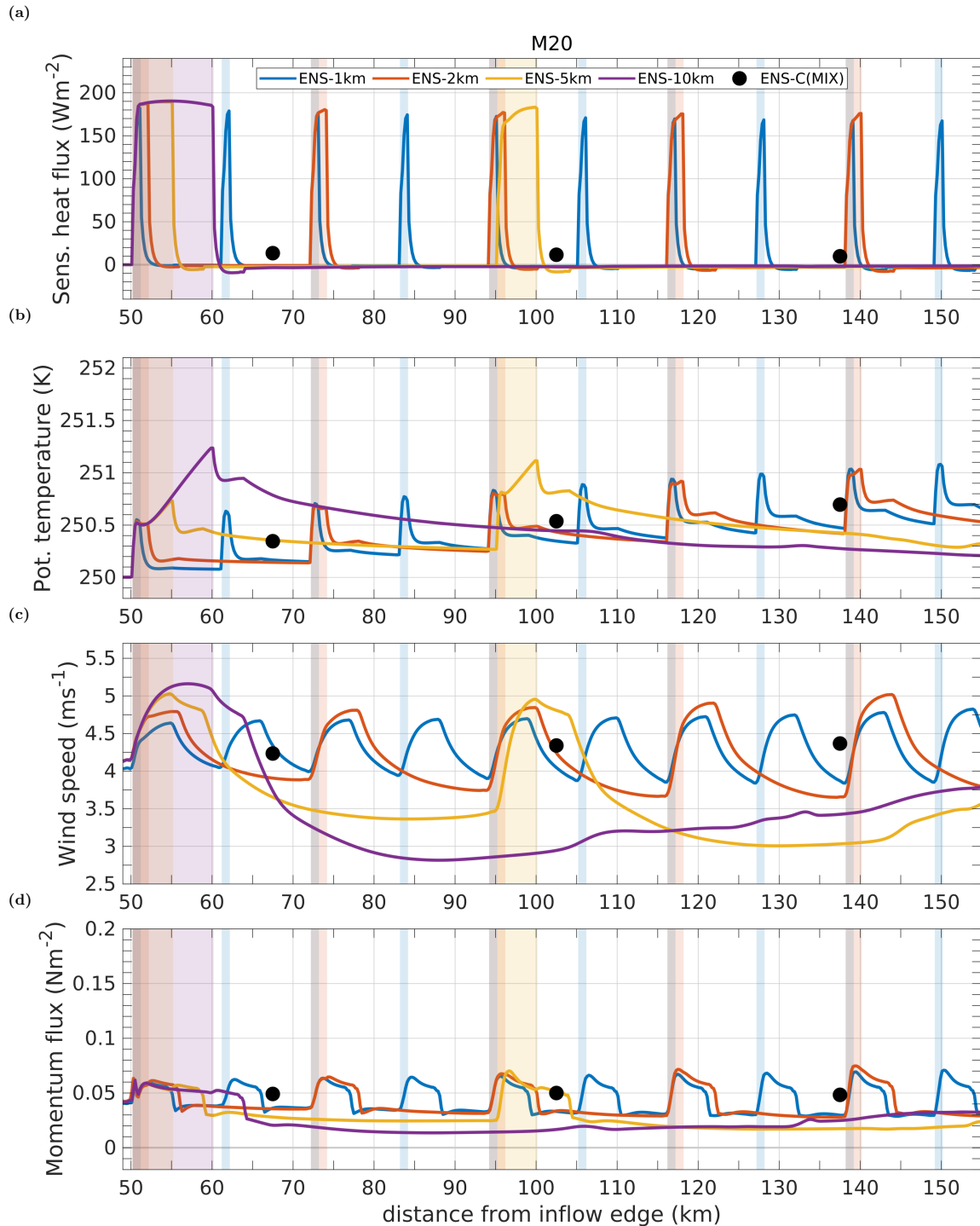


Figure 4.6: Horizontal development of four different quantities at height $z = 10$ m as a function of distance obtained with METRAS using the M20 parametrization (see section 2.5.1) for the four lead cases ENS-1km, ENS-2km, ENS-5km, and ENS-10km and by the simulation C(MIX) for the case ENS-C (see Figure 4.4 for the cases). The coloured rectangles denote the positions of the leads. The flow is from left (North) to right (South).

increase in potential temperature is obtained over the first kilometre, followed by a less strong increase towards the downwind lead edges. An influence of the lead width on the temperature distribution over the domain can also be derived from this figure. For example, while for case

ENS-10km, a near-surface potential temperature of approximately 251.3 K is obtained at the downwind edge of the single lead, lower values are obtained for the other three lead cases at the downwind edges of the respective southernmost leads. Regarding case ENS-C, as expected from Figure 4.5a, the potential temperature monotonically increases with increasing distance y .

The development of the horizontal wind speeds reveals two basic features (Figure 4.6c). First, the wind speed increases over the leads in all cases, but the position of the maximum wind speed differs with respect to the lead width. While for case ENS-1km, maximum wind speeds are obtained approximately 5 km downwind of the corresponding leads, for the cases ENS-5km and ENS-10km, the maxima are obtained rather directly at the corresponding downwind lead edges. Second, with increasing lead width, the wind speed minimum in the downwind region of the respective leads becomes more pronounced. This indicates that the stability of the stable IBL over the downwind sea ice (see chapter 1) increases with increasing lead width. Moreover, for case ENS-10km, a slightly inhomogeneous wind speed development is obtained over the downwind region starting at approximately 55 km distance to the upwind lead edge, which denotes weak gravity waves in the strengthening stable IBL.

Pronounced maxima over the leads are obtained also for the near-surface momentum fluxes (Figure 4.6d). In the cases ENS-1km, ENS-2km, and ENS-5km, these maxima become slightly more pronounced with increasing distance and, thus, increasing lead number. Averaged over the whole region, slightly higher fluxes are obtained for the case ENS-C than for the lead cases. This difference to case ENS-C is largest for the cases ENS-5km and ENS-10km.

In Figure 4.7, similar results as in Figure 4.6 are shown, but for a height of $z = 290$ m, which is close to the top of the upwind ABL at 300 m. The heat flux patterns of the four lead cases clearly show vertical entrainment up to -45 Wm^{-2} above the leads or close to the lead's downwind edges over the downwind sea ice (Figures 4.7a). In contrast, the simulation for case ENS-C does not show any vertical entrainment.

An influence of the lead width is obvious also on upper ABL temperatures (Figure 4.7b), not only downwind but also upwind of the leads. Obviously, the subsidence close to the ABL's top upwind of the northernmost leads becomes more pronounced with increasing lead width so that the corresponding temperatures slightly differ. Note, this subsidence has been obtained also in the simulations of the corresponding single-lead cases with both LES and METRAS (see chapter 2). Further downwind, the effect of the leads on the upper ABL temperature is shown by consistently larger values in the lead cases than in the case ENS-C. The temperature difference to case ENS-C is most pronounced for the cases ENS-5km and ENS-10km.

An impact of leads and their width is also obvious in the modelled horizontal wind speed at $z = 290$ m (Figure 4.7c). On average, the results obtained for the case ENS-C agree best with those for ENS-5km and ENS-10km, but for the cases ENS-1km and ENS-2km, the mean wind speeds are consistently higher than for case ENS-C. In the development of the vertical momentum fluxes (Figure 4.7d), differences between all cases are not much pronounced and the fluxes are almost constantly close to zero.

In Appendix C, additional figures similar to Figures 4.6 and 4.7 are shown (Figures C1 to C4). For Figures C1 and C2, the M20 parametrization with a varying ABL height $z_i(y)$ as derived in section 3.5.1 was used for simulations of the four lead cases (model runs M20- $z_i(y)$). For Figures C3 and C4, the local closure was used for simulations of all cases (model runs MIX).

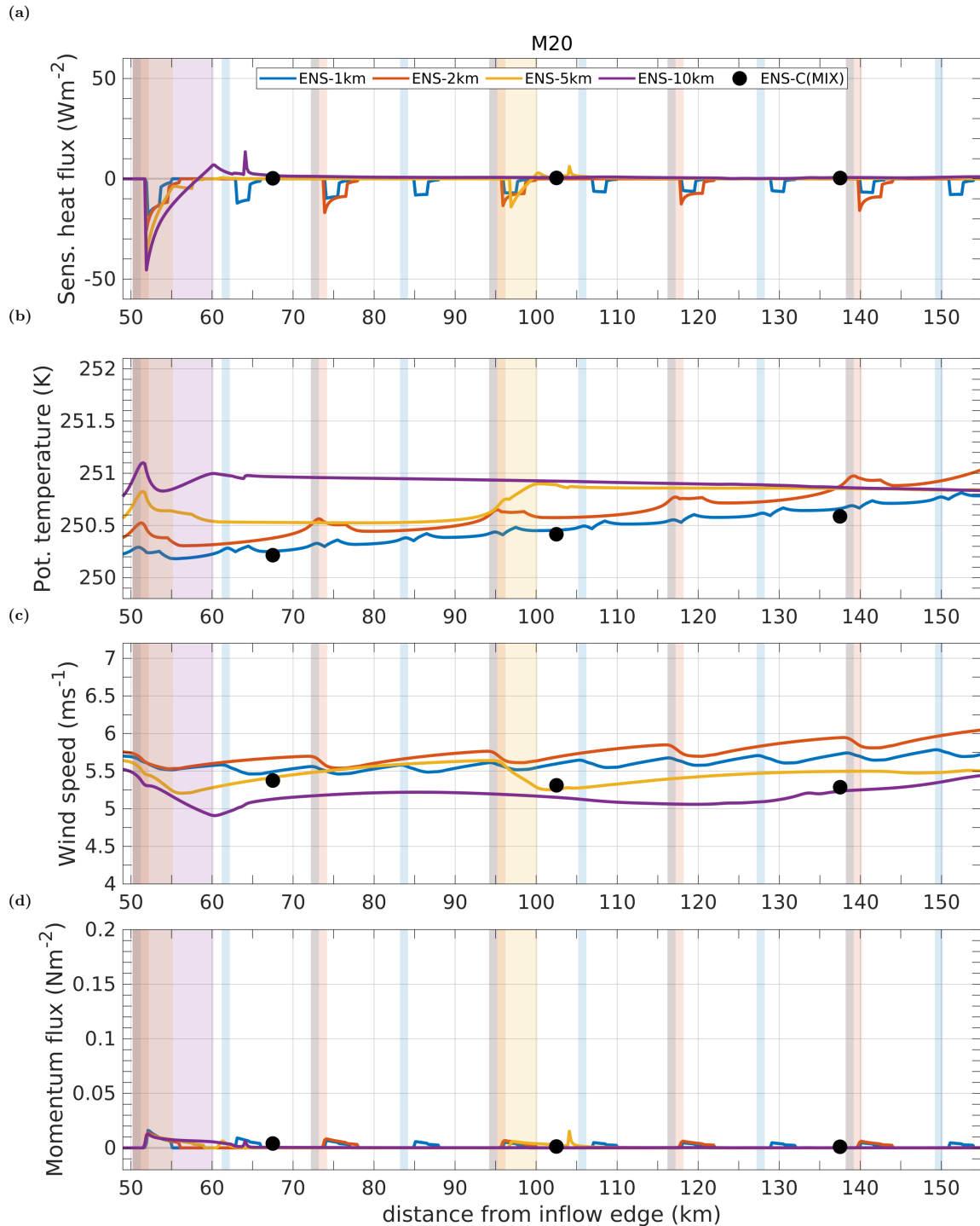


Figure 4.7: Same as Figure 4.6, but the horizontal development at height $z = 290$ m is shown.

4.2.2.3 Domain-averaged profiles of different ABL quantities

Figures 4.8 and 4.9 show domain-averaged ABL profiles of the previously considered quantities obtained by all simulations considered in this section for all cases. For the cases ENS-1km, ENS-2km, ENS-5km, and ENS-10km, the profiles were obtained for a region of 105 km width starting from the upwind edge of the northernmost lead. The corresponding domain-averaged SIC is approximately 91 % in all cases. For case ENS-C, the profiles were obtained for a region

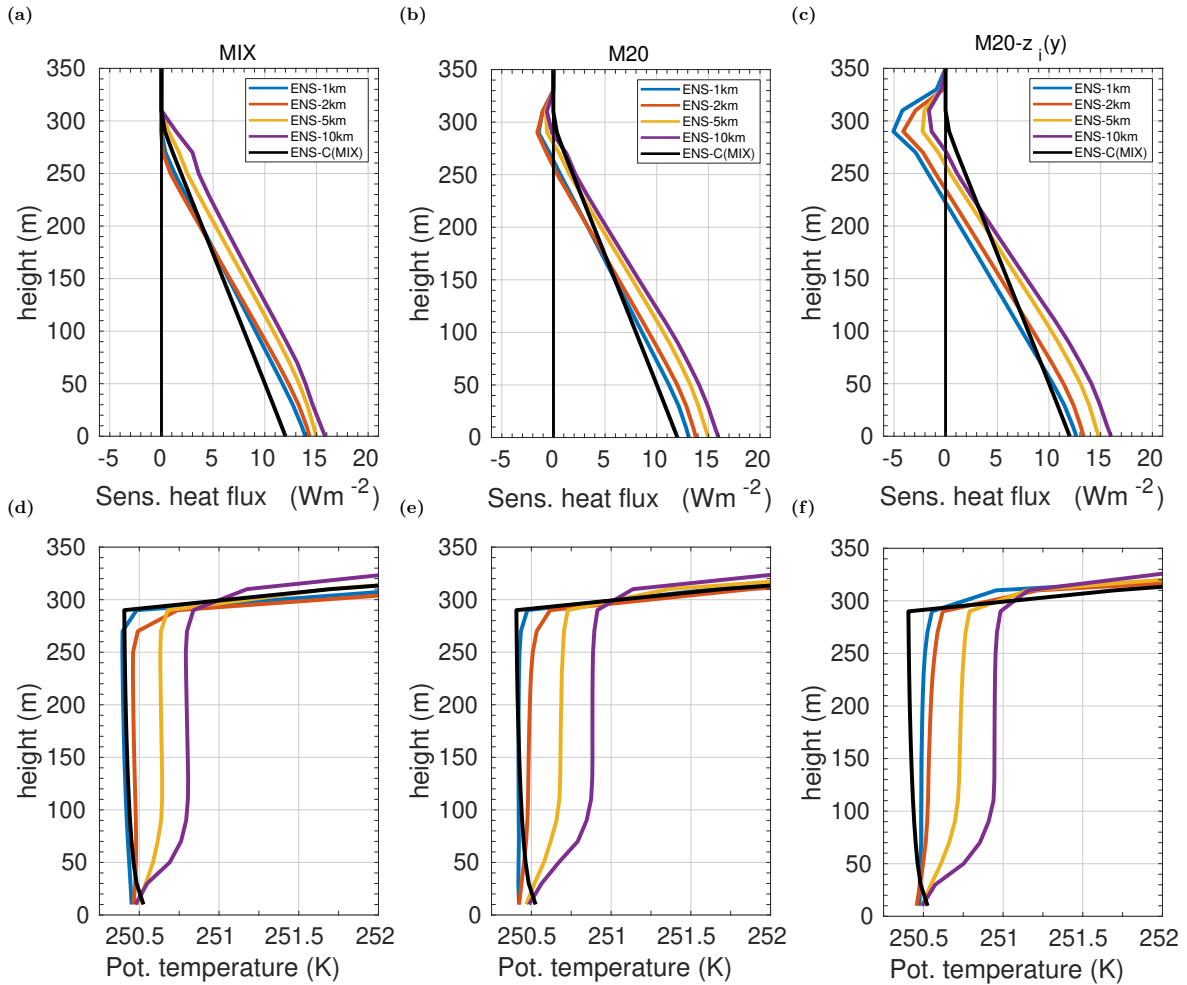


Figure 4.8: Vertical profiles averaged over a region of 105 km width and with an average SIC of 91 % obtained for the five different cases shown in Figure 4.4 with METRAS using different parametrizations for the sensible heat flux (a, b, and c) and the potential temperature (d, e, and f). Simulations of the cases ENS-1km, ENS-2km, ENS-5km, and ENS-10km were obtained using either the local closure (model runs MIX, section 2.2.2.2.1), the M20 parametrization (model runs M20, section 2.5.1), or the M20 parametrization using a varying ABL height as described in section 3.5.1 (model runs M20- $z_i(y)$). Profiles for case ENS-C were obtained with the simulation C(MIX).

of the same width and of the same mean SIC, which corresponds to the results averaged over three grid cells (see also Figure 4.4).

The effect of the leads and their geometry on the domain-averaged profiles is obvious for all quantities. Regarding the average heat flux profiles (Figures 4.8a, 4.8b, and 4.8c), for case ENS-C, average heat fluxes of approximately $12 Wm^{-2}$ are obtained at the surface, but for the lead-resolving model runs, the average surface fluxes are up to 30 % larger. This difference is most pronounced between the cases ENS-C and ENS-10km and almost independent on the applied parametrization. The effect of the lead width also becomes obvious by slightly different values of the domain-averaged surface sensible heat fluxes in each case, where the deviation compared to case ENS-C decreases with decreasing lead width. Especially for the cases ENS-1km and ENS-2km, the average surface sensible heat fluxes slightly depend on the applied parametrization.

Besides the surface values, also the general shapes of the mean vertical flux profiles differ among the cases, where the effects by different parametrizations are clearly shown. In all profiles obtained by the runs MIX, negative heat fluxes close to the ABL top and, thus, vertical entrainment are completely missing (Figure 4.8a). Small negative fluxes of about -1 Wm^{-2} to -2 Wm^{-2} on average are obtained for the lead cases by the simulations M20 (Figure 4.8b). As expected, in the results of the runs M20- $z_i(y)$, the average negative heat flux minima near z_i are more pronounced (Figure 4.8c). Note, in section 4.1 it was shown that results obtained by the run M20- $z_i(y)$ represented the most realistic results for the case with wide leads. For cases with narrow leads, vertical entrainment as obtained with M20- $z_i(y)$ is slightly overestimated compared to LES (not shown). Nevertheless, also for those cases, vertical entrainment is principally obtained with the LES (see section 4.1 and also chapter 2), whereas it is not simulated by the run C(MIX) (see Figure 4.8). Hence, the missing entrainment in case ENS-C points to a possible underestimation of the exchange between the ABL and the free troposphere in climate models in regions with leads.

Large differences depending on the respective case are shown also in the domain-averaged vertical profiles of the potential temperature (Figures 4.8d, 4.8e, and 4.8f). First, especially for the cases ENS-5km and ENS-10km, in the lowest 100 m, a strongly stable IBL is obtained on average, whereas this is completely missing in the result for case ENS-C. Note, Chechin et al. (2019) also showed that leads cause strongly stable IBLs over the downwind sea ice. Moreover, the stable IBL shown for the lead cases is obtained also with the local closure, but not as pronounced as in the results obtained with the runs M20 and M20- $z_i(y)$. Second, higher average ABL temperatures can be expected with increasing lead width. This effect is obvious especially in the results of the runs M20 and M20- $z_i(y)$, most probably by both counter-gradient transport and vertical entrainment in addition to the warming by the leads (Figures 4.8e and 4.8f). Thus, on average, differences in the ABL potential temperatures of more than 0.5 K are shown depending on the distribution of open-water and sea ice surfaces. Third, for the cases ENS-C and ENS-1km, there are only small quantitative differences between the corresponding domain-averaged temperature profiles. However, considering the simulations M20 and M20- $z_i(y)$ for case ENS-1km, the corresponding results are qualitatively fundamentally different as compared with the run C(MIX). Namely, on average, an unstable stratification is obtained for case ENS-C, whereas for case ENS-1km, rather a neutral or slightly stable stratification is obtained.

Differences among the respective cases and simulations are also obvious for the domain-averaged vertical profiles of the horizontal wind speed (Figures 4.9a, 4.9b, and 4.9c). The largest differences among the five cases are obtained with the runs MIX (Figure 4.9a). Especially in the region between $z = 50 \text{ m}$ and $z = 350 \text{ m}$, the results converge when the M20 parametrization is used (Figures 4.9b and 4.9c). Almost independent on the applied parametrization, the largest difference is obtained close to the surface, where the wind speed is approximately 3.5 ms^{-1} on average for the cases ENS-5km and ENS-10km and rather 4.2 ms^{-1} for the cases ENS-1km, ENS-2km, and ENS-C. This is also related to the influence of the stable IBL over sea ice downwind of the leads, which is most pronounced in the cases ENS-5km and ENS-10km (see also Figure 4.6). Close to the top of the ABL, the difference between the results of case ENS-C and the four lead cases is most pronounced for the cases ENS-1km and ENS-2km. Thus, the

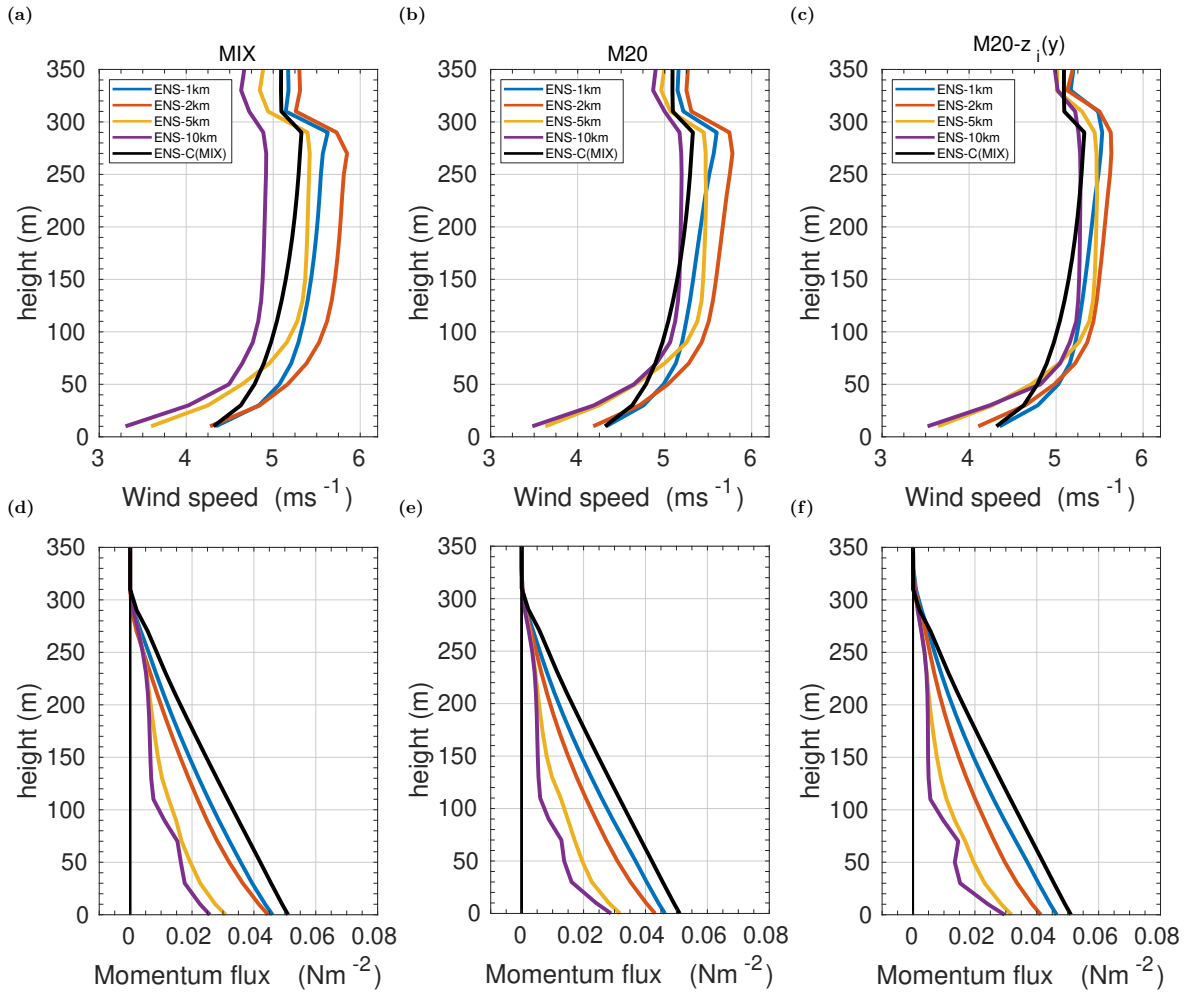


Figure 4.9: Same as Figure 4.8, but domain-averaged profiles of horizontal wind speed (a, b and c) and vertical momentum flux (d, e, and f) are shown.

effect of leads and their width is obvious also for the domain-averaged horizontal wind speed profiles.

Unlike the heat fluxes, the highest surface vertical momentum fluxes are obtained for the case ENS-C (approximately 0.05 Nm^{-2}) as compared with the other cases (Figures 4.9d, 4.9e, and 4.9f). Regarding the four lead cases, the domain-averaged surface momentum fluxes decrease with increasing lead width, independent on the parametrization. Thus, the surface values obtained for the case ENS-10km (approximately 0.025 Nm^{-2}) are about 50 % lower as compared with the result for case ENS-C. However, the corresponding deviation of the surface fluxes for the case ENS-1km amounts only to 10 %. Large differences between case ENS-C and the four lead cases are also obvious when comparing the shapes of the vertical momentum flux profiles, especially for the cases ENS-5km and ENS-10km. Especially by the simulation M20-z_i(y) for case ENS-10km, clearly a non-linear vertical momentum flux profile is obtained, with even minimally increasing values with height in the layer between $z = 50 \text{ m}$ and $z = 70 \text{ m}$ (Figure 4.9f). This phenomenon is probably also related to the strongly stable IBL over the sea ice region downwind of the 10 km-wide lead.

4.2.3 Discussion

Based on the comparison of the five different cases investigated in this section, an impact of leads and lead geometry on different ABL patterns is clearly visible. This is in good agreement with the preliminary conclusions by Lüpkes (2010). The impact can be summarised in terms of three main aspects. First, the impact of leads and their widths was obvious in the model results of all ABL quantities shown in this section, so in both the turbulent fluxes and the mean ABL quantities. Based on the domain-averaged vertical profiles, not only surface values but also the shapes of the profiles differed among the five different cases. Partly, the differences in the fluxes between the case with fractional SIC (case ENS-C) and the four lead cases amounted up to 50 %. The largest differences occurred between case ENS-C and the cases ENS-5km and ENS-10km, respectively. All this indicates a strong relevance of not only inhomogeneities in the sea ice cover but also their distribution, so, of the lead geometry, on the energy budget of the ABL over sea ice.

Second, the simulation results shown in this section partly differed depending on the applied turbulence parametrization. For example, with the local mixing-length closure, no vertical entrainment is obtained (see also the horizontal development close to the ABL's top in Figure C4, Appendix C). However, also the results obtained with the used non-local closure slightly differed depending on whether the modification of a varying ABL height (see section 3.5.1) was considered or not. Especially for the cases ENS-5km and ENS-10km, probably the most realistic domain-averaged entrainment rates and temperature profiles are obtained when using this modification (see section 4.1 for the case L5c-U5, similar to case ENS-5km). With the corresponding runs M20- $z_i(y)$, the largest differences are obtained between the lead cases and the case ENS-C, concerning at least temperatures and the turbulent fluxes in the ABL.

Third, several implications for large-scale, non-convection-resolving models can be concluded based on the analysis in this section. For example, the actual distribution of sea ice and open water affects turbulent fluxes at the surface. For a domain with only fractional sea ice cover, on average, heat fluxes seem to be slightly underestimated and momentum fluxes rather overestimated when compared to cases of explicitly prescribed leads. Thus, traditional closures used to calculate the surface fluxes in large-scale models need to be improved by accounting for the microscale processes related to the convection over leads. Another example concerns the stabilisation effect in the lowest 100 m of the ABL by leads, which is not obtained in the climate run (case ENS-C). Especially for the cases with wide leads, this causes also a fundamental difference in the average heat transport. While a gradient transport is obtained on average in the climate run, the average transport is counter-gradient in the cases with explicitly prescribed leads. Furthermore, the absence of vertical entrainment in the result of case ENS-C implies that climate models might underestimate the transport of heat through the capping inversion in lead-dominated regions.

Altogether, the sensitivity study presented here points at limitations of large-scale, non-convection-resolving atmospheric models in lead-dominated sea ice regions. Obviously, it is important to consider the numerous microscale effects by individual convective plumes developing over leads. This should include also the lead geometry and a proper representation of both vertical entrainment and counter-gradient transport. Since the latter two effects could be

obtained close to LES only by a non-local closure, such a closure scheme would be needed to properly parametrize the convective ABL over lead-dominated regions in large-scale models (see also Lüpkes, 2010). Similar sensitivity studies including variations of the ABL height and of the wind would be helpful to evaluate situations also for other meteorological forcing than used in this study. With a microscale model as used here, this can be realised with only little numerical effort, roughly with 1/1000 of the CPU time needed for LES (L08).

In addition, not only idealised scenarios but also observed lead distributions as, for example, investigated by Tetzlaff (2016) can be considered. Further studies with leads of different width in only one model domain might also be carried out to evaluate the findings by, for example, Marcq and Weiss (2012). They state that a parametrization of surface heat fluxes based on only the mean lead width in a single grid cell of a large-scale model is most likely not appropriate due to the seemingly strong relevance of the actual lead geometry in the grid cell. Note, Marcq and Weiss (2012) formulated this mainly based on their results for small leads of less than 50 m width, which are not resolved by the microscale model in its current version applied here. Nevertheless, the investigation presented in this section marks another step towards an improved representation of small-scale processes in large-scale models and it might help to derive improved parametrizations of the surface fluxes over the lead-dominated marginal sea ice zone for such models.

5 Summary and outlook

In this thesis, a detailed investigation was performed on the convection generated over leads in sea ice, including a fundamental analysis of the associated effects on the polar atmosphere and a quantification of the governing physical processes. Predominantly, small-scale atmospheric model simulations were performed and the corresponding quasi-stationary results were analysed and also validated with either time-averaged results of an LES model or airborne observations. The main part of the thesis focused on the derivation of an improved set of mathematical equations to correctly parametrize turbulent fluxes in the spatially strongly inhomogeneous environment over single leads for different idealised and observed situations varying in the lead geometry and in the atmospheric forcing.

Idealised lead scenarios: Modelling and derivation of a new parametrization

In the first major part of this thesis (chapter 2), the focus was on the development of an improved turbulence parametrization adapted to the inhomogeneous convective conditions over leads to be used in non-eddy-resolving, microscale atmosphere (RANS) models. Such an environment is characterised by a convective IBL (convective plumes) developing over the lead, whose characteristics differ considerably from horizontally homogeneous convective conditions. The main goal was to derive an approach in which the geometry of the leads, namely, their width, is taken into account. The starting point for the new approach was the parametrization developed by L08, who considered leads of only one particular width (1 km), but whose approach already accounts for the inhomogeneous conditions of the dry convection over leads including non-local effects on the heat fluxes. Ten idealised cases of a nearly lead-perpendicular ABL flow over leads of widths ranging from 500 m to 10 km were considered, all representing typical springtime conditions of a near-neutral polar ABL capped by a strong inversion. Microscale simulations with the model METRAS using the new closure, the previous non-local closure of L08, or a local mixing-length closure were evaluated using new time-averaged LES results, which also helped to analyse the integrated effects of lead-generated convection on the turbulent ABL.

As the LES results showed, the general characteristics of the flow over leads of different width remained similar to those analysed by L08 for 1km-wide leads. Strongly inclined plumes were obtained over the leads, which rapidly decayed over the downwind sea ice. In addition, vertical entrainment seemed to play an important role especially for wide leads, which represented cases where the convection interacted with the capping inversion already above the lead. With the LES model, not only an increase of temperature but also a stabilisation of the entire ABL was obtained downwind of the lead, which clearly showed the non-local nature of the heat transport in the convective plume. This result supported the basic ideas of L08 for their parametrization, which are the application of a non-local closure, the assumption of separating turbulence regimes in- and outside the plume region, and the assumption of decaying turbulence downstream of the lead. Hence, these principles also formed the basis for the new parametrization presented in chapter 2, which means that both eddy diffusivity for heat and the non-local transport term

depend on the distance to the lead edges. The fundamental step to then include the lead width as a parameter in the new approach was to distinguish between fully developed convection above the leads and a decay region only over sea ice downwind of the leads.

A good agreement between microscale model results using the new parametrization and time-averaged LES results was shown for many different ABL patterns for various meteorological conditions in an ABL of height $z_i = 300$ m, where this concerned leads of all widths considered. Moreover, all microscale model results were obtained with the same set of values for the unknown parameters in the new parametrization, which were all derived using the LES results. For one parameter needed for the parametrization of the counter-gradient heat flux, a perfect agreement was obtained with the value proposed by Holtslag and Moeng (1991) in their study of convection over homogeneous surfaces. Their value had also been derived based on LES and their approach also formed the basis for the new parametrization presented in this thesis.

Despite the generally good agreement with LES, there is room for further improvements. For example, humidity transport could be included. This was already tested and, basically, the resulting latent heat fluxes agreed with values obtained from literature (e.g., Marcq & Weiss, 2012). Other possible improvements, which were also already discussed in chapter 2, concerned the possibility to include inhomogeneities in the convective plumes and improved entrainment.

METRAS results obtained with a local turbulence closure clearly showed some drawbacks for the cases of neutral inflow conditions. This pointed at difficulties potentially occurring in mesoscale studies of atmospheric processes over the marginal sea ice zone, when such a closure is used. The main drawback with the local approach belonged to the absence of the stabilising impact of convection over leads on an ABL flow in near-neutral upwind conditions. Moreover, the turbulent flux patterns differed partly considerably from the LES results. Hence, the main conclusion of chapter 2 can be summarised as follows: To reproduce physical processes related to convection over leads of variable width in good agreement with LES, a non-local, lead-width-dependent closure adapted to the strongly inhomogeneous conditions is required. This holds for neutral inflow conditions.

Modelling and parametrizing convection over leads compared with airborne measurements

In the second major part of this thesis (chapter 3), METRAS simulations for the flow over leads were validated with airborne measurements, mainly with those that had been obtained in the whole turbulent ABL over the marginal sea ice zone Northwest of Svalbard during the campaign STABLE. Three different observed cases of a predominantly lead-perpendicular ABL flow were analysed. Those cases were characterised not only by different lead width, surface temperature, and background wind as in the idealised cases from chapter 2 but also by different ABL height and by partly stable stratification upwind of the leads. The main goal of the study shown in sections 3.1 to 3.7 was to evaluate the quality of microscale model results obtained with either the mixing-length closure or the new non-local parametrization derived in chapter 2 for the observed cases. Observations are available of mean variables as temperature and wind, as well as of turbulent fluxes of heat and momentum, which were calculated from the high-frequent measurements using the eddy covariance method. Two aspects were investigated, first, advantages of the non-local closure compared to the local one, and, second, the need for

further modifications of the non-local one. The same goals were also pursued in the study shown in section 3.8, where METRAS results were compared with observations obtained by an UAS for the turbulent flow over a lead in the Weddell Sea sea ice region.

The study of the observed cases from STABLE revealed some advantages of the non-local closure as compared to the local closure, but the differences among the corresponding model results were not as pronounced as shown for the idealised cases discussed in chapter 2. Partly, observed heat flux profiles over the leads below the inversion layer (i.e., below z_i) were even slightly better represented by the local closure. However, once again, it was shown that a more realistic reproduction of heat and momentum transport in the ABL over leads required the application of a non-local approach since several limitations occurred for the local closure for regions with observed vertical entrainment and, especially, counter-gradient transport. Similar conclusions can be formulated based on the results obtained for the UAS-case. All this supports the main conclusion formulated for chapter 2.

An improved representation of the observed effects due to vertical entrainment and stable upwind stratification was obtained using two modifications introduced in chapter 3 for the new non-local parametrization. First, a varying ABL height $z_i(y)$ was introduced, where the vertical location of the bottom of the capping inversion was determined diagnostically at each horizontal position y during the model integration. This enabled a spatially varying upper boundary for the upper IBL height $\delta(y)$ in the new parametrization and the plume growth was not longer limited by a fixed vertical location of z_i unlike the simplified original assumption made in section 2.5.1. Hence, the interaction of the convective plume with the capping inversion was better represented and several improvements were obtained. Second, the stable upwind stratification in two observed cases caused a more inclined plume than in neutral conditions, and an improved representation of the plume inclination was obtained due to alternative values derived for one of the tunable parameters in the new parametrization (a) using the measurements. Moreover, a direct linkage between $\delta(y)$ and the upwind stratification via a was proposed resulting a similar $\delta(y)$ -formulation as previous parametrizations by other authors (see Weisman, 1976; Renfrew & King, 2000), but in contrast to those formulations, the new one was valid for both neutral and stable upwind stratification, and no singularity was shown in case of neutral stratification.

The comparison with the observations also revealed that even with the modifications introduced for the new non-local parametrization, some observed structures were still not reproduced, especially concerning momentum transport. This showed the need for continuous improvements of such a turbulence parametrization in future, also to include more effects. Nevertheless, based on the analysis in chapter 3 three important conclusions can be made. First, a large variety of airborne observations represents a very useful basis for validating small-scale model results and for improving turbulence parametrizations. Second, even though some observed features can be reproduced by using a simple local approach, for a physically correct representation of the effects due to lead-generated convection, a non-local scheme is obviously required. Third, the applied non-local scheme can be further modified with only little effort, which leads to a considerable extension of its range of applicability in inhomogeneous convective conditions.

Modelling of the flow over idealised lead ensemble scenarios

In chapter 4, the idealised flow over more than only a single lead was modelled with the following

two goals. First, the quality of microscale model results obtained with different parametrizations should be evaluated when the model is applied to simulate the flow over more than only one lead. As a starting point, the results for the flow over two consecutive leads were compared with time-averaged LES results. Second, the relevance of different lead configurations on ABL patterns should be investigated for a domain, which can be regarded as representative for a few grid cells of a large-scale model wherein leads and lead-generated convection are not explicitly resolved. For achieving both goals, mainly domain-averaged profiles were analysed.

In section 4.1, domain-averaged profiles as obtained by METRAS using either the mixing-length closure or the new non-local parametrization were compared with LES for two idealised cases of the ABL flow over two consecutive leads of 1 km or 5 km width. A very good representation of the LES profiles was obtained for the 1 km-case for a region of about 89 % SIC on average, slightly better with the non-local than with the local closure. For the 5 km-case, where the average SIC was 67 %, the deviations to LES were larger than in the 1 km-case. Again, the non-local closure showed slight advantages, especially regarding the qualitative representation of the LES profiles. Moreover, the deviations were minimised in another METRAS simulation using the new non-local parametrization with the varying ABL height introduced in chapter 3.

In section 4.2, METRAS results for five idealised cases were discussed, four of them representing different lead ensembles, and a fifth case representing a few grid cells of a typical regional climate model with a fractional sea ice cover of 91 % in each cell. To maintain comparability among these five different configurations, ABL characteristics were compared for regions of the same width (105 km) and the same average sea ice concentration (91 %). A comparison of the corresponding domain-averaged profiles revealed differences in both mean quantities and turbulent fluxes not only between the four lead cases and the case with fractional sea ice cover but also among the model runs for each lead case. Hence, a clear impact on the ABL flow was obtained not only by leads in general but also by their geometry. This was most pronounced for wide leads of 5 km and 10 km width. Furthermore, also for this investigation, different parametrizations were applied for each lead case, which resulted in partly differing domain-averaged profiles for a single case. Differences caused by the parametrizations in the microscale model runs mainly affected the upper half of the ABL. In summary, the analysis presented in section 4.2 clearly pointed at the necessity to consider the microscale effects caused by lead-generated convective plumes in large-scale, non-convection-resolving models.

The three key research questions formulated for this thesis can be answered as follows:

1. A non-local, lead-width-dependent closure is useful to improve the representation of inhomogeneous convective conditions over leads of different geometry in sea ice using small-scale, non-eddy-resolving models.
2. Observed ABL structures over leads can be basically represented with microscale, non-eddy-resolving modelling. Different types of turbulence parametrizations can be applied including a simple mixing-length scheme. However, the physically most reasonable representation of processes is obtained with the new non-local closure as proposed in this thesis. This closure proved to be the best one, especially when neutral inflow was considered and when the results were compared with LES.

-
3. The large-scale effects of leads and different lead configurations are expressed by differences in terms of surface values and mean vertical profiles of both mean atmospheric quantities as well as turbulent fluxes. These differences imply drawbacks for typical regional large-scale models wherein lead-generated effects cannot be explicitly resolved.

Outlook

The new non-local parametrization derived in the framework of this thesis represents an important step forward but there is still room for further development, for example, to overcome still existing discrepancies to LES. For example, in both chapters 2 and 3, there was certain evidence for an effect on the turbulent momentum fluxes not captured in the current version of the new closure. This drawback might be overcome with modifications of the eddy diffusivity for momentum. Moreover, further closure schemes might be tested, either approaches based on alternative formulations for the eddy diffusivities and the non-local term (e.g., Troen & Mahrt, 1986; Noh et al., 2003), or with an alternative treatment of turbulent contributions following the EDMF scheme (Siebesma et al., 2007). In addition, an extension of the region of applicability of the new closure regarding, for example, moisture transport, inflow direction, and air-sea ice interaction would mark a considerable step forward in the representation of small-scale effects over leads, for which further validation with LES or observations would then be needed.

Regarding the implications for large-scale meteorological modelling, the results shown in this thesis clearly call for improvements to be considered in such models for an improved representation of atmospheric effects related to leads in the polar sea ice regions. For large structures, this might be achieved already by further increasing the model resolution so that the leads are explicitly resolved. A promising development regarding an explicit resolution of leads in sea ice models is more and more achieved (see, for example, Wang et al., 2016; Hutter et al., 2018). It is further to be evaluated, if this would also improve atmospheric structures when implemented in climate models despite the drawbacks that can be expected due to the rough resolution of those models, which have also been described in this thesis (see chapter 4 and Appendix B.3). Another possibility would be to use the results of chapter 4 and to try to improve parametrizations for the lead-generated effects on the ABL in climate models, especially for surface fluxes.

Finally, the application of the newly developed parametrization might not be limited to the convection over leads. One could perhaps generalise the approach and could adjust it to different kinds of inhomogeneously heated surfaces. For example, a similar situation as the convective flow over leads in sea ice is the flow over an urban area that is warmer than the surrounding rural environment, especially in clear-sky conditions in winter during nighttime (Urban Heat Island, see, for example, Oke, 1995). Other examples are the convective flow over large Arctic river deltas or over motorways also depending on environmental factors. An improved representation of the corresponding small-scale effects might then help to improve regional climate projections also for such situations.

Acknowledgements

For conducting my PhD at the Alfred-Wegener-Institute (AWI) and for finishing this thesis, I received valuable support and assistance, which is why I would like to pay my special regards to the following people and organisations.

I gratefully acknowledge the support due to funding by the Deutsche Forschungsgemeinschaft (German Research Foundation, DFG) with the corresponding project number 268020496 TRR 172 within the Transregional Collaborative Research Center ArctiC Amplification: Climate Relevant Atmospheric and SurfaCe Processes, and Feedback Mechanisms (AC)³. I would also like to thank for the support due to the DFG grant LU 818/5-1 within the priority program "Antarctic Research with comparative investigations in Arctic ice areas" SPP 1158.

First and foremost, I wish to express my deepest gratitude to Dr. Christof Lüpkes for being such a great supervisor of my PhD. I would like to thank him for his huge support due to the large number of suggestions I received from him to develop and conduct my PhD project, for the valuable discussions, and also for the very constructive remarks. Moreover, I thank him a lot for giving me the opportunity to take part in the airborne expedition AFLUX in April 2019.

I want to thank also my other two PhD committee members, Prof. Thomas Jung and Dr. Jörg Hartmann. I am deeply thankful for their valuable comments during our meetings, which considerably helped me in the course of my PhD. Moreover, I gratefully acknowledge Prof. Thomas Jung for reviewing my thesis and I thank Dr. Jörg Hartmann a lot for already supervising both my internship at the AWI and my master's thesis, which also encouraged me to pursue this PhD project. I would also like to gratefully acknowledge Prof. Dr. Christian Haas for accepting to review my thesis.

I also want to thank all my co-authors for their support. I wish to acknowledge Xu Zhou and Dr. Micha Gryscha from the University of Hannover for providing the LES model data and for the valuable discussions during our project meetings. I also wish to thank Dr. Amelie Schmitt from the University of Hamburg a lot for her support regarding the evaluation of the observations from STABLE. Finally, I gratefully acknowledge the support and advice by Dr. Vladimir M. Gryanik and thank him for any time providing very useful information, including that from his huge collection of (Obukhov-)anecdotes.

A very special thank goes to my office colleagues Stephanie Carstensen and Niels Fuchs. I really enjoyed sharing the office with them including all the conversations we had together during our regular "fika"-sessions. Furthermore, I would like to thank my colleagues from the Polar Meteorology section at the AWI for their advice, especially, Wolfgang Cohrs for providing technical support whenever needed. I also thank Tim Gollnik for his valuable support regarding the installation of the applied model at the beginning of my PhD and Dr. Amelie Driemel for the uncomplicated support of uploading data sets to PANGAEA. And I would like to thank all other colleagues at AWI, who provided such a comfortable working environment.

In addition, I would like to show my gratitude to the POLMAR graduate school including Dr. Claudia Hanfland and Dr. Claudia Sprengel, especially for providing financial support regarding

my participation at the AGU Fall Meeting in December 2019 and for the valuable courses and seminars they offer. I am also very thankful for having been part of a great DokTeam at AWI and therefore thank Joyce Nieva, Melissa Käß, Miriam Seifert, Nora Pauli, Saeid Bagheri, and Sebastian Böckmann for the wonderful time. In addition, I would like to thank the participants of the AFLUX campaign a lot for the great time I could spend with them in Svalbard.

I truly appreciate the support by Christopher Schläfke and Dr. Christof Lüpkes due to proof-reading parts of my dissertation. Furthermore, I wish to thank all my friends not only for always encouraging me, but also for the urgently needed distraction. Especially, I would like to thank my classmates from the meteorology studies at the University of Hamburg, where I am deeply grateful to regularly spend time with them also after having finished the studies.

Last but not least, I wish to express my deepest gratitude to my family, especially to my parents Ágota and Frank and to my sister Sarah for supporting and encouraging me ever since I decided to become a meteorologist. And I would like to thank Juliane for her unconditional support and for always being there for me.

A Appendix for chapter 1

The Navier-Stokes equations (A.1) to (A.5) provide a mathematical description of the Earth's atmosphere. Equation A.1 is the equation of motion based on the conservation of momentum. Equation A.2 is the continuity equation based on the conservation of mass. Equation A.3 ensures also the conservation of heat, water, or other scalar quantities. Equation A.4 is the ideal gas law, and Equation A.5 is the definition of the potential temperature θ . These equations can be written as follows (see also Schlünzen, Flagg, et al., 2012):

$$\frac{\partial \mathbf{v}}{\partial t} + (\mathbf{v} \cdot \nabla) \mathbf{v} = -\frac{1}{\rho} \nabla p - 2(\Omega \times \mathbf{v}) - \nabla \Phi + \mathbf{F} \quad (\text{A.1})$$

$$\frac{\partial \rho}{\partial t} + \nabla(\rho \mathbf{v}) = 0 \quad (\text{A.2})$$

$$\frac{\partial \chi}{\partial t} + \mathbf{v} \cdot \nabla \chi = Q_\chi \quad (\text{A.3})$$

$$\nu_i = \frac{R_i T}{p} \quad (\text{A.4})$$

$$\theta = T \left(\frac{1000 \text{ hPa}}{p} \right)^{\frac{R_0}{c_p}} \quad (\text{A.5})$$

Equation A.1 contains the 3-D wind vector \mathbf{v} , the Nabla operator ∇ , the air density ρ , the air pressure p , the Earth's angular velocity Ω , the geopotential Φ , and the time t . The term \mathbf{F} represents molecular forces. χ represents any scalar quantity with Q_χ as its sources and sinks, ν_i is the specific volume, R_i is the individual gas constant, T is the atmospheric temperature, and $c_p \approx 1005 \text{ J}(\text{kgK})^{-1}$ is the specific heat at constant pressure. ν_0 and R_0 correspond to dry air, where $R_0 = 287.1 \text{ J}(\text{kgK})^{-1}$.

Filtering the Navier-Stokes equations with a method depending on the used model type (see chapter 1) and using a scale analysis leads to filtered and simplified approximated model equations designed for the phenomena to be modelled (see also chapter 1). For the models used in this thesis, a full description of the corresponding equations is given by Maronga et al. (2015) for the LES model PALM and by Schlünzen, Flagg, et al. (2012) for the non-eddy-resolving RANS model METRAS. In METRAS, which is applied in this thesis as a microscale, non-eddy-resolving model, the so-called Boussinesq-approximation is applied to the filtered model equations, which means that deviations from the basic state air density (ρ_0) are only considered in the buoyancy term. In the unfiltered equations, this term corresponds to the first term on the right-hand side of Equation A.1. Furthermore, a constant Coriolis parameter valid for a certain reference latitude is assumed, which is a useful assumption for phenomena of less than 1500 km horizontal extension (see Schlünzen, Flagg, et al., 2012). In addition, molecular forces are neglected in METRAS (Schlünzen, Flagg, et al., 2012).

In both models, subgrid-scale turbulent transport terms result from filtering the equations (A.1) to (A.5) as part of the resulting diffusion terms (see Schlünzen, Flagg, et al., 2012; Maronga et al., 2015, respectively). Here, the focus is on their vertical components, which can be written as

$$F_h = c_p \rho_0 \overline{w'\theta'} \quad (\text{A.6})$$

$$F_e = l_3^1 \rho_0 \overline{w'q'_v} \quad (\text{A.7})$$

$$F_\tau = \rho_0 \left(\overline{w'u'^2} + \overline{w'v'^2} \right)^{1/2}, \quad (\text{A.8})$$

where F_h and F_e are the turbulent fluxes of sensible and latent heat, respectively, $l_3^1 = 2.83 \cdot 10^6 \text{ J(kg)}^{-1}$ is the specific latent heat of sublimation, and F_τ is the total vertical turbulent flux of horizontal momentum. For the explanation of the covariances, see chapter 1. In this thesis, positive values of F_h and F_e refer to upward transport and negative values to downward transport. The values given for F_τ refer to the absolute value of the momentum flux vector and a more detailed separation between upward and downward momentum transport is not considered here.

B Appendix for chapter 2¹

B.1 Determination of the parameters d_w and d_θ

L08 state that their decay length scale D , which determines the strength of the exponential decay of w_l (Equation 2.9), can be expressed by $D \propto U\tau$, where τ is the large-eddy turnover time with $\tau \approx z_l/w_* \approx z_l^{2/3}/B_l^{1/3}$. We apply this relation to determine the corresponding decay length scale of the new parametrization, D_w , which is used in Equation 2.19,

$$D_w = d_w \cdot U \frac{z_l^{2/3}}{B_l^{1/3}} = d_w \cdot U \frac{z_l^{2/3}}{\left(\frac{g}{\theta_0} \overline{w'\theta'}|_s\right)^{1/3}} = d_w \cdot U \frac{z_l^{2/3}}{\left(\frac{g}{\theta_0} \frac{\overline{F}_{h,s,l}}{\rho_{0,s} c_p}\right)^{1/3}}, \quad (\text{B.1})$$

where $\rho_{0,s} = 1.4 \text{ kg m}^{-3}$ is the air density at the surface. Values of $\overline{F}_{h,s,l}$ are shown in Table 2.1 (see chapter 2). Furthermore, we define D_w as the distance ($y - L$) to the downstream lead edge, where fluctuations of the vertical velocity weakened to the fraction of $1/e$, where e is Euler's number. The vertical velocity fluctuations are, in turn, proportional to the convective velocity scale w_* in horizontally homogeneous conditions in the centre of the ABL at $z = 0.4z_l$ (Holtslag & Moeng, 1991). Thus, we consider the square root of the vertical velocity variance, $(\overline{w'^2})^{1/2}$, from LES to determine D_w . Hence, we solve Equation B.1 for the proportionality factor d_w and we can determine its value taking all open quantities (d_w, U, z_l, B_l) from LES.

We use all cases with $L \geq 5 \text{ km}$ (Table 2.1, wide leads) for this determination since we can write $w_l = w_*$ at $y = L$ due to our assumption of horizontally homogeneous conditions if $\delta_L = z_l$ (see section 2.5.1). With linear regression (Figure B1a), we obtain $d_w \approx 1.7$. Furthermore, we consider Equation B.1 with $d_w \approx 1.7$ to determine D_w also for all our simulations with $L < 5 \text{ km}$ since we assume D_w to be independent on L .

Unlike L08, we apply a decay function also for the convective temperature scale θ_l to consider decaying temperature fluctuations $\overline{\theta'^2}$ in the lead's downstream region. Furthermore, we assume differences between decaying temperature and vertical velocity variations; hence, we introduce another decay length scale D_θ . To determine D_θ , we consider the results of Nieuwstadt and Brost (1986), who studied the decay of convective turbulence in the ABL using LES. They proposed that fluctuations in temperature decrease faster than fluctuations in vertical velocity when upward surface heat flux is suddenly stopped. Here, we have a comparable situation, where our results are quasi-stationary on a temporal, but variable on a spatial scale due to suddenly vanishing upward surface heat fluxes at the transition from the lead to the downstream ice. Thus, the convective turbulence decays with increasing distance ($y - L$) to the downstream lead edge and based on the LES results of Nieuwstadt and Brost (1986), we expect that temperature variations decay after a shorter distance than vertical velocity variations.

¹This appendix was published as part of the article entitled *Influence of lead width on the turbulent flow over sea ice leads: Modeling and parametrization* in *Journal of Geophysical research: Atmospheres* by Michaelis et al. (2020) (see chapter 2 in this thesis). The appendices B.1-B.3 correspond with the appendices A-C of the publication, and the content of Appendix B.4 was published as supporting information.

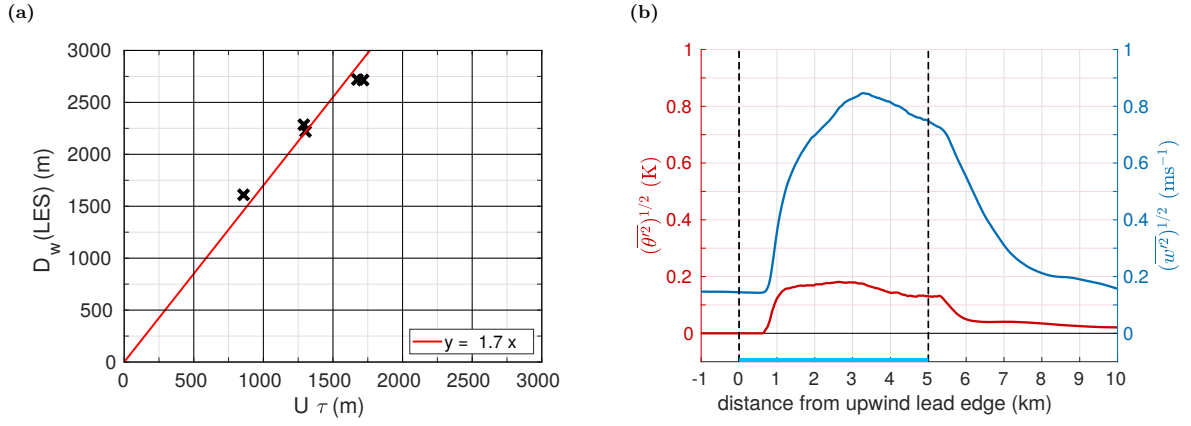


Figure B1: (a) Decay length scale of vertical velocity variations from LES of cases with $L \geq 5$ km (Table 2.1, chapter 2), D_w , against $U\tau$ (crosses). The parameter d_w was gained by linear regression (red curve with $y = D_w$ and $x = U\tau$). (b) Square roots of the variances of potential temperature in K (red) and vertical velocity in ms^{-1} (blue), $(\overline{\theta'^2})^{1/2}$ and $(\overline{w'^2})^{1/2}$, at $z = 0.4z_i$ along the distance from the upstream lead edge as obtained by the LES of case L5c-U5. The lead is between 0 and 5 km distance.

Namely, Nieuwstadt and Brost (1986) formulated two subgrid time scales for the transfer of momentum and temperature, τ_m and τ_h , and found that $\tau_h \approx 0.3\tau_m$. Therefore, similar to Equation B.1, we define

$$D_\theta = d_\theta \cdot U \frac{z_i^{2/3}}{B_l^{1/3}}. \quad (\text{B.2})$$

Then, we calculated the square root of the variances of both temperature and vertical velocity, $(\overline{\theta'^2})^{1/2}$ and $(\overline{w'^2})^{1/2}$, at $z = 0.4z_i$ along the distance y from the LES of case L5c-U5 (Figure B1b). Indeed, from this figure, we find that temperature fluctuations already decrease at $y - L \approx 1$ km to a constant level, whereas vertical velocity fluctuations reach a constant level at $y - L \approx 3$ km. Thus we confirm the finding

$$d_\theta \approx 0.3 d_w \quad (\text{B.3})$$

of Nieuwstadt and Brost (1986) with our LES results and use this in the new parametrization.

B.2 Determination of the parameters c and a

Also c and a (values see section 2.5.1) were obtained using our LES results. The parameter c acts as an adjustable constant for the convective velocity scale $w_l(y)$ (Equation 2.19 in chapter 2) in the new parametrization. When we assume the validity of Equation 2.26, which goes back to Holtslag and Moeng (1991), we can obtain an equation for c . The first step is to use the definitions (2.14) and (2.15) in Equation 2.26 for S and Z and replace w_l then by Equation 2.19 (see chapter 2 for those equations). We need to consider only the upper line of Equation 2.19 because we aim to validate the assumption $c = 1$ for the region over the lead where $\delta(y) = z_i$. The next step is to solve this equation for c , which results in

$$c(y, z) = \left(\frac{\overline{w'^2}(y, z)^{3/2} - 1.6^{3/2} u_*^3(y) \left(1 - \frac{z}{\delta(y)}\right)^{3/2}}{1.2 B_l(y) z \left(1 - 0.9 \frac{z}{\delta(y)}\right)^{3/2}} \right)^{1/3}, \quad 0 \leq y \leq L, \quad (\text{B.4})$$

where $u_*(y)$, $\overline{w'^2(y, z)}$, and $B_l(y)$ are calculated from LES. To obtain $\delta(y)$ from LES results, we used for each considered case a linear approximation of the upper plume boundary in the region $0 \leq y \leq y_{z_i}$, where y_{z_i} denotes the intersection of δ with z_i . For $y > y_{z_i}$, the value of δ was set to z_i . The linear fit was derived from Figures B8 and B9 showing the heat flux obtained with LES since there the upper plume boundary $\delta(y)$ is clearly visible. The distribution of $c(y, z)$ as obtained finally from Equation B.4 with the help of LES is shown in Figure B2 for all cases with $L \geq 5$ km.

It is shown that $c(y, z)$ as obtained from Equation B.4 varies in both horizontal and vertical direction, especially in the region for which $\delta(y) < z_i$ (Figure B2). However, in the region with $\delta(y) = z_i$, the value $c(y, z) = 1$ dominates. This holds especially for the cases L5c-U3 and L10c-U5 where horizontally homogeneous conditions over the lead are most pronounced (see Figures 2.2a and 2.2g in chapter 2). Furthermore, averaged over the respective regions where $\delta(y) = z_i$, we obtain $\langle c(y, z) \rangle \approx 1$ (Figure B2). Despite the deviations of c from 1 in some regions, we found that this value could be used in all our cases as a rough approximation, also where $\delta(y) < z_i$ and also in the lead's downstream region. Note also that with our assumptions, w_l depends only on y but not on z , while $\overline{w'^2}$ depends on both y and z .

The parameter a determines the plume inclination. After transforming Equation 2.20, we obtain:

$$a = \begin{cases} \left(\frac{\delta(y)}{\left(\frac{2}{3} \frac{B_l^{1/3}}{U} y \right)^{3/2}} \right)^{2/3}, & 0 \leq y \leq L \\ \left(\frac{\delta(y)}{\left(\frac{2}{3} \frac{B_l^{1/3}}{U} L \right)^{3/2} \left(1 + \frac{D_w}{L} (1 - \exp(-\frac{L-y}{D_w})) \right)^{3/2}} \right)^{2/3}, & y > L \end{cases}, \quad (\text{B.5})$$

To determine a , we use both B_l and U from LES and assume again a linear increase of $\delta(y)$ with y (see Figures B8 and B9). Thus, we can insert any arbitrary pair of $\delta(y)$ and y resulting from the linear line $\delta(y)$ obtained from LES in the above equation. This leads finally to the values for a shown in Table B1 for all cases. Obviously, they range from 0.98 to 1.45. Table B1 also shows that a depends on B_l , U , and L . However, for simplicity, we prescribe the value $a = 1.2$ for all cases (see also section 2.5.4).

Table B1: Values derived based on Figures B8 and B9 for all cases to obtain the parameter a in the new parametrization that has been derived in section 2.5.1^a.

| Wide leads | | | | | |
|---------------|--------|--------|--------|---------|----------|
| | L5c-U3 | L5c-U5 | L5c-U7 | L10c-U5 | L5w-U5 |
| y_{z_i} (m) | 1300 | 1600 | 2000 | 1600 | 2100 |
| a | 0.99 | 1.21 | 1.25 | 1.22 | 1.21 |
| Narrow leads | | | | | |
| | L1c-U3 | L1c-U5 | L1c-U7 | L1w-U10 | L0.5c-U5 |
| y_{z_i} (m) | 1180 | 1570 | 1950 | 3720 | 1650 |
| a | 1.14 | 1.34 | 1.45 | 1.45 | 1.45 |

^a For each case (see Table 2.1 in chapter 2), y_{z_i} is approximately the position (m) where the plume intersects with the height of the inversion at $z_i = 300$ m as simulated with LES (see Figures B8 and B9). Values for a are obtained via Equation B.5.

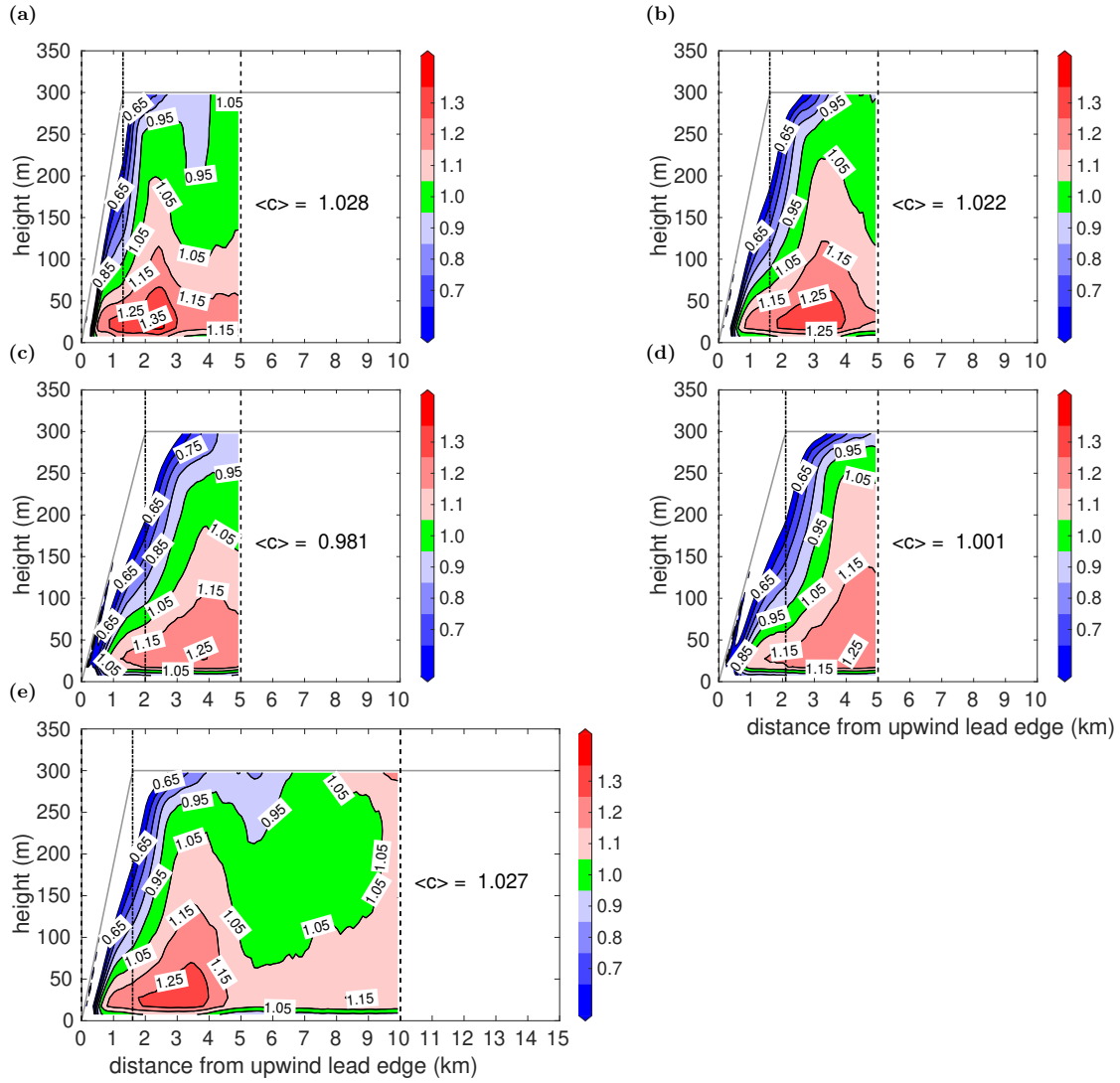


Figure B2: Distribution of $c(y, z)$ via Equation B.4 from LES for all cases with $L \geq 5$ km and mean values $\langle c \rangle$ for the region where $y_{z_l} \leq y < L$ (between the dashed-dotted and dashed lines) and where $0 < z < z_l$. Cases are L5c-U3 (a), L5c-U5 (b), L5c-U7 (c), L5w-U5 (d), and L10c-U5 (e). The solid grey lines are linear approximations of the IBL height $\delta(y)$ obtained from LES (Figures B8 and B9). The position of the lead is between 0 km and the vertical dashed black line. For the cases, see Table 2.1 in chapter 2.

B.3 Sensitivity of microscale model results on the horizontal resolution

For case L5c-U5, we repeated the METRAS simulations using the new parametrization for horizontal grid sizes of $\Delta_{x_2} = 100, 500, 1000,$ and 2500 m (Figures B3 and B4). Both figures show that the overall structure of the patterns depends only marginally on Δ_{x_2} up to $\Delta_{x_2} = 1000$ m, which is equal to $L/5$ in this case. With $\Delta_{x_2} = 2500$ m and, thus, only two grid points to resolve the lead, some structures change significantly (Figures B3g, B3h, B4g, and B4h). Thus, to reproduce detailed flow structures over the lead, grid sizes of not more than $L/5$ seem necessary to obtain a reasonable agreement with LES.

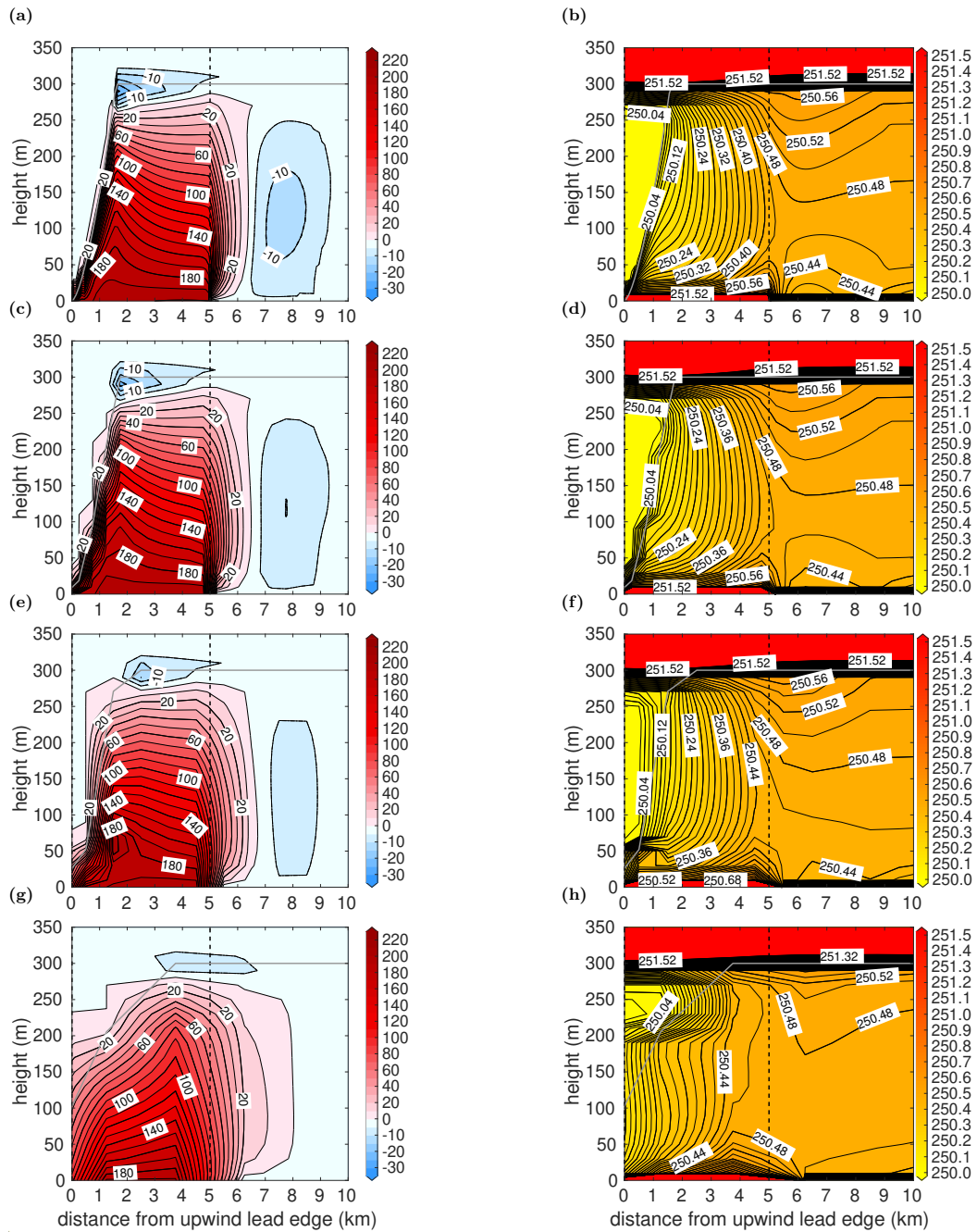


Figure B3: METRAS results of heat flux in Wm^{-2} (left column) as in Figure 2.7c (see chapter 2) and potential temperature in K (right column), but obtained with other horizontal grid sizes. $\Delta x_2 = 100$ m (a, b), $\Delta x_2 = 500$ m (c, d), $\Delta x_2 = 1000$ m (e, f), and $\Delta x_2 = 2500$ m (g, h). For the corresponding LES results, see Figure 2.2c in chapter 2. The case is L5c-U5 (see Table 2.1 in chapter 2).

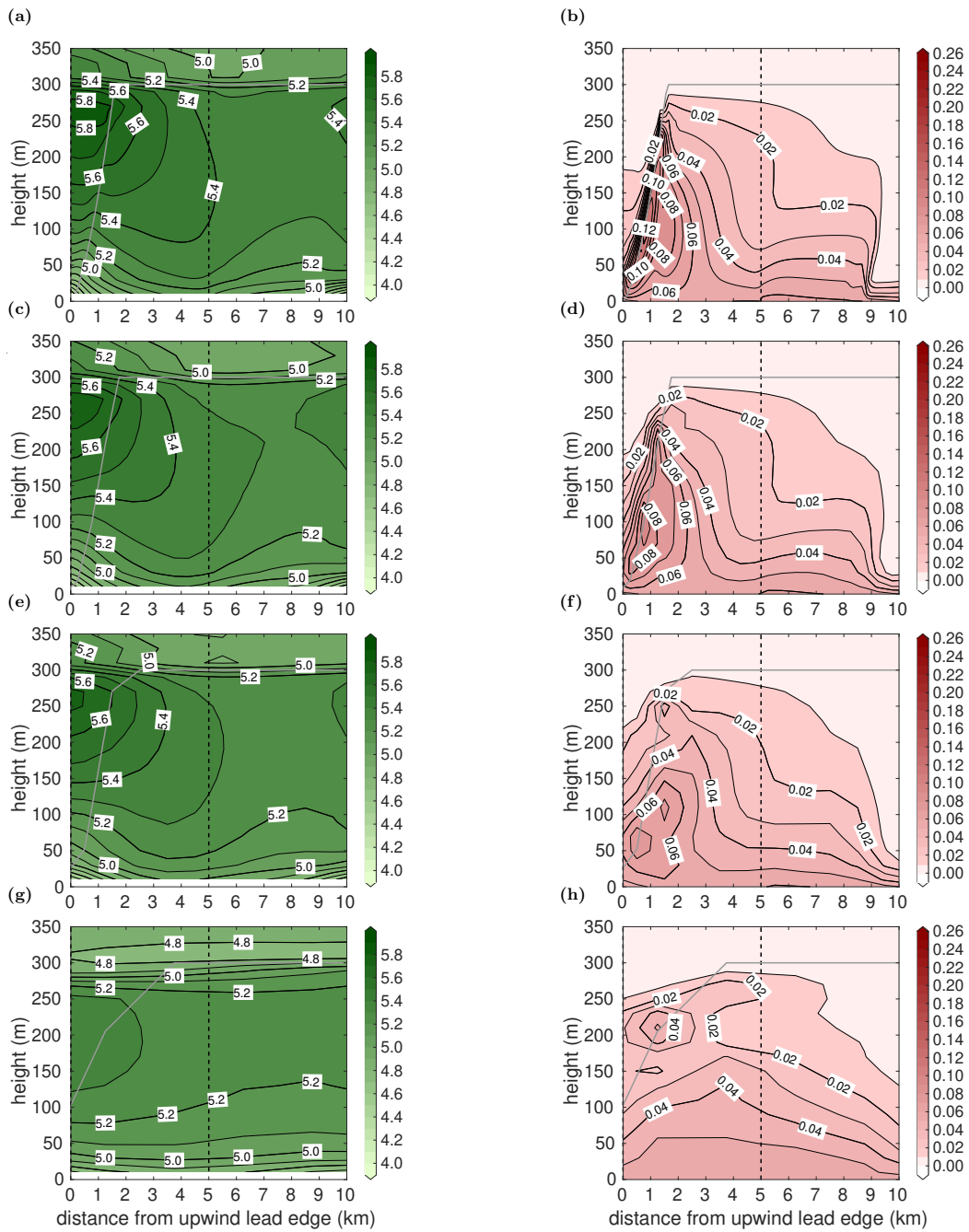


Figure B4: METRAS results of horizontal wind speed in ms^{-1} (left column) and vertical momentum flux in Nm^{-2} (right column) as in Figures 2.8c and 2.8d (see chapter 2), but obtained with different horizontal grid sizes. $\Delta_{x_2} = 100 \text{ m}$ (a, b), $\Delta_{x_2} = 500 \text{ m}$ (c, d), $\Delta_{x_2} = 1000 \text{ m}$ (e, f), and $\Delta_{x_2} = 2500 \text{ m}$ (g, h). For the corresponding LES results, see Figures 2.3c and 2.3d in chapter 2. The case is L5c-U5 (see Table 2.1 in chapter 2).

B.4 Supplementary figures

This section contains five figures (Figures B5 to B9) with additional simulation results of the applied models in the study shown in chapter 2 in this thesis.

Figure B5 shows results of the gradient Richardson number Ri (see Schlünzen, Flagg, et al., 2012, their Equation 3.39) and the momentum flux in Nm^{-2} obtained with large eddy simulation (LES) and the microscale model (METRAS) using the three different parametrizations that are explained in sections 2.2.2.2 and 2.5.1.

Figure B6 shows the sensible heat flux (Wm^{-2}) and vertical potential temperature gradient (K per 100 m) obtained with METRAS using the new parametrization (see section 2.5.1), but with different values for the constant b that are used in other parametrizations (case L5c-U5, see Table 2.1 in chapter 2). For Figures B6a and B6b, as in the L08 parametrization, $b = 0.6$ is used, and for Figures B6c and B6d, $b = 3$ is used, which was applied by Lüpkes and Schlünzen (1996) in their parametrization for cold-air outbreaks. In chapter 2, the corresponding METRAS results with $b = 2$, which is the value we use in the new parametrization, are shown in Figures 2.7c and 2.7d and the corresponding LES results in Figures 2.2c and 2.2d.

Figure B7 shows new LES results of the sensible heat flux in Wm^{-2} (left column) and of the potential temperature in K (right column) for all our cases with $L = 1$ km (see Table 2.1 in chapter 2). The results are shown for a lead 10 km downstream of another lead to ensure comparability with the study of L08. The corresponding METRAS results obtained with the new parametrization are shown in Figure 2.11 in chapter 2. The reason for the blank areas shown in Figure B7 is that the model domain of the LES ended at 8 km distance from the upwind lead edge of the second lead.

Figures B8 and B9 show LES results of the sensible heat flux in Wm^{-2} for all discussed idealised cases shown in Table 2.1 in chapter 2 (wide lead cases in Figure B8 and narrow lead cases in Figure B9). Those two figures show our method how we obtained the height of the upper internal boundary layer and the position where it intersects the inversion layer (y_{zi}) from the LES results. This was necessary to determine the parameter a in the new parametrization (see also Appendix B.2).

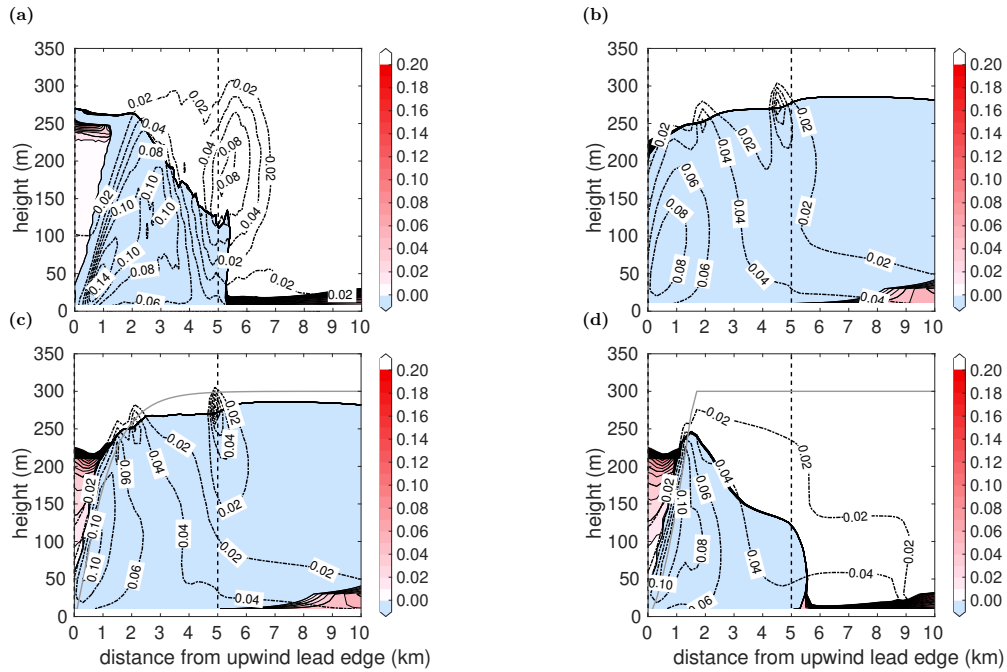


Figure B5: Results of the Richardson number Ri (coloured) and the momentum flux in Nm^{-2} (dashed-dotted black contour lines) for case L5c-U5 (see Table 2.1 in chapter 2) obtained with LES (a) and METRAS using different turbulence parametrizations (b, c, and d). For (b), the mixing-length closure, for (c), the non-local closure of L08 (for both, see section 2.2.2.2), and for (d), the new non-local closure (see section 2.5.1) are used. The solid grey lines show the upper IBL height according to Equation 2.11 in (c) and Equation 2.20 in (d). See chapter 2 for both equations.

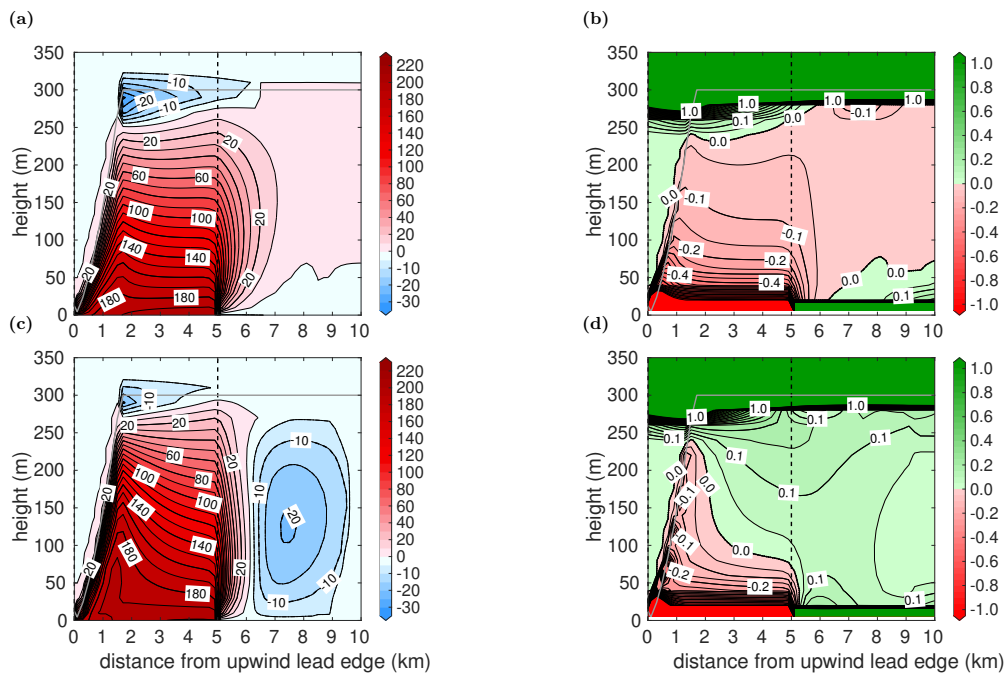


Figure B6: Sensible heat flux in Wm^{-2} (left column) and vertical potential temperature gradient in K per 100 m (right column) for case L5c-U5 (see Table 2.1 in chapter 2) obtained with METRAS using the new parametrization (section 2.5.1) as in Figures 2.7c and 2.7d, but with other values for the parameter b . In (a) and (b), $b = 0.6$ (L08 parametrization, see section 2.2.2.2) and in (c) and (d), $b = 3$ (parametrization of Lüpkes & Schlünzen, 1996). The corresponding LES results are shown in Figures 2.2c and 2.2d and the results with METRAS using the new parametrization with $b = 2$ in Figures 2.7c and 2.7d (for both, see chapter 2).

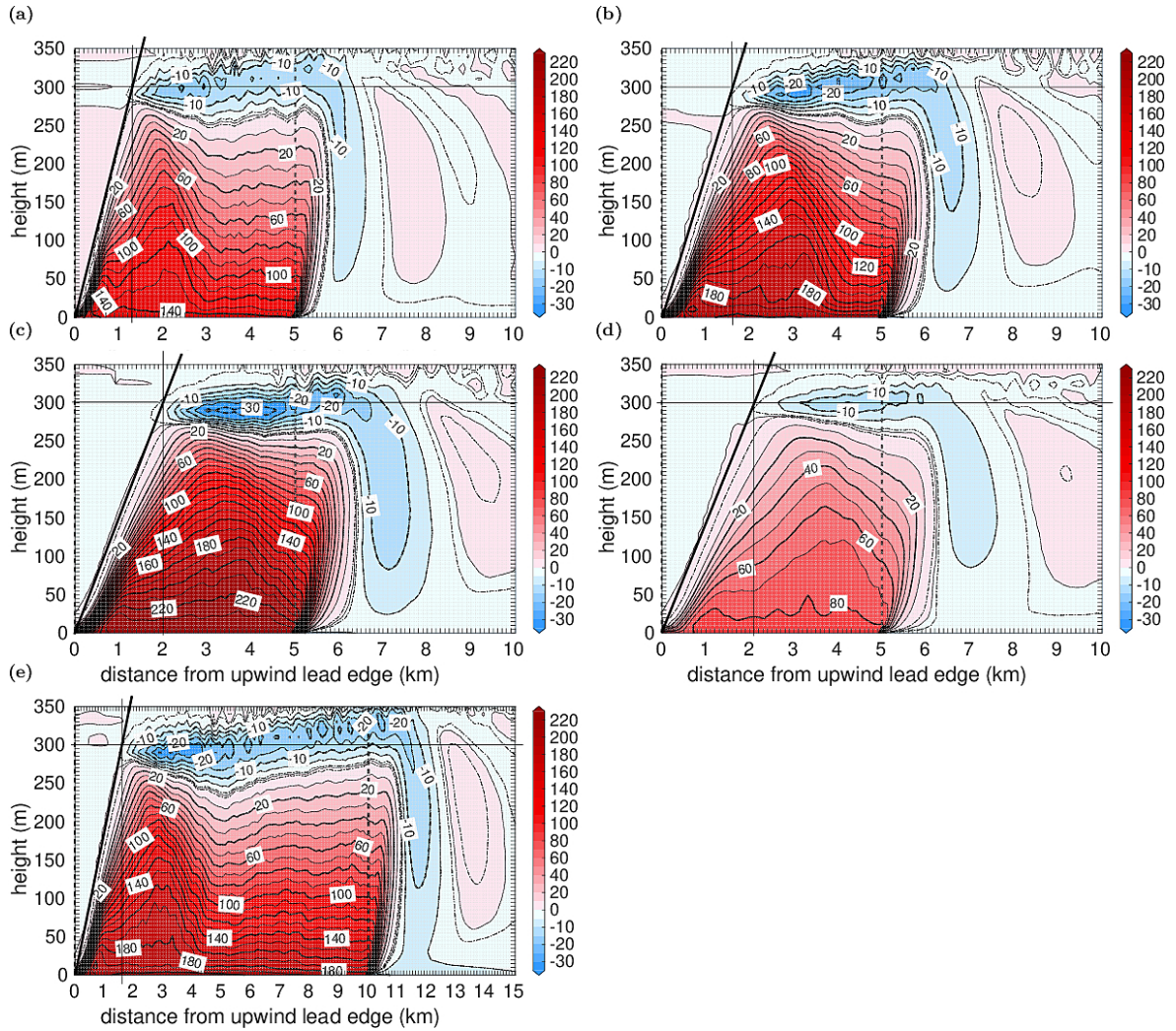


Figure B8: LES results of the sensible heat flux in Wm^{-2} for all discussed cases of wide leads (see Table 2.1 in chapter 2). (a) L5c-U3, (b) L5c-U5, (c) L5c-U7, (d) L5w-U5, and (e) L10c-U5. The leads are between 0 km distance and the vertical dashed black lines. The thin horizontal solid black lines are all at 300 m height. The thin vertical solid black lines denote the position y_{z_i} , where the internal boundary layers reach the ABL height at $z_i = 300$ m. The thick solid black lines denote a linear approximation of the internal boundary layer height. The distance between heat flux contour lines is 5 Wm^{-2} for negative fluxes. The dashed-dotted black lines mark the contour lines of 1 Wm^{-2} and -1 Wm^{-2} .

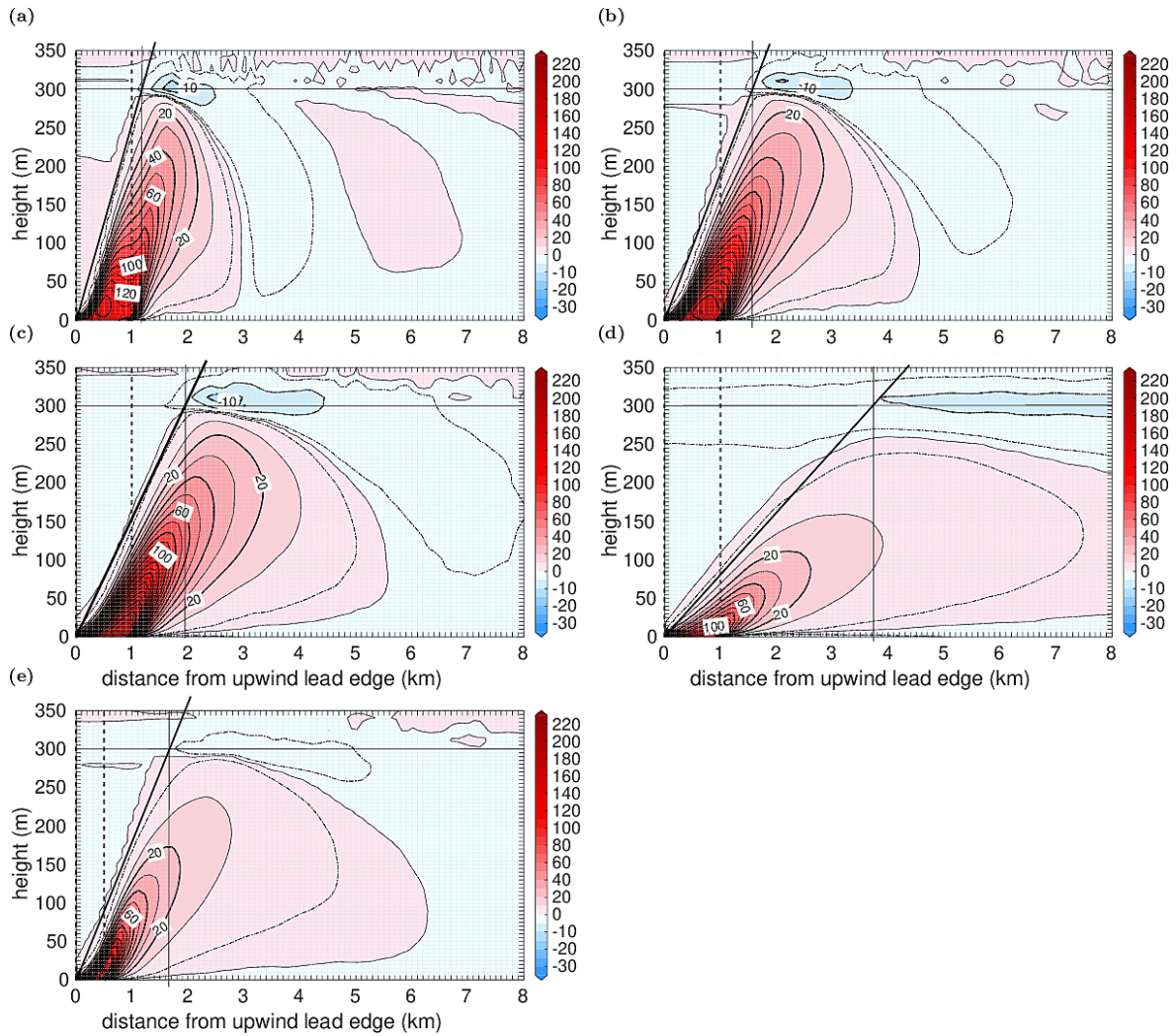


Figure B9: LES results of the sensible heat flux in Wm^{-2} for all discussed cases of narrow leads (Table 2.1 in chapter 2). (a) L1c-U3, (b) L1c-U5, (c) L1c-U7, (d) L1w-U10, and (e) L0.5c-U5. The leads are between 0 km distance and the vertical dashed black lines. The thin horizontal solid black lines are all at 300 m height. The thin vertical solid black lines denote the position y_{z_i} , where the internal boundary layers reach the ABL height at $z_i = 300$ m. The thick solid black lines denote a linear approximation of the internal boundary layer height. The distance between heat flux contour lines is 5 Wm^{-2} for negative fluxes. The dashed-dotted black lines mark the contour lines of 1 Wm^{-2} and -1 Wm^{-2} .

C Appendix for chapter 4

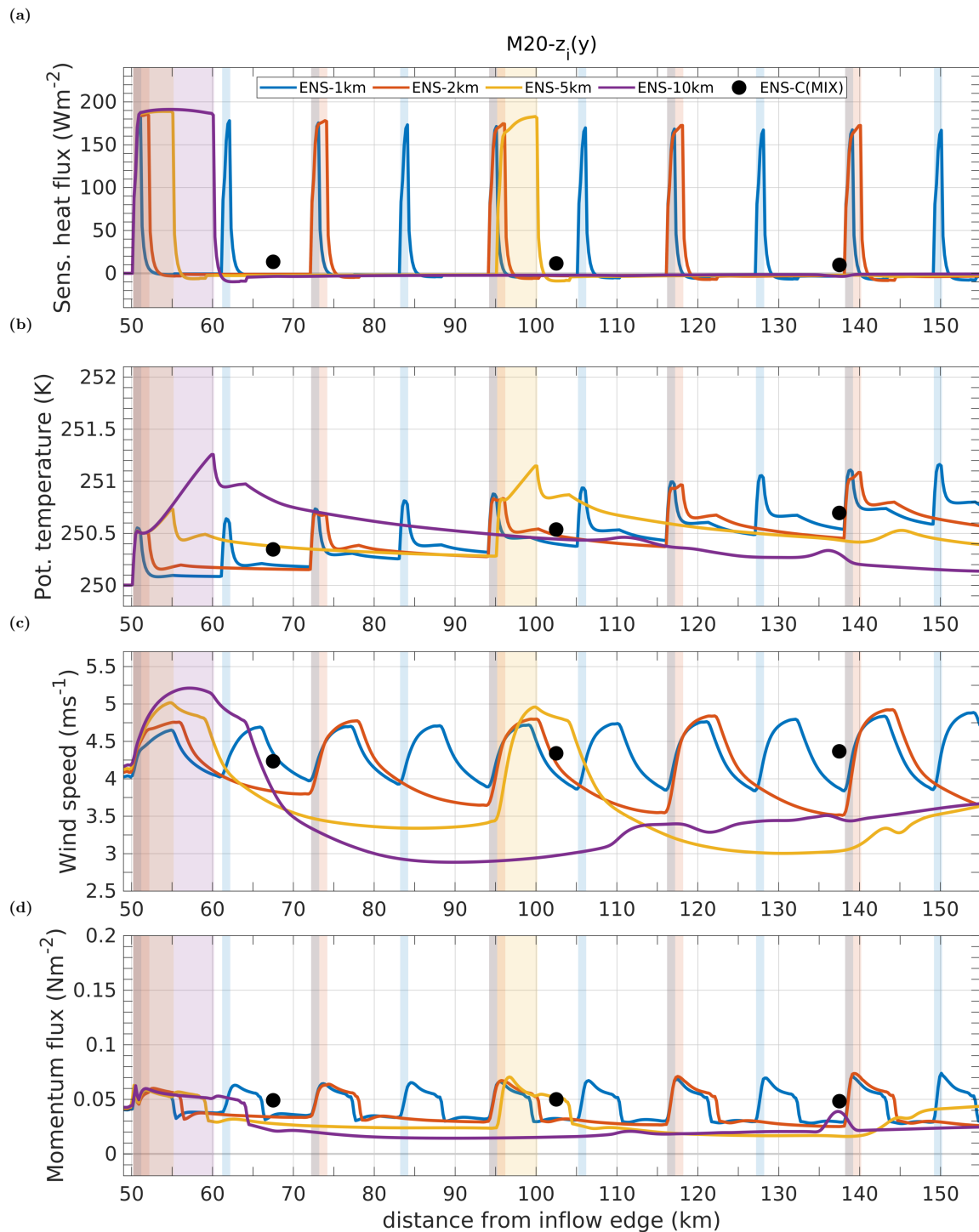


Figure C1: Same as Figure 4.6 (see chapter 4), but model results at height $z = 10$ m of the simulations "M20- $z_i(y)$ " are shown (METRAS using the non-local closure derived in section 2.5.1, but with a varying ABL height $z_i(y)$ as derived in section 3.5.1).

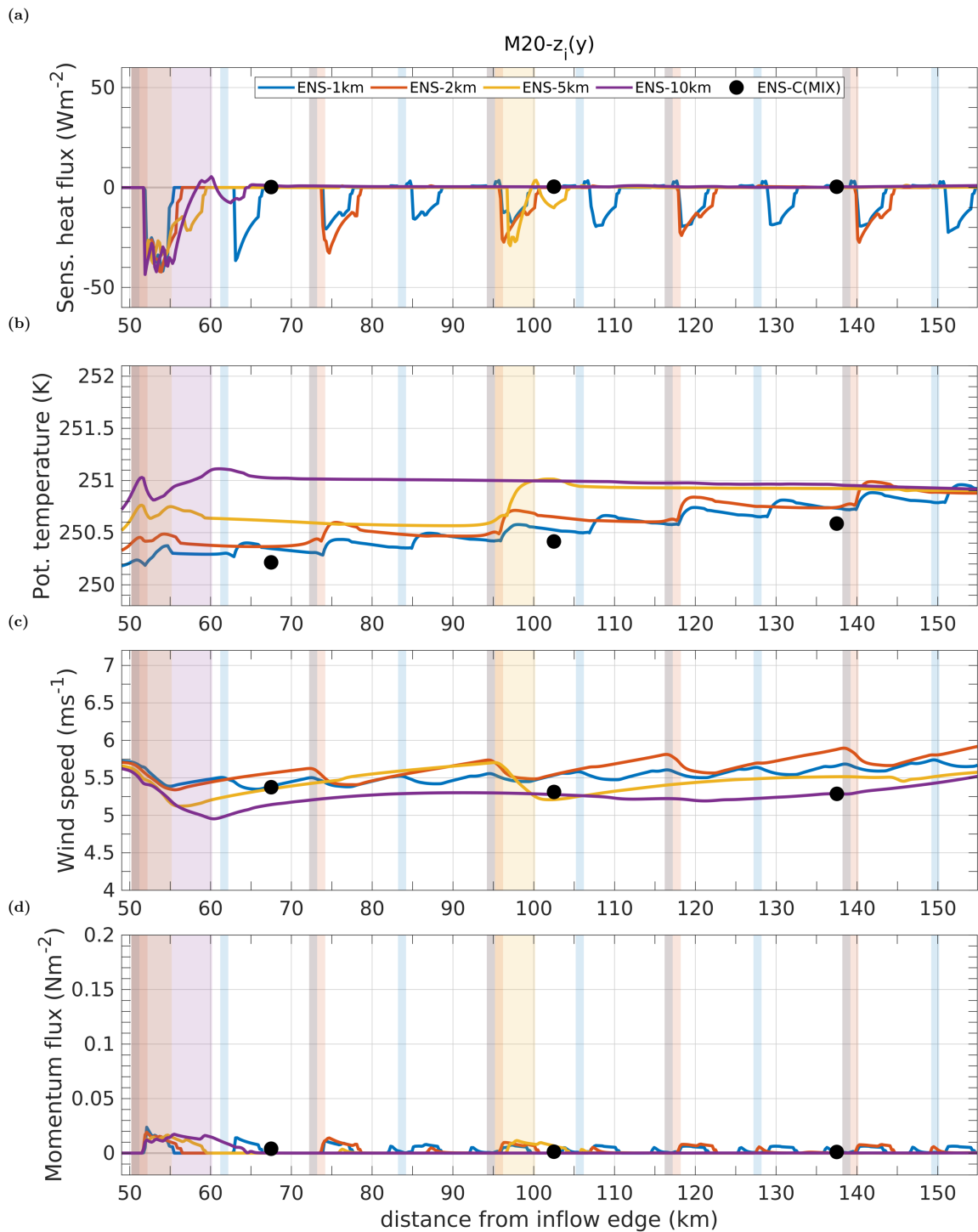


Figure C2: Same as Figure 4.7 (see chapter 4), but model results at height $z = 290$ m of the simulations "M20- $z_i(y)$ " are shown (METRAS using the non-local closure derived in section 2.5.1, but with a varying ABL height $z_i(y)$ as derived in section 3.5.1).

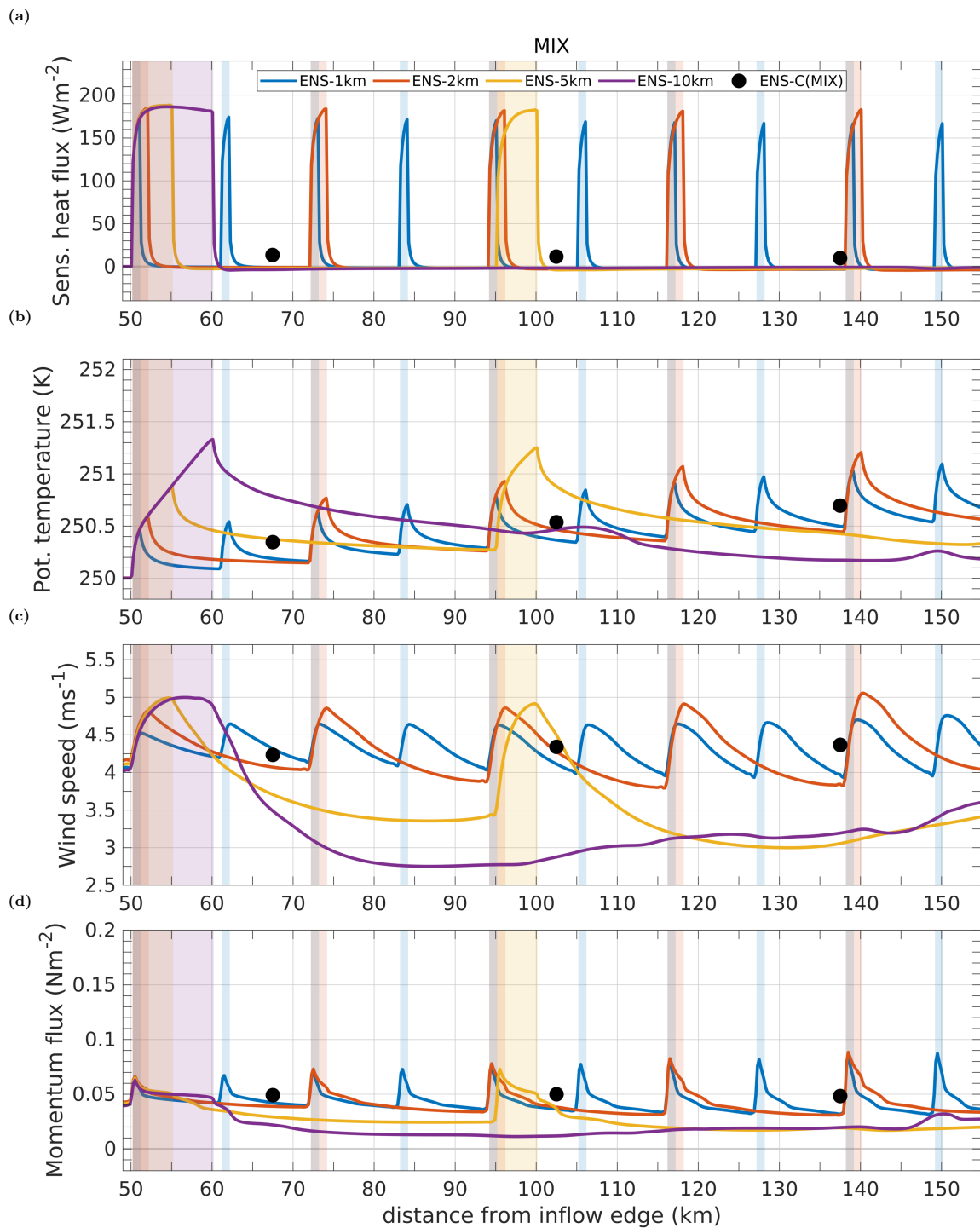


Figure C3: Same as Figure 4.6 (see chapter 4), but model results at height $z = 10$ m of the simulations "MIX" are shown (METRAS using the local closure shown in section 2.2.2.1).

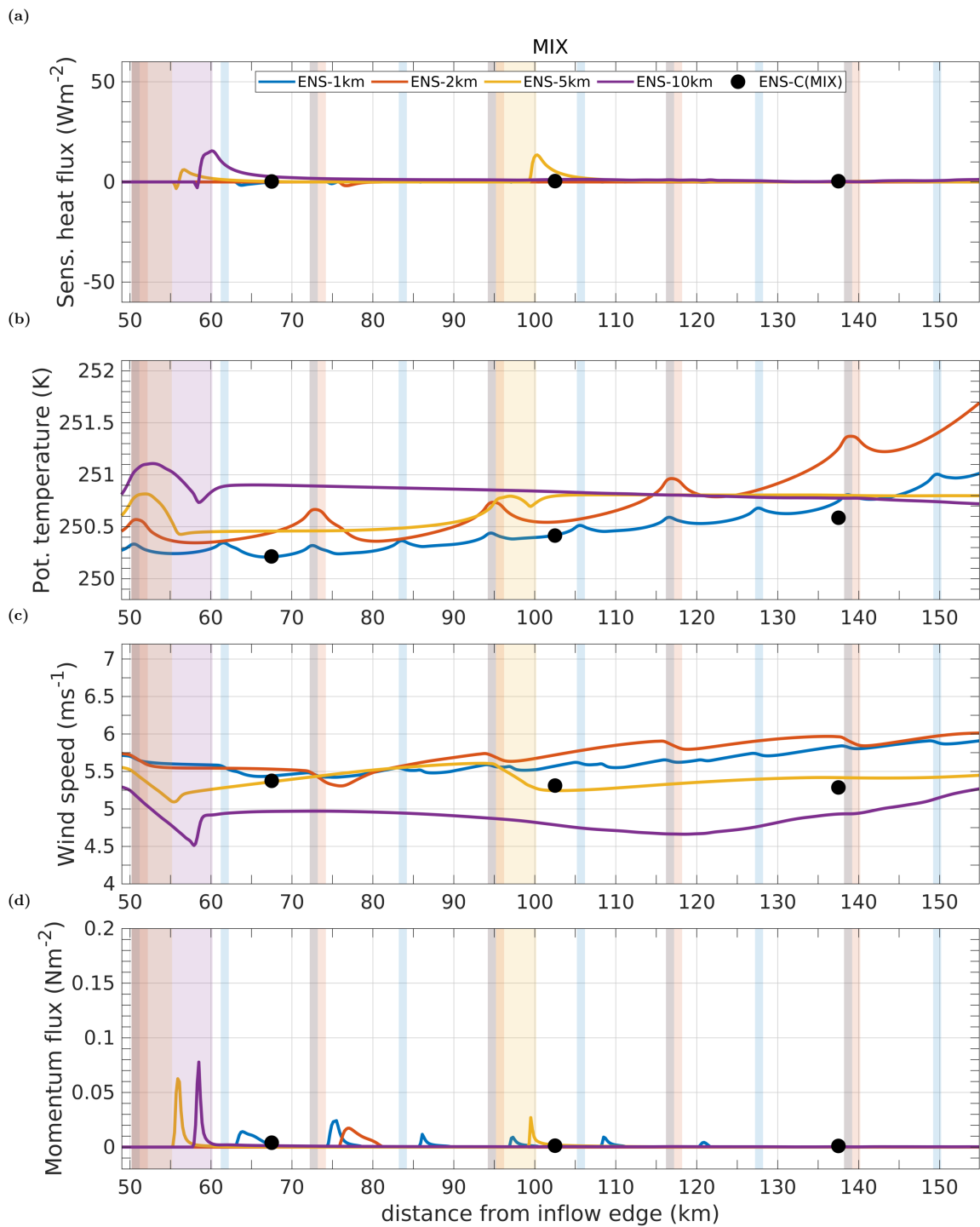


Figure C4: Same as Figure 4.7 (see chapter 4), but model results at height $z = 290$ m of the simulations "MIX" are shown (METRAS using the local closure shown in section 2.2.2.1).

Publications within this thesis

First author publication no. 1: Michaelis et al. (2020)

Janosch Michaelis, Christof Lüpkes, Xu Zhou, Micha Gryschka, and Vladimir M. Gryanik (2020). Influence of lead width on the turbulent flow over sea ice leads: Modelling and parametrization. *Journal of Geophysical Research: Atmospheres*, **125(15)**, e2019JD031996. <https://doi.org/10.1029/2019JD031996>

Author contribution

In Michaelis et al. (2020), I derived the new parametrization and implemented the equations into the code of the applied microscale model METRAS. I also selected the case studies, performed the corresponding simulations with METRAS, and evaluated and visualised all model results, including those from the applied LES model. The execution of the LES model runs was done by Xu Zhou with support by Micha Gryschka. Discussions with Christof Lüpkes and Vladimir M. Gryanik and their suggestions helped to further improve the new parametrization. Finally, I wrote the manuscript, which was reviewed and improved mainly by Christof Lüpkes. The other co-authors also contributed to the discussion and helped to improve the manuscript.

First author publication no. 2: Michaelis et al. (accept.)

Janosch Michaelis, Christof Lüpkes, Amelie U. Schmitt, and Jörg Hartmann (2020). Modelling and parametrization of the convective flow over leads in sea ice and comparison with airborne observations. *Quarterly Journal of the Royal Meteorological Society*. <https://doi.org/10.1002/qj.3953> (accepted on December 1, 2020).

Author contribution

In Michaelis et al. (accept.), I selected and performed the model simulations and derived the modifications of the applied non-local parametrization from Michaelis et al. (2020). Discussions with Christof Lüpkes and suggestions by Vladimir M. Gryanik (co-author of the above-mentioned article Michaelis et al., 2020) helped to improve these modifications. Regarding the observations from the airborne campaign STABLE, predominantly the data of Tetzlaff et al. (2015) is used, provided by Jörg Hartmann, where I performed new calculations for the observed turbulent fluxes, supported by discussions with Christof Lüpkes and Amelie U. Schmitt. Furthermore, I analysed all simulations, plotted the corresponding data, and wrote the manuscript, which was reviewed and improved mainly by Christof Lüpkes. Amelie U. Schmitt contributed to the

discussion and also helped to improve the manuscript.

Co-authored publication: Lampert et al. (2020)

A. Lampert, B. Altstädter, K. Bärfuss, L. Bretschneider, J. Sandgaard, **J. Michaelis**, L. Lobitz, M. Asmussen, E. Damm, R. Käthner, T. Krüger, C. Lüpkes, S. Nowak, A. Peuker, T. Rausch, F. Reiser, A. Scholtz, D. Sotomayor Zakharov, G. Gaus, S. Bansmer, B. Wehner and F. Pätzold. Unmanned Aerial Systems for Investigating the Polar Atmospheric Boundary Layer—Technical Challenges and Examples of Applications. *Atmosphere*, 11(4), 416.

<https://doi.org/10.3390/atmos11040416>

Author contribution

In Lampert et al. (2020), I mainly contributed to the content shown in their section 4.1, which includes the setup and the execution of the model simulation using METRAS and the visualisation of model results together with the corresponding measurements. I also wrote the text about the model simulation results in Lampert et al. (2020, their section 4.1), which was reviewed and improved by Christof Lüpkes, who also co-authored the publication.

Acronyms

- ABL** atmospheric boundary layer
- AIDJEX** Arctic Ice Dynamics Joint EXperiment
- AWI** Alfred-Wegener-Institute
- EDMF** eddy-diffusivity mass-flux scheme
- IBL** internal boundary layer
- IPCC** Intergovernmental Panel of Climate Change
- L08** Abbreviation for the reference Lüpkes, Gryanik et al., 2008
- LEADEX** Arctic Leads Experiment
- LES** large eddy simulation
- LLJ** low-level jet
- M²AV** Meteorological Mini Aerial Vehicle
- M20** Abbreviation for the reference Michaelis et al., 2020
- METRAS** MEscale TRansport And Stream model
- MIZ** Marginal (Sea) Ice Zone
- PALM** PArallelized Large Eddy Simulation model
- RANS** Reynolds-Averaged Navier-Stokes
- RV** research vessel
- SHEBA** Surface Heat Budget of the Arctic Ocean
- SIC** sea ice concentration
- STABLE** SpringTime Arctic Boundary Layer Experiment
- T15** Abbreviation for the reference Tetzlaff et al., 2015
- TKE** turbulent kinetic energy
- UAS** Unmanned Aerial System
- WARPS** Winter Arctic Polynya Study

List of symbols

Latin symbols

a adjustable parameter in parametrizations of L08 and M20

a_e adjustable parameter in parametrizations of L08 and M20

a_m adjustable parameter in parametrizations of L08 and M20

b adjustable parameter in parametrizations of, for example, L08 and M20

b_1 constant in a function linking the parameter a with the vertical potential temperature gradient

b_2 constant in a function linking the parameter a with the vertical potential temperature gradient

B_l surface buoyancy flux over the lead's surface

B_s surface buoyancy flux

c adjustable parameter in parametrizations of L08 and M20

c_p specific heat capacity of air at constant pressure

C_2 constant, used in formula for Z_{hp}

$C_{HN,r}$ bulk transfer coefficient of sensible heat at neutral stratification at reference height r

d_θ adjustable parameter in parametrization of M20

d_w adjustable parameter in parametrization of M20

D decay length scale in L08 parametrization

D_θ decay length scale for temperature fluctuations in M20 parametrization

D_w decay length scale for vertical wind fluctuations in M20 parametrization

e Euler's number

$e_{sat,i}$ saturation vapour pressure over ice

f Coriolis parameter

F_{crit} critical value for the non-local sensible heat flux (parameter in closures of L08 and M20)

F_e (vertical) turbulent latent heat flux

F_h (vertical) turbulent sensible heat flux

$F_{h,nl}$ non-local sensible heat flux

$\overline{F}_{h,s,l}$ lead-averaged surface sensible heat flux

$F_{h,s}$ surface sensible heat flux

\mathbf{F} molecular forces

F_τ total vertical turbulent flux of horizontal momentum

g gravitational acceleration

K_h eddy diffusivity for heat

K_m eddy diffusivity for momentum

K_p eddy diffusivity for heat at the surface layer's top

K_{qv} eddy diffusivity for humidity

l_3^1 specific latent heat of sublimation

l_{max} maximum mixing-length

l_n mixing-length for neutral stratification

L lead width

n empirical constant

N Brunt-Väisälä-frequency

p atmospheric pressure

p_0 surface pressure

q_v specific humidity

$q_{v,*}$ scaling value for specific humidity

$q_{v,sat}$ saturation specific humidity

Q_χ sources of χ

Ri Richardson number

R_i Individual gas constant of any compound i (e.g., R_0 for dry air)

Ri_c critical Richardson number

S stability parameter w_l/u_*

t time

T atmospheric temperature

$T_{s,i}$ surface temperature of sea ice

$T_{s,l}$ surface temperature of lead

T_s surface temperature

U_r horizontal wind speed at reference height r

u horizontal component of the wind vector in x_1 -direction

u_e horizontal entrainment velocity

u_g height-independent lead-perpendicular component of the geostrophic wind

u_* friction velocity

$u_{*,l}$ lead-averaged value of the friction velocity u_*

U vertically averaged horizontal wind speed in the upwind ABL

U_\perp lead-perpendicular component of the horizontal wind in the upwind ABL

v horizontal component of the wind vector in x_2 -direction

\mathbf{v} three-dimensional wind vector

v_g height-independent lead-parallel component of the geostrophic wind

\mathbf{v}_h horizontal wind vector

w vertical component of the wind vector (x_3 -direction)

$\overline{w'^2}$ vertical velocity variance

w_e vertical entrainment velocity

w_l fetch-dependent convective velocity scale over leads

w_{max} maximum vertical velocity of the turbulent eddies in the ABL

w_* convective velocity scale

x lead-parallel direction in the model runs

x_1 horizontal Cartesian coordinate in West-East direction

x_2 horizontal Cartesian coordinate in South-North direction

x_3 vertical Cartesian coordinate

y distance from the upwind lead edge

y_{z_i} distance y at which δ intersects with z_i

z height

z_0 roughness length for momentum

z_{qv} roughness length for humidity

z_t roughness length for heat

z_{hp} plume penetration height

z_i height of the ABL

z_p height of the surface layer's top

Z non-dimensional height z/δ

Z_p nondimensional height z_p/δ

Greek symbols

β constant entrainment coefficient

Γ counter-gradient correction term for the temperature flux

Γ_{qv} counter-gradient correction term for the humidity flux

δ upper IBL height/upper plume boundary

δ_d lower IBL height/lower plume boundary

δ_L upper IBL height/upper plume boundary at downwind lead edge

δ_{obs} observed upper IBL height/upper plume boundary

Δ_{x_1} horizontal grid increment in x_1 -direction

Δ_{x_2} horizontal grid increment in x_2 -direction

Δ_{x_3} vertical grid increment (x_3 -direction)

θ potential temperature

θ_0 potential temperature in the surface layer

θ_s potential temperature at the surface

$\overline{\theta'^2}$ potential temperature variance

θ_f convective temperature scale

θ_l fetch-dependent convective temperature scale over leads

θ_r potential temperature at reference height r

θ_* scaling value for temperature

$\theta_{*,l}$ lead-averaged value of the scaling value for temperature θ_*

$(\partial\theta/\partial z)_p$ constant in a function linking the parameter a with the vertical potential temperature gradient

κ Kármán's constant

ν_i specific volume of any compound i

ρ air density

ρ_0 basic state air density

$\sigma_{T_{s,l}}$ standard deviation in the surface temperature of a lead

τ eddy turnover time

τ_m subgrid time scale for momentum

τ_h subgrid time scale for heat

ϕ any quantity

$\bar{\phi}$ mean value of any quantity ϕ

ϕ' (turbulent) fluctuation of any quantity ϕ

Φ geopotential

Φ_h Monin-Obukhov similarity function for heat

Φ_m Monin-Obukhov similarity function for momentum

χ any scalar quantity

Ω angular velocity of the Earth

Mathematical operators

∇ Nabla operator

\mathcal{O} order of magnitude

Bibliography

- Alam, A., & Curry, J. A. (1995). Lead-induced atmospheric circulations. *Journal of Geophysical Research: Oceans*, *100*(C3), 4643–4651. doi: <https://doi.org/10.1029/94JC02562>
- Alam, A., & Curry, J. A. (1997). Determination of surface turbulent fluxes over leads in Arctic sea ice. *Journal of Geophysical Research: Oceans*, *102*(C2), 3331–3343. doi: <https://doi.org/10.1029/96JC03606>
- Andreas, E. L., & Cash, B. A. (1999). Convective heat transfer over wintertime leads and polynyas. *Journal of Geophysical Research: Oceans*, *104*(C11), 25721–25734. doi: <https://doi.org/10.1029/1999JC900241>
- Andreas, E. L., Guest, P. S., Persson, P. O. G., Fairall, C. W., Horst, T. W., Moritz, R. E., & Semmer, S. R. (2002). Near-surface water vapor over polar sea ice is always near ice saturation. *Journal of Geophysical Research: Oceans*, *107*(C10), SHE 8-1-SHE 8-15. doi: <https://doi.org/10.1029/2000JC000411>
- Andreas, E. L., Horst, T. W., Grachev, A. A., Persson, P. O. G., Fairall, C. W., Guest, P. S., & Jordan, R. E. (2010). Parametrizing turbulent exchange over summer sea ice and the marginal ice zone. *Quarterly Journal of the Royal Meteorological Society*, *136*(649), 927–943. doi: <https://doi.org/10.1002/qj.618>
- Andreas, E. L., & Murphy, B. (1986). Bulk transfer coefficients for heat and momentum over leads and polynyas. *Journal of Physical Oceanography*, *16*(11), 1875–1883. doi: [https://doi.org/10.1175/1520-0485\(1986\)016<1875:BTCFHA>2.0.CO;2](https://doi.org/10.1175/1520-0485(1986)016<1875:BTCFHA>2.0.CO;2)
- Andreas, E. L., Paulson, C. A., William, R. M., Lindsay, R. W., & Businger, J. A. (1979). The turbulent heat flux from Arctic leads. *Boundary-Layer Meteorology*, *17*(1), 57–91. doi: <https://doi.org/10.1007/BF00121937>
- Badgley, F. I. (1966). Heat balance at the surface of the Arctic Ocean. *Proceedings of the Symposium on the Arctic Heat Budget and Atmospheric Circulation*, 215–246.
- Bange, J., Beyrich, F., & Engelbart, D. A. M. (2002). Airborne measurements of turbulent fluxes during LITFASS-98: Comparison with ground measurements and remote sensing in a case study. *Theoretical and applied climatology*, *73*(1-2), 35–51. doi: <https://doi.org/10.1007/s00704-002-0692-6>
- Batrak, Y., & Müller, M. (2018). Atmospheric response to kilometer-scale changes in sea ice concentration within the marginal ice zone. *Geophysical Research Letters*, *45*(13), 6702–6709. doi: <https://doi.org/10.1029/2018GL078295>
- Blackadar, A. K. (1962). The vertical distribution of wind and turbulent exchange in a neutral atmosphere. *Journal of Geophysical Research*, *67*(8), 3095–3102. doi: <https://doi.org/10.1029/JZ067i008p03095>

- Blackadar, A. K. (2012). *Turbulence and diffusion in the atmosphere: lectures in Environmental Sciences*. Springer. doi: <https://doi.org/10.1007/978-3-642-60481-2>
- Brown, A. R. (1996). Evaluation of parametrization schemes for the convective boundary layer using large-eddy simulation results. *Boundary-Layer meteorology*, *81*(2), 167–200. doi: <https://doi.org/10.1007/BF00119064>
- Budyko, M. I. (1969). The effect of solar radiation variations on the climate of the Earth. *tellus*, *21*(5), 611–619. doi: <https://doi.org/10.3402/tellusa.v21i5.10109>
- Burk, S. D., Fett, R. W., & Englebretson, R. E. (1997). Numerical simulation of cloud plumes emanating from Arctic leads. *Journal of Geophysical Research: Atmospheres*, *102*(D14), 16529–16544. doi: <https://doi.org/10.1029/97JD00339>
- Businger, J. A., Wyngaard, J. C., Izumi, Y., & Bradley, E. F. (1971). Flux-profile relationships in the atmospheric surface layer. *Journal of the Atmospheric Sciences*, *28*(2), 181–189. doi: [https://doi.org/10.1175/1520-0469\(1971\)028<0181:FPRITA>2.0.CO;2](https://doi.org/10.1175/1520-0469(1971)028<0181:FPRITA>2.0.CO;2)
- Chechin, D. G., & Lüpkes, C. (2017). Boundary-layer development and low-level baroclinicity during high-latitude cold-air outbreaks: A simple model. *Boundary-Layer Meteorology*, *162*(1), 91–116. doi: <https://doi.org/10.1007/s10546-016-0193-2>
- Chechin, D. G., Makhotina, I. A., Lüpkes, C., & Makshtas, A. P. (2019). Effect of wind speed and leads on clear-sky cooling over Arctic sea ice during polar night. *Journal of the Atmospheric Sciences*, *76*(8), 2481–2503. doi: <https://doi.org/10.1175/JAS-D-18-0277.1>
- Cohen, J., Screen, J. A., Furtado, J. C., Barlow, M., Whittleston, D., Coumou, D., Francis, J., Dethloff, K., Entekhabi, D., Overland, J., & Jones, J. (2014). Recent Arctic amplification and extreme mid-latitude weather. *Nature Geoscience*, *7*(9), 627–637. doi: <https://doi.org/10.1038/ngeo2234>
- Dare, R. A., & Atkinson, B. W. (1999). Numerical modeling of atmospheric response to polynyas in the Southern Ocean sea ice zone. *Journal of Geophysical Research: Atmospheres*, *104*(D14), 16691–16708. doi: <https://doi.org/10.1029/1999JD900137>
- Dare, R. A., & Atkinson, B. W. (2000). Atmospheric response to spatial variations in concentration and size of polynyas in the Southern Ocean sea-ice zone. *Boundary-Layer Meteorology*, *94*(1), 65–88. doi: <https://doi.org/10.1023/A:1002442212593>
- Deardorff, J. W. (1970). Convective velocity and temperature scales for the unstable planetary boundary layer and for Rayleigh convection. *Journal of the atmospheric sciences*, *27*(8), 1211–1213. doi: [https://doi.org/10.1175/1520-0469\(1970\)027<1211:CVATSF>2.0.CO;2](https://doi.org/10.1175/1520-0469(1970)027<1211:CVATSF>2.0.CO;2)
- Deardorff, J. W. (1972). Theoretical expression for the countergradient vertical heat flux. *Journal of Geophysical Research*, *77*(30), 5900–5904. doi: <https://doi.org/10.1029/JC077i030p05900>

- Deardorff, J. W., & Peterson, E. W. (1980). The boundary-layer growth equation with Reynolds averaging. *Journal of the Atmospheric Sciences*, 37(6), 1405–1409. doi: [https://doi.org/10.1175/1520-0469\(1980\)037<1405:TBLGEW>2.0.CO;2](https://doi.org/10.1175/1520-0469(1980)037<1405:TBLGEW>2.0.CO;2)
- Deardorff, J. W., Willis, G. E., & Stockton, B. (1980). Laboratory studies of the entrainment zone of a convectively mixed layer. *Journal of Fluid Mechanics*, 100(1), 41–64. doi: <https://doi.org/10.1017/S0022112080001000>
- De Roode, S. R., Frederikse, T., Siebesma, A. P., Ackerman, A. S., Chylik, J., Field, P. R., Fricke, J., Gryscha, M., Hill, A., Honnert, R., Krueger, S. K., Lac, C., Lesage, A. T., & Tomassini, L. (2019). Turbulent transport in the gray zone: A large eddy model intercomparison study of the CONSTRAIN cold air outbreak case. *Journal of Advances in Modeling Earth Systems*, 11(3), 597–623. doi: <https://doi.org/10.1029/2018MS001443>
- Dyer, A. J. (1974). A review of flux-profile relationships. *Boundary-Layer Meteorology*, 7(3), 363–372. doi: <https://doi.org/10.1007/BF00240838>
- Ebert, E. E., & Curry, J. A. (1993). An intermediate one-dimensional thermodynamic sea ice model for investigating ice-atmosphere interactions. *Journal of Geophysical Research: Oceans*, 98(C6), 10085–10109. doi: <https://doi.org/10.1029/93JC00656>
- Ebner, L., Schröder, D., & Heinemann, G. (2011). Impact of Laptev Sea flaw polynyas on the atmospheric boundary layer and ice production using idealized mesoscale simulations. *Polar Research*, 30(1), 7210. doi: <https://doi.org/10.3402/polar.v30i0.7210>
- Esau, I. N. (2007). Amplification of turbulent exchange over wide Arctic leads: Large-eddy simulation study. *Journal of Geophysical Research: Atmospheres*, 112(D8). doi: <https://doi.org/10.1029/2006JD007225>
- Esau, I. N., & Sorokina, S. (2010). Climatology of the arctic planetary boundary layer. In P. R. Lang & F. S. Lombargo (Eds.), *Atmospheric turbulence: Prediction, measurement, and effects* (pp. 3–58). Nova Science Publishers.
- Fiedler, E. K., Lachlan-Cope, T. A., Renfrew, I. A., & King, J. C. (2010). Convective heat transfer over thin ice covered coastal polynyas. *Journal of Geophysical Research: Oceans*, 115(C10). doi: <https://doi.org/10.1029/2009JC005797>
- Flato, G. M., Marotzke, J., Abiodun, B., Braconnot, P., Chou, S. C., Collins, W., Cox, P., Driouech, F., Emori, S., Eyring, V., Forest, C., Gleckler, P., Guilyardi, E., Jakob, C., Kattsov, V., Reason, C., & Rummukainen, M. (2013). Evaluation of Climate Models. In *Climate Change 2013: The Physical Science Basis. Contribution of Working Group I to the Fifth Assessment Report of the Intergovernmental Panel on Climate Change* [Stocker, T. F., D. Qin, G.-K. Plattner, M., Tignor, S. K. Allen J. Boschung, A. Nauels, Y. Xia, V. Bex and P. M. Midgley (Eds.)]. Cambridge University Press, Cambridge, United Kingdom and New York, NY, USA.
- Flato, G. M., & Ramsden, D. (1997). Sensitivity of an atmospheric general circulation model to the parameterization of leads in sea ice. *Annals of Glaciology*, 25, 96–101. doi: <https://doi.org/10.1017/S0260305500013859>

- Fröhlich, J. (2006). *Large eddy simulation turbulenter Strömungen* (Vol. 1). Springer. doi: <https://doi.org/10.1007/978-3-8351-9051-1>
- Garratt, J. R. (1990). The internal boundary layer — a review. *Boundary-Layer Meteorology*, 50(1-4), 171–203. doi: <https://doi.org/10.1007/BF00120524>
- Garratt, J. R. (1994). The atmospheric boundary layer. *Earth-Science Reviews*, 37(1-2), 89–134. doi: [https://doi.org/10.1016/0012-8252\(94\)90026-4](https://doi.org/10.1016/0012-8252(94)90026-4)
- GISTEMP Team. (2020). *GISS Surface Temperature Analysis (GISTEMP), version 4*. NASA Goddard Institute for Space Studies. Website. (Dataset accessed 2020-08-17 at <https://data.giss.nasa.gov/gistemp/>)
- Glendening, J. W. (1994). Dependence of a plume heat budget upon lateral advection. *Journal of the Atmospheric Sciences*, 51(23), 3517–3530. doi: [https://doi.org/10.1175/1520-0469\(1994\)051<3517:DOAPHB>2.0.CO;2](https://doi.org/10.1175/1520-0469(1994)051<3517:DOAPHB>2.0.CO;2)
- Glendening, J. W., & Burk, S. D. (1992). Turbulent transport from an Arctic lead: A large-eddy simulation. *Boundary-Layer Meteorology*, 59(4), 315–339. doi: <https://doi.org/10.1007/BF02215457>
- Gollnik, T. (2008). *Parametrisierung turbulenter Flüsse über Eisrinnen mit einem mikroskaligen Atmosphärenmodell* (Diploma thesis). Universität Bremen, Germany.
- Grachev, A. A., Andreas, E. L., Fairall, C. W., Guest, P. S., & Persson, P. O. G. (2013). The critical Richardson number and limits of applicability of local similarity theory in the stable boundary layer. *Boundary-Layer Meteorology*, 147(1), 51–82. doi: <https://doi.org/10.1007/s10546-012-9771-0>
- Grachev, A. A., Fairall, C. W., Persson, P. O. G., Andreas, E. L., & Guest, P. S. (2005). Stable boundary-layer scaling regimes: the SHEBA data. *Boundary-layer meteorology*, 116(2), 201–235. doi: <https://doi.org/10.1007/s10546-004-2729-0>
- Grötzner, A., Sausen, R., & Claussen, M. (1996). The impact of sub-grid scale sea-ice inhomogeneities on the performance of the atmospheric general circulation model ECHAM3. *Climate Dynamics*, 12(7), 477–496. doi: <https://doi.org/10.1007/s003820050122>
- Gryschka, M., Drüe, C., Etling, D., & Raasch, S. (2008). On the influence of sea-ice inhomogeneities onto roll convection in cold-air outbreaks. *Geophysical Research Letters*, 35(23). doi: <https://doi.org/10.1029/2008GL035845>
- Gryschka, M., Fricke, J., & Raasch, S. (2014). On the impact of forced roll convection on vertical turbulent transport in cold air outbreaks. *Journal of Geophysical Research: Atmospheres*, 119(22), 12–513. doi: <https://doi.org/10.1002/2014JD022160>
- Hartmann, J., Albers, F., Argentini, S., Borchert, A., Bonafé, U., Cohrs, W., Conidi, A., Freese, D., Georgiadis, T., Ippoliti, A., Kaleschke, L., Lüpkes, C., Maixner, U., Mastrantonio, G., Ravegnani, F., Reuter, A., Trivellone, G., & Viola, A. (1999). Arctic Radiation and

Turbulence Interaction Study (ARTIST). *Berichte zur Polarforschung*, 305. doi: https://doi.org/10.2312/BzP_0305_1999

Hartmann, J., Kottmeier, C., & Wamser, C. (1992). Radiation and Eddy Flux Experiment 1991 (REFLEX I). *Berichte zur Polarforschung*, 105. doi: https://doi.org/10.2312/BzP_0105_1992

Herbert, F., & Kramm, G. (1985). Trockene Deposition reaktionsträger Substanzen, beschrieben mit einem diagnostischen Modell der bodennahen Luftschicht. In: Becker K.H., Löbel J. (Eds.) *Atmosphärische Spurenstoffe und ihr physikalisch-chemisches Verhalten*. doi: https://doi.org/10.1007/978-3-642-70531-1_11

Holtslag, A. A. M., & Moeng, C.-H. (1991). Eddy diffusivity and countergradient transport in the convective atmospheric boundary layer. *Journal of the Atmospheric Sciences*, 48(14), 1690–1698. doi: [https://doi.org/10.1175/1520-0469\(1991\)048<1690:EDACTI>2.0.CO;2](https://doi.org/10.1175/1520-0469(1991)048<1690:EDACTI>2.0.CO;2)

Hutter, N., Losch, M., & Menemenlis, D. (2018). Scaling properties of arctic sea ice deformation in a high-resolution viscous-plastic sea ice model and in satellite observations. *Journal of Geophysical Research: Oceans*, 123(1), 672–687. doi: <https://doi.org/10.1002/2017JC013119>

IPCC. (2013). *Climate Change 2013: The Physical Science Basis. Contribution of Working Group I to the Fifth Assessment Report of the Intergovernmental Panel on Climate Change* [Stocker, T. F., D. Qin, G.-K. Plattner, M., Tignor, S. K. Allen J. Boschung, A. Nauels, Y. Xia, V. Bex and P. M. Midgley (Eds.)]. Cambridge University Press, Cambridge, United Kingdom and New York, NY, USA, 1535 pp.

IPCC. (2014). Climate Change 2014: Synthesis Report. Contribution of Working Groups I, II and III to the Fifth Assessment Report of the Intergovernmental Panel on Climate Change. In *Climate Change 2013: The Physical Science Basis. Contribution of Working Group I to the Fifth Assessment Report of the Intergovernmental Panel on Climate Change* [Core Writing Team, R. K. Pachauri and L.A. Meyer (Eds.)]. IPCC, Geneva, Switzerland, 151 pp.

Kataoka, H., & Mizuno, M. (2002). Numerical flow computation around aeroelastic 3 D square cylinder using inflow turbulence. *Wind and Structures*, 5(2/4), 379–392. doi: https://doi.org/10.12989/was.2002.5.2_3_4.379

König-Langlo, G. (2013a). Continuous meteorological surface measurement during POLARSTERN cruise ANT-XXIX/6 [data set]. PANGAEA. doi: <https://doi.org/10.1594/PANGAEA.820733>

König-Langlo, G. (2013b). Upper air soundings during POLARSTERN cruise ANT-XXIX/6 (AWECS) to the Antarctic in 2013. [data set]. PANGAEA. doi: <https://doi.org/10.1594/PANGAEA.842810>

Kort, E. A., Wofsy, S. C., Daube, B. C., Diao, M., Elkins, J. W., Gao, R. S., Hints, E. J., Hurst, D. F., Jimenez, R., Moore, F. L., Spackman, J. R., & Zondlo, M. A. (2012). Atmo-

spheric observations of Arctic Ocean methane emissions up to 82° north. *Nature Geoscience*, 5(5), 318–321. doi: <https://doi.org/10.1038/ngeo1452>

Kottmeier, C., Hartmann, J., Wamser, C., Bochert, A., Lüpkes, C., Freese, D., & Cohrs, W. (1994). Radiation and Eddy Flux Experiment 1993 (REFLEX II). *Berichte zur Polarforschung*, 133. doi: https://doi.org/10.2312/BzP_0133_1994

Kraus, H. (2008). *Grundlagen der Grenzschicht-Meteorologie: Einführung in die Physik der atmosphärischen Grenzschicht und in die Mikrometeorologie*. Springer-Verlag.

Lampert, A., Altstädter, B., Bärfuss, K., Bretschneider, L., Sandgaard, J., Michaelis, J., Lobitz, L., Asmussen, M., Damm, E., Käthner, R., Krüger, T., Lüpkes, C., Nowak, S., Peuker, A., Rausch, T., Reiser, F., Scholtz, A., Sotormayor Zakharov, D., Gaus, G., Bansmer, S., Wehner, B., & Pätzold, F. (2020). Unmanned Aerial Systems for Investigating the Polar Atmospheric Boundary Layer—Technical Challenges and Examples of Applications. *Atmosphere*, 11(4), 416. doi: <https://doi.org/10.3390/atmos11040416>

Lemke, P. (2014). The expedition of the research vessel "Polarstern" to the Antarctic in 2013 (ANT-XXIX/6). *Berichte zur Polar-und Meeresforschung*, 679. doi: http://doi.org/10.2312/BzPM_0679_2014

Li, X., Krueger, S. K., Strong, C., Mace, G. G., & Benson, S. (2020). Midwinter Arctic leads form and dissipate low clouds. *Nature Communications*, 11(1), 1–8. doi: <https://doi.org/10.1038/s41467-019-14074-5>

Lindsay, R. W., & Rothrock, D. A. (1994). Arctic Sea Ice Surface Temperature from AVHRR. *Journal of Climate*, 7(1), 174–183. doi: [https://doi.org/10.1175/1520-0442\(1994\)007<0174:ASISTF>2.0.CO;2](https://doi.org/10.1175/1520-0442(1994)007<0174:ASISTF>2.0.CO;2)

Lindsay, R. W., & Rothrock, D. A. (1995). Arctic sea ice leads from advanced very high resolution radiometer images. *Journal of Geophysical Research: Oceans*, 100(C3), 4533–4544. doi: <https://doi.org/10.1029/94JC02393>

Lund, T. S., Wu, X., & Squires, K. D. (1998). Generation of turbulent inflow data for spatially-developing boundary layer simulations. *Journal of computational physics*, 140(2), 233–258. doi: <https://doi.org/10.1006/jcph.1998.5882>

Lüpkes, C. (2010). Summary report on the small scale modelling of the impact of leads on the ABL, report D2.2-08 of project DAMOCLES (Developing Arctic Modelling and Observation Capabilities for long-term Environment Studies), 22 pp.

Lüpkes, C., Gryanik, V. M., Witha, B., Gryschka, M., Raasch, S., & Gollnik, T. (2008). Modeling convection over arctic leads with LES and a non-eddy-resolving microscale model. *Journal of Geophysical Research: Oceans*, 113(C9). doi: <https://doi.org/10.1029/2007JC004099>

Lüpkes, C., Hartmann, J., Birnbaum, G., Cohrs, W., Yelland, M., Pascal, R., Spiess, T., & Buschmann, M. (2004). Convection over Arctic leads (COAL). In U. Schauer & G. Kattner (Eds.), *The expedition ARKTIS XIX/1 a, b and XIX/2 of the research vessel POLARSTERN*

in 2003 (Vol. 481, p. 47-62). Alfred Wegener Institute for Polar and Marine Research. doi: https://doi.org/10.2312/BzPM_0481_2004

Lüpkes, C., & Schlünzen, K. H. (1996). Modelling the Arctic convective boundary-layer with different turbulence parameterizations. *Boundary-Layer Meteorology*, 79(1-2), 107–130. doi: <https://doi.org/10.1007/BF00120077>

Lüpkes, C., Vihma, T., Birnbaum, G., Dierer, S., Garbrecht, T., Gryanik, V. M., Gryschka, M., Hartmann, J., Heinemann, G., Kaleschke, L., Raasch, S., Savijärvi, H., Schlünzen, K. H., & Wacker, U. (2012). Mesoscale modelling of the Arctic atmospheric boundary layer and its interaction with sea ice. In *Arctic climate change* (pp. 279–324). Springer.

Lüpkes, C., Vihma, T., Birnbaum, G., & Wacker, U. (2008). Influence of leads in sea ice on the temperature of the atmospheric boundary layer during polar night. *Geophysical Research Letters*, 35(3). doi: <https://doi.org/10.1029/2007GL032461>

Makshtas, A. P., & Nikolaev, I. V. (1991). *The heat budget of Arctic ice in the winter*. International Glaciological Society.

Marcq, S., & Weiss, J. (2012). Influence of sea ice lead-width distribution on turbulent heat transfer between the ocean and the atmosphere. *The Cryosphere*, 6, 143–156. doi: <https://doi.org/10.5194/tc-6-143-2012>

Maronga, B., Gryschka, M., Heinze, R., Hoffmann, F., Kanani-Sühring, F., Keck, M., Ketelsen, K., Letzel, M. O., Sühring, M., & Raasch, S. (2015). The Parallelized Large-Eddy Simulation Model (PALM) version 4.0 for atmospheric and oceanic flows: model formulation, recent developments, and future perspectives. *Geoscientific Model Development Discussions* 8 (2015), Nr. 2, 1539–1637. doi: <https://doi.org/10.15488/27>

Massom, R. A. (1988). The biological significance of open water within the sea ice covers of the polar regions. *Endeavour*, 12(1), 21–27. doi: [https://doi.org/10.1016/0160-9327\(88\)90206-2](https://doi.org/10.1016/0160-9327(88)90206-2)

Mauritsen, T., Svensson, G., & Grisogono, B. (2005). Wave flow simulations over Arctic leads. *Boundary-Layer Meteorology*, 117(2), 259–273. doi: <https://doi.org/10.1007/s10546-004-1427-2>

Maykut, G. A. (1978). Energy exchange over young sea ice in the central Arctic. *Journal of Geophysical Research: Oceans*, 83(C7), 3646–3658. doi: <https://doi.org/10.1029/JC083iC07p03646>

Maykut, G. A. (1982). Large-scale heat exchange and ice production in the central Arctic. *Journal of Geophysical Research: Oceans*, 87(C10), 7971–7984. doi: <https://doi.org/10.1029/JC087iC10p07971>

Michaelis, J., Lüpkes, C., Schmitt, A. U., & Hartmann, J. (accept.). Modelling and parametrization of the convective flow over leads in sea ice and comparison with airborne observations. doi: <https://doi.org/10.1002/qj.3953>

- Michaelis, J., Lüpkes, C., Zhou, X., Gryschka, M., & Gryanik, V. M. (2020). Influence of lead width on the turbulent flow over sea ice leads: Modeling and parametrization. *Journal of Geophysical Research: Atmospheres*, *125*(15), e2019JD031996. doi: <https://doi.org/10.1029/2019JD031996>
- Miles, M. W., & Barry, R. G. (1998). A 5-year satellite climatology of winter sea ice leads in the western Arctic. *Journal of Geophysical Research: Oceans*, *103*(C10), 21723–21734. doi: <https://doi.org/10.1029/98JC01997>
- Monin, A. S., & Yaglom, A. M. (1971). *Statistical fluid dynamics Vol. 1*. MIT Press, Cambridge Mass.
- Müller, M., Batrak, Y., Kristiansen, J., Kjøltzow, M. A., Noer, G., & Korosov, A. (2017). Characteristics of a Convective-Scale Weather Forecasting System for the European Arctic. *Monthly Weather Review*, *145*(12), 4771–4787. doi: <https://doi.org/10.1175/MWR-D-17-0194.1>
- Neukom, R., Steiger, N., Gómez-Navarro, J. J., Wang, J., & Werner, J. P. (2019). No evidence for globally coherent warm and cold periods over the preindustrial Common Era. *Nature*, *571*, 550–554. doi: <https://doi.org/10.1038/s41586-019-1401-2>
- Nieuwstadt, F. T. M., & Brost, R. A. (1986). The decay of convective turbulence. *Journal of the Atmospheric Sciences*, *43*(6), 532–546. doi: [https://doi.org/10.1175/1520-0469\(1986\)043<0532:TDOCT>2.0.CO;2](https://doi.org/10.1175/1520-0469(1986)043<0532:TDOCT>2.0.CO;2)
- Noh, Y., Cheon, W., Hong, S., & Raasch, S. (2003). Improvement of the K-profile model for the planetary boundary layer based on large eddy simulation data. *Boundary-layer meteorology*, *107*(2), 401–427. doi: <https://doi.org/10.1023%2FA%3A1022146015946>
- Oke, T. R. (1995). The heat island of the urban boundary layer: characteristics, causes and effects. In J. E. Cermak, A. G. Davenport, E. J. Plate, & D. X. Viegas (Eds.), *Wind climate in cities* (pp. 81–107). Springer, Dordrecht. doi: https://doi.org/10.1007/978-94-017-3686-2%5C_5
- Orlanski, I. (1975). A rational subdivision of scales for atmospheric processes. *Bulletin of the American Meteorological Society*, 527–530.
- Orlanski, I. (1976). A simple boundary condition for unbounded hyperbolic flows. *Journal of computational physics*, *21*(3), 251–269. doi: [https://doi.org/10.1016/0021-9991\(76\)90023-1](https://doi.org/10.1016/0021-9991(76)90023-1)
- Overland, J. E., McNutt, S. L., Groves, J., Salo, S., Andreas, E. L., & Persson, P. O. G. (2000). Regional sensible and radiative heat flux estimates for the winter Arctic during the Surface Heat Budget of the Arctic Ocean (SHEBA) experiment. *Journal of Geophysical Research: Oceans*, *105*(C6), 14093–14102. doi: <https://doi.org/10.1029/1999JC000010>
- Paulson, C. A., & Smith, J. D. (1974). The AIDJEX lead experiment. In A. Johnson (Ed.), *AIDJEX Bulletin No. 23* (p. 1-8). Seattle, Washington: University of Washington.

Persson, P. O. G., Fairall, C. W., Andreas, E. L., Guest, P. S., & Perovich, D. K. (2002). Measurements near the Atmospheric Surface Flux Group tower at SHEBA: Near-surface conditions and surface energy budget. *Journal of Geophysical Research: Oceans*, *107*(C10), SHE-21. doi: <https://doi.org/10.1029/2000JC000705>

Persson, P. O. G., Ruffieux, D., & Fairall, C. (1997). Recalculations of pack ice and lead surface energy budgets during the Arctic Leads Experiment (LEADDEX) 1992. *Journal of Geophysical Research: Oceans*, *102*(C11), 25085–25089. doi: <https://doi.org/10.1029/97JC02045>

Pielke Sr., R. A. (2013). *Mesoscale meteorological modeling*. Academic Press.

Pinto, J. O., Alam, A., Maslanik, J. A., Curry, J. A., & Stone, R. S. (2003). Surface characteristics and atmospheric footprint of springtime Arctic leads at SHEBA. *Journal of Geophysical Research: Oceans*, *108*(C4). doi: <https://doi.org/10.1029/2000JC000473>

Pinto, J. O., Curry, J. A., & McInnes, K. L. (1995). Atmospheric convective plumes emanating from leads: 1. Thermodynamic structure. *Journal of Geophysical Research: Oceans*, *100*(C3), 4621–4631. doi: <https://doi.org/10.1029/94JC02654>

Priestley, C. H. B., & Swinbank, W. C. (1947). Vertical transport of heat by turbulence in the atmosphere. *Proceedings of the Royal Society of London. Series A. Mathematical and Physical Sciences*, *189*(1019), 543–561. doi: <https://doi.org/10.1098/rspa.1947.0057>

Pruppacher, H. R., & Klett, J. D. (2010). Microstructure of atmospheric clouds and precipitation. In *Microphysics of Clouds and Precipitation, Vol. 18* (pp. 10–73). Springer, Dordrecht. doi: https://doi.org/10.1007/978-0-306-48100-0_2

Raasch, S., & Schröter, M. (2001). PALM - A large-eddy simulation model performing on massively parallel computers. *Meteorologische Zeitschrift*, *10*(5), 363–372. doi: <https://doi.org/10.1127/0941-2948/2001/0010-0363>

Renfrew, I. A., & King, J. C. (2000). A simple model of the convective internal boundary layer and its application to surface heat flux estimates within polynyas. *Boundary-layer meteorology*, *94*(3), 335–356. doi: <https://doi.org/10.1023/A:1002492412097>

Ruffieux, D., Persson, P. O. G., Fairall, C. W., & Wolfe, D. E. (1995). Ice pack and lead surface energy budgets during LEADDEX 1992. *Journal of Geophysical Research: Oceans*, *100*(C3), 4593–4612. doi: <https://doi.org/10.1029/94JC02485>

Savelyev, S. A., & Taylor, P. A. (2005). Internal boundary layers: I. Height formulae for neutral and diabatic flows. *Boundary-Layer Meteorology*, *115*(1), 1–25. doi: <https://doi.org/10.1007/s10546-004-2122-z>

Schlünzen, K. H., Bungert, U., Flagg, D. D., Fock, B. H., Gierisch, A., Grawe, D., Kirschner, P., Lüüpkes, C., Reinhardt, V., Ries, H., Schoetter, R., Spensberger, C., & Uphoff, M. (2012). Technical Documentation of the Multiscale Model System M-SYS (METRAS, MITRAS, MECTM, MICTM, MESIM) (Tech. Rep. No. 3).

<https://www.mi.uni-hamburg.de/en/arbeitsgruppen/memi/modelle/dokumentation/msys-technical-documentation.pdf>: Meteorologisches Institut, Universität Hamburg.

Schlünzen, K. H., Flagg, D. D., Fock, B. H., Gierisch, A., Lüüpkes, C., Reinhardt, V., & Spensberger, C. (2012). Scientific Documentation of the Multiscale Model System M-SYS (METRAS, MITRAS, MECTM, MICTM, MESIM) (Tech. Rep. No. 4). <https://www.mi.uni-hamburg.de/en/arbeitsgruppen/memi/modelle/dokumentation/msys-scientific-documentation.pdf>: Meteorologisches Institut, Universität Hamburg.

Schnell, R. C., Barry, R. G., Miles, M. W., Andreas, E. L., Radke, L. F., Brock, C. A., McCormick, M. P., & Moore, J. L. (1989). Lidar detection of leads in Arctic sea ice. *Nature*, 339(6225), 530. doi: <https://doi.org/10.1038/339530a0>

Sellers, W. D. (1969). A global climatic model based on the energy balance of the earth-atmosphere system. *Journal of Applied Meteorology*, 8(3), 392–400. doi: [https://doi.org/10.1175/1520-0450\(1969\)008<0392:AGCMBO>2.0.CO;2](https://doi.org/10.1175/1520-0450(1969)008<0392:AGCMBO>2.0.CO;2)

Serreze, M. C., Barrett, A. P., Stroeve, J. C., Kindig, D. N., & Holland, M. M. (2009). The emergence of surface-based Arctic amplification. *The Cryosphere*, 3(1), 11. doi: <https://doi.org/10.5194/tc-3-11-2009>

Serreze, M. C., & Barry, R. G. (2011). Processes and impacts of arctic amplification: A research synthesis. *Global and Planetary Change*, 77(1), 85 - 96. doi: <https://doi.org/10.1016/j.gloplacha.2011.03.004>

Serreze, M. C., & Francis, J. A. (2006). The Arctic amplification debate. *Climatic change*, 76(3-4), 241–264. doi: <https://doi.org/10.1007/s10584-005-9017-y>

Siebesma, A. P., Soares, P. M. M., & Teixeira, J. (2007). A combined eddy-diffusivity mass-flux approach for the convective boundary layer. *Journal of the atmospheric sciences*, 64(4), 1230–1248. doi: <https://doi.org/10.1175/JAS3888.1>

SIMIP Community. (2020). Arctic Sea Ice in CMIP6. *Geophysical Research Letters*, 47(10), e2019GL086749. doi: <https://doi.org/10.1029/2019GL086749>

Skyllingstad, E. D., & Denbo, D. W. (2001). Turbulence beneath sea ice and leads: A coupled sea ice/large-eddy simulation study. *Journal of Geophysical Research: Oceans*, 106(C2), 2477–2497. doi: <https://doi.org/10.1029/1999JC000091>

Smith, S. D., Anderson, R. J., Hartog, G. D., Topham, D. R., & Perkin, R. G. (1983). An investigation of a polynya in the Canadian Archipelago: 2. Structure of turbulence and sensible heat flux. *Journal of Geophysical Research: Oceans*, 88(C5), 2900–2910. doi: <https://doi.org/10.1029/JC088iC05p02900>

Smith, S. D., Muench, R. D., & Pease, C. H. (1990). Polynyas and leads: An overview of physical processes and environment. *Journal of Geophysical Research: Oceans*, 95(C6), 9461–9479. doi: <https://doi.org/10.1029/JC095iC06p09461>

- Spiess, T., Bange, J., Buschmann, M., & Vörsmann, P. (2007). First application of the meteorological Mini-UAV 'M2AV'. *Meteorologische Zeitschrift*, *16*(2), 159–169. doi: <https://doi.org/10.1127/0941-2948/2007/0195>
- Stirling, I. (1997). The importance of polynyas, ice edges, and leads to marine mammals and birds. *Journal of Marine Systems*, *10*(1-4), 9–21. doi: [https://doi.org/10.1016/S0924-7963\(96\)00054-1](https://doi.org/10.1016/S0924-7963(96)00054-1)
- Stull, R. B. (1988). *An introduction to boundary layer meteorology*. Dordrecht, The Netherlands: Kluwer Academic Publishers. doi: <https://doi.org/10.1007/978-94-009-3027-8>
- Sullivan, P. P., Moeng, C.-H., Stevens, B., Lenschow, D. H., & Mayor, S. D. (1998). Structure of the entrainment zone capping the convective atmospheric boundary layer. *Journal of the Atmospheric Sciences*, *55*(19), 3042–3064. doi: [https://doi.org/10.1175/1520-0469\(1998\)055<3042:SOTEZC>2.0.CO;2](https://doi.org/10.1175/1520-0469(1998)055<3042:SOTEZC>2.0.CO;2)
- Taylor, P. C., Hegyi, B. M., Boeke, R. C., & Boisvert, L. N. (2018). On the increasing importance of air-sea exchanges in a thawing Arctic: a review. *Atmosphere*, *9*(2), 41. doi: <https://doi.org/10.3390/atmos9020041>
- Tetzlaff, A. (2016). *Convective processes in the polar atmospheric boundary layer: a study based on measurements and modeling* (Doctoral dissertation). Retrieved from epic.awi.de (<http://hdl.handle.net/10013/epic.46755>). Bremen, Germany: Universität Bremen.
- Tetzlaff, A., Lüpkes, C., & Hartmann, J. (2015). Aircraft-based observations of atmospheric boundary-layer modification over Arctic leads. *Quarterly Journal of the Royal Meteorological Society*, *141*(692), 2839–2856. doi: <https://doi.org/10.1002/qj.2568>
- Thorndike, A. S., Rothrock, D. A., Maykut, G. A., & Colony, R. (1975). The thickness distribution of sea ice. *Journal of Geophysical Research*, *80*(33), 4501–4513. doi: <https://doi.org/10.1029/JC080i033p04501>
- Troen, I. B., & Mahrt, L. (1986). A simple model of the atmospheric boundary layer; sensitivity to surface evaporation. *Boundary-Layer Meteorology*, *37*(1-2), 129–148. doi: <https://doi.org/10.1007/BF00122760>
- Turner, J. S. (1986). Turbulent entrainment: the development of the entrainment assumption, and its application to geophysical flows. *Journal of Fluid Mechanics*, *173*, 431–471. doi: <https://doi.org/10.1017/S0022112086001222>
- Valkonen, T., Vihma, T., & Doble, M. (2008). Mesoscale modeling of the atmosphere over Antarctic sea ice: A late-autumn case study. *Monthly weather review*, *136*(4), 1457–1474. doi: <https://doi.org/10.1175/2007MWR2242.1>
- Vihma, T. (2014). Effects of Arctic sea ice decline on weather and climate: A review. *Surveys in Geophysics*, *35*(5), 1175–1214. doi: <https://doi.org/10.1007/s10712-014-9284-0>

- Vihma, T., Pirazzini, R., Fer, I., Renfrew, I. A., Sedlar, J., Tjernström, M., Lüpkes, C., Nygard, T., Notz, D., Weiss, J., Marsan, D., Cheng, B., Birnbaum, G., Gerland, S., Chechin, D., & Gascard, J. C. (2014). Advances in understanding and parameterization of small-scale physical processes in the marine Arctic climate system: a review. *Atmospheric Chemistry and Physics (ACP)*, *14*(17), 9403–9450. doi: <https://doi.org/10.5194/acpd-13-32703-2013>
- von Salzen, K., M. Claussen, M., & Schlünzen, K. H. (1996). Application of the concept of blending height to the calculation of surface fluxes in a mesoscale model. *Meteorologische Zeitschrift*, *5*(2), 60-66. doi: <https://dx.doi.org/10.1127/metz/5/1996/60>
- Wang, Q., Danilov, S., Jung, T., Kaleschke, L., & Wernecke, A. (2016). Sea ice leads in the Arctic Ocean: Model assessment, interannual variability and trends. *Geophysical Research Letters*, *43*(13), 7019-7027. doi: <https://doi.org/10.1002/2016GL068696>
- Weinbrecht, S., & Raasch, S. (2001). High-resolution simulations of the turbulent flow in the vicinity of an Arctic lead. *Journal of Geophysical Research: Oceans*, *106*(C11), 27035–27046. doi: <https://doi.org/10.1029/2000JC000781>
- Weisman, B. (1976). On the criteria for the occurrence of fumigation inland from a large lake. *Atmospheric Environment (1967)*, *10*(2), 172–173.
- Weiss, A. I., King, J., Lachlan-Cope, T., & Ladkin, R. (2011). On the effective aerodynamic and scalar roughness length of Weddell Sea ice. *Journal of Geophysical Research: Atmospheres*, *116*(D19). doi: <https://doi.org/10.1029/2011JD015949>
- Wendisch, M., Brückner, M., Burrows, J. P., Crewell, S., Dethloff, K., Ebell, K., Lüpkes, C., Macke, A., Notholt, J., Quaas, J., Rinke, A., & Tegen, I. (2017). Understanding causes and effects of rapid warming in the Arctic. *Eos*, *98*. doi: <https://doi.org/10.1029/2017EO064803>
- Wenta, M., & Herman, A. (2018). The influence of the spatial distribution of leads and ice floes on the atmospheric boundary layer over fragmented sea ice. *Annals of Glaciology*, *59*(76pt2), 213–230. doi: <https://doi.org/10.1017/aog.2018.15>
- Wernecke, A., & Kaleschke, L. (2015). Lead detection in Arctic sea ice from CryoSat-2: quality assessment, lead area fraction and width distribution. *The Cryosphere*, *9*(5), 1955–1968. doi: <https://doi.org/10.5194/tc-9-1955-2015>
- Wetzel, C., & Brümmer, B. (2011). An Arctic inversion climatology based on the European Centre Reanalysis ERA-40. *Meteorologische Zeitschrift*, *20*(6), 589–600. doi: <https://doi.org/10.1127/0941-2948/2011/0295>
- Witha, B. (2013). *Untersuchung des turbulenten Wärmeflusses über Eisrinnen mit hochaufgelösten Large-Eddy Simulationen* (Doctoral dissertation). Technische Informationsbibliothek und Universitätsbibliothek Hannover (TIB).
- Zhou, X., & Gryschka, M. (2019). Convection over sea ice leads: large eddy simulation data [data set]. PANGAEA. doi: <https://doi.pangaea.de/10.1594/PANGAEA.908520>

Zulauf, M. A., & Krueger, S. K. (2003a). Two-dimensional cloud-resolving modeling of the atmospheric effects of Arctic leads based upon midwinter conditions at the Surface Heat Budget of the Arctic Ocean ice camp. *Journal of Geophysical Research: Atmospheres*, *108*(D10). doi: <https://doi.org/10.1029/2002JD002643>

Zulauf, M. A., & Krueger, S. K. (2003b). Two-dimensional numerical simulations of Arctic leads: Plume penetration height. *Journal of Geophysical Research: Oceans*, *108*(C2). doi: <https://doi.org/10.1029/2000JC000495>